Modeling of Compressed Air Energy Storage for Power System Performance Studies

by

Ivan Calero

A thesis
presented to the University of Waterloo
in fulfillment of the
thesis requirement for the degree of
Doctor of Philosophy
in
Electrical and Computer Engineering

Waterloo, Ontario, Canada, 2020

Examining Committee Membership

The following served on the Examining Committee for this thesis. The decision of the Examining Committee is by majority vote.

Supervisor:	Claudio Canizares Professor, University of Waterloo
Co-Supervisor:	Kankar Bhattacharya Professor, University of Waterloo
Internal Member:	Magdy Salama Professor, University of Waterloo
Internal Member:	John Simpson-Porco Professor, University of Waterloo
Internal-External Member:	Zhongchao Tan Professor, University of Waterloo
External Examiner:	Bala Venkatesh Professor, Ryerson University

I hereby declare that I am the sole author of this thesis. This is a true copy of the thesis, including any required final revisions, as accepted by my examiners.

I understand that my thesis may be made electronically available to the public.

Abstract

In the effective integration of large renewable generation for grid scale applications, pumped-storage hydro and Compressed Air Energy Storage (CAES) are currently economically and technically feasible alternatives to properly manage the intrinsic intermittency of energy sources such as wind or solar, with CAES being less restrictive in terms of its location. Furthermore, the relative fast response, and the possibility of physically decoupling the charging and discharging drive trains interfacing the grid through synchronous machines make CAES a suitable asset to provide ancillary services in addition to arbitrate, such as black start, spinning reserve, frequency regulation, and/or voltage regulation. Nevertheless, although the economic value of CAES having multiple stream revenues has been studied in the context of planning and operation of power systems, the actual impact of CAES facilities on the electrical grids have not been properly addressed in the literature, in part due to the lack of suitable models.

The existing CAES models proposed for power system studies fail to represent the dynamics, nonlinear relations, and physical restrictions of the main mechanical subsystems, by proposing simplifications that result in unrealistic dynamic responses and operating points when considering the entire CAES operating range, as is required in most ancillary services or during grid disturbances. Furthermore, the detail of these models and the controls used are inconsistent with the state-of-the-art modeling of other storage technologies such as batteries and flywheels. Hence, in order to bridge the gap in CAES modeling and control, this thesis propose a comprehensive physically-based dynamic mathematical model of a diabatic CAES system, considering two independent synchronous machines as interface with the grid, which allows simultaneous charging and discharging of the cavern, such as the recently inaugurated 1.75 MW CAES plant in Goderich, Ontario.

Detailed and simplified models are proposed based on the configuration of the Huntorf plant, in Germany, which is one of the only two existing large CAES facilities currently operating in the world. The system modeled comprises a multi-stage compressor with intercoolers and aftercooler, driven by a synchronous motor in the charging stage, an underground cavern as storage reservoir, a multi-stage expander with a recuperator and reheater between stages, and a synchronous generator in discharging mode, such as the aforementioned small CAES Ontario plant. The proposed thermodynamic-based dynamic models of the compressors and expanders allow calculating internal system variables, such as pressures, temperatures and power, some of which are used as controllable variables. Furthermore, different approximations to model the nonlinear relations between mass flow rate, pressure ratio, and rotor speed in the CAES compressors and expanders, determined by so called "maps", are proposed based on Neural Networks and physically-based nonlinear

functions; these constrain the operation of the turbomachinery, but are usually ignored in existing models.

A control strategy for active and reactive power of the CAES system is also proposed. The active power controller allows primary and secondary frequency regulation provision by the turbine and compressor. Special controllers are proposed to restrict the charging and discharging power of the turbine and compressor, to avoid pressure ratios that violate the restriction imposed by the cavern pressure. A surge detection controller for the compressor, and a controller that regulates the inlet temperature at each expansion stage are also presented, and these controls are complemented by a state of charge logic controller that shuts down the compressor or turbine when the cavern is fully charged or runs out of air, respectively. A coordinated droop-based reactive power control is also proposed for the parallel operation of the two synchronous machines, which is used to provide voltage regulation assuming both machines operate synchronized with grid. Finally, the implementation of a block-diagram based CAES model for transient stability studies in the DSATools TSAT® software is presented, based on a generic model architecture of the different CAES system's components and their interrelations.

The performance of the proposed models, with different levels of detail, are examined in various electrical system studies. First, the potential of a CAES system to provide primary and secondary frequency regulation in a test power system with high penetration of wind generation is evaluated in Simulink®, where the proposed CAES models are also compared with existing models. The voltage regulation, oscillation damping capability, and frequency and transient stability impact of CAES are also studied in a modified WSCC 9-bus test system using TSAT®. It is demonstrated that CAES is more effective than equivalent gas turbines to regulate frequency and voltage and damp low frequency oscillations, with the simultaneous charging and discharging operation significantly reducing the frequency deviation of the system in the case of large power variations in a wind farm. Furthermore, the effects on the overall frequency regulation performance of incorporating detailed models for some of the CAES components, such as expansion air valve, compressor and turbine maps and associated controls is also assessed, demonstrating how modeling these sub systems restricts the CAES response, especially in charging mode. Finally, the effect of the stage of charge control on the frequency stability of the system for different cavern sizes is investigated, concluding that if the power rating of the CAES system is large enough, small cavern sizes may not allow proper provision of frequency regulation.

Acknowledgements

First, I want to thank God for enlightening my path when I could not see further, for giving me strength when I felt weak, and for brining peace to my soul when I most needed it.

I would like to express my deepest gratitude to my supervisors, Professor Claudio Canizares and Professor Kankar Bhattacharya, for their outstanding guidance, encouragement and support during my graduate studies at the University of Waterloo. It was through their valuable knowledge and experience that I was able to complete this thesis work. As grad student, they opened many doors for me, for which I am truly grateful. It has been a privilege and honor to be supervised by such extraordinary professionals and human beings.

My sincere appreciation to my Ph.D. Committee members for their valuable comments and observations: Professor Magdy Salama and Professor John Simpson-Porco, from the Department of Electrical and Computer Engineering at University of Waterloo; Professor Zhongchao Tan, from the Department of Mechanical and Mechatronics Engineering at the University of Waterloo; and Professor Bala Venkatesh, from the Department of Electrical and Computer Engineering at Ryerson University.

I thankfully acknowledge the funding and support provided by the SENESCYT in Ecuador, the Canadian Natural Sciences and Engineering Research Council (NSERC), Ontario Centre for Excellence, Rocky Mountain Power, Ontario Power Generator, NRStor, Union Gas, Compass Minerals, and the NSERC Energy Storage Technology Network. My recognition goes also to the CAES research group at the University of Waterloo, especially Professor Maurice Dusseault, Professor Roydon Fraser, Sean, Jorge and Sid.

I am greatly indebted to my colleagues from the Institute of Control Systems at the Karlsruhe Institute of Technology, in Germany, especially Professor Soren Hohmann, for hosting me and making my research visit very pleasant.

I want to thank my friends and colleagues from the EMSOL lab: Amir, Baheej, Behnam, Bharat, Carlos, Chioma, Dario, Dante, David, Edson, Emin, Enrique, Fabricio, Hisham, Indrajit, Jean-Michell, Juan Carlos, Mauricio, Mariano, Matheus, Mostafa, Nafeesa, Nitin, Omar, Samuel, Sofia, Talal, and William. It was a pleasure sharing all this time with you.

Finally, I am eternally grateful to my parents, Gladys and Fabian, my sister Diana, my brother Fabian, and especially my wife Jessica, for their tireless support during the past years, and for always encouraging me to be the best I can be.

Dedication

I dedicate this thesis to the love of my heart, Ivanna.

Table of Contents

List of Tables

List of Figures

List of Acronyms

AGC Automatic Generation Control
AVR Automatic Voltage Regulator

BESS Battery Energy Storage System

CAES Compressed Air Energy Storage
CCT Critical Clearing Time
CMB Compressor Map Block

DAE Differential-algebraic System of Equations
DLB Dynamically Linked Control Block

EPRI Electric Power Research Institute
ESS Energy Storage System

FACTS Flexible AC Transmission Systems

GT Gas Turbine

IESO Independent Electricity System Operator
IGV Inlet Guide Vane
ISO Independent System Operator

LFC Load Frequency Control

NN Neural Network

PFR Primary Frequency Regulation
PI Proportional Integral
PID Proportional Integral and Derivative
PMSM Permanent Magnet Synchronous Machine
PSS Power System Stabilizer

SC Supper Capacitor
SFR Secondary Frequency Regulation
SLC Surge Logic Control
SMES Superconducting Magnetic Energy Storage
SoC State of Charge
SVC Static VAR Compensator

UDM User Defined Model

VSC Voltage Source Converter

WECC Western Electricity Coordinating Council

Nomenclature

Parameters

$\Delta\pi_{mrg}$	Surge control margin [kg.s^{-1}/unit of pressure ratio]
$\Delta p_{\min}$	Minimum pressure drop in the discharging valve [bar]
ΔT_o	Nominal inlet temperature rise of the LP expander with respect to HP expander [K]
$\dot{\lambda}_{\max}$,$\dot{\lambda}_{\min}$	Valve rate limits [p.u./s]
ϵ	Effectiveness
η	Efficiency [p.u./p.u.]
γ	Heat capacity ratio c_p/c_v
$\lambda_{\max}, \lambda_{\min}$	Valve maximum and minimum limits [p.u.]
μ	Flow coefficient due to friction
ν_w	Wind speed [m/s]
Φ	Compressor's stage power constant [p.u./K]
π	Pressure ratio
ρ	Air density [kg/m^3]

τ	Time constant [s]
τ'_{d0}, τ''_{d0}	d-axis open circuit transient and subtransient time constants, respectively [s]
τ'_{q0}, τ''_{q0}	q-axis open circuit transient and subtransient time constants, respectively [s]
τ_3	Radiation shield time constant [s]
τ_4	Thermocouple time constant [s]
τ_{AV}	Air valve positioner time constant [s]
τ_{CA}	Compressor air dynamics time constant [s]
τ_{CD}	Compressor volumetric time constant [s]
τ_{Dr}	Compressor transient droop time constant [s]
τ_{hx}	Inter/aftercooler time constant [s]
τ_{IGV}	IGV system time constant [s]
τ_P	Power transducer time constant [s]
τ_R	Recuperator time constant [s]
τ_{SF}	Fuel system time constant [s]
τ_S	Fuel valve positioner time constant [s]
τ_{TD}	Turbine discharge delay [s]
τ_{TD}	Turbine's air transportation delay time constant [s]
ζ	Stability margin
A	Compressor equivalent cross sectional area in Greitzer's model [m^2]
A_T	Throttle equivalent cross sectional area in Greitzer's model [m^2]

a_1	Compressor's map coefficient
a_2	Compressor's map coefficient
b	Compressor map parameter
c_2	No-load fuel consumption constant [p.u.]
c_p	Specific heat capacity at constant pressure [kJ/kg.K]
c_v	Specific heat capacity at constant volume [kJ/kg.K]
D	Damping power coefficient [p.u.]
F	Fuel control limit [p.u.]
FL	Flag to operate machines as synchronous condensers
$g_{\max}, g_{\min}$	Turbine's air mass flow rate limits [p.u.]
H	Inertia constant [MW.s/MVA]
K_4	Radiation shield gain
K_5	Radiation shield gain
K_{AGC}	AGC gain
K_{c_d}	Compressor's governor derivative gain
K_{c_f}	Frequency of filter differentiator
K_{c_i}	Compressor's governor integral gain
K_{c_p}	Compressor's governor proportional gain
K_{cv}	Compressor's pressure limit controller gain
K_c	Compressor valve constant [bar/p.u.]

K_{droop}	Compressor transient droop
K_{sgn}	Surge detection controller gain
K_{sgp}	Surge detection controller gain
K_{T_i}	Temperature controller integral gain
K_{t_i}	Turbine's governor integral gain
K_{T_p}	Temperature controller proportional gain
K_{t_p}	Turbine's governor proportional gain
K_{vr}	Proportional gain of reactive power controllers
L	Compressor equivalent length in Greitzer's model [m]
L_T	Throttle equivalent length in Greitzer's model [m]
$l_{\max}, l_{\min}$	IGV maximum and minimum limits [p.u.]
N	Compressor speed [rpm]
p_{offset}	Pressure offset of compressor's pressure limit controller [p.u.]
R	Regulation characteristic [p.u.]
r	Machine's armature resistance [ohm]
Sn	Nominal apparent power [MVA]
$T_{hx_{in}}$	Inter/aftercooler cold-side input temperature [K]
T_s	Cavern temperature [K]
X_d, X'_d, X''_d	Steady-state, transient, and subtransient d-axis reactance [p.u.]
X_q, X'_q, X''_q	Steady-state, transient, and subtransient q-axis reactance [p.u.]

R	Specific gas constant [J/kg.K]
v	Volume [m^3]

Variables

β	Reactive power sharing factor
χ	Specific volume [m^3/kg]
Δ	Variation
δ	Machine's rotor angle [rad]
$\dot{m}_f$	Fuel mass flow rate [kg/s]
$\dot{m}$	Air mass flow rate [kg/s]
$\dot{q}$	Heat transfer rate [W]
Γ	Compressor's stage temperature gain
Λ	Cross-sectional area [m^2]
λ	Dimensionless cross-sectional area [p.u.]
λ'	Turbine's governor output
H	Enthalpy [J]
ν_s	PSS control signal [p.u.]
ω	Rotor speed [rad/s]
ϕ	Machine's power factor [rad]
Π	Effective pressure ratio
π	Pressure ratio

σ	Specific internal energy [J/kg]
θ_V	Machine's terminal voltage angle [rad]
C	Heat capacity rate [W/K]
E	Electromotive force (emf) [V]
E''_d, E''_q	Subtransient emfs in d- and q-axis, respectively [V]
E'_d, E'_q	Transient emfs in d- and q-axis, respectively [V]
E_f	Internal machine emf proportional to field voltage [V]
h	Specific enthalpy [J/kg]
I	Current [A]
I_d, I_q	Machine's current in d- and q-axis, respectively [A]
m	Mass [kg]
m_d	Discharging air mass flow rate in Greitzer's model [kg/s]
P	Active Power [MW]
p	pressure [bar]
Q	Reactive Power [MVAr]
q	Heat transfer [J]
SoC	State of Charge [p.u.]
srg	Boolean output signal of SLC block
T	Temperature [K]
U	Internal energy [J/kg]

u	Boolean output signal of SoC logic control
V	Voltage [V]
v	Dynamic state variable [p.u.]
V_d, V_q	Machine's terminal voltage in d- and q-axis, respectively [V]
W	Work [J]
y	temperature controller PI's output variable
$\bar{}$	Per unit
$\tilde{}$	Phasor quantity
$\dot{}$	Rate of change

Sub- and Super- scripts

max	Maximum
min	Minimum
w	Wind
am	Ambient
b	Inlet to the high pressure burner
c	Compressor
crr	Corrected
d	Inlet to expander
f	Fuel
g	Generator

HP	High pressure
hx	Heat exchanger
i	Isentropic
in	Input
j	Index of compression stages
k	Index of expansion stages $k = \{LP, HP\}$
LP	Low pressure
m	Mechanical
map	Quantity on compressor map
mot	Motor
o	Nominal
out	Output
pl	Plenum
r	Recuperator
ref	Reference or initial value
ref	Reference value
s	Cavern
ss	Steady-state
t	Turbine
v	Valve
x	Exhaust

Chapter 1

Introduction

1.1 Motivation

In modern times, energy has played a transcendental role in society, and among the different sources that comprise the energy mix, electricity is preponderant, especially nowadays with the electrification of heating systems and transportation. Moreover, the climate change problem has influenced governments to implement and enforce legislations to migrate from fossil-fuel-based energy supply to renewable-based or "green" energy. In this context, the integration of renewable generation, such as wind and solar in electricity grids has been growing significantly in recent years, to help achieve this goal. Actions have also been taken on the demand side, to reduce the energy consumption by increasing the efficiency of equipment and processes, and by substituting fossil-fuel-driven equipment with electrical appliances, as in the case of gas furnaces and water heaters. Furthermore, the automobile industry has also started large-scale manufacturing of electric vehicles as an alternative to conventional fuel engine vehicles. However, all these developments and transition to new technologies rely on efficient and reliable electrical grids, which are the central tenent for an effective integration.

In this scenario, researchers have made significant efforts in studying the mechanisms and developing new technologies to enhance the reliability and security of power systems, while also taking into account their efficiency, sustainability and economic aspects. As a result, power system components, such as Flexible AC Transmission Systems (FACTS) and Energy Storage System (ESS) have emerged, with several technological barriers being overcome and production costs decreasing [1].

In the case of ESS, these have proved to be suitable to provide support to the electricity grid by enhancing the system reliability (adequacy and security) by damping the effects of the variability of renewable generation and demand, providing voltage and frequency regulation, enhancing power quality, etc. [1, 2]. In particular, large-scale ESS provide Independent System Operators (ISOs) with the flexibility required for electric transmission grids [3]. Pumped-storage hydro and Compressed Air Energy Storage (CAES) are the only two economically and technically feasible alternatives for bulk storage [4, 5], with CAES being less restrictive in terms of its location, especially in North America, where abundant geological formations suitable to host underground caverns for air storage are available [6].

In the province of Ontario, in Canada, the potential of energy storage to enhance grid operations is being evaluated by the Independent Electricity System Operator (IESO) through a two-phase procurement of 50 MW of ESS, deployed at specific locations within the province [7], one of which is a 1.75 MW adiabatic CAES facility with decoupled charging and discharging phases in Goderich, Ontario [8]. Based on the experiences gained, the IESO has provided some recommendations for future ESS developments. For instance, it suggests that new investments in ESS projects, seeking to connect to Ontario's grid, should consider the provision of multiple services, in addition to energy arbitrage for them to become economically viable. It also identifies large cyclicity durations as another factor that positively influences the success of ESS ventures. Therefore, since CAES is capable of providing multiple services and has the size advantage over other storage technologies, the expectation of success from CAES is high.

To this effect, studies to determine if a particular ESS installation is able to operate without grid restrictions, are needed, because there may exist some electrical regions where grid limitations due to transmission congestion can impede their optimal and efficient operation. Consequently, CAES can be envisioned to participate not only in the energy market, but also in ancillary services such as operating reserve markets, thus expanding the business opportunities for investors. This necessitates evaluating the performance of CAES in these additional markets. In particular, frequency regulation provision from CAES is attractive because of their fast ramping capability, relatively large size, and the inertia added to the system, which might not be the case for other ESS technologies [6, 9].

From the geological perspective, there are some places in Ontario where salt and porous-rock deposits spread out, and where hydrocarbons have also been discovered [10]. These porous-rock caverns are mostly available above the Guelph reefs. The authors claim in [10] that some depleted hydrocarbon reservoirs in the Lambton County, which lie within the Guelph reefs, and have been converted into natural-gas storage deposits, can be feasible option for CAES facilities. Furthermore, bedded-salt deposits exist along the western margin of the Michigan basin, from Amherstburg northward to Kincardine, and the Windsor region, where previously-mined sites could be exploited as CAES reservoirs. Also, since southwestern Ontario has solar and wind resources, this region is even more attractive for CAES to mitigate the associated intermittencies of their supply. This requires power system studies for bulk CAES facilities connected to the grid, taking into account the operational constraints associated with injecting energy at this location [7].

From the aforementioned discussions, it can be concluded that CAES systems can yield significant and unique benefits to the system from participating in different markets, compared to other ESS technologies, and that there exists the appropriate geology, particularly in Ontario, to host new CAES facilities. However, there are still barriers that need be overcome for effective deployments of this technology, one of which is the lack of adequate models that allow to assess the actual value of these systems, based on the understanding of their technical capabilities and limitations.

The lack of models can be attributed to the limited data availability and little research on CAES, because only few actual CAES projects have been installed worldwide, despite being a relatively old storage technology. Only two bulk CAES facilities are currently operating: the 290 MW Huntorf CAES plant in Germany, and the 110 MW McIntosh facility in Alabama, USA [6, 11–13], and some small-scale prototypes [4–6, 8], while other large-scale projects are still under development, such as the 324 MW Bethel CAES project in Texas, USA, planned to be in commercial operation in 2022 [14]. Accurate enough CAES models would allow the ISOs, utilities and project developers to evaluate the impacts of new CAES systems connected to power grids, when these operate in normal and abnormal conditions, and also to understand their potential to provide services in addition to arbitrage, such as voltage and frequency regulation. For this, the models should be able to represent the CAES system for its entire operating range; therefore, limits and controls need to be modeled as well.

Most of the existing CAES models aim to study the thermodynamic properties of its components, such as the efficiency of the compressor and expander [15], while only a few attempted to model the CAES system connected to an electric grid. However, such works have several limitations, such as the use of impractical electrical machines as interface with the grid, unrealistic representation of the turbomachinary (compressor and turbine), and limited or lack of control systems.

An additional issue that grid planners face when representing a new system, such as ESS, for grid studies, is the lack of generic models that allow comparison of different equipment designs, specifications, or even different providers by simply parameterizing the model. In this context, proposing generic ESSs models which can be realized in commercial power system software has been the focus of several researchers; for example, the Western Electricity Coordinating Council (WECC) and the Electric Power Research Institute (EPRI) in [16] have proposed generic transient-stability models of Battery Energy Storage Systems (BESSs), which have been adopted by various software packages including Powertech's TSAT®, [17]. However, while researchers have concentrated on standardizing these models for storage technologies such as BESS or Flywheels, Compressed Air Energy Storage has received little attention.

Based on the aforementioned discussions, it is clear that the development of new models to study CAES systems connected to the grid should help provide sufficient insights into their interaction with the rest of the system, overcome the lack of information, and allow developing adequate market and operation rules, thus enabling effective future CAES deployments. This is specially important for Ontario, not only because of the interest of the IESO to promote installation of ESS, but also to exploit the favorable geological features in the western region of the province for hosting CAES caverns; thus, the effective incorporation of a bulk CAES facility would enhance Ontario's grid performance and efficiency.

The main objective of this research is, therefore, to fill some of the aforementioned gaps by proposing generic steady-state and dynamic models of a CAES facility. These models need to be suitable for power system applications, and could be used to study the performance of the CAES system to improve the overall grid stability, and its effectiveness to provide different grid services, such as frequency and voltage regulation. This research will concentrate on modeling multi-stage diabatic CAES systems, since the two existing large CAES facilities are diabatic, i.e., the air is preheated using natural gas before expansion; one of the leading technology developers of CAES systems worldwide, Siemens Dresser-Rand, which was in charge of developing the McIntosh CAES facility, has proposed new diabatic CAES systems as an efficient solution for large facilities, enhanced by more efficient multi-stage axial and centrifugal compressors and multi-stage expanders with burners within stages [9]; and the new large-scale Bethel project is both diabatic and has independent charging and discharging phases [14].

1.2 Literature Review

The literature review presented in this section exclusively concentrates on CAES modeling and applications to power systems; operational and planning models are not addressed here as these are out of the scope of this thesis. The literature review is organized to cover the two main areas addressed in this research: state-of-art of CAES modeling and applications.

1.2.1 Sate-of-the-art in Compressed Air Energy Storage Modeling for Power Systems

Thermodynamic Based Steady-state and Dynamic Models

Most of the existing research on CAES modeling concentrates on describing the thermodynamic processes involved in the compression of the air in the cavern and its expansion when out of the cavern, with the aim of quantifying its performance through the calculation of efficiencies for specific steady-sate conditions [15, 18]. In these works, the changes in the pressure and temperature, and the mechanical work done at each expansion and compression stage are modeled either as polytropic or isentropic processes, assuming that the air behaves as an ideal gas. Some of the models also incorporate dynamic behaviour of the variables, such as in [19], where an adiabatic CAES plant is modeled, considering the dynamics of the rotational inertia in the compression and expansion trains, the thermal inertia of the heat exchangers and thermal storage element, and the long-term dynamics of the cavern. Similarly, [20] studies the maximum energy that can be stored in a CAES cavern (exergy) for three different types of cavern walls: adiabatic, isothermal, and one in which heat can be transferred through the cavern's walls as a result of finite temperature difference between the air and its surroundings. Dynamic models for each type of cavern walls are presented, and the dynamic response of a CAES facility for fixed charging and discharging mass flow rates in both constant-volume (isochoric) and constant-pressure (isobaric) caverns is simulated. Similar models have been used in [21] and [22] to study the long-term dynamics in the charging and discharging of the cavern, while [23] performs a sensitivity analysis of the efficiency of the charging and discharging processes for different operating conditions. Although all these models accurately represent the thermodynamic relations of the CAES internal elements, they have several disadvantages that limit their direct application for power system studies. The most noticeable is that these neglect the electrical machines, and consequently, there are no explicit interfaces that allow their interconnection with electrical systems. Indeed, in the few cases where dynamics of the spinning masses of the rotors are considered, the electrical power is assumed to be a fixed parameter; otherwise, the mechanical power consumed or supplied by the CAES system is directly assumed to be equal to the electrical power multiplied by an efficiency representing the conversion process. Furthermore, the control systems are not modeled, as these works assume that the CAES system is capable of modifying the control variables such as airflow or electrical power at command, and thus the effects of the controllers and their dynamics on the turbomachinary response are neglected. Finally, these models assume that the compressor cannot be controlled as its operating point is fully defined by the pressure in the cavern.

CAES Models Proposed for Power Systems

The aforementioned limitations have been partially addressed by models specifically proposed for CAES systems connected to electrical grids, involving the exchange of active and reactive power. The most relevant are discussed next.

References [24] and [25] propose the model of a CAES facility for transient stability analysis, which includes: an induction machine used as motor/generator, the compressor, and the turbine. A reciprocating compressor is modeled using algebraic equations in which the compressor displacement is a linear function of the rotor speed, while the turbine mechanical power as a linear function of the fuel flow and rotor speed as in a traditional Gas Turbine (GT) model. The proposed control uses a PI regulator to modify the turbine power by acting on the fuel control system to maintain the speed at its nominal value. The CAES system is tested in a single-machine connected-to-the-grid system, and on a single-machine supplying a load for various contingencies. However, the proposed model in [24] and [25] has several flaws; for example, for large-scale CAES applications, axial and centrifugal compressors are the preferred turbomachinery, as opposed to reciprocating or scroll compressors, which are mostly used in small-scale isothermal compression. The storage reservoir is not modeled either; hence, the compressor pressure ratio is fixed and its mechanical power becomes a linear function of the rotor speed only. Also, the use of an induction machine is not justified, since compressors and turbines, being highly sensitive to variations of their speed, cannot be properly controlled using induction machines, thus having negative impacts on the CAES performance during transients. Furthermore, the proposed control assumes the CAES system is controlled as a GT, i.e., the output power of the turbine is controlled by burning gas; however, in actual CAES systems, the output power is controlled by adjusting the airflow in the expansion [13].

In [26], the use of CAES for frequency control in systems with high levels of wind penetration is investigated. Two different configurations of CAES are described: an external compressed-air tank to enhance the combustion in the chamber of a regular GT; and an independent CAES system comprising a tank, a synchronous generator, a GT that uses the remanent heat from the expansion of another regular GT (as in a combine-cycle), and an independent synchronous motor driving a compressor to compress the air in the tank. The thermodynamic model of both options, and the control schemes for their operation are presented. For the second option, which is more relevant to this thesis, it is shown that the fast response of the CAES unit in supplying power to the system, enhances system frequency regulation. Similarly, when operating in charging mode, the input power of the motor can be reduced by decreasing the mass of air injected into the compressor by appropriate control of its inlet guide vanes. The CAES system does not burn gas;

conversely, it is assumed that the exhaust heat of the main GT is enough to increase the air temperature before the expansion in the CAES; however, this heat is not constant and depends on the power generated by the main GT, which is not considered by the authors. Also, the compressor is modeled as an isothermal process, which is not realistic for large systems, and requires additional controls, which have not been modeled either, to keep its temperature constant. Furthermore, the intercoolers and aftercooler in the compressor are not modeled, but assumed to reduce the discharge temperature of the compressor up to the tank temperature, regardless of its operating point. However, this temperature varies with the pressure ratio because the compressor does not have temperature control. Finally, the electrical machines are not modeled, because the CAES is study for frequency regulation.

Reference [27] presents a dynamic adiabatic CAES model comprising heat exchangers, heat storage, air storage (tank), and ideal compressor and expander to investigate the control and management of the heat storage and tank. The compression and expansion are modeled as adiabatic processes, while the heat exchangers are modeled as distributed-parameter devices. The tank model considers pressure dynamics and the heat storage device considers temperature dynamics. However, this model assumes individual electrical machines per stage of compression and expansion, which is unrealistic, especially for the size of the system (50 kW). Furthermore, a PI controller is said to be used to control the electrical power of the machines to a reference value; however, neither the control system nor the electrical machines and their interconnection with the mechanical systems are discussed.

Some CAES models have been proposed in which the active power exchanged with the grid is first rectified through a Voltage Source Converter (VSC), and then re-converted to ac power through another VSC before being injected back into the grid. The reason for this additional conversion process is to either couple the CAES system with other devices in a dc link, as in [28, 29], or to have a more efficient control assuming asynchronous machines are used as in [30]. Thus, in [28] a steady-state multistage compression-expansion CAES facility coupled with a wind farm is studied. However, the work neglects the dynamics associated with CAES operation, such as the control systems, measurement systems, and intercoolers. Furthermore, the key elements such as the cavern, heat storage or gas burners if the system burns gas, are not modeled either. The model of [28] has also been used in [29], and improved in [30] by adding active and reactive power controls and the pressure dynamics in the storage reservoir. Thus, in [30], a VSC is used as interface between the grid and two CAES induction machines (one acting as motor and the other as generator), which is based on a dq0-frame control for independent active and reactive power. However, it assumes a single stage of compression and expansion, which is not realistic for a cavern pressure of 30 bar. Also, since gas is not burned, the CAES system in [30] must be adiabatic; however, the source of heat is neither discussed nor modeled. Furthermore, the use of two VSCs to connect the CAES induction machines would considerably increase the cost, compared to two synchronous machines, because the converters must be properly sized to handle large discharging and charging powers. Finally, a linearized version of a CAES system is also proposed in [30], which further neglects the tank dynamics; thereby, the CAES system is only represented by the spinning masses of the rotor.

In [31], a CAES model is discussed in which a self-excited induction machine connected to the grid through a back-to-back VSC is used, which drives the compressor and turbine. In this system, there is no valve to control the expansion of the air; therefore, the mechanical power in the discharging mode changes with the pressure in the storage tank, thus limiting the use of the CAES system for active power control. Furthermore, the CAES turbine and compressor models are simple, as the generated/consumed power is a linear function of the mass flow rate.

The model of a CAES system to smoothen the power delivered to the grid by a 2 MW wind turbine is presented in [32]. As in [30], a VSC is used as interface; however, the CAES system, which is used as buffer for the wind energy is connected to a common dc link between the rectified wind power and the electrical grid. Also, the CAES electrical machines are not modeled, and thus the interactions between these and the converters are ignored. The system is modeled by steady-state equations only, except for the cavern, and the CAES side converter controller is just a first-order transfer function with a proportional gain for active power control.

The model of a CAES system operating along with a Supper Capacitor (SC) is presented in [33]. The CAES unit is connected to the grid through back-to-back VSCs and the SC coupled in the dc link. In this hybrid system, the CAES tank is charged and discharged by a pneumatic turbine/compressor attached to a Permanent Magnet Synchronous Machine (PMSM). The SC is used to smoothen the power exchanged with the grid, as the tank is charged/discharged to maximize the efficiency of the pneumatic machine. Research on modeling small CAES systems similar to [33] is found in, for example, [34], [35] and [36]. However, the type of electrical machines (reluctance machines, PMSM), and compressors and expanders (pneumatic or reciprocating machines) modeled in these works have not been used and are not practical in either adiabatic or diabatic bulk CAES systems; therefore, neither the models nor the controls are relevant for the studies presented in this thesis.

Even though some works have proposed using VSCs to interface the CAES electrical machines with the power grid, this configuration is impractical for bulk CAES systems. First, large converter ratings would be required to handle the also large charging and discharging powers, thus increasing the overall cost of the CAES system. Second, the additional converter losses would reduce the overall system efficiency. Finally, since synchronous machines connected to compressors or turbines can effectively regulate frequency and voltage, adding VSCs for control purposes is redundant. It is important to mention that the advantages of VSCs for small generator such as diesel and microturbines, which allow to decouple the system frequency from the generator speed to improve the mechanical systems efficiency [37], would not be advantageous for large CAES applications, since this would negatively affect the frequency control characteristics of the plant, reducing inertia and complicating the frequency controls of the system [38, 39]. Furthermore, induction machines, which operate at different speeds depending on the load, would complicate the CAES turbine's control, especially for the compressor, which is sensitive to speed [40]; synchronous machines, on the other hand, do not deviate much from their nominal (synchronous) speed.

Studying CAES to provide grid services, such as frequency regulation, or to evaluate its behaviour during disturbances requires simulating the system on a wide range of operating conditions. In this context, modeling the nonlinear relations between the mass flow rate, rotor speed, and pressure ratio in the compressor and expander is important, as these impose physical limits on the CAES operation. However, the CAES models proposed for power systems, discussed thus far, assume that the mechanical power is linear with respect to the mass flow rate (or volume flow rate), which is used as an independent control variable. This assumption greatly simplifies the model complexity, but is not realistic as the aforementioned existing nonlinear relations between the turbomachinery variables, captured in compressor and turbine maps provided by equipment manufacturers, are ignored.

Few CAES models that incorporate compressor and turbine maps have been proposed. Thus, in [41], for example, a small-scale CAES system, mechanically coupled with a wind turbine, is modeled, wherein a scroll-compressor is used for both compression and expansion, both modeled as orifices. The mass flow rate is a function of the pressure ratio and input temperature at the compressor or turbine; however, only the dynamics of the storage tank are modeled. In [42], the turbine map of a diabatic CAES system is modeled using the so-called Stodola equation [43], while the compressor map is represented by an empirical nonlinear equation. However, the electrical systems are not considered, and although some control strategies for the operation of the CAES system are mentioned, their modeling and implementation is not addressed. Furthermore, a distributed-parameter heat-exchanger model is used, requiring the solution of partial differential equations for each step of integration, which would make its application less practical and cumbersome for implementation in a commercial power system software package. Similarly, in [44], the charging and discharging processes of the CAES cavern are analyzed assuming choked and unchoked airflow conditions through a nozzle (inlet to the cavern); however, the compressor and turbine are not explicitly modeled. Furthermore, the charging and discharging powers of the CAES system cannot be controlled, as these two variables are modeled as a function of the pressure in the storage tank; the electrical systems are not modeled either.

In [45] and [46], a CAES system is modeled using compressor and turbine maps. However, the maps are incorporated through look-up tables, which require an iterative process and interpolation to yield the current operating point of compressor or turbine in the map, thus increasing the simulation times considerably and therefore, is not practical for power systems studies involving grid connection.

1.2.2 Compressed Air Energy Storage Applications in Power Systems

In this section, research work that concentrates more on studying CAES for particular power system applications, rather than on the modeling, are discussed. Thus, references [47] and [48] use a CAES system to enhance the transient stability of a wind farm by providing dynamic reactive power compensation. The authors propose using a CAES system as a synchronous condenser when it is in discharging or idling operating modes. The simulations show that CAES could be more effective than a Static VAR Compensator (SVC) to improve the transient stability of stall-controlled wind turbines under fault conditions by regulating the voltage at the wind farms's terminals. However, the mechanical systems are not modeled, and therefore, the effects of active power controls (e.g., primary frequency regulation) in response to system disturbances are not properly captured. Furthermore, the voltage regulation of the CAES system is studied for charging mode only.

In [26], the authors conclude that CAES can be used to improve the frequency regulation of the system by increasing the turbine power and reducing the compressor power when the frequency drops; however, this is not fully analyzed. In [49], the connection of a synchronous-generator-based CAES system to a power grid supplied by another synchronous generator is also studied. The voltage and frequency regulation of the system, which are provided by the main synchronous generator, is simulated when a load change occurs, followed by the connection of the CAES system. Since the CAES system is considered in discharing mode, its output power helps recover the system frequency faster; therefore, the authors conclude that CAES has the potential to contribute to the frequency regulation. However, the output power of the CAES is modeled using a pre-defined look-up table that maps Δt to P_{out}; hence, its potential to contribute to the frequency regulation is not properly captured. Furthermore, since the CAES is based on synchronous machines, which are not modeled, its ability to provide voltage support is also omitted.

In [50], an adiabatic CAES system is used to smoothen the power injected by a wind turbine into an electrical grid. In the system studied, the wind turbine, compressor, expander, and PMSM are attached to the same rotor, with the generator being connected to the grid through a back-to-back VSC. Valves to control the compressor and turbine are used to complement the mechanical power when the wind speed is too low, or use the compressor to consume the excess of mechanical power when the wind speed is too high. Similar applications are studied in [32]. However, in these works, the CAES system is not connected to a power grid, hence, the effective integration of the wind power is not demonstrated.

1.2.3 Discussion

Tables 1.1 and 1.2 summarize the main characteristics of the CAES models and applications reviewed in the previous Section. In the second column of Table 1.1, the main features of the existing CAES technical literature are organized in five groups: CAES configuration, electrical subsystems, mechanical subsystems, controls, and power system applications and studies, with sub-classifications. In Table 1.2, the same information is organized in matrix form, which helps to visualize the state-of-the-art on CAES modeling and applications. The columns represent the features or sub-classifications numbered in Table 1.1, while the rows represent the reference numbers. When a reference has proposed or used a CAES model with a particular feature, the corresponding matrix entry is colored in blue. Since this thesis concentrates on modeling two-machine diabatic bulk CAES systems, references that do not focus on these characteristics have been colored in red. A diabatic CAES model and applications consistent with the objectives of the present research should have the whole row colored blue, except columns 1, 5, 6, and 8.

Observe that most of the references with fairly complete mechanical models do not include controls, neglect the electrical systems, and do not consider power system applications. Conversely, those references that model the electrical subsystems use incomplete models for the mechanical systems, and, most importantly, are based on either induction machines, PMSM, or VSC, which are not the preferred options for bulk CAES systems, as previously discussed, which use synchronous machines [13]. Furthermore, some works focus on small-scale applications only, and are not suitable for bulk CAES system applications, because the latter have additional components that are not considered in small systems, such as burners, intercoolers, recuperators, etc. Finally, most of the CAES systems proposed for electrical studies are adiabatic, while this thesis concentrates on diabatic systems.

Table 1.1: Literature review summary

	Model Features and Applications	References
	CAES Configuration	
1	Adiabatic	[18, 19, 26–34, 42, 46, 50]
2	Diabatic (gas required)	[15, 22–25, 35, 36]
	Electrical Subsystems	
3	Independent motor and generator (2 machines)	[26, 30, 45, 46]
4	Both synchronous machines	[32, 47, 48]
5	Induction machines, PMSM or other machines	[24, 25, 28, 30, 31, 33–35, 41, 45, 46]
6	VSC interface	[29–31, 33, 34]
	Mechanical Subsystems	
7	Polytropic, isentropic or adiabatic compressor and expander.	[15, 18, 19, 23, 26–30, 32, 36, 42, 45, 46, 50]
8	Linear function for compressor or turbine power	[24, 31, 49]
9	Heat exchangers	[15, 18, 19, 23, 26, 27, 32, 42, 50]
10	Burners (diabatic)	[15, 23]
11	Dynamics of thermal systems	[19, 27, 42]
12	Air dynamics	[26]
13	Rotating masses dynamics	[19, 24–26, 28, 30, 31, 33, 34, 41, 42, 45–48]
14	Multistage compression or expansion	[15, 18, 27, 28]
15	Compressor/turbine maps or approximate functions	[15, 19, 41, 42, 44–46]
16	Cavern dynamics modeled	[15, 18–22, 26–28, 30, 32–34, 41, 42, 44–46, 50]
	Controls	
17	Active power control	[24–26, 30, 32–34, 45, 46]
18	Reactive power control	[30, 47, 48]
19	Frequency regulation	[24–26]
20	Mass of flow rate control	[30, 42]
21	Fuel flow control (diabatic)	[24, 25]
	Power System Applications and Studies	
22	CAES connected to a power system	[24–26, 30, 47–49]
23	Frequency regulation	[26, 49]
24	Reactive power compensation	[47–49]
25	Transient stability	[24, 25, 28, 30, 47, 48]
26	CAES supplying fixed load or buffering energy	[15, 19, 22, 31–35, 41, 42, 45, 46, 50]
27	Efficiency, exergy or temperatures calculations	[15, 18–23, 27–29, 42, 44–46]

Table 1.2: Matrix of model features and applications

Ref.	Conf.		Elec. subsys.				Mech. subsys.										Controls					Applications					
	1	2	3	4	5	6	7	8	9	10	11	12	13	14	15	16	17	18	19	20	21	22	23	24	25	26	27
[15]																											
[18]																											
[19]																											
[20]																											
[21]																											
[22]																											
[23]																											
[24]																											
[25]																											
[26]																											
[27]																											
[28]																											
[29]																											
[30]																											
[31]																											
[32]																											
[33]																											
[34]																											
[35]																											
[36]																											
[41]																											
[42]																											
[44]																											
[45]																											
[46]																											
[47]																											
[48]																											
[49]																											
[50]																											

Blue: model with features as per column headers. Red: undesirable features for 2-machine diabatic CAES.

Achieving the large pressure ratios to compress the air from ambient conditions to cavern pressure and expand the air from cavern pressure to ambient pressure requires multiple stages of compression and expansion. Although such modeling approach has been presented in a few works aiming to study the efficiency of a CAES system, none have been used in models for power systems. Not modeling the compressor and turbine as multi-stage devices has implications in the mechanical power, mass of air flow and temperatures, calculations, as well as in the dynamics of the components that are, as a result, not modeled, such as intercoolers and reheaters.

A major limiting factor in CAES operations are the actual nonlinear relations between the air flow, speed and pressure ratios in the turbine, especially in the compressor. These nonlinearities are modeled through compressor and turbine maps, which are neglected in most models, especially in those involving electrical studies. Indeed, most of the proposed models have a significant flaw in the calculation of the mechanical power of the compressor or expander, as these assume that the pressure ratio and air flow (or volume flow) are independent. This simplistic assumption facilitates the control and the model implementation, which is not accurate, especially for the compressor.

Very few works consider two independent machines, and only one assumes these are synchronous machines, for the expansion and compression stages, which is one of the main contributions of this thesis. Furthermore, no work has explored the operation of one synchronous machine in idling, while the other injects/consumes power from the grid, or their simultaneous operation in charging/discharging modes, which can be advantageous to enhance the participation of CAES in different markets as suggested in [9] and [14].

Modeling the dynamics of the CAES components and their controls are two areas where significant and relevant contributions are made in this thesis. The dynamics of the rotating masses and the long-term dynamics of the cavern are commonly modeled, as noted in the reviewed works; however, important dynamics, such as those in the intercoolers and after-cooler, delays due to air inertia, valves, measurement systems, transducer, etc., have not been modeled. Furthermore, proper control strategies are superficially addressed in some papers, most of which claim to have power tracking capability, but without actually introducing those controls. A couple of works propose actual controls for frequency regulation; however, these are limited to primary frequency regulation, and the simplifications these make on the mechanical system modeling compromises their practical validity, because physical limits are not considered. Furthermore, in diabatic CAES, the fuel (gas) control system, which is necessary to adjust the temperature of the air at the expanders' inlets has not been studied although its operation has significant impact on the active power during transients. Also, reactive power control has not been addressed for a CAES system where two machines operate in parallel, as is the system considered in this thesis, which requires a special control logic to redistribute the reactive power between the two machines

No controls associated with the State of Charge (SoC) have been proposed, and no study has been carried out to understand the effects of the cavern pressure on the compressor and turbine controls, which may restrict the dynamic response of a CAES system when connected to a power grid. Similarly, surge prevention control, which is an undesirable condition that could occur during transients involving fast reduction of air flow, has not been considered in any CAES model proposed thus far for power systems. Finally, even though some of the discussed papers introduce models to address a particular CAES application, none of them have proposed a unified model that includes all its components, i.e., cavern, turbine, compressor, generator, motor, and controls.

In terms of applications, it can be observed that the work related to CAES concentrates mostly on studying the thermodynamic processes for different plant configurations and assumptions, e.g., with and without heat storage, isentropic versus polytropic processes, with and without heat exchangers, multiple stage versus single stage compression and expansion, etc. Very few works deal with modeling the CAES system for power system dynamic studies, such as frequency and voltage regulation or transient stability studies. Indeed, to the best of the author's knowledge, only two works have studied CAES for reactive power compensation, only one uses it for frequency regulation, while six others discuss CAES for transient stability. Hence, a detailed assessment of the frequency regulation capability of CAES for different conditions, such as charging, discharging, simultaneous charging/discharging, transitions from charging to discharging and vice versa are yet to be addressed.

1.3 Research Objectives

Based on the aforementioned literature review of the state-of-the art in CAES modeling and applications for power system studies, and the associated identified gaps, the main objectives of this thesis are the following:

- Develop a comprehensive mathematical model of the diabatic CAES system suitable for power system applications, considering two independent synchronous machines (generator and motor), in which the main CAES facility components such as valves, heat exchangers, burners, expanders, compressors, electrical machines, etc., are independently represented and modeled as physical-based subsystems of more complex systems (charging and discharging CAES trains), while considering the interrelations between these through appropriate interfaces.

- Incorporate approximations of compressor and turbine maps in the CAES mechanical system models, which could readily be implemented in power system analysis packages.

- Propose adequate control strategies for CAES system to ensure its stable operation, and enhance the provision of services associated with the exchange of active and reactive power with the electrical grid. These controls should consider the physical restrictions in the CAES operating points, imposed by the cavern pressure, compressor and turbine maps, compressor surge, flow choking conditions in the expanders, and reactive power sharing between the synchronous motor and generator.

- Study the implications of modeling the nonlinearities and limits imposed by the two main mechanical subsystems, compressor and turbine, in the CAES dynamic performance.

- Propose and implement a generic transient stability model of CAES in a commercial software packages for power system analysis, demonstrating the benefits of CAES for improving power system transient stability by studying it in a benchmark power system.

- Determine the practical effectiveness of CAES to provide frequency regulation in a power system with high penetration of renewable generation, especially when compressor and turbine maps, and associated controls, are modeled.

- Study the CAES system's practical capability to provide dynamic voltage support for various grid conditions.

1.4 Thesis Outline

The rest of the thesis is organized as follows:

- Chapter 2 presents a detailed review of CAES systems focusing on the modeling aspects of its individual components, and the relevant background related to CAES applications studied in this thesis, i.e., frequency and voltage regulation, and system stability.

- Chapter 3 describes the CAES models and controls proposed in this research, and discusses their implementation in a Matlab-Simulink environment and DSATools' TSAT® for dynamic studies of the power system.

- Chapter 4 presents, compares and discusses the results of simulations of the proposed versus existing CAES models for frequency regulation in a power system with high penetration of wind generation, and studies the use of CAES for voltage regulation, and its impact on the frequency and transient stability of the WSCC 9-bus test system.

- Chapter 5 summarizes the thesis content, and presents the main conclusions, contributions from the research, as well as discusses the possible scope for future work.

Chapter 2

Background Review

2.1 Energy Storage Systems

Energy Storage Systems (ESSs), in the context of power systems, are devices that by converting electricity into another form of energy, can be used to efficiently store energy, and then reverse this process to inject this stored energy back to the grid when required. ESS breakes the paradigm that electricity must be generated at the same instant when it is required, thus providing more flexibility for optimal system operation and planning. The time span the energy is stored, the efficiency of the conversion process, the speed of response, and the size determine the application of a particular ESS, as illustrated in Figure 2.1. The most common ESSs, besides CAES, and their applications can be summarized as follows [1, 2, 51]:

- Superconducting Magnetic Energy Storage (SMES) uses a superconducting coil that stores energy in its magnetic field, which works as a source of dc current. Hence, a power electronic conditioner (Current Source Converter (CSC) or VSC) is necessary to charge and discharge the coil. This technology is characterized by its fast response and high efficiency; as a result, typical power system applications that are currently under research include: load leveling, frequency support (damping oscillations), enhancement of transient stability, voltage support, and power quality improvement.
- In Battery Energy Storage System (BESS), the energy is stored as chemical energy in low-voltage battery cells properly arranged to increase the desired nominal power. The major drawback of this technology is related to the cycling capability of the

batteries, and their disposal; however, BESS is a mature ESS technology with high efficiency and speed of response, and is the most cost effective storage for medium and small-size applications. Due to its versatility, the power system applications of BESS are extensive: load leveling, frequency control, spinning reserve service, power factor correction, and grid voltage support.

- Flywheels store kinetic energy in a spinning mass, and are being commonly used in power systems for very short-term applications such as frequency regulation, although they are capable of providing continuous power for longer periods, thus making them also suitable for power quality, stability enhancement, and peak shaving applications.

- Supper Capacitors (SCs) store energy in the electric field formed across the capacitor plates, which keeps positive and negative charges separated from each other through an insulating material. Currently, supercapacitors are limited to low voltage applications such as support for power electronic converters, voltage-sag support, and electric vehicles, although grid level applications have also been reported in the literature [34].

- Pumped hydro facilities store energy by pumping water to a higher altitude, thus

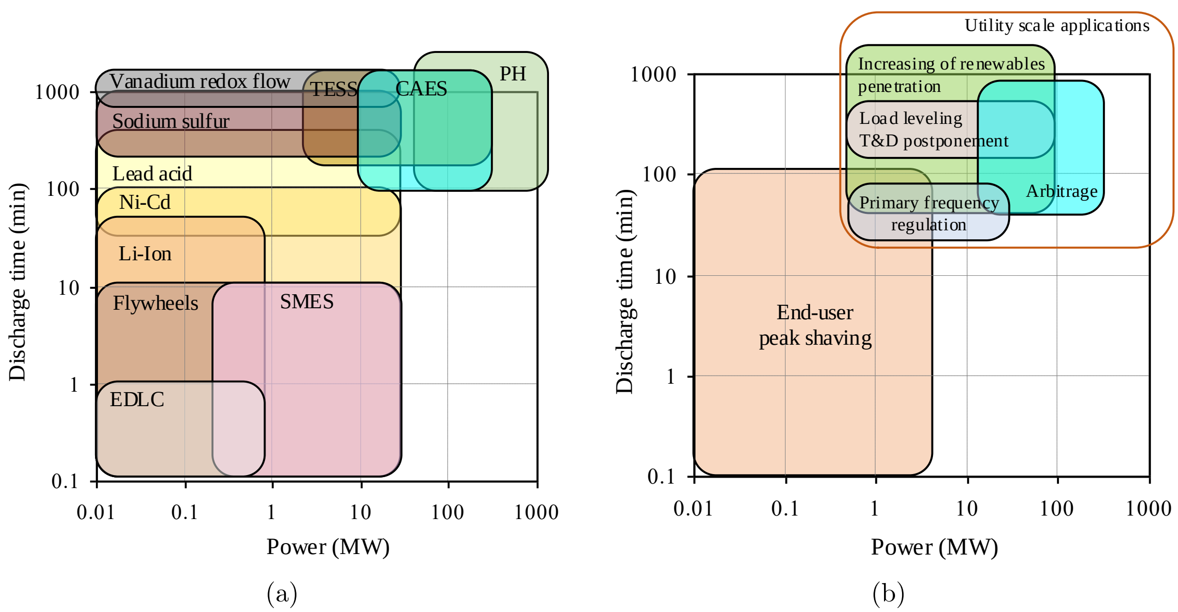

Figure 2.1: Overview of ESS (a) technologies, and (b) applications [1]

increasing its potential energy, and keeping it in a reservoir to be used later in a conventional hydroelectric generation plant. The size of the reservoir determines the storage capacity; consequently, these systems do not face major technological or economical barriers, but environmental issues may arise. Along with CAES, pumped hydro is the most cost-effective option for bulk power system applications such as load leveling, peak shaving, and energy arbitrage.

2.2 Compressed Air Energy Storage

The CAES technology uses air as a medium to store energy by compressing it in tanks or natural reservoirs, such as caverns, which can be later expanded in a turbine to drive a generator and inject electricity into the grid. A generic CAES system and its main components are presented in Figure 2.2, and its operation consists of the following three modes:

- Compression or charging mode: The air, at ambient conditions, is pressurized by a compressor, which is driven by an electric motor fed by the electrical grid. The compressed air is conducted through pipes to a reservoir where it remains stored, and as the air is injected, the internal pressure of the reservoir and its potential energy increases. To efficiently store the air in the reservoir, several stages of compression might be necessary with intercoolers between stages and also an aftercooler to reduce the temperature of the air further, and thus avoid thermal stress in the reservoir [11]. During this operation mode, the CAES system behaves as a load.

- Generation or discharging mode: The air is carried through the pipes from the storage reservoir, preheated and then expanded in a turbine. The expansion train is usually multistage with reheat between stages. In this operational mode, the CAES system behaves as a generator.

- Idling mode: In this mode, the CAES is neither charging nor discharging, but synchronized with the grid being able to provide voltage support.

CAES systems differentiate from conventional GTs, which also have a compressor and turbine in their thermal cycle, in that the masses of the rotor of the generator, the compressor, and the turbine are lumped on the same shaft in GTs; therefore, approximately 2/3 of the power delivered by the turbine is used to drive the compressor [52]. On the other hand, in CAES, these are totally decoupled and can be controlled independently; therefore, the average efficiency of CAES is higher, in the range of $40-89\%$ [2,53], depending on the specific type of CAES types and configuration.

A single machine can be used in a CAES system, as in Huntorf or McIntosh [12], which can act as a generator or motor by means of a clutch that detaches the compressor or turbine accordingly. However, in this thesis the CAES system is modeled using two synchronous machines, operated and controlled independently as in [6,9,11], as in the case of Bethel [14] and Goderich [8]. The use of synchronous machines enhance the voltage regulation control of the system and facilitates the compressor and turbine control as the rotor speed variations are low, even during transients.

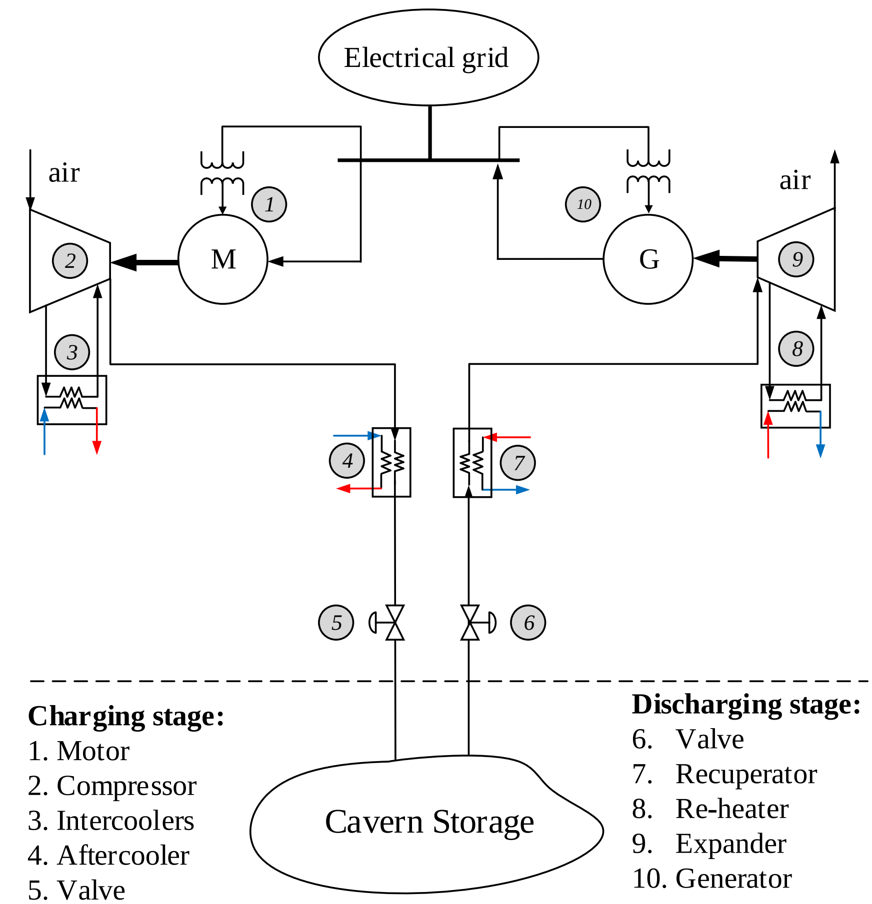

Figure 2.2: Generic CAES system.

Typically, five types of geological formations could be used as reservoirs for underground

CAES [23, 52, 54]: salt caverns, solid rock formations, limestone caverns, natural porous rock aquifers, and depleted gas fields; however, salt caverns are among the most convenient, because of their relatively low overall cost [11], and leak-proof characteristics [55]. The capacity of energy storage depends on the size of the cavern, which is to some extent independent of the size of the turbo machinery. Consequently, the energy-to-power ratio of a CAES system is more flexible than other ESS technologies. For above-ground reservoirs, steel tanks can be used for small CAES applications [2, 11].

Some important features of CAES technology are the following [2, 9, 52, 54]:

- It is suitable for secondary reserve services, since the start-up time from cold state to full load is about 15 minutes.
- It can provide demand response by appropriate scheduling of the charging operation, and adapting its load shape, as the charging demand of the CAES facility (compression mode) can be sized to be different from that of the generator, if required, by utilizing different machines for the generation/compression stages.
- Can provide frequency and voltage regulation.
- It is more reliable than simple-cycle combustion turbines, due to lower temperatures inside of turbine (e.g., 1500 °F for a 220 MW system, as compared to 2200 °F for a similar simple-cycle conventional gas generator).
- Its fuel consumption is only $30 - 40\%$ of a conventional combustion turbine plant.
- It has high nominal ramp rates in the range of 22 to 33% of nameplate power per minute. Furthermore, in [11], the following ramp specifications for CAES are presented: 0 to 100% of rated power in less than 10 minutes; ramp up from 10 to 100% in 4 min, and 2 min in case of emergency; and ramping from 50 to 100 % in less than 15 seconds.
- It is practical for bulk storage applications that require the energy to be discharged over long periods; usually, longer than 5 hours at nominal output power.

In the next sections, the most common types of CAES systems, namely diabatic, adiabatic, and isothermal are discussed.

2.2.1 Diabatic CAES

The main characteristic of this type of CAES system is that it burns natural gas to increase the temperature of the air before being expanded in the turbine. Figure 2.3 depicts the main components and interrelations of an underground diabatic CAES facility, based on [12] and [13].

The compression train comprises a low-pressure (LP) axial compressor and a high-pressure (HP) multi-stage centrifugal compressor to achieve the desired range of operating pressures in the cavern. A regulating valve is used to throttle down the compressor's

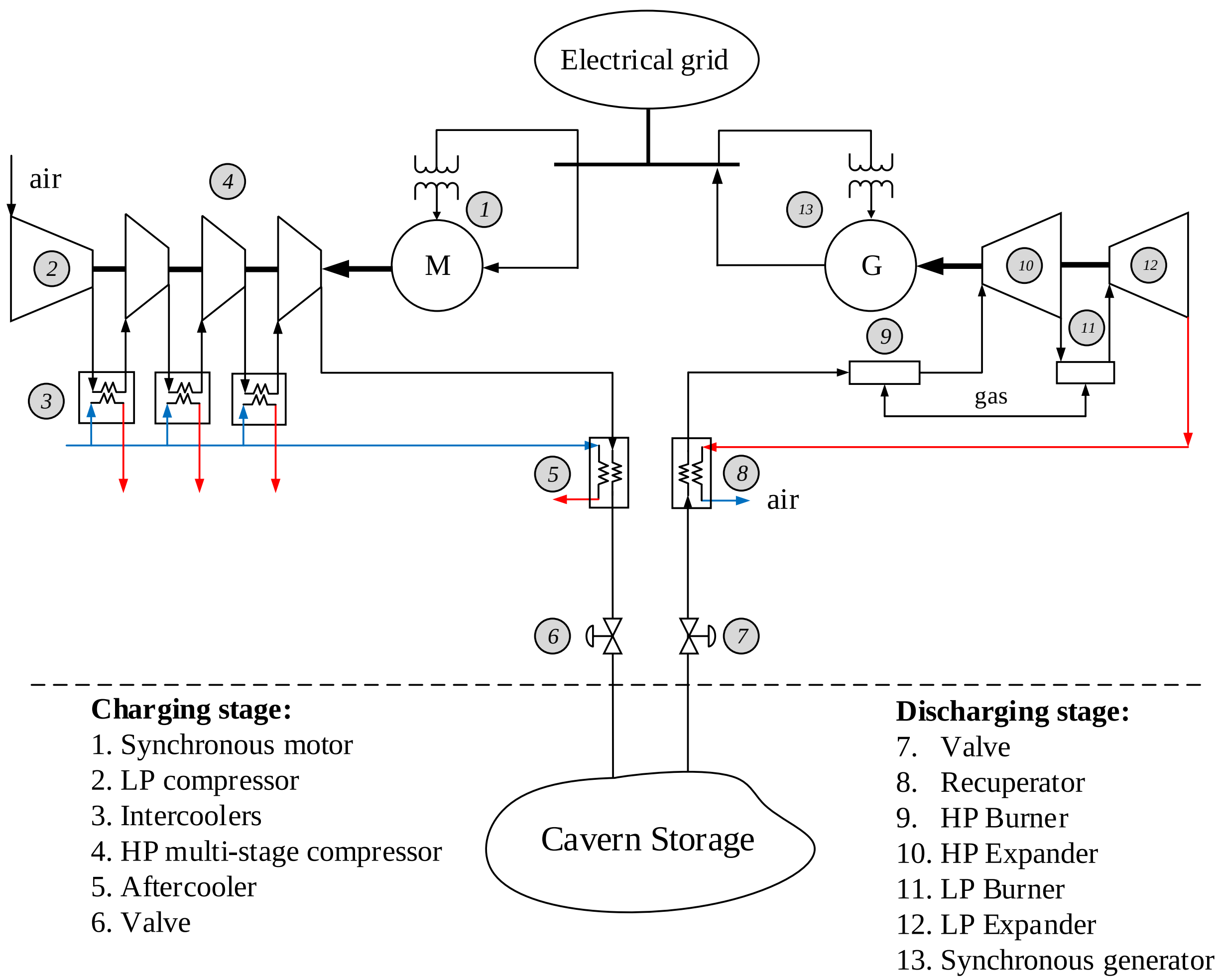

Figure 2.3: Basic configuration of a diabatic CAES system.

discharge pressure to actual cavern pressure. The intercoolers are designed to reduce the inlet temperature at the different stages to approximate isothermal compression, and thus reduce the power required from the motor. The aftercooler is present to reduce losses and thermal stress on the cavern [56]; in this configuration, the heat obtained in the hot side of the intercoolers is not used. In the Huntorf CAES facility, three intercoolers are used, one after the LP compressor and two between each of the three stages of the HP compressor.

The turbine has two main components: the combustion chamber (or burner) and the expander. As in the compression, multiple stages are used in the expansion; in Huntorf, a high-pressure (HP) and low-pressure (LP) expanders are used. The air from the cavern is preheated in the recuperator using the remanent heat of the exhaust air of the LP expander to increase efficiency [52], which is then combined with fuel and burned in the HP combustion chamber to achieve the desired inlet temperature to the HP expander. After, the air is reheated in a LP burner and expanded in the LP expander, which increases the efficiency of the expansion cycle, as the expansion work is proportional to the inlet temperature in a turbine; gas is consumed in this process.

The turbine can operate in two modes: constant input pressure and variable input pressure [15]. In the former, the air is throttled so that the burner inlet pressure remains constant regardless of the cavern pressure, while in the latter, the burner inlet pressure is the cavern pressure.

The two existing large CAES facilities, Huntorf and McIntosh, and the facility being developed at Bethel [14], are diabatic, with round-trip efficiencies of 46% and 54% respectively [18].

2.2.2 Adiabatic CAES

Figure 2.4 presents the basic configuration of a typical adiabatic CAES system. In this configuration, the heat produced during the compression process is recovered from the intercoolers and aftercoolers, and then stored in a liquid or solid form, such as molten salt or special ceramics in the "thermal storage" Block 6 shown in figure 2.4. The stored hot fluid is pumped to the turbine during expansion to preheat the air coming from the cavern and reheat it between expansion stages. The fluids leaving the cold side of the preheater and reheaters are pumped to a cold storage element, and then used to remove the compressors' heat in the intercooler and aftercooler. Since the thermal cycle does not involve burning of gas, the adiabatic CAES efficiency is higher than that of the diabatic CAES, which is reported to be between 60 and 70% [18, 57]; however, this largely depends on the efficiency of the inter and aftercoolers and reheaters [18]. Similarly, the thermal storage must be capable of operating at very high temperatures (600C° – 700C°) to heat up the air from the cavern to an optimal inlet turbine temperature [57]. Therefore, the thermal storage requires high discharging temperatures from the compressor (higher than the storage temperature), which entails especial turbomachinery designs [57]. An example of adiabatic CAES is the 1.75 MW facility in Goderich, Ontario, Canada, developed by Hydrostore [8].

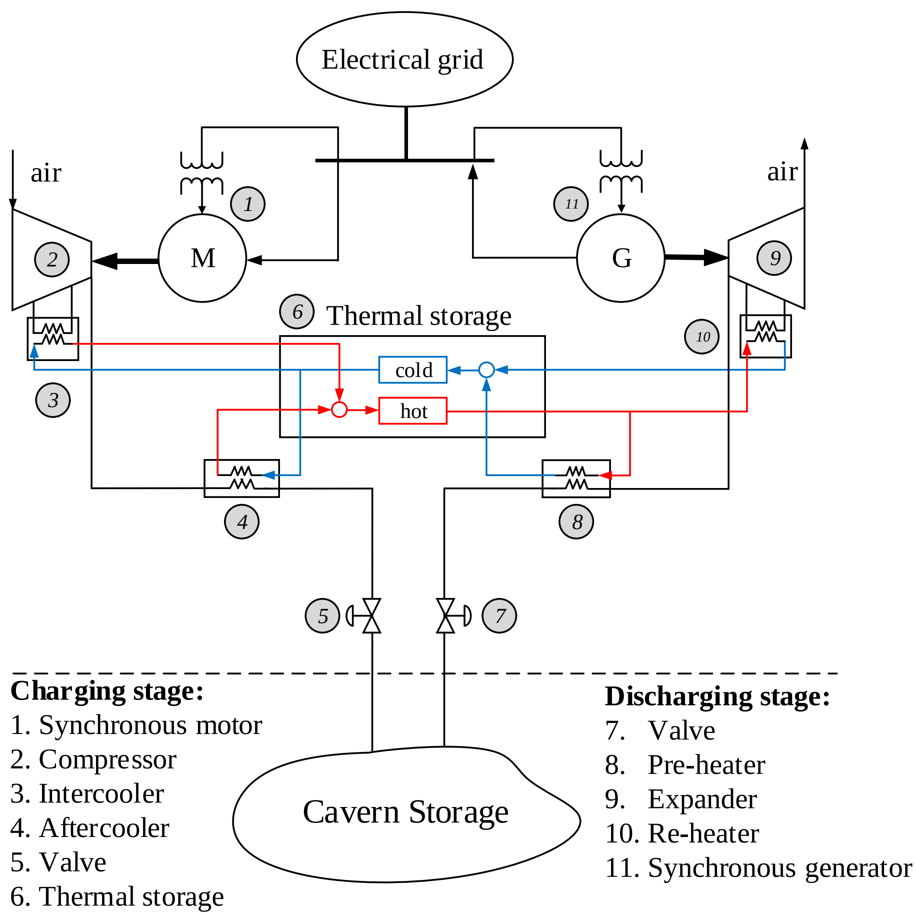

Figure 2.4: Basic configuration of an adiabatic CAES system.

2.2.3 Isothermal CAES

Isothermal CAES aim to keep the temperature through the compression and expansion processes almost constant, which, in theory, eliminates the need for the high-temperature heat storage unit used in adiabatic CAES. Isothermal compression requires less amount of work from the motor for the same pressure ratio, whereas the turbine can deliver more power to the generator [58], thus increasing the round-trip efficiency of the system to $70\% - 80\%$ [58, 59]. To achieve isothermal condition, the compression and expansion must be performed slowly enough so that the heat can be added or removed effectively. This technology avoids the need for multiple stages of compression and expansion, but requires special mechanisms to continuously remove/add heat during the compression and expansion cycles, which is implemented through a piston-based machinery, such as reciprocating machines or scroll machines [59]. Isothermal CAES is still under research and currently limited to small-scale applications, such as the proposed 1.5 MW facility by SustainX in Seabrook, NH, USA [60].

2.3 Modelling and Control of Electromechanical Systems

Models of the turbomachinery and electromechanical equipment used in CAES, namely compressor, turbine, and electrical machines are well described in the literature; however, their intended applications determine the modeling approach, level of details of the components, and simplifications and assumptions made. In principle, diabatic CAES is based on the same principle and turbomachinery used in GTs; however, the compression and expansion of the air takes place at different times and in machines that are physically decoupled. Models of GTs for power system dynamic studies are mature; therefore, the CAES models proposed in this research have similar structures and are based on similar approximations as those of GTs. On the other hand, compressor models are not very common in power systems, because loads of this kind are usually aggregated or represented as simplified mechanical torques in electrical motors. Consequently, the models and controls proposed for the CAES compressor for power system studies are novel contributions of this research. Thus, in this section, common models of synchronous machines, gas turbines, and axial and centrifugal compressors are discussed.

2.3.1 Synchronous Machines

Synchronous machines convert mechanical power into electrical power if they operate as generators, and vice versa if used as motors. The synchronous machine is usually modeled by a set of non-linear Differential-algebraic System of Equations (DAE) to represent the stator and rotor windings, and their electromagnetic coupling. Typically, Park's transformation is used to remove the time dependency from the machine inductances, which vary with the position of the rotor, and to convert the stator "*abc*" ac variables into "0*dq*" dc variables, which considerably reduces the modeling complexity [61]. The order of the DAE depends on the number of stator and rotor windings considered, as shown in Figure 2.5; one winding for each of the three phases of the stator ($a - a', b - b', c - c'$), and up to four windings in the rotor, namely field winding ($F - F'$), damper winding aligned with the *d*-axis ($D - D'$), damper winding aligned with *q*-axis ($Q_1 - Q_1'$) and a *q*-axis winding representing the induced currents circulating in the body of the rotor ($Q_2 - Q_2'$), which occurs especially in round-rotor machines as those used in GTs.

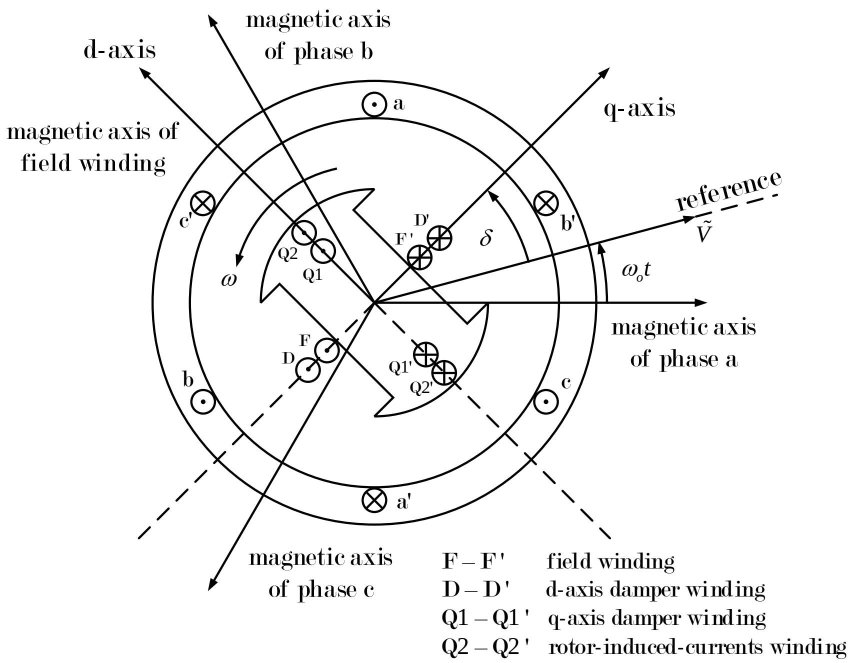

Figure 2.5: Synchronous machine diagram.

One of the most commonly used models of synchronous machines for transient stability studies is the classical subtransient model, which neglects the dynamics of the flux linkages in the stator windings as these die out much faster than the rotor's, and that the rotor speed is approximately equal to the synchronous speed ($\omega \approx \omega_o$) in the stator voltage equation [62]. The resulting state variables of this model are the d and q components of the internal emfs $\bar{E}'_d$ and $\bar{E}'_q$, and $\bar{E}''_d$ and $\bar{E}''_q$ produced by the transient and subtransient flux linkages [62]. The full set of equations of the subtransient model of a synchronous generator is summarized below [62,63]:

- Differential equations:

$$\frac{d\bar{E}''_q}{dt} = \frac{1}{\tau''_{d0}}\left(-\bar{E}''_q + \bar{E}'_q + \left(X'_d - X''_d\right)\bar{I}_d\right) \tag{2.1}$$

$$\frac{d\bar{E}''_d}{dt} = \frac{1}{\tau''_{q0}}\left(-\bar{E}''_d + \bar{E}'_d - \left(X'_q - X''_q\right)\bar{I}_q\right) \tag{2.2}$$

$$\frac{d\bar{E}'_q}{dt} = \frac{1}{\tau'_{d0}}\left(\bar{E}_f - \bar{E}\right) \tag{2.3}$$

$$\frac{d\bar{E}'_d}{dt} = \frac{1}{\tau'_{q0}}\left(-\bar{E}'_d - \left(X_q - X'_q\right)\bar{I}_q\right) \tag{2.4}$$

$$\frac{d\overline{\omega}}{dt} = \frac{1}{2H}\left(\bar{P}_m - (\bar{P} + r\bar{I}^2) - D\bar{\omega}\right) \tag{2.5}$$

$$\frac{d\delta}{dt} = \omega_o\left(\bar{\omega} - 1\right) \tag{2.6}$$

- Algebraic equations:

$$0 = -\bar{E} + \bar{E}'_q - \left(X_d - X'_d\right)\bar{I}_d \tag{2.7}$$

$$0 = -\bar{E}''_q + \bar{V}_q + r\bar{I}_q - X''_d\bar{I}_d \tag{2.8}$$

$$0 = -\bar{E}''_d + \bar{V}_d + r\bar{I}_d + X''_q\bar{I}_q \tag{2.9}$$

$$0 = -\bar{P} + \bar{V}_d\bar{I}_d + \bar{V}_q\bar{I}_q \tag{2.10}$$

$$0 = -\bar{Q} + \bar{V}_d\bar{I}_q - \bar{V}_q\bar{I}_d \tag{2.11}$$

$$0 = -\bar{V}_d - \bar{V}\sin\left(\delta - \theta_V\right) \tag{2.12}$$

$$0 = -\bar{V}_q + \bar{V}\cos\left(\delta - \theta_V\right) \tag{2.13}$$

$$0 = -\bar{I}_d - \bar{I}\sin\left(\delta - \theta_V + \phi\right) \tag{2.14}$$

$$0 = -\bar{I}_q + \bar{I}\cos\left(\delta - \theta_V + \phi\right) \tag{2.15}$$

where the variables and parameters are defined in the Nomenclature section, and in more detail next:

- $\bar{E}''_d$ and $\bar{E}''_q$ are the emfs proportional to the subtransient flux linkages $\bar{\psi}''_d$ and $\bar{\psi}''_q$ in p.u., respectively.
- $\bar{E}'_d$ is the emf proportional to the field flux linkage $\bar{\psi}_F$ in p.u.
- $\bar{E}'_q$ is the emf proportional to the rotor current $\bar{i}_{Q2}$ in p.u.
- $\bar{E}$ is the stator air gap emf proportional to the field current $\bar{i}_F$ in p.u.
- $\bar{E}_f$ is the emf proportional to the field voltage $\bar{v}_F$ in p.u. The field voltage $\bar{v}_F$ and hence $\bar{E}_f$ are controlled by the AVR. In steady-state, $\bar{E} = \bar{E}_f$.
- X''_d, X'_d, X_d, X''_q, X'_q and X_q are the d-axis and q-axis subtransient, transient and steady-state reactances of the machine in p.u., respectively.
- r is the stator resistance in p.u.
- τ''_{d0}, τ''_{d0}, τ''_{q0}, τ'_{q0} are the d-axis and q-axis open circuit subtransient and transient time constants in s.
- $\bar{I}$ and $\bar{V}$ are the generator's terminal current and voltage respectively in p.u.
- $\bar{\omega}$ is the rotor speed in p.u.
- ω_o is the nominal rotor speed in electrical rad/s.
- θ_V is the angle of the terminal voltage V in rad.
- ϕ is the power factor angle in rad.
- δ is the angular difference between the q-axis (aligned with the magnetic axis of the field winding) and a rotating reference aligned with the magnetic axis of phase a at $t = 0$ in rad.
- H is the inertia constant of the generator in MW.s/MVA.
- D is the damping constant in p.u.
- $\bar{P}$ and $\bar{Q}$ are the active and reactive power at the generator's terminals in p.u., respectively. Thus, $\bar{P} + r\bar{I}^2$ is the active power transferred across the air gap.

- $\bar{P}_m$ is the mechanical power produced by the turbine in p.u.

In this model, the mechanical and electromagnetic torques are approximated by power values, since $\omega_t \approx \omega_o$.

Equations (2.1)-(2.15) form a DAE model of the machine. Hence, in order for this model to be completely defined, two boundary variables must be know. Hence, in this case, it is assumed that the bus voltage $\bar{V}\angle\theta_V$ is known, and thus, the machines become a source of current (or power) to the system at which it is connected; however, any other set of two variables could also be used instead. A detailed discussion on the base values used in this model can be found in [62].

The representation of the transient, subtransient and steady-state emfs as voltage phasors behind reactances in both d- and q-axes facilitates their calculation using basic circuit theory, as shown for example in Figure 2.6 for $\tilde{E}$. The phasor diagram in Figure 2.7 depicts the algebraic relations of all emfs, which are valid during transient and steady state.

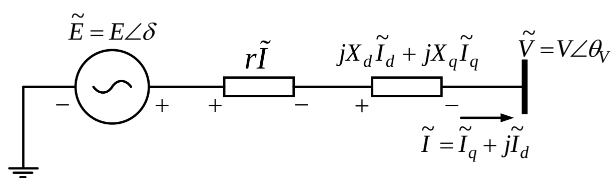

Figure 2.6: Steady-state phasor circuit of a generator.

The model of a synchronous motor is the same as the one described here for a synchronous generator, except that in the motor, the mechanical torque is negative and the electrical torque positive, as the motor now drives a mechanical load [61].

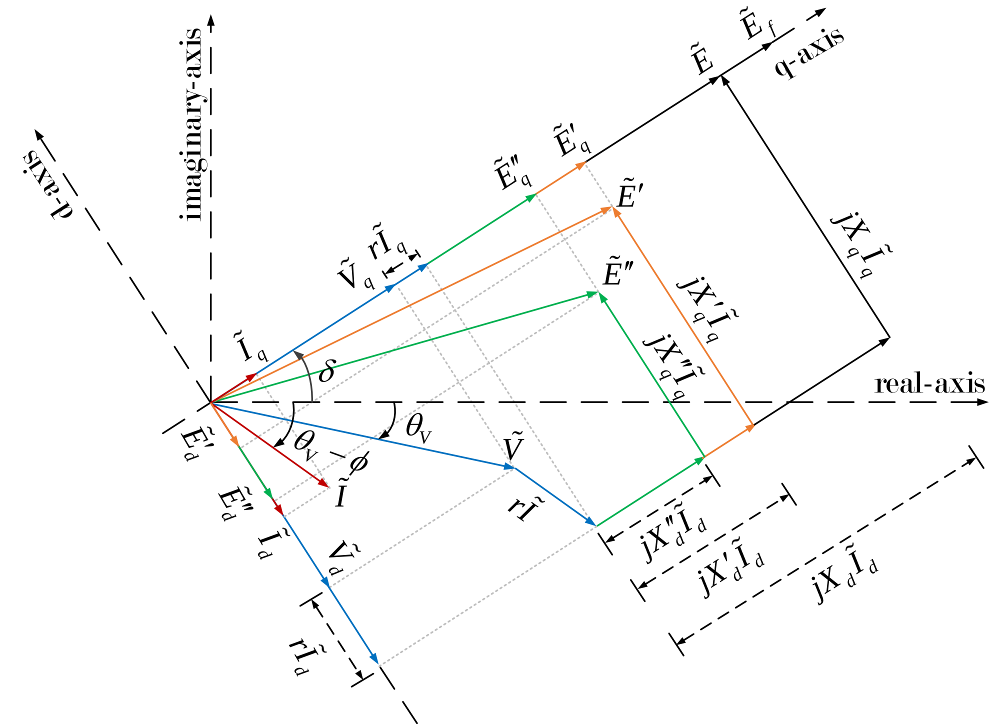

Figure 2.7: Synchronous generator phasor diagram; all parameters and variables are in p.u.

2.3.2 Gas Turbines and Compressors

A typical GT comprises a compressor physically attached to the rotor of a turbine, and a combustion chamber where the compressed air is combined with gas and burned to increase the temperature of the air before the expansion, as depicted in Figure 2.8(a). A GT operates under a Brayton cycle summarized in Figures 2.8 (a) and (b).

The ideal Brayton cycle comprises: isentropic compression of the air from 1 to 2, isobaric heat addition from 2 to 3, isentropic expansion from 3 to 4 and isobaric heat rejection from 4 to 1. During the 1-2 isentropic compression, i.e., constant etropy s, adiabatic and reversible, work W_{in} is done on the system by the compressor, which increases the temperature from T_1 to T_2. There is no heat transfer with the surroundings and, therefore, the work W_{in} increases the internal energy (no losses), changing its enthalpy from h_1 to h_2. The output pressure of the compressor increases from ambient condition p_1 to p_2, while its volume decreases. The temperature change ΔT_{1-2}, and thus, the enthalpy change

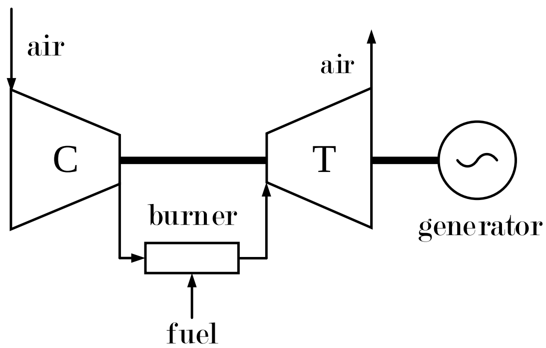

(a)

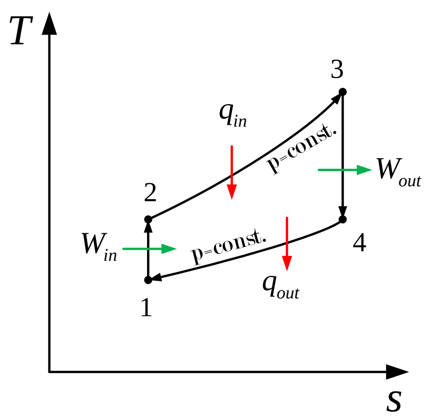

(b)

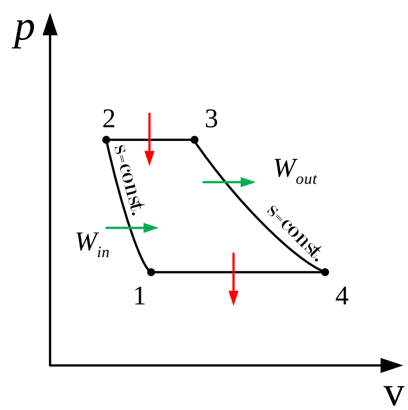

(c)

Figure 2.8: (a) GT, (b) T-s, and (c) p-v diagrams.

Δh_{1-2} depends on the pressure ratio of the compressor $\pi_c = p_2/p_1$. In the combustion chamber, heat q_{in} is added during 2 to 3, thus increasing the air temperature to T_3 and the enthalpy to h_3 without changing the pressure. In the 3-4 expander, the temperature and enthalpy change to T_4 and h_4, respectively, while the air pressure reduces to ambient conditions $p_4 = p_1$. The enthalpy drop Δh_{3-4} is transformed into useful work W_{out}, which is converted into mechanical torque to move the generator. The cycle is closed through the turbine surroundings, changing the air temperature from T_4 to ambient conditions T_1 by releasing heat to the atmosphere at ambient pressure $p_1 = p_4$. If reheaters or intercoolers are used, this cycle is modified by adding stages of isobaric heat addition or rejection as necessary. In actual turbines, the isentropic idealization is adiabatic, which is modeled by means of isentropic efficiencies η_i.

The pressure ratio π in the compressor and turbine depends on their geometry, inlet conditions (pressure p and temperature T), rotor speed N, and mass flow rate $\dot{m}$. The nonlinear relation $\pi = f(N, \dot{m}, T, p)$ is established, using compressor and turbine maps, which are usually provided by the manufacturers of the equipment. In these maps, the horizontal axis shows the corrected mass flow rate $\dot{m}\sqrt{T/T_{am}}/(p/p_{am})$, defined as the mass flow rate through the device if the inlet conditions (T, p) were ambient conditions at sea level (T_{am}, p_{am}). The corrected mass flow rate is mapped to the pressure ratio through corrected speed lines $N/\sqrt{T/T_{am}}$. In Figure 2.9, an example of a compressor map is presented for illustration purposes [64]. Similar curves are used for the efficiency of the machines.

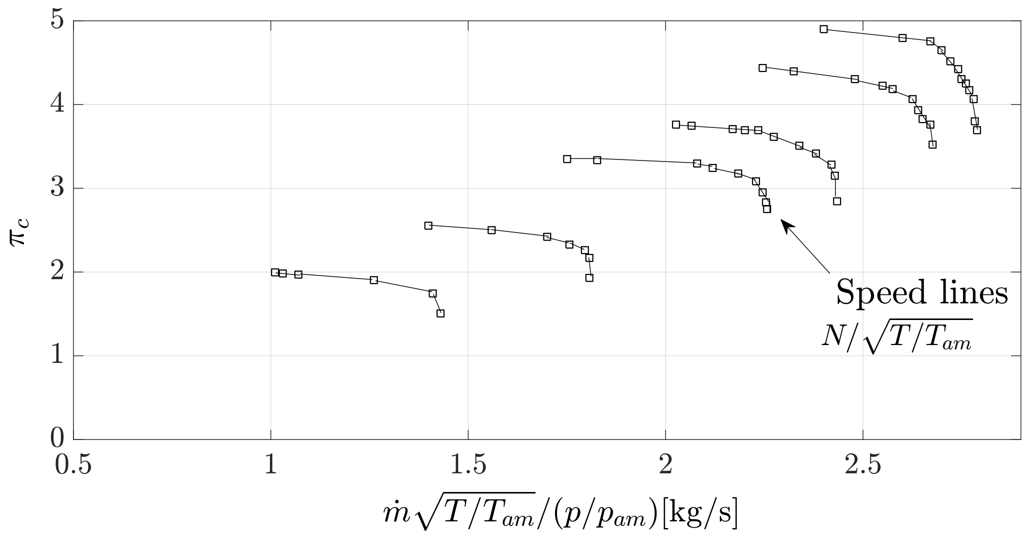

Figure 2.9: Example of a compressor map reproduced from [64].

Two types of GT models are mainly used for dynamic studies in power systems: the Rowen's model [65], and the IEEE model [66]. Other GT models such as the WECC [67], CIGRE [68], GAST [69], or the one proposed in [70] are variations of the original Rowen's or IEEE models. The main difference between the two is that the IEEE model considers the physical characteristics of the equipment, represented by their thermodynamics, whereas the Rowen's model mostly concentrates on the control loops associated with the operation of the turbine, while simplifying the thermodynamics by linear functions.

The Rowen's model, presented in Figure 2.10, has three main control loops: power control, acceleration control and temperature control, all of them acting in the gas supply system. The power control corresponds to the governor and is used to realize the desired

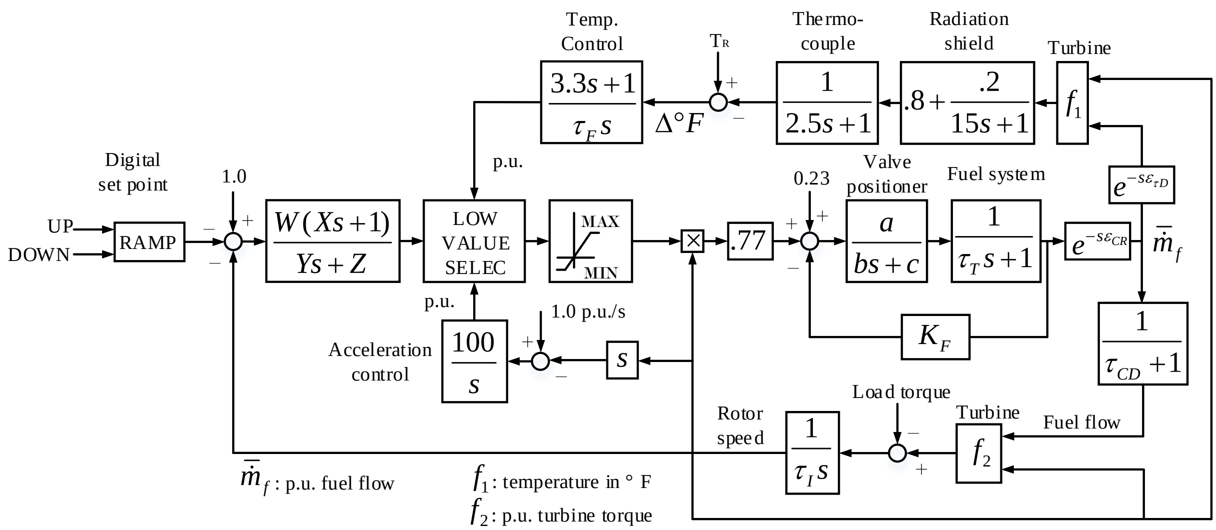

Figure 2.10: Rowen's GT model [65].

output power; it also allows primary frequency control by the proper selection of a gain W. To avoid overheating due to large power requirements by the governor path, the temperature control limits the gas supply if the exhaust temperature of the GT is excessive. This control compares the measured (using a thermocouple) GT exhaust temperature, calculated as a function f_1 of the gas flow and rotor speed, with a reference. If the resulting temperature is higher than the reference, the temperature control overrides the governor, by means of a low value selector (LVS) block, and reduces the gas injected into the turbine. Finally, the acceleration control is used during start up to prevent the rotor to over accelerate until synchronization. In this control, the rotor speed is passed through a derivative block to generate the acceleration signal, which is compared with a reference value, and, if over-speed is detected, the control also overrides the governor to limit the gas injection, as in the temperature controller. Summarizing, the LVS passes the signal with the least amount of fuel required from the turbine, which is sent to the fuel flow system.

The dynamics of the fuel flow system comprising the valve positioner and the gas distribution manifold delay are modeled by two first-order transfer functions (the feedback K_F is used if the fuel is a liquid). Two additional delay blocks are used to represent the combustion reaction time and gas transportation delay through the turbine, and a first order transfer function for the compressor discharge volume. The 0.23 value represents the gas consumption at no load condition.

The output power of the turbine is calculated as a linear function of the flow and rotor speed, with the latter representing mechanical losses due to friction. By removing some control loops and neglecting the transportation delays, the model can be simplified to represent a stiffer turbine.

The IEEE model presented in Figures 2.11 and 2.12, unlike Rowen's, considers the thermodynamic relations, to calculate the mechanical power and exhaust temperature. Figure 2.11 depicts the main relations between the control system and the physical model of the GT. Observe that two control variables are proposed in the IEEE model as opposed to the single one used in Rowen's; the first representing the air mass flow rate ($\dot{m}_t$) and the second for the fuel flow rate ($\dot{m}_f$). In the mechanical power calculations (refer to [66] for details), the compressor and turbine pressure ratios are assumed to be linear functions of the air mass flow rate. However, in actual turbines, these relations are determined by the compressor and turbine maps correspondingly. An improvement in the IEEE model is discussed [70], in which empirical functions are used to represent the nonlinearities of the compressor maps in the air flow calculation.

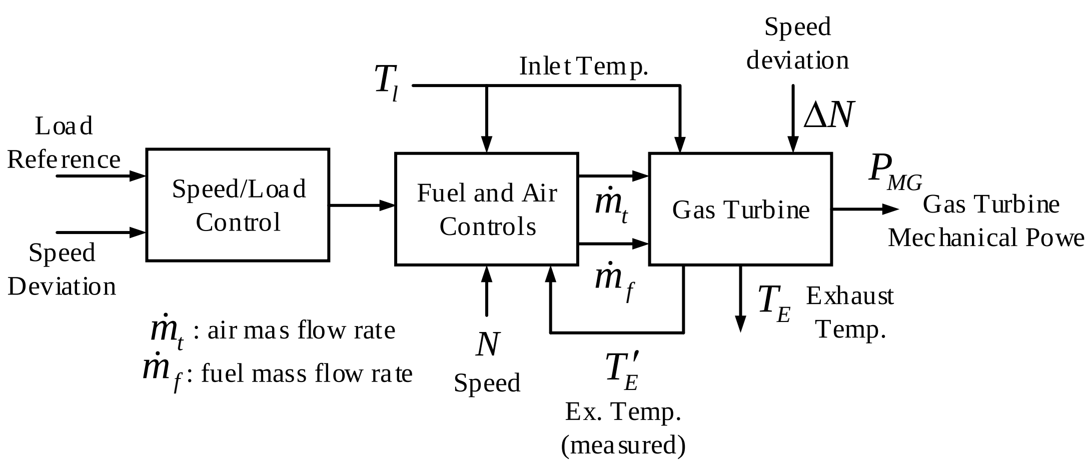

Figure 2.11: IEEE GT model [66].

The power control system in the IEEE model is essentially the same as the one proposed by Rowen, except that two independent control loops, one for air flow and the other for fuel flow, are proposed in the IEEE model. The control of the air flow allows independent control of the inlet temperature of the air before expansion, which is used to improve the efficiency of the GT during partial loading conditions, a feature that will be used in the proposed CAES control. On the other hand, the output of the the power control system (fuel demand signal F_D) is used in the fuel control system, which is the same as the Rowen's model. Notice that the required air flow is calculated in Block A, in Figure

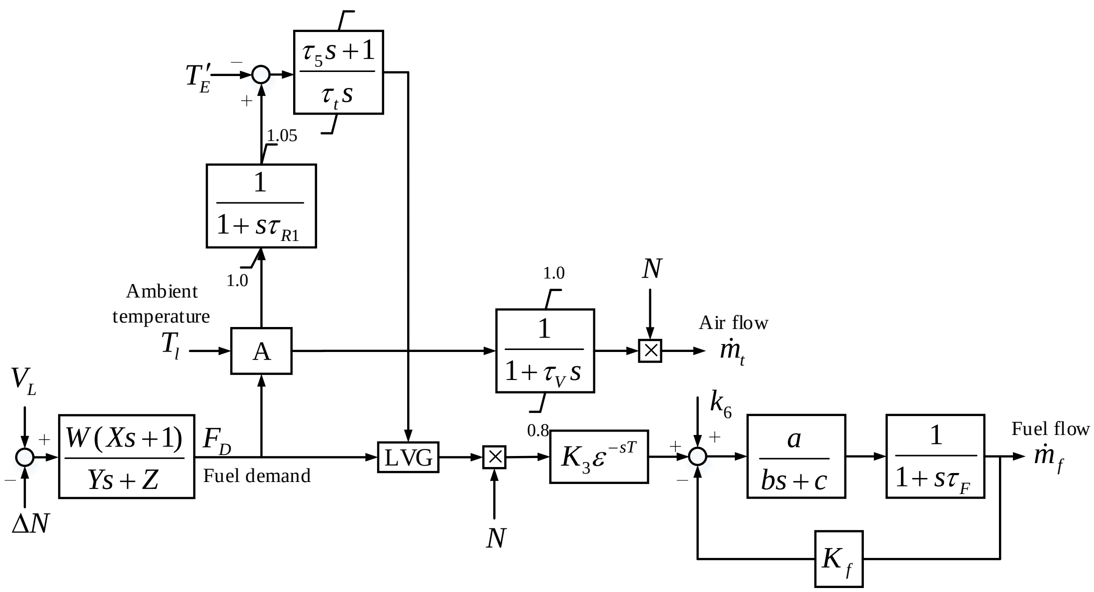

Figure 2.12: IEEE model to represent air flow and fuel flow controls [66]

2.12, which solves a system of nonlinear equations to find the required air flow, having F_D and the ambient temperature T_l as inputs. The dynamics of the air valve are modeled by a first order transfer function of time constant τ_V. Notice that the dynamics in a GT are mostly introduced from the control systems, since the burner is assumed to operate almost instantly (although short delays are used in some models). However, this changes if a recuperator is used, as these devices have thermal inertia with relatively large time constants.

In the GT models discussed so far, the air flow and fuel flow controls, combined with the thermodynamics and the approximate compressor and turbine maps, determine the operating point of the GT. As discussed earlier, one of the assumptions is the linear relation between the air flow and the compressor and turbine pressure ratios. However, this approximation is not accurate if the compressor is modelled and controlled independently, as in CAES, because the turbine no longer drives the compressor, but an independent motor. In this context, the dynamic model of a compressor operating alone must be considered.

The most widely used model to study the compressor dynamics is the Greitzer model illustrated in Figure 2.13 [71]. Greitzer describes a system comprised of a compressor connected to a plenum[1] through a duct, and a throttle or valve at the end to discharge

[1]The plenum is a closed volume where gases mix at a pressure higher than the ambient pressure.

the air flow at ambient pressure. The compressor is represented by an actuator disk[2], which compresses the air from ambient pressure $p_{c_{in}}$ to a steady-state pressure $p_{c_{out\_ss}}$, with the latter being determined by the compressor map, represented by the function $\pi_c(\dot{m}_c, \omega_c)$. Since $p_{c_{out\_ss}}$ is not developed instantly at the output of the compressor, Greitzer proposes a first order transfer function with time constant τ_{CD}, to model the dynamics of the actual discharge pressure $p_{c_{out}}$. Changes in the operating point of the compressor

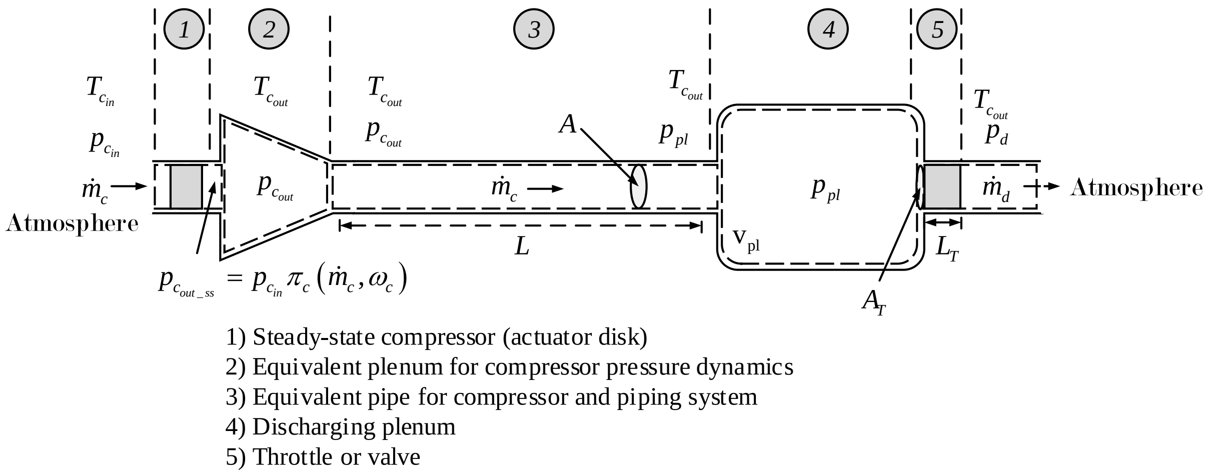

Figure 2.13: Compressor representation in the Greitzer model [71]

creates pressure differences between the compressor output and the plenum $(p_{c_{out}} - p_{pl})$, since, as the air faces a restriction in the output of the plenum due to the valve, it starts to accumulate mass, creating a capacitive effect[3], thus increasing its pressure, with the latter being modeled by a differential equation. This pressure difference results in air flow dynamics that can be explained by the conservation of momentum law. The time constant of the air flow dynamics in the compressor+pipe body is a function of the equivalent length of the pipe and compressor (L), and the equivalent cross sectional area A. These dynamics are particularly relevant in CAES, because the air flows through long pipes before entering the cavern. Finally, the air flow in the valve is modeled by the equation of an incompressible flow in a nozzle, and its steady-state value is determined by the pressure difference between the plenum and system discharge pressure $p_{pl}^{ss} - p_d$; notice that $p_d = p_{am}$ in Figure 2.13.

[2]The pressure drop across the actuator disk is allowed to vary discontinuously, while the flow is assumed to be continuous.

[3]As an analogy, the plenum behaves as a capacitor in which the potential is pressure instead of voltage, and accumulates mass instead of electrical charge, and the air flow is analogous to the charge flow or electric current.

The corresponding set of differential equations can be summarized below:

$$\frac{d\dot{m}_c}{dt} = \frac{1}{L/A} \left(p_{c_{out}} - p_{pl}\right) \tag{2.16}$$

$$\frac{d\dot{m}_d}{dt} = \frac{1}{L_T/A_T} \left[(p_{pl} - p_d) - (p_{pl}^{ss} - p_d)\right] \tag{2.17}$$

$$\frac{dp_{c_{out}}}{dt} = \frac{1}{\tau_{CD}} \left(\pi_c \left(\dot{m}_c, \omega_c\right) p_{c_{in}} - p_{c_{out}}\right) \tag{2.18}$$

$$\frac{dp_{pl}}{dt} = \frac{\gamma \mathrm{R} T_{c_{out}}}{\mathrm{v}_p} \left(\dot{m}_c - \dot{m}_d\right) \tag{2.19}$$

$$0 = -(p_{pl}^{ss} - p_d) + \frac{\dot{m}_d^2}{2\rho A_T^2} \tag{2.20}$$

where, as defined in the Nomenclature section:

- $\dot{m}_c$ is the air mass flow rate through the compressor and pipe in kg/s.
- $\dot{m}_d$ is the air mass flow rate leaving the throttle in kg/s.
- p_{pl} is the pressure in the plenum in Pa.
- $p_{c_{out}}$ is the dynamic output pressure of the compressor in Pa.
- $p_{c_{in}}$ is the input pressure of the compressor in Pa.
- $[p_{pl}^{ss} - p_d]$ is the steady-state pressure drop in the valve in Pa.
- $\pi \left(\dot{m}_c, \omega_c\right) p_{c_{in}}$ is the steady-state output pressure of the compressor in Pa.
- L and A are the equivalent length and cross sectional area of the compressor and pipe, respectively in m and m^2, respectively.
- L_T and A_T are the equivalent length and cross sectional area of the throttle in m and m^2, respectively.
- $p_{c_{in}}$ is the compressor input pressure in Pa, which in this case is equal to the system discharge pressure p_d.
- τ_{CD} is the time constant of the compressor dynamic output pressure in s.
- $T_{c_{out}}$ is the discharge temperature of the compressor in K.

- v_{pl} is the volume of the plenum in m^3.
- γ, R, ρ are the heat capacity ratio (no units), specific gas constant in J/kg.K, and air density in kg/m^3, respectively.

It is to be noted that the notation used in this thesis is different from that in [71]. Also, [71] describes the differential equations in terms of pressure rises or drops, while the pressure ratio π_c is used here instead to relate the input and output pressures. The thermodynamic relations that govern the temperature changes and required work injection during the compression are the same as in the turbine, and are therefore not discussed here.

A simplification of the Greitzer model combined with the thermodynamic relations presented at the beginning of this section are used here to develop the novel compressor model of the CAES system, discussed later. On the other hand, the turbine and its controls are based on the Rowen's and IEEE GT models.

2.3.3 Control Strategies in CAES Systems

Four individual control systems are required in a CAES system: active power control for the turbine-generator and motor-compressor sets, and reactive power control for the synchronous generator and motor.

Active Power

The active power control logic for the turbine-generator set is similar to that in GTs; thus, a governor controls the mechanical power of the turbine, which includes a feedback of the speed to add primary frequency regulation capability. The air flow is controlled to deliver the desired output power, while the inlet temperature in the expanders (low and high pressure) are kept constant by controlling the fuel in the burners (two control loops) [13]. This is clearly different from the control logic of GTs, in which the gas in the burner is adjusted to control the turbine power. The compression air flow rate of the CAES system is regulated by moving the compressor's variable Inlet Guide Vanes (IGVs) to control the power consumption of the motor within a load range of 65 to 110% of the rated power [9], which may vary depending on the manufacturer. Unlike the turbine, the compressor does not have a temperature controller, although intercoolers and an aftercooler are used to reduce the temperature between the stages. Additional controls are necessary to prevent the compressor from operating in surge or stall conditions [72].

Reactive Power

The reactive power is controlled through the excitation system of the synchronous machines, which has the objective of regulating the terminal voltage by controlling the dc voltage applied to the field winding (v_F or its equivalent emf E_f). The main components of a typical excitation system are [61]:

- The exciter provides the dc power to the synchronous machine field winding. The exciter could be dc, ac or static. Dc generators, self- or separately excited, are used as sources of power in dc excitation system, while ac alternators along with ac/dc rectifiers are used in ac exciters. Static exciters rectify the ac power obtained from the terminals of the main generator, to produce the dc voltage fed to the field winding.
- The Automatic Voltage Regulator (AVR) processes the input signals to control the exciter and thus achieve the desired terminal voltage. Additional devices might be necessary to amplify the low-power signals from the voltage transducers to a level capable of controlling the exciter.
- Voltage transducers are used to measure and transform the terminal voltage to a level that is suitable to handle by the AVR. Compensation circuits might be added to regulate the voltage at points within or beyond the terminal voltage.
- Power System Stabilizers (PSSs) introduce a compensating signal to the AVR, to damp low-frequency oscillations in the system by adding a supplementary damping torque to the electrical power through the field circuit.
- Limiters and protective circuits are used to prevent the machine and exciter to operate beyond their capability.

The IEEE Type DC1A excitation system model presented in Figure 2.14 [61], is a dc exciter commonly used in synchronous machines with dc exciters for transient stability studies, and is therefore used in this thesis for both CAES synchronous machines, since the Huntorf CAES facility, which is used here for modeling and comparison purposes, likely uses these types of exciters given its age. The AVR is represented by a lead or lag compensator and the amplifier by a first order transfer function with limits. The function S_E is used to represent saturation in the magnetic circuit of the exciter. Special stabilizing feedback signals are added to the regulator path to enhance the dynamic response of the system to compensate for the delays introduced by the different components of the excitation system. The variable $\bar{V}_C$ is the measured voltage, and $\bar{V}_S$ is the external signal coming from the

PSS. The HV gate is used to let the $\bar{V}_{UEL}$ signal to by-pass the main regulator if the underexcitation limit of the machine is violated.

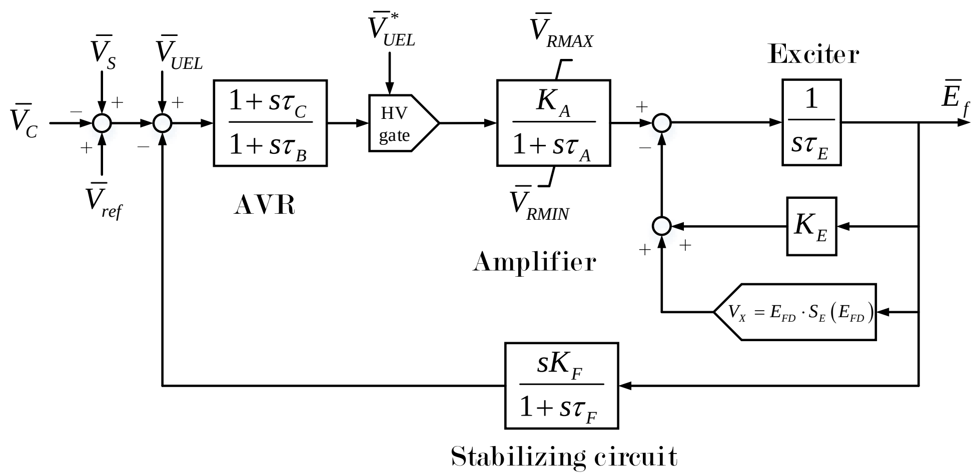

Figure 2.14: IEEE type DC1A excitation system [61]

2.4 Frequency Regulation

Maintaining the system frequency within acceptable ranges is very important for the correct functioning of generating plants and some electrical loads such as motors. Therefore, control of the frequency is a fundamental task in the operation of power systems. Variations in the frequency occur when generation does not match demand, which cannot be controlled (in most cases), and is unpredictable and highly variable. Contingencies in the system such as load shedding, generation tripping, faults, large loads being connected or disconnected are also responsible for this mismatch. When generation surpasses the demand, the system accelerates due to the excess of kinetic energy stored in the rotating masses of the rotors and the frequency increases; on the other hand, when generation is less than the demand, the latter behaves as an electrical break, slowing down the rotors and thus the frequency falls below its nominal value. The instantaneous deviation of the frequency is dependent on the inertia of the system. Thus, for a single machine system, the speed deviation can be determined using the following swing equation:

$$\frac{2H}{\omega_o}\frac{d\Delta\omega}{dt} = \bar{P}_m - \bar{P} - D\Delta\bar{\omega} \tag{2.21}$$

The objective of frequency regulation is to adjust the mechanical torque of the generator such that it matches the electrical torque to, first, arrest the machine acceleration or deacceleration ($\Delta\dot{\omega} = 0$) through a control action known as Primary Frequency Regulation (PFR) or inertial response, and then to bring the frequency back to its nominal value ($\Delta\omega = 0$) by complementary actions in some generators, known as Secondary Frequency Regulation (SFR). The frequency control acts on the generator's prime mover and is performed by the governor, which sends appropriate commands to the turbine actuators, such as valves, gates, etc., to adjust the mechanical power.

The PFR control action is based on a proportional speed-droop control, using the speed deviation $\Delta\omega$ (frequency error) as feedback signal, thus yielding a steady-sate error in $\Delta\omega$ that is proportional to the magnitude of the system disturbance ΔP_L. The control gain is defined by the parameter R known as the governor droop or regulation characteristic, which defines a linear relation, of negative slope, between the speed change and the output power variation as follows [61]:

$$R = \frac{\text{percent of speed or frequency change}}{\text{percent power output change}} \times 100\% \tag{2.22}$$

$$= \left(\frac{\omega_{NL} - \omega_{FL}}{\omega_o} \right) \times 100\% \tag{2.23}$$

where ω_{NL} is the rotor speed at no-load, and ω_{FL} the rotor speed at full load. The speed-droop characteristic allows generators connected to the same system share the active power imbalance in proportion to their own R. A basic speed-droop governor integrated in a generating station is shown in Figure 2.15.

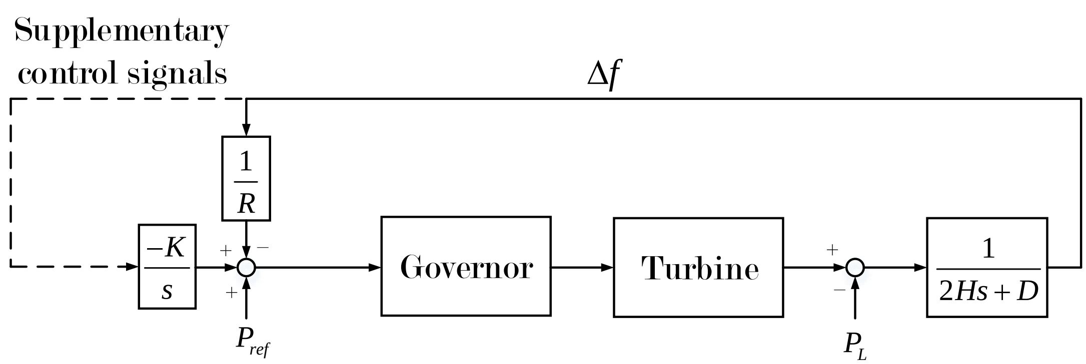

Figure 2.15: Block diagram of a generating unit with a governor [61]

In order to recover the frequency to its nominal value after the PFR acts, selected generators, which are required to operate in Automatic Generation Control (AGC) mode, provide SFR by modifying their load reference setpoints in an outer control loop that integrates the speed error. The SFR control is slower than the PFR and therefore, takes place several seconds after the frequency has been stabilized following a disturbance. Typically, hydro units provide this service due to their fast response and zero operating cost. In interconnected power systems, Δf is replaced by a more complex signal, remotely calculated by the ISO, which aims to not only recover the frequency, but also maintain the power flows on the tie-lines to their scheduled values, so that the steady-state generators' schedules in each area, are adjusted in response to the disturbances occurring in their own areas only. This signals are called Area Control Error (ACE).

2.5 Power System Stability [63]

Power System stability is defined as "the ability of the grid to return to a normal operating condition after being subjected to a perturbation", i.e., the electrical variables should be within acceptable limits (as defined by the system operator), and the system topology should not suffer major changes. The stability problem can be classified in three main groups: angle stability, voltage stability, and frequency stability.

Angle stability is directly related to the operation of the synchronous generators and their ability to remain in synchronism. It can further be classified as small-signal stability and transient stability. The first refers to the ability of the system to withstand small perturbations which, in some circumstances, can produce system oscillations that must be properly damped. Transient stability studies monitor the system behaviour, specially the rotor angles, subjected to large disturbances such as faults, tripping of transmission lines or generators, etc.

Voltage stability refers to the ability of the system to maintain the voltages at normal operating conditions after a small or large perturbation in the system. It can be subclassified as short-term and long-term voltage stability. Short-term voltage stability is associated with the effect of the operation of dynamic voltage compensation devices such as voltage regulators, FACTS devices used for reactive power support e.g., (SVC and STATCOM), synchronous condensers, etc. Long-term voltage stability, on the other hand, focuses on determining the capacity of the grid to provide the necessary reactive power to the load to prevent a voltage collapse.

Frequency stability is defined as the ability of the system to maintain an acceptable frequency after a system disturbance resulting in a significant imbalance between generation and load. Frequency deviations can lead to critical changes in other system variables, and impact the operation of protection devices that trigger generators shut-down to avoid damages, especially in turbines. These actions may lead to the formation of electrical islands or result in blackouts.

Different theories and methods to study transient stability from a more conceptual point of view are available, such as the Equal Area Criterion or the use of Lyapunov's functions; however, these approaches are difficult to apply to large power systems, which makes them impractical, in addition to other drawback summarized in [73]. Hence, computational simulations is the preferred method for transient stability studies, which requires special integration techniques to solve the models usually expressed as DAEs, with the parametrization of these being a challenge.

In the study of transient stability using computational simulations, usually the rotor angles δ of the generators are observed; in unstable systems, these angles tend to separate from each other, as the machines accelerate by accumulating kinetic energy. The severity of a contingency can be measured by the appropriate indices, such as the power angle-based stability margin defined as [17]:

$$\zeta = \frac{360 - \delta_{\max}}{360 + \delta_{\max}} 100, \quad -100 < \zeta < 100 \tag{2.24}$$

where $\delta_{\max}$ is the maximum angle separation of any two generators in the post-fault response. Here, $\zeta > 0$ and and $\zeta < 0$ correspond to stable and unstable conditions, respectively [17]. A positive value of ζ could be defined to provide a security margin in a contingency evaluation, e.g., $\zeta = 33 \rightarrow \delta_{\max} = 180°$.

Another common index to evaluate the severity of a contingency is the Critical Clearing Time (CCT), which is defined as the maximum time a disturbance can be withstood before the system looses its stability. Large CCTs represent more stable systems.

2.6 Summary

In this Chapter, an overview about the most common types of CAES systems, including adiabatic, diabatic, and isothermal were discussed. Furthermore, models of the main electromechanical equipment used in CAES, namely synchronous machines, gas turbines, compressors, and their associated controls were presented. Finally, the concept of frequency regulation and system stability, which will be used to evaluate the impact of CAES in the electrical grid, were briefly discussed.

Chapter 3

Modelling and Control of Compressed Air Energy Storage Systems for Power System Applications

In this Chapter, a comprehensive mathematical model of a diabatic CAES system suitable for power system studies considering two independent synchronous machines (motor and generator) is proposed, based on the system designs in [9] and [13]. Two CAES models are proposed, a detailed one, which includes all the components depicted in Figure 2.3, and a simplified model, which considers a reduced number of elements but facilitates its implementation in common power system packages for dynamic simulations, without significantly compromising its accuracy. Different levels of complexity are discussed for some specific model components, namely compressor maps, turbine maps, cavern, and expander valve, which can further simplify the model implementation.

3.1 CAES General Configuration

The detailed model proposed in the following sections is based on the CAES system depicted in Figure 3.1, based on Figure 2.3. The proposed detailed and simplified models are based on the following general assumptions:

- The proportion of gas to air in the expander is very small, i.e., $\dot{m}_t + \dot{m}_f \approx \dot{m}_t$ [66].

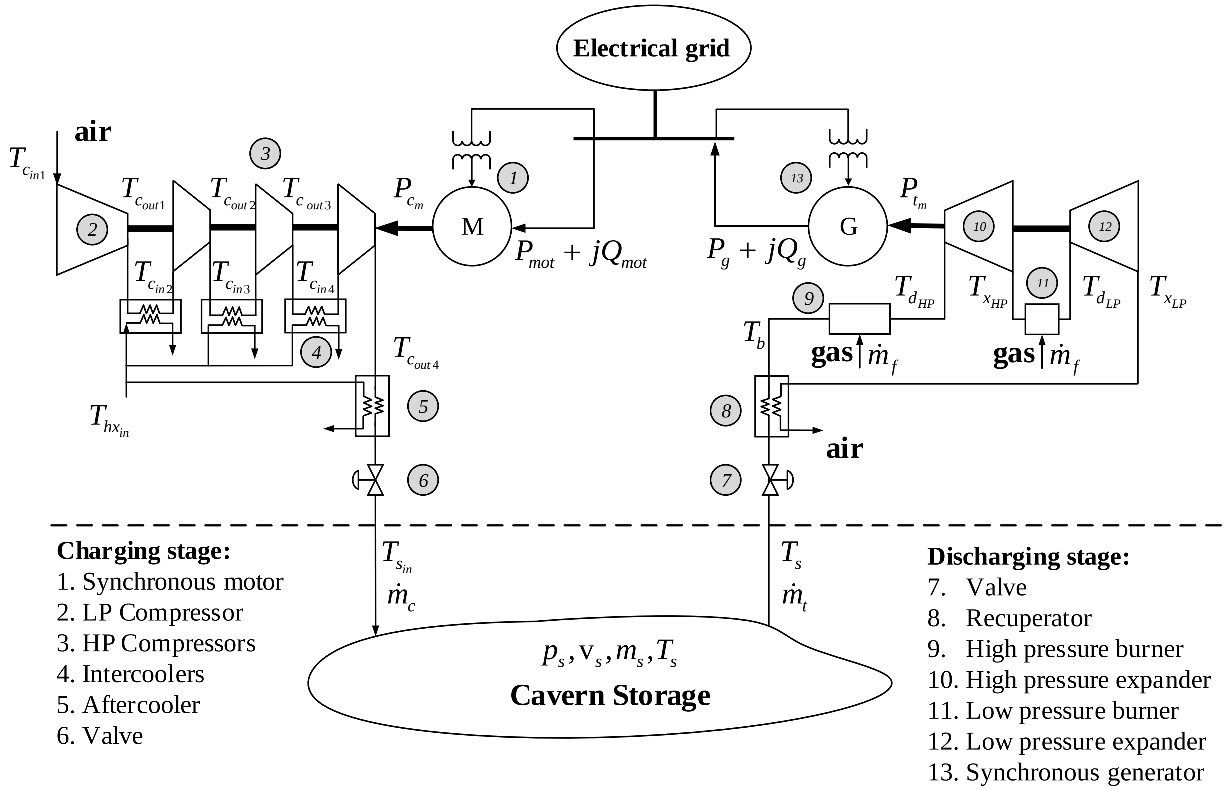

Figure 3.1: Configuration of a diabatic, two-machine CAES system based on [13]. All variables are defined in the Nomenclature.

- The air behaves as an ideal gas, i.e., $\Delta h = c_p \Delta T$ for expansion and compression [74].
- The turbine, compressor, recuperator, intercoolers and aftercooler, and cavern are represented by steady-flow processes, i.e, the fluid properties can change from point to point within the control volume, but at any fiexed point they remain the same during the entire process [74]. Hence, their input-output relations can be modeled through steady-state equations.
- All efficiencies are constant.
- Changes in kinetic and potential energy in the processes are negligible, i.e., $q - W = \Delta \mathrm{H}$ [74].
- In simulations, the CAES system will be operating at ambient conditions at sea level, i.e., $p_{am} = 1$ atm and T_{am} =288.15 K. All temperatures are expressed in Kelvin [K].

- The synchronous machines remain synchronized with the grid at all times [9], i.e., if one machine is not injecting power (positive or negative), it operates as a synchronous condenser, and can inject reactive power.

3.2 CAES Models in Discharging Mode

The CAES system components operating during the discharging mode are: the discharging air valve, recuperator, high-pressure and low-pressure burners, the high-pressure and low-pressure expanders, and the synchronous generator. The proposed models and their interrelations are presented next.

3.2.1 Detailed Model

Recuperator

The recuperator is modeled as an isobaric counter-flow heat exchanger. Its hot side is fed by the exhaust gases at temperature of the low-pressure turbine $T_{x_{LP}}$, while the air coming from the cavern enters the cold side at temperature T_s, reaching T_b at its outlet. Given that the outlet temperature of the recuperator is unknown, the heat exchanging process can be described by its effectiveness ϵ_r, defined as the ratio of the actual regenerated heat transfer rate over the maximum possible heat transfer rate, as follows [75]:

$$\epsilon_r = \frac{\dot{q}}{\dot{q}_{\max}} = \frac{\dot{m}_t \left(h_b - h_s\right)}{\dot{m}_t \left(h_{x_{LP}} - h_s\right)} \tag{3.1}$$

Where the variables and parameters are defined on the Nomenclature section. Under the ideal gas assumption, ϵ_r can be expressed as a function of temperatures, as follows:

$$\epsilon_r = \frac{c_p \left(T_b - T_s\right)}{c_p \left(T_{x_{LP}} - T_s\right)} = \frac{T_b - T_s}{T_{x_{LP}} - T_s} \tag{3.2}$$

where c_p is the specific heat capacity at constant pressure in [kJ/kg.K]. From (3.2), and assuming that the same fluid (turbine air flow) passes through the hot and cold sides of the recuperator at the same time (no flow variations), T_b in p.u. of its nominal value T_{b_o}, can be calculated as:

$$\bar{T}_b = \frac{T_s}{T_{b_o}} + v_r \tag{3.3}$$

where v_r is the temperature rise (due to the heat transferred from the exhaust air flow to the cavern air flow) in the recuperator, in p.u. of the nominal high-pressure burner inlet temperature T_{b_o}.

The heat is not recovered in the recuperator instantly, as this is a dynamic process that can be modeled by partial differential equations representing the unsteady heat transfer between hot gas side to the wall, from the cold gas side to the wall, and from the hot to cold side through the wall [76]. However, according to [77], the unsteady heat recovered in the recuperator, i.e., that transferred from the hot to the cold side through the wall, can be approximated by a single first order differential equation. Based on this, the temperature rise v_r can be calculated as follows:

$$\frac{dv_r}{dt} = \frac{1}{\tau_R}\left[\epsilon_r \left(\frac{\bar{T}_{x_{LP}} T_{x_{LPo}} - T_s}{T_{b_o}}\right) - v_r\right] \tag{3.4}$$

where τ_R is the time constant of the recuperator in sec., $\bar{T}_{x_{LP}}$ is the exhaust temperature of the LP expander in per unit of its own nominal value $T_{x_{LPo}}$, and T_s is the cavern temperature. The effectiveness ϵ_r can be calculated by solving (3.3) and (3.4) in steady-state condition, considering $\bar{T}_b = 1$ and $\bar{T}_{x_{LP}} = 1$.

This model assumes that the temperature in the cold side of the heat exchanger increases at the same rate as the hot side, because both have the same heat capacity rate defined as $C = \dot{m}c_p$. The input temperatures at the cold and hot side are algebraic variables, while the output temperatures, which are state variables, experience the exact same dynamics. If the heat capacity rates were different, the dynamics would still be the same, but the fluid with lower C would experience a larger temperature change. In the aftercooler and intercooler models discussed later, the same first order approximation will be used; however, their hot- and cold-side dynamics are different from the recuperator, because in the former, two independent flows circulate in their cold and hot thermal circuits.

Combustion Chambers or Burners

The combustion in the burners is produced by a mixture of fuel (gas) and air, which occurs so fast that its dynamics can be neglected. In the high-pressure and low-pressure burners, the inlet temperatures to their respective expanders $T_{d_{HP}}$ and $T_{d_{LP}}$ rise as the amount of fuel injected into the burners increases (fuel mass flow rate $\dot{m}_f$), and cool down as the air mass flow rate $\dot{m}_t$ increases. It is assumed that the fuel flows in the two burners are controlled by the same controller; hence, these vary proportionally, and thus the per-unit rate of fuel flow in both burners is the same, i.e., $\bar{\dot{m}}_{f_{HP}} = \bar{\dot{m}}_{f_{LP}} = \bar{\dot{m}}_f$. From the energy balance of the combustion chamber, and assuming isobaric heat addition, the output temperature of the HP and LP burners, in p.u. of their nominal values, can be obtained as follows [66]:

$$\bar{T}_{d_{HP}} = \bar{T}_b \left(\frac{T_{b_o}}{T_{d_{HPo}}} \right) + \frac{T_{d_{HPo}} - T_{b_o}}{T_{d_{HPo}}} \left(\frac{\bar{\dot{m}}_f}{\bar{\dot{m}}_t} \right) \tag{3.5}$$

$$\bar{T}_{d_{LP}} = \bar{T}_{x_{HP}} \left(\frac{T_{x_{HPo}}}{T_{d_{LPo}}} \right) + \frac{T_{d_{LPo}} - T_{x_{HPo}}}{T_{d_{LPo}}} \left(\frac{\bar{\dot{m}}_f}{\bar{\dot{m}}_t} \right) \tag{3.6}$$

where the inlet temperature of the air at the HP burner is T_b, while the inlet temperature at the LP burner is equal to the exhaust temperature of the HP turbine $T_{x_{HP}}$. The temperature $T_{d_{HPo}}$ is a known turbine parameter; therefore, T_{b_o} can be calculated by solving (3.5) for $\bar{T}_b = 1$ p.u., $\bar{T}_{d_{HP}} = 1$ p.u., $\bar{\dot{m}}_t = 1$ p.u., and $\bar{\dot{m}}_f = 1$ p.u. The terms $\left(T_{d_{HPo}} - T_{b_o}\right)/T_{d_{HPo}}$ and $\left(T_{d_{LPo}} - T_{x_{HPo}}\right)/T_{d_{LPo}}$ are the design temperature rise of the HP and LP combustors in per unit of their respective nominal firing temperatures. In this model, the output temperature of the burner varies linearly with the per unit fuel mass flow rate $\bar{\dot{m}}_f$, while varying inversely with the air mass flow rate $\bar{\dot{m}}_t$. Furthermore, the air mass flow rate is the same through the expansion stage and that the heat addition in the burners is isobaric, i.e., no pressure drops.

Expander

For isentropic air expansion at each stage k, the corresponding isentropic exhaust temperatures $T_{x_{i_k}}$ becomes a function of the turbine's stage pressure ratio π_{t_k} and inlet temperature, as follows [74]:

$$\frac{T_{x_{i_k}}}{T_{d_k}} = \pi_{t_k}^{-\frac{\gamma-1}{\gamma}} \tag{3.7}$$

where $\gamma = c_p/c_v$ is the heat capacity ratio, and $k \in \{LP, HP\}$. However, the actual temperature change deviates from the isentropic idealization, which can be accounted for by the isentropic efficiency $\eta_{t_{i_k}}$, as follows [74]:

$$\eta_{t_{i_k}} = \frac{h_{d_k} - h_{x_k}}{h_{d_k} - h_{x_{i_k}}} \tag{3.8}$$

From (3.7) and (3.8), and since $\Delta T = c_p \Delta h$ for ideal gases, the exhaust temperature of the high-pressure and low-pressure expanders, in p.u., can be calculated as follows:

$$\bar{T}_{x_{HP}} = \frac{T_{d_{HPo}} \bar{T}_{d_{HP}}}{T_{x_{HPo}}} \left[1 - \left(1 - \frac{1}{\pi_{t_{HP}}^{\frac{\gamma-1}{\gamma}}} \right) \eta_{t_{i_{HP}}} \right] \tag{3.9}$$

$$\bar{T}_{x_{LP}} = \frac{T_{d_{LPo}} \bar{T}_{d_{LP}}}{T_{x_{LPo}}} \left[1 - \left(1 - \frac{1}{\pi_{t_{LP}}^{\frac{\gamma-1}{\gamma}}} \right) \eta_{t_{i_{LP}}} \right] \tag{3.10}$$

$T_{d_{HPo}}$ is a known turbine parameter; hence, $T_{x_{HPo}}$ can be calculated by solving (3.9) for $\bar{T}_{d_{HP}} = 1$ p.u., $\bar{T}_{x_{HP}} = 1$ p.u., and $\pi_{t_{HP}} = \pi_{t_{HPo}}$. The inlet temperature $T_{d_{LPo}}$ can be calculated by solving (3.6) for $\bar{T}_{x_{HP}} = 1$ p.u., $\bar{T}_{d_{LP}} = 1$ p.u., , $\bar{\dot{m}}_t = 1$ p.u., and $\bar{\dot{m}}_f = 1$ p.u.; thus, $T_{x_{LPo}}$ is found by solving (3.10) for $\bar{T}_{d_{LP}} = 1$ p.u., $\bar{T}_{x_{HP}} = 1$ p.u., and $\pi_{t_{LP}} = \pi_{t_{LPo}}$.

Since both turbine stages ($k \in \{LP, HP\}$) are lumped to the same rotor, and given that for a steady-flow the rate of change of the internal energy of a turbine is zero, the total mechanical power delivered to the generator shaft can be computed as the summation of the difference between the inlet and outlet rate of change of enthalpy $\dot{H}$ of each expansion stage, as follows:

$$P_{t_m} = \sum_k P_{t_{m_k}} = \sum_k \left(\dot{H}_{d_k} - \dot{H}_{x_k} \right) \tag{3.11}$$

If the enthalpy is expressed as the specific enthalpy times the mass, then the turbine's mechanical power becomes a function of the rate of change of the mass and the temperature difference between the turbine's inlet and outlet. Hence, assuming that friction losses are represented by the mechanical efficiency $\eta_{t_{k_m}}$, the output mechanical power of each expansion stage, in per unit of the total nominal turbine power $P_{t_{m_o}}$ in MW, can be approximated by:

$$\bar{P}_{t_{m_{LP}}} = \frac{\eta_{t_{LPm}} c_p \dot{m}_{t_o} \bar{\dot{m}}_t}{10^3 P_{t_{m_o}}} \left(T_{d_{LPo}} \bar{T}_{d_{LP}} - T_{x_{LPo}} \bar{T}_{x_{LP}} \right) \tag{3.12}$$

$$\bar{P}_{t_{m_{HP}}} = \frac{\eta_{t_{HPm}} c_p \dot{m}_{t_o} \bar{\dot{m}}_t}{10^3 P_{t_{m_o}}} \left(T_{d_{HPo}} \bar{T}_{d_{HP}} - T_{x_{HPo}} \bar{T}_{x_{HP}} \right) \tag{3.13}$$

$$\bar{P}_{t_m} = \bar{P}_{t_{m_{LP}}} + \bar{P}_{t_{m_{HP}}} \tag{3.14}$$

where $\eta_{t_{LPm}}$ and $\eta_{t_{HPm}}$ are the mechanical efficiencies of the LP and HP expanders, c_p is the specific heat capacity at constant pressure [kJ/kg.K], and m_{t_o} is the nominal mass flow rate of the turbine in [kg/s]. By solving (3.11)-(3.14) for rated conditions, i.e., all per-unit quantities equal to unity, the nominal air mass flow rate $\dot{m}_{t_o}$ can be calculated.

Turbine Maps

A turbine map models the pressure ratio π_t used in the thermodynamic equations described in the previous section. In the models proposed in this thesis, it is assumed that the pressure ratios π_{t_k} are not directly defined by the cavern pressure p_s and ambient pressure p_{am}, unlike most of the existing CAES models. It is further assumed here that these two pressure define limits for the maximum pressure ratio in the expanders, and minimum pressure ratios in the compressor. These assumptions are possible due to the valves used in the air flow paths to and from the cavern (elements 6 and 7 in Figure 3.1), which allow controlling the charging and discharging powers by changing the mas flow rate and pressure ration in the expanders and compressors.

In Figure 3.2, a turbine map is presented, which illustrates the relation between the corrected mass flow rate ($\dot{m}\sqrt{T_{in}/T_{am}}/p_{in}/p_{am}$) and pressure ratio in one expansion stage for different rotor speeds. Notice that as the pressure ratio increases, the corrected mass flow rate approaches a saturation point where it cannot further increase, which is known as chocking. In effect, it is the speed of the flow and the volume flow ($\dot{V} = \dot{m}/\rho$) of the turbine variables that become chocked, whereas the air flow rate $\dot{m}$ could be still increased if the input pressure or temperature changes [78]. Furthermore, the turbine maps assume constant inlet conditions (p_{in}, T_{in}); hence, the pressure ratio in the horizontal axis varies with the output pressure only.

Three approximations to represent these maps are discussed next: independent pressure ratio and air flow at each expansion stage, pressure ratio as a linear function of the air mass flow rate, and nozzle approximation of the pressure ratio. Thus, the simplest, but

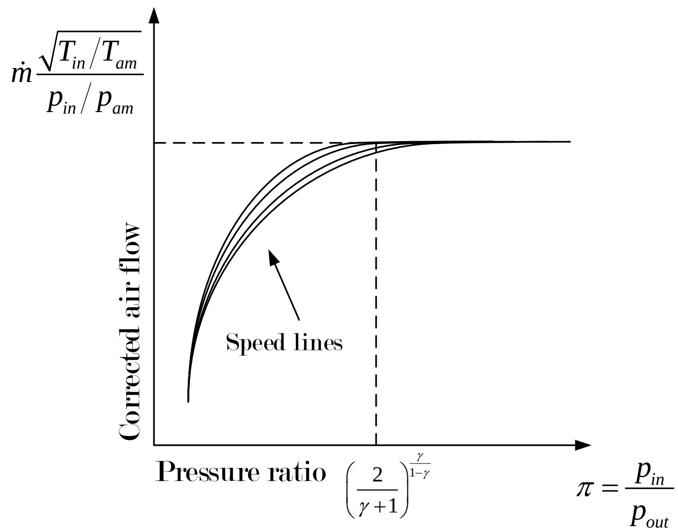

Figure 3.2: Turbine map.

least accurate, representation of the turbine map is to assume that the pressure ratio and the air mass flow rate are independent of each other [28–30], as follows:

$$\pi_{t_k} = \frac{p_{t_{k_{in}}}}{p_{t_{k_{out}}}} \tag{3.15}$$

where $k \in \{LP, HP\}$, and $p_{t_{k_{in}}}$ and $p_{t_{k_{out}}}$ are the input and output pressures of the corresponding stage k. If the size of the cavern is large enough, this approximation results in a constant pressure ratio, i.e. $\pi_{t_k} = \pi'_{t_k}$, where π'_{t_k} is a constant pressure ratio in stage k. This assumption might be valid for quasi steady-state studies in which the air flow is approximately constant and its value depends on the pressure-ratio-airflow relation defined by an actual map as, for example, during nominal operation, i.e, $\pi_{t_k} = \pi_{t_{ko}}$ and $\dot{m}_t = \dot{m}_{t_o}$, or at an operating point close to this condition. This model could be used for long-term stability studies, by choosing appropriate $\{\pi_{t_k}, \dot{m}_t\}$ values for each operating point.

A second more realistic approach to model the turbine map, which is used in [66], assumes a linear relation between the air mass flow rate and the pressure ratio, as follows:

$$\pi_{t_k} = \pi_{t_{ko}} \bar{\dot{m}}_t \tag{3.16}$$

where $\pi_{t_{k_o}}$ is the pressure ratio of stage k at nominal conditions. Hence, when the turbine operates at nominal air flow, the pressure ratio is nominal as well.

The third approach, which is closer to actual turbine maps, involves approximating the air mass flow rate at each expansion stage as compressible flow through a nozzle, which is described as follows [78, 79]:

$$\dot{m}_t = \mu \Lambda_k p_{t_{k_{in}}} \sqrt{\frac{2}{\mathrm{R} T_{d_k}}} \sqrt{\frac{\gamma}{\gamma - 1} \left(\Pi_{t_k}^{-\frac{2}{\gamma}} - \Pi_{t_k}^{-\frac{\gamma+1}{\gamma}} \right)} \tag{3.17}$$

$$\Pi_{t_k} = \min \left\{ \pi_{t_k}, \left(\frac{2}{\gamma + 1} \right)^{\frac{\gamma}{1-\gamma}} \right\} \tag{3.18}$$

where $k \in \{LP, HP\}$; μ is the flow coefficient due to friction; Λ_k is the throttle cross-sectional area of the k-stage expander wheel; R $=$287.058 [J/kg.K] is the specific gas constant; $\gamma = 1.4$ is the specific heat capacity ratio of air; and $\pi_{t_k} = p_{t_{k_{in}}} / p_{t_{k_{out}}}$, T_{d_k}, and $p_{t_{k_{in}}}$ are the pressure ratio, input temperature and input pressure of the expansion stage k, respectively.

From (3.17) and assuming a fixed cross-sectional area at each expander stage, the per unit air mass flow rate $\bar{\dot{m}}_t$, with respect to nominal conditions represented by subindex o, can be calculated as follows:

$$\bar{\dot{m}}_t = \frac{\bar{p}_{t_{k_{in}}}}{\sqrt{\bar{T}_{d_k}}} \sqrt{\frac{\Pi_{t_k}^{-\frac{2}{\gamma}} - \Pi_{t_k}^{-\frac{\gamma+1}{\gamma}}}{\Pi_{t_{k_o}}^{-\frac{2}{\gamma}} - \Pi_{t_{k_o}}^{-\frac{\gamma+1}{\gamma}}}} \tag{3.19}$$

When the pressure ratio π_{t_k} in stage k is larger than $\left(\frac{2}{\gamma+1}\right)^{\frac{\gamma}{1-\gamma}}$, the air flow through the stage becomes choked, i.e., it does not further increase with π_{t_k}; thus, the effective pressure ratio Π_{t_k} in (3.18) is used to calculate the actual air flow in (3.17). In CAES systems, the cavern pressure is usually high, resulting in large pressure ratios at each expansion stage; therefore, it is assumed here that the HP and LP expanders operate choked for the entire range of cavern pressure, i.e., $\Pi_{t_k} = \left(\frac{2}{\gamma+1}\right)^{\frac{\gamma}{1-\gamma}}$. Hence, $\bar{\dot{m}}_t$ in (3.19) can be simplified as follows:

$$\bar{\dot{m}}_t = \frac{\bar{p}_{t_{k_{in}}}}{\sqrt{\bar{T}_{d_k}}} \tag{3.20}$$

This approximation is valid for any rotor speed, as the speed lines in a turbine map are very close to each other when it operates choked, as depicted in Figure 3.2. By substituting $p_{t_{k_{in}}} = \pi_{t_k} p_{t_{k_{out}}}$ in (3.20), where $p_{t_{k_{in}}}$ and $p_{t_{k_{out}}}$ are the actual inlet and outlet pressures of the expander at the stage k, the following expression for the pressure ratio π_{t_k} as a function of $\bar{\dot{m}}_t$ can be obtained:

$$\pi_{t_k} = \bar{\dot{m}}_t \pi_{t_{k_o}} \sqrt{\bar{T}_{d_k}} \left(\frac{p_{t_{k_{out_o}}}}{p_{t_{k_{out}}}} \right) \tag{3.21}$$

In Figure 3.3(a) the mass flow rate as a function of the pressure ratio π_t, for a single-stage turbine of nominal mass flow rate and pressure ratio of 417 kg/s and 1.89 respectively, is presented as an example of a map approximation based on (3.17), assuming constant inlet conditions, i.e., T_d =1358 K, p_{in} =191.8 kPa. On the other hand, Figure 3.3(b) shows the mass flow rate as a function of the pressure ratio for a turbine based on (3.20), assuming that it always operates choked (even for low pressure ratios) and for an actual turbine, but with its output pressure constant and variable input pressure, as in the discharging stage of a CAES system when the cavern is being depleted. Under these assumptions, if the inlet temperature is constant, the mass flow rate is a linear function of π_t, for $\pi_t \geqslant \left(\frac{2}{\gamma+1}\right)^{\gamma/(1-\gamma)}$ (≈ 1.89 for air), thus is a linear function of $p_{t_{in}}$ as well, while $\dot{m}_t$ keeps increasing despite the turbine being choked; the reason for this is that the turbine's inlet pressure changes. Notice also that the always-choked approximation deviates from the actual flow for pressure ratios lower than 1.89 p.u.; hence, if the pressure ratio across the turbine is large enough, as expected in CAES systems, the always-choked approximation is valid.

From (3.21) and assuming that the output pressure of the LP expander is constant (approximately ambient pressure), the LP pressure ratio $\pi_{t_{LP}}$ can be calculated as:

$$\pi_{t_{LP}} = \bar{\dot{m}}_t \pi_{t_{LP_o}} \sqrt{\bar{T}_{d_{LP}}} \tag{3.22}$$

where $\pi_{t_{LP_o}}$ and $\bar{T}_{d_{LP}}$ are the nominal pressure ratio and per-unit inlet temperature, respectively, of the LP expander.

Depending on the air valve model, which is discussed in the next section, the expression in (3.21) can be further simplified to calculate the HP expander pressure ratio $\pi_{t_{HP}}$. For example, if it is assumed that the valve controlling the air flow from the cavern (Figure 3.4) is also modeled as a choked nozzle, that the air mass flow rate $\bar{\dot{m}}_t$ is the same through the valve and both expansion stages, and that cavern temperature is constant ($\bar{T}_s = 1$),

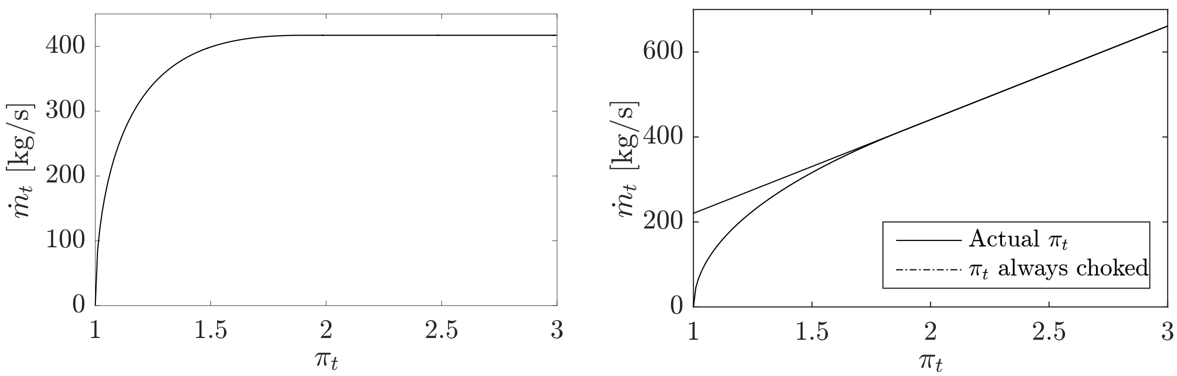

(a) (b)

Figure 3.3: Mass flow rate vs pressure ratio (a) assuming constant inlet conditions, and (b) assuming constant outlet conditions and variable inlet pressure.

then, from (3.20) and (3.21), an expression for $\pi_{t_{HP}}$ can be derived as follows:

$$\pi_{t_{HP}} = \bar{\dot{m}}_t \left(\frac{\pi_{t_{HPo}}}{\bar{p}_s} \right) \sqrt{\frac{\bar{T}_{d_{HP}}}{\bar{T}_{d_{LP}}}} \tag{3.23}$$

where p_s is the per-unit cavern pressure, $\pi_{t_{HPo}}$ is the HP nominal pressure ratio, and $\bar{T}_{d_{HP}}$ and $\bar{T}_{d_{LP}}$ are the inlet temperatures of the HP and LP expanders.

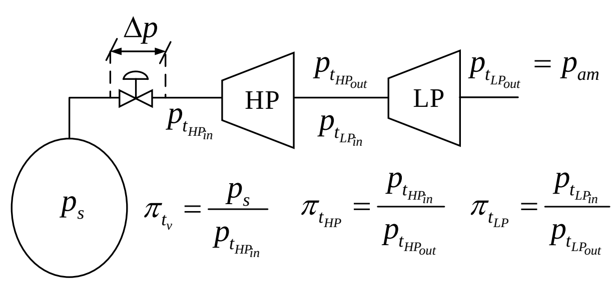

Figure 3.4: Expansion stage pressures.

Equation (3.23) can be further simplified by assuming that $(\bar{T}_{d_{HP}}/\bar{T}_{d_{LP}})^{1/2} \approx 1$ for any operating condition, because a temperature controller (discussed later) is used to adjust the fuel flow injected in the HP and LP burners to keep the inlet temperature of the expanders constant at their nominal values (variations in the range of $\pm 2\%$ were found during transients in simulations for $(\bar{T}_{d_{HP}}/\bar{T}_{d_{LP}})^{1/2}$). This simplification reduces the simulation time, and makes the model more stable, because the algebraic loops between $T_{x_{HP}} = f(\pi_{t_{HP}})$, $T_{d_{LP}} = f(T_{x_{HP}})$, and $\pi_{t_{HP}} = f(T_{d_{LP}})$ are avoided. Thus, the HP pressure ratio can be calculated as follows:

$$\pi_{t_{HP}} = \bar{\dot{m}}_t \left(\frac{\pi_{t_{HPo}}}{\bar{p}_s} \right) \tag{3.24}$$

This implies that, when the valve operates choked, as pressure in the cavern $\bar{p}_s$ drops, the air flow has to increase to maintain the pressure ratio constant.

If the controlling valve is not choked, it can be demonstrated that the HP turbine operates at its nominal pressure $\pi_{t_{HPo}}$. By substituting actual values in (3.20), the HP stage pressure ratio is obtained:

$$\pi_{t_{HP}} = \bar{\dot{m}}_t \pi_{t_{HPo}} \sqrt{\bar{T}_{d_{HP}}} \left(\frac{p_{t_{HPo_{out}}}}{p_{t_{HP_{out}}}} \right) \tag{3.25}$$

Since $p_{t_{HP_{out}}} = p_{t_{LP_{in}}}$ and $p_{t_{LP_{in}}} = \pi_{t_{LP}} p_{t_{LP_{out}}}$, it follows that:

$$\pi_{t_{HP}} = \bar{\dot{m}}_t \pi_{t_{HPo}} \sqrt{\bar{T}_{d_{HP}}} \left(\frac{\pi_{t_{LPo}}}{\pi_{t_{LP}}} \right) \tag{3.26}$$

Substituting (3.22) in (3.26), and further assuming that $\sqrt{\bar{T}_{d_{HP}}} \approx \sqrt{\bar{T}_{d_{LP}}}$ due to the operation of the temperature controller, the following simplified expression for $\pi_{t_{HP}}$ is obtained:

$$\pi_{t_{HP}} = \pi_{t_{HPo}} \tag{3.27}$$

Air Valve

The valve controlling the mass flow rate from the cavern can also be modeled using (3.19), but with a variable cross-sectional area, which allows air flow control. The cavern's temperature and pressure (T_s, p_s) are the valve's inlet temperature and pressure, respectively, which yields:

$$\bar{\dot{m}}_t = \frac{\lambda \bar{p}_s}{\sqrt{\bar{T}_s}} \sqrt{\frac{\Pi_{t_v}^{-\frac{2}{\gamma}} - \Pi_{t_v}^{-\frac{\gamma+1}{\gamma}}}{\Pi_{t_{vo}}^{-\frac{2}{\gamma}} - \Pi_{t_{vo}}^{-\frac{\gamma+1}{\gamma}}}} \tag{3.28}$$

$$\Pi_{t_v} = \min\left\{\pi_{t_v}, \left(\frac{2}{\gamma+1}\right)^{\frac{\gamma}{1-\gamma}}\right\} \tag{3.29}$$

where $\lambda = \Lambda_v/\Lambda_{v_o}$ is the per-unit cross-sectional area of the valve, having the value of zero when it is fully closed, and π_{t_v} its pressure ratio. Hence, the total expansion pressure ratio π_t, from cavern pressure p_s to ambient pressure $p_{t_{LP_{out}}}$ (see Figure 3.4), is $\pi_t = \pi_{t_v}\pi_{t_{HP}}\pi_{t_{LP}}$. The nominal equivalent turbine pressure $\pi_{t_{HPo}}\pi_{t_{LPo}}$ must be lower than the minimum cavern pressure in normal conditions; therefore, there is always a pressure drop Δp (Figure 3.4) across the valve. If $\pi_{t_v} \geqslant \left(\frac{2}{\gamma+1}\right)^{\gamma/(1-\gamma)}$, then the valve operates choked. Large cavern pressures combined with low output power in the expander (thus, low pressure ratios) might choke the valve or at least drive it close to this condition. When the valve is choked, the mass flow rate can be controlled by changing λ in (3.28). Thus, assuming constant cavern temperature $\bar{T}_s = 1$ p.u., the air mass flow rate through the valve can be calculated as follows:

$$\bar{\dot{m}}_t = \lambda \bar{p}_s \tag{3.30}$$

A further approximation assumes a linear relation between $\dot{m}_t$ and Λ_v, thus $\bar{\dot{m}}_t = \lambda$ (linear valve). Conversely, if the valve is not choked, (3.28) and (3.29) should be used to model the valve. However, if the valve pressure ratio is close to unity, the air mass flow rate can be calculated using the equation of an incompressible flow through a nozzle [80]:

$$\dot{m}_t = \Lambda_v \sqrt{2\rho\left(p_s - p_{t_{HP_{in}}}\right)} \tag{3.31}$$

where ρ is the density of the air in [kg/m^3]. Assuming that when the cavern pressure is at its minimum "economical" pressure p_s' defined in Section 3.5.1, the turbine is able to operate at nominal conditions. Hence:

$$\dot{m}_{t_o} = \Lambda_{v_o}\sqrt{2\rho\Delta p_{\min}} \tag{3.32}$$

where $\Delta p_{\min} = p'_{s_{\min}} - p_{t_{HPo_{in}}}$ is the minimum pressure drop across the valve required to generate nominal power, $\dot{m}_{t_o}$ is the nominal air mass flow rate, and Λ_{v_o} is the cross-sectional area required to let $\dot{m}_{t_o}$ pass when the valve pressure drop is $\Delta p_{\min}$. Hence, using the incompresibilty approximation and nominal mass flow rate in (3.31) and (3.32), respectively, the per-unit turbine air flow can be obtained as follows:

$$\bar{\dot{m}}_t = \lambda \sqrt{\frac{p_s - p_{t_{HP_{in}}}}{\Delta p_{\min}}} \tag{3.33}$$

This expression can be used to map λ values to $\bar{\dot{m}}_t$ values; hence, the limits for λ can be calculated as a function of the limits of mass flow rate.

3.2.2 Simplified Model

A simplified model to represent the two-stage CAES expander is proposed in this section, assuming two identical HP and LP turbines. The objective of this model is to obtain the same mechanical output power as the detailed model, but only specifying HP-expander inlet parameters and LP-expander outlet parameters, as done in single-stage turbines. The proposed simplified model is based on the following assumptions:

- The LP and HP pressure ratios are approximately equal, $\pi_{t_{HP}} \approx \pi_{t_{LP}}$; thus, $\pi_t^{1/2} = \pi_{t_{LP}} = \pi_{t_{HP}}$.
- The isentropic efficiency of both stages is approximately the same, i.e., $\eta_{t_{HPi}} \approx \eta_{t_{LPi}} = \eta_{t_i}$.
- The mechanical efficiency of both stages is approximately the same, i.e., $\eta_{t_{HPm}} \approx \eta_{t_{LPm}} = \eta_{t_m}$.
- The above three assumptions also result in the same temperature drop in the HP and LP expanders, i.e., $T_{d_{HP}} - T_{x_{HP}} = T_{d_{LP}} - T_{x_{LP}}$.
- $T_{d_{LP}} > T_{d_{HP}}$, as in the Huntorf CAES plant [13].

Substituting (3.9) and (3.10), in (3.12) and (3.13), respectively, the output mechanical power in the HP and LP expanders can be calculated as follows:

$$\bar{P}_{t_{m_{HP}}} = \frac{\eta_{t_m} \eta_{t_i} c_p \dot{m}_{t_o} \bar{\dot{m}}_t}{10^3 P_{t_{m_o}}} \left(1 - \frac{1}{\pi_t^{\frac{\gamma-1}{2\gamma}}}\right) T_{d_{HP}} \tag{3.34}$$

$$\bar{P}_{t_{m_{LP}}} = \frac{\eta_{t_m} \eta_{t_i} c_p \dot{m}_{t_o} \bar{\dot{m}}_t}{10^3 P_{t_{m_o}}} \left(1 - \frac{1}{\pi_t^{\frac{\gamma-1}{2\gamma}}}\right) T_{d_{LP}} \tag{3.35}$$

Thus, the total mechanical power is:

$$\bar{P}_{t_m} = \bar{P}_{t_{m_{HP}}} + \bar{P}_{t_{m_{LP}}} \tag{3.36}$$

Since $T_{d_{LP}} > T_{d_{HP}}$, and from (3.7) $T_{d_{HP}} > T_{x_{HP}}$, in order to remove the dependency of $T_{d_{LP}}$ on (3.36), and to represent the effects of the LP burner in the mechanical power calculation, the following expression can be used for $T_{d_{LP}}$, based on the burner model proposed in [66]:

$$T_{d_{LP}} = T_{d_{HP}} + \Delta T_o \left(\frac{\bar{\dot{m}}_f}{\bar{\dot{m}}_t} \right) \tag{3.37}$$

where the term ΔT_o represents the nominal inlet temperature rise of the LP expander with respect to the inlet temperature of the HP expander $T_{d_{HP}}$. Thus, replacing (3.37) in (3.34)-(3.36), the CAES system turbine's total mechanical power for both LP and HP stages can be calculated as follows:

$$\bar{P}_{t_m} = \frac{\eta_{t_i} \eta_{t_m} c_p \dot{m}_t \left[2T_d + \Delta T_o \left(\frac{\bar{\dot{m}}_f}{\bar{\dot{m}}_t} \right) \right]}{10^3 P_{t_{m_o}}} \left(1 - \frac{1}{\pi_t^{\frac{\gamma-1}{2\gamma}}} \right) \tag{3.38}$$

where ΔT_o is calculated for nominal conditions, i.e., $\bar{P}_{t_m} = 1$, $T_d = T_{d_o}$, $\bar{\dot{m}}_f = 1$, $\bar{\dot{m}}_t = 1$ and $\pi_t = \pi_{t_o}$; and η_{t_m} and η_{t_i} are the equivalent mechanical and isentropic efficiencies of the expansion, respectively. The recuperator, the HP burner (now referred to as burner), and the control system remain the same as in the detailed model, substituting T_x for $T_{x_{LP}}$. Similarly, the turbine exhaust temperature can be calculated by substituting (3.37) in (3.10) as follows:

$$\bar{T}_x = \frac{T_{d_o} \bar{T}_d + \Delta T_o \left(\frac{\bar{\dot{m}}_f}{\bar{\dot{m}}_t} \right)}{T_{x_o}} \left[1 - \left(1 - \frac{1}{\pi_t^{\frac{\gamma-1}{2\gamma}}} \right) \eta_{t_i} \right] \tag{3.39}$$

3.2.3 Synchronous Generator

The synchronous machine model is the one described in Section 2.3.1 for the generator. In the machine model equations, the subindex t is used for the turbine's mechanical power, rotor speed, and inertia constant P_{m_t}, ω_t, and H_t, respectively, and g is used to differentiate electrical generator variables from motor variables, e.g., active power P_g, current I_g, etc.

3.3 Charging Mode

The components involved in this operational mode of the CAES system are the compressor, intercoolers, aftercooler, and the synchronous motor, as depicted in Figure 3.1. The HP compressor is modeled as a multi-stage compression system with an intercooler between each stage, while the LP compressor is modeled as a single-stage compression unit [56]; an intercooler is also used between the LP and HP compressors. The index $j \in \{\mathrm{LP}, \mathrm{HP}_1, \mathrm{HP}_2, \mathrm{HP}_3\}$ identifies the different compression stages.

3.3.1 Detailed Model

Compressor

The thermodynamic model of the compressor is similar to that of the turbine, but in the former, the energy from an electric motor flows into the compressor. Thus, assuming isentropic compression at each stage j, the discharging temperature $T_{c_{out_{i_j}}}$ is calculated as follows [74]:

$$\frac{T_{c_{out_{i_j}}}}{T_{c_{in_j}}} = \pi_{c_j}^{\frac{\gamma-1}{\gamma}} \tag{3.40}$$

$$\pi_{c_j} = \frac{p_{c_{out_j}}}{p_{c_{in_j}}} \tag{3.41}$$

where $T_{c_{in_j}}$, π_{c_j}, $p_{c_{in_j}}$, and $p_{c_{out_j}}$ are respectively the inlet temperature, pressure ratio, input pressure, and output pressure of the compression stage j.

Using the isentropic efficiency, defined as:

$$\eta_{c_{i_j}} = \frac{h_{c_{out_{i_j}}} - h_{c_{in_j}}}{h_{c_{out_j}} - h_{c_{in_j}}} \tag{3.42}$$

and since $\Delta T = c_p \Delta h$, the discharge temperature of the stage j can be calculated as:

$$T_{c_{out_j}} = T_{c_{in_j}} \left\{ 1 + \left(\pi_{c_j}^{\frac{\gamma-1}{\gamma}} - 1 \right) \frac{1}{\eta_{c_{i_j}}} \right\} \tag{3.43}$$

The total mechanical power required to drive the compressors in all stages j can be calculated using the same assumptions as in (3.12)-(3.14), as follows:

$$\bar{P}_{c_{m_j}} = \frac{c_p \dot{m}_{c_o} \bar{\dot{m}}_c}{10^3 \eta_{c_{m_j}} P_{c_{m_o}}} \left(T_{c_{out_j}} - T_{c_{in_j}} \right) \tag{3.44}$$

$$\bar{P}_{c_m} = \sum_j \bar{P}_{c_{m_j}} \tag{3.45}$$

where $\bar{P}_{c_{m_j}}$ is the mechanical power of stage j in per unit of the total nominal compression power $P_{c_{m_o}}$ in [MW]; $\dot{m}_{c_o}$ is the nominal air mass flow rate of the compressor in [kg/s], $\eta_{c_{m_j}}$ is the mechanical efficiency of the compressor in stage j; and c_p is the specific heat capacity at constant pressure in [kJ/kg.K].

The Greitzer's model discussed in Section 2.3.2 is used here to model the main dynamics of the CAES system compressor; however, some simplifications are made to reduce the overall CAES model complexity. Thus, in Figure 3.5, a schematic of the charging stage is depicted, in which the multi-stage compressor is assumed to be represented by a single-stage as in [71] to reduce complexity, and the air is not discharged to the atmosphere, but to the cavern. The full set of differential equations, without any simplification of the system presented in Figure 3.5, based on the Greitzer's model is:

$$\frac{d\dot{m}_c}{dt} = \frac{1}{L/A} \left(p_{c_{out}} - p_{pl} \right) \tag{3.46}$$

$$\frac{d\dot{m}_d}{dt} = \frac{1}{L_T/A_T} \left[(p_{pl} - p_s) - (p_{pl}^{ss} - p_s) \right] \tag{3.47}$$

$$\frac{dp_{c_{out}}}{dt} = \frac{1}{\tau_{CD}} \left(\pi_c \left(\dot{m}_c^{ss}, \omega_c \right) p_{c_{in}} - p_{c_{out}} \right) \tag{3.48}$$

$$\frac{dp_{pl}}{dt} = \frac{\gamma \mathrm{R} T_{c_{out}}}{\mathrm{v}_{pl}} \left(\dot{m}_c - \dot{m}_d \right) \tag{3.49}$$

$$0 = -(p_{pl}^{ss} - p_s) + \frac{\dot{m}_d^2}{2\rho A_T^2} \tag{3.50}$$

where $\dot{m}_c^{ss}$ is the instantaneous mass flow rate circulating through the compressor as a result of the controlling action of the IGVs, and p_s is the cavern pressure in Pa. Since the proposed air flow control is performed by the IGV rather than the throttling valve (element 5 in Figure 3.5), the latter will not be modeled in detail. In fact, it is proposed here that this valve is modeled as an actuator disk rather than by the incompressible fluid through a nozzle approximation used in [71]. This assumption implies a continuous air flow through the valve:

$$\bar{\dot{m}}_c = \bar{\dot{m}}_d \tag{3.51}$$

Notice that (3.51) eliminates the differential equation of the plenum (3.49), i.e., $\dot{p}_{pl} = 0$.

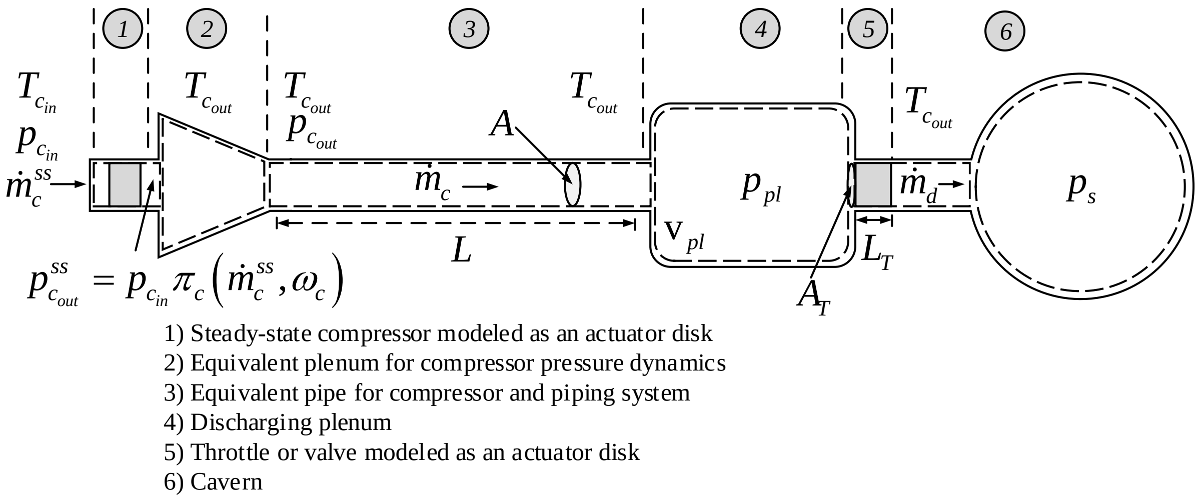

Figure 3.5: Dynamic model of the CAES compressor, based on Figure 2.13.

Furthermore, based on (3.51), (3.46) and (3.47) can be combined in a single equation, as follows:

$$\frac{d\dot{m}_c}{dt} = \frac{1}{L_{eq}/A_{eq}} \left(p_{c_{out}} - p_{pl}\right) \tag{3.52}$$

where L_{eq} and A_{eq} are the equivalent length and cross-sectional area respectively of the combined compressor, pipe, and valve.

Finally, the airflow-pressure-ratio relation in the valve is modeled using the choked air flow through a nozzle equation (3.30), which assumes constant inlet temperature, variable inlet pressure, and constant output pressure. Notice the the output pressure of the throttle is the cavern pressure p_s, which can be considered constant as it changes relatively slow with respect to the compressor dynamics. Hence, the valve can be modeled as follows:

$$\bar{\dot{m}}_c = \lambda_c \frac{p_{pl}}{p_{pl_o}} \tag{3.53}$$

where λ_c represents the per-unit cross-sectional area of the valve. Observe that $\bar{\dot{m}}_c$ is a linear function of p_{pl}, and thus is a linear function of the pressure drop across the valve $p_{pl} - p_s$; however, in order for this linear relation to be valid, the cross-sectional area λ_c must be continuously adjusted, while p_s slowly changes. Hence, an approximation of a linear valve model is proposed as follows:

$$\bar{\dot{m}}_c = K_c^{-1} \left(p_{pl} - p_s\right) \tag{3.54}$$

where K_c depends on λ_c and p_{pl_o}. Equation (3.54) replaces (3.50); then, based on (3.54), replacing p_{pl} in (3.52) and expressing $\dot{m}_c$ in p.u. yields:

$$\frac{d\bar{\dot{m}}_c}{dt} = \frac{A_{eq}}{\dot{m}_{c_o} L_{eq}} \left(p_{c_{out}} - K_c \bar{\dot{m}}_c - p_s\right) \tag{3.55}$$

$$= \frac{A_{eq} K_c}{\dot{m}_{c_o} L_{eq}} \left(\frac{p_{c_{out}}}{K_c} - \frac{p_s}{K_c} - \bar{\dot{m}}_c\right) \tag{3.56}$$

Based on the aforementioned discussion, the proposed compressor model can be summarized by the following two differential equations:

$$\frac{d\bar{\dot{m}}_c}{dt} = \frac{1}{\tau_{CA}} \left(\frac{p_{c_{out}}}{K_c} - \frac{p_s}{K_c} - \bar{\dot{m}}_c\right) \tag{3.57}$$

$$\frac{dp_{c_{out}}}{dt} = \frac{1}{\tau_{CD}} \left[\pi_c \left(\bar{\dot{m}}_c^{ss}, \bar{\omega}_c\right) p_{c_{in}} - p_{c_{out}}\right] \tag{3.58}$$

where $\tau_{CA} = \dot{m}_{c_o} L_{eq} / A_{eq} K_c$ is the time constant representing the air flow dynamics due to air inertia in the compressor body and pipes, and τ_{CD} is the discharging compressor time constant or volumetric time constant.

In Figure 3.6 an electric circuit equivalent of the dynamic system is presented for illustration purposes. Furthermore, note that (3.57) and (3.58) have the structure of a first order system, i.e., $\dot{x}(t) = (1/\tau)\left[u(t) - x(t)\right]$; hence, both can be represented by first order transfer functions. Thus, since the compressor power, as per (3.43)-(3.45), is function of $\bar{\dot{m}}_c$ and $p_{c_{out}}/p_{c_{in}} = \pi_c$, two first-order transfer functions are proposed to model the dynamics of the compressor described in (3.57) and (3.57), as depicted in Figure 3.7.

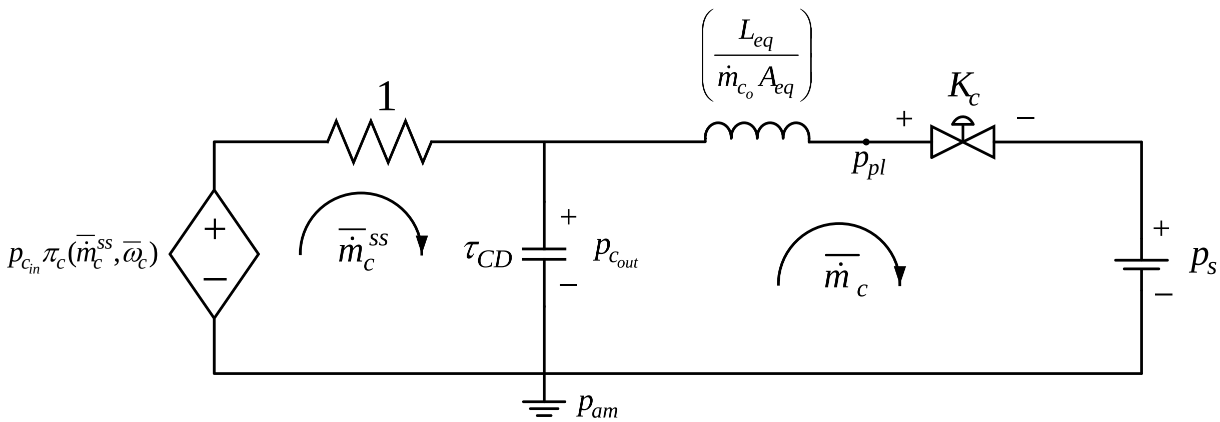

Figure 3.6: Electric circuit equivalent of the compressor dynamic model.

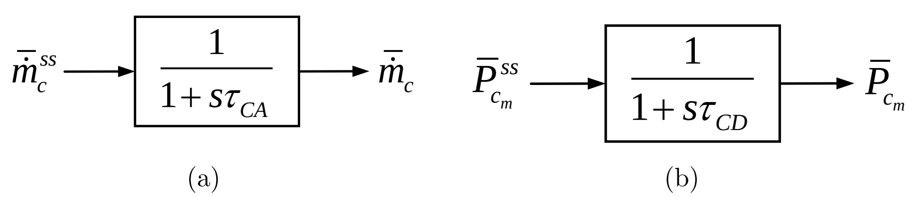

Figure 3.7: Equivalent transfer function of (a) mass flow rate (b) mechanical power of the compressor.

Compressor Maps

Three approaches are proposed to model the pressure ratio of each compression stage π_{c_j}, which are functions of the mass flow rate $\dot{m}_c$ and rotor speed ω_c, as determined by the following compressor map models: ellipse model approximation, Neural-Network-based map, and a nonlinear function based on physical characteristics of the compressor.

In the first approach, the compressor map is modeled using the equation of an ellipse, as suggested in [81]. Hence, the pressure ratio of each compressor stage can be calculated as follows:

$$\pi_{c_j}(\bar{\dot{m}}_c) = a_{1_j}\sqrt{1-\left(\frac{\bar{\dot{m}}_c}{a_{2_j}}\right)^2} \tag{3.59}$$

$$\pi_{c_j}(\bar{\dot{m}}_{c_o}) = \pi_{c_{j_o}} \tag{3.60}$$

$$\pi_{c_j}(0.5\bar{\dot{m}}_{c_o}) = 1.12\pi_{c_{j_o}} \tag{3.61}$$

This model requires the definition of any two operating points given by (3.60) and (3.61), which are used to find the parameters a_{1_j} and a_{2_j}. The points can be obtained from the actual compressor to be modeled for the nominal rotor speed $\bar{\omega}_c = 1$. The main drawback of this approach is that the effects of variations of the rotor speed $\bar{\omega}_c$ on the pressure ratio are lost. However, this can be compensated by multiplying the output of the air flow control by the rotor speed, thus obtaining an adjusted air flow that is used in (3.59), as discussed later in Section 3.5.3.

Neural Networks (NNs) have been widely used to represent compressor maps in GTs, due to their ability to accurately reproduce highly nonlinear relations that are difficult to model, as is the case of compressor maps. In this thesis, different NN configurations were tested to model a CAES compressor map. In Figure 3.8, the results of some of the topologies tested to replicate a compressor map, shown in Figure 2.9 [64], are illustrated. Several NN topologies were tested, obtaining the best performance using one hidden layer with 6 neurons, and two neurons in the input layer, one for the corrected mass flow rate $\dot{m}_{crr}$ and the other for the corrected rotor speed N_{crr}. Observe that topolgies using 3 and 20 neurons fail to estimate the actual measurements and do not properly represent new iso-speed lines, which the 6-neuron configuration does successfully.

A third approach, based on the physical characteristics of a compressor is proposed in this thesis. The following proposed non-linear polynomial function was developed based on the cubic characteristic function of the pressure rise, impeller blade speed, non-dimensional compressor rise, and non-dimensional mass flow rate, discussed in [82–84]:

$$\begin{aligned}\pi_c\left(N_{crr}, \dot{m}_{crr}\right) = 1 + b_0 N_{crr}^2 + b_1 N_{crr}^4 + b_2 N_{crr}^3 + b_3 \dot{m}_{crr}^2 + \\ b_4 N_{crr} \dot{m}_{crr}^2 + b_5 N_{crr}^2 \dot{m}_{crr}^2 + b_6 \frac{\dot{m}_{crr}^3}{N_{crr}} + b_7 \dot{m}_{crr}^3 + b_8 N_{crr} \dot{m}_{crr}^3\end{aligned} \tag{3.62}$$

This equation is discussed in detail in Appendix A, with the coefficients being estimated using the Matlab curve fitting toolbox. Figure 3.9 shows 3-D plots of the 6-neuron NN map and the polynomial non-linear function. The Root Mean Square Error (RMSE) of both alternatives are very close, i.e., 0.9862 and 0.983 for the polynomial function and the NN map, respectively. A closer look at both surfaces reveals that, for the domain of interest $(N_{crr}, \dot{m}_{crr}) \in \mathcal{D}$ at which the pressure ratio is positive and the compressor is not

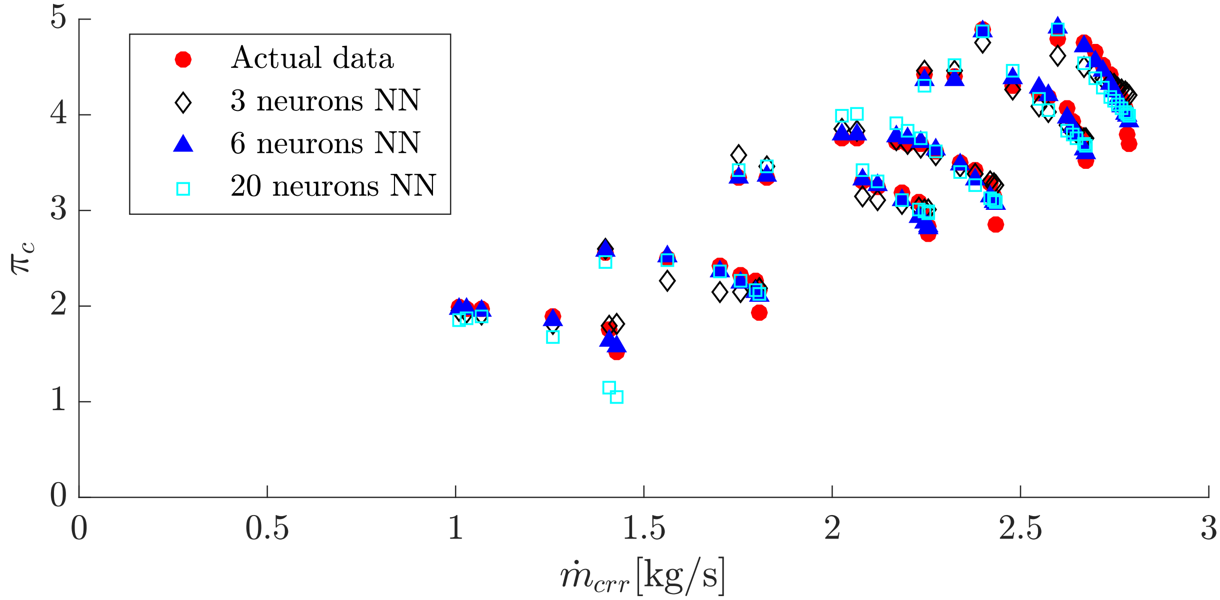

(a)

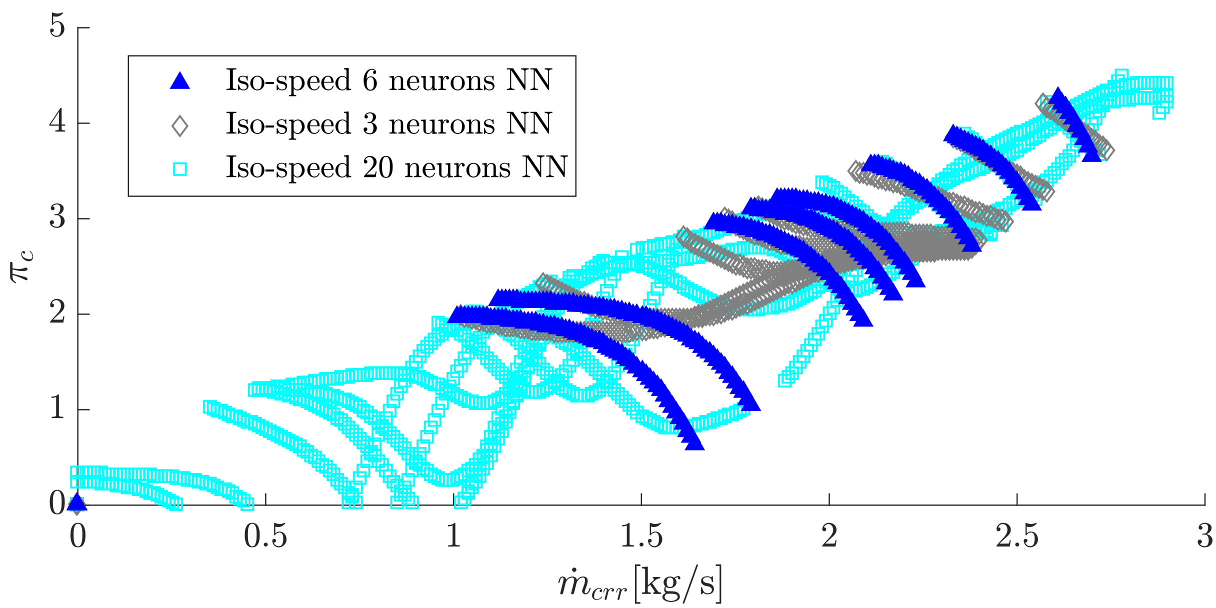

(b)

Figure 3.8: NN-based compressor map models: (a) estimated points, (b) iso-speed maps.

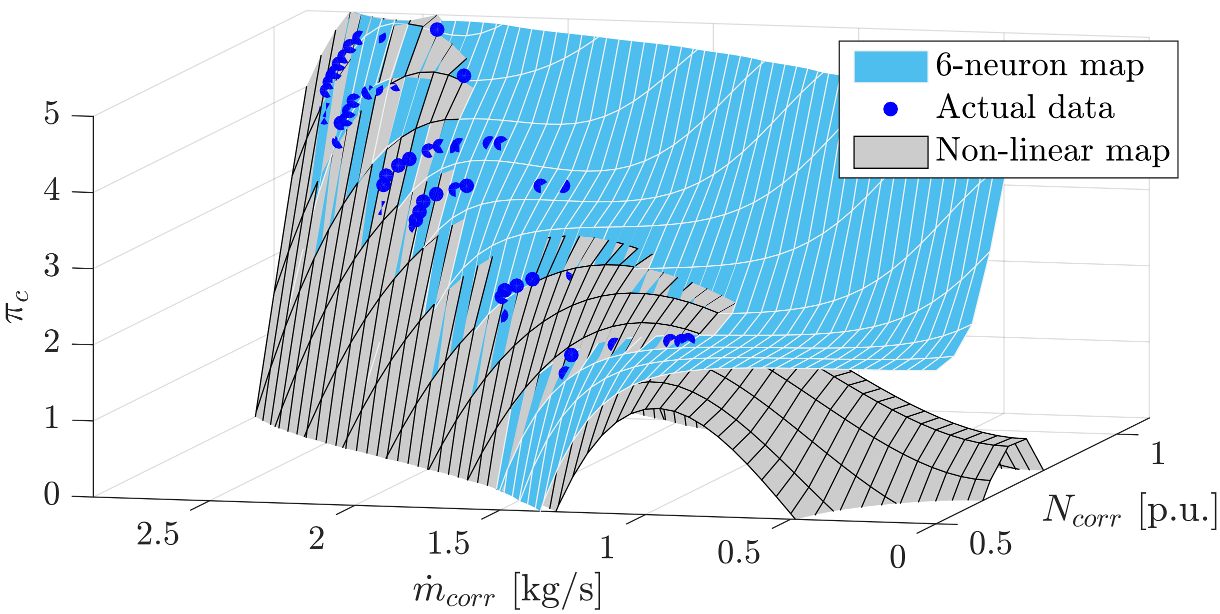

Figure 3.9: Projected compressor map using a 6-neuron NN and the proposed non-linear polynomial function.

operating in surge, both alternatives are almost identical.

The reproduced compressor maps in some cases cannot be directly used in the compressor model, because its size is not adequate for the compressor used in the proposed CAES system. For example, the nominal pressure ratio of the reproduced map (referred to as available map, hereafter), could be too small compared to the pressure ratio of the HP compressor in the CAES system, or the nominal mass flow rate in this map could be different from that of the CAES compressor; compressor scaling is necessary in these cases.

Linear scale factors were used to scale the compressor at each stage j [40]. This requires the definition of the nominal (design) operating point for both the available compressor map ($N_{crr_o}^{map}$,$\dot{m}_{crr_o}^{map}$,$\pi_{c_o}^{map}$) and the desired compressor map (N_{crr_o}, $\dot{m}_{crr_o}$,π_{c_o}). This approach finds equivalent values of the desired corrected speed N_{crr} and air mass flow rate $\dot{m}_{crr}$, in the available compressor map (N_{crr}^{map}, $\dot{m}_{crr}^{map}$), which are used to find the pressure ratio π_c^{map} that is then transformed back to the desired pressure π_c, i.e., the actual pressure ratio in the stage. The map scaling procedure is illustrated in Figure 3.10, referred hereafter as the Compressor Map Block (CMB), and is used for each compression stage j. The CMB is parametrized by the vector of parameters $\mathbf{B}_j^T = [\dot{m}_{c_o}, N_{c_o}, T_{am}, p_{am}, N_{crr_{jo}}, N_{crr_{jo}}^{map}, \dot{m}_{crr_{jo}}, \dot{m}_{crr_o}^{map}, \pi_{c_{jo}}, \pi_{c_{jo}}^{map}]$, and requires the input vector of variables $\mathbf{Y}_j^T = [\bar{\dot{m}}_c, \bar{\omega}_c, T_{c_{in_j}}, p_{c_{in_j}}]$. The available compressor map is represented in the Figure 3.10 as $f(\dot{m}_{crr}^{map}, N_{crr_j}^{map})$, which could be either represented by (3.62) or the proposed 6-neuron NN. The parameters $\{\dot{m}_{crr_{j_o}}^{map}, N_{crr_{j_o}}^{map}, \pi_{c_{j_o}}^{map}\}$ define a nominal operating point in the available map for compression stage j, while $\{\dot{m}_{crr_{j_o}}, N_{crr_{j_o}}, \pi_{c_{j_o}}\}$ define the nominal point in the desired scaled map of compression stage j, which are calculated as follows:

$$\dot{m}_{crr_{j_o}} = \dot{m}_{c_o} \frac{\sqrt{T_{in_{j_o}}/T_{am}}}{p_{c_{in_{j_o}}}/p_{am}} \tag{3.63}$$

$$N_{crr_{j_o}} = \frac{N_{c_o}}{\sqrt{T_{in_{j_o}}/T_{am}}} \tag{3.64}$$

The output of the CMB is the pressure ratio of the compression stage j, $\pi_{c_j} = f(\bar{\dot{m}}_c, \bar{\omega}_c, T_{c_{in_j}})$, which is a function of the mass flow rate $\bar{\dot{m}}_c$, rotor speed $\bar{\omega}_c$ and inlet temperature $T_{c_{in_j}}$ at the compression stage j.

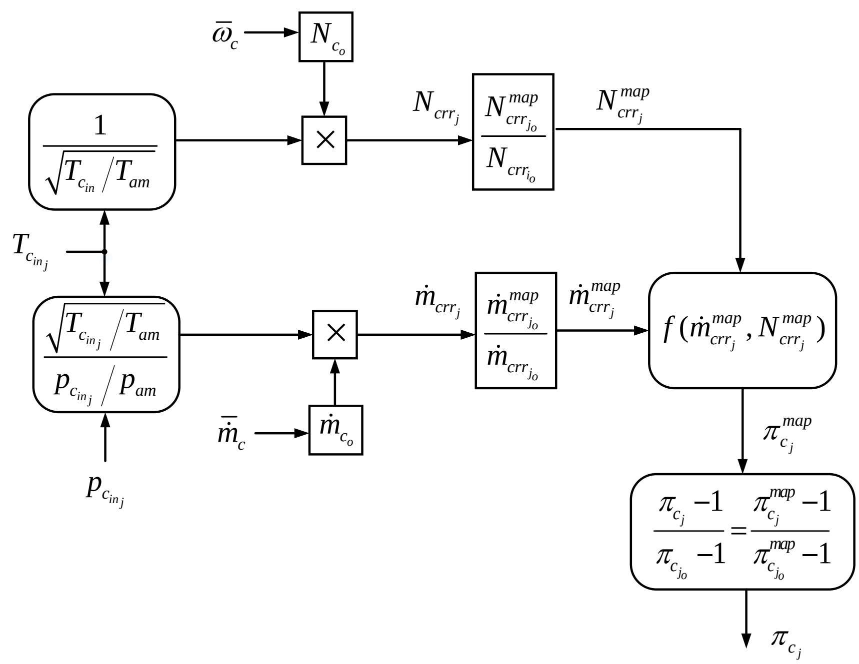

Figure 3.10: Compressor Map Block (CMB).

Intercooler

The intercoolers are modeled as isobaric heat exchangers, as in the case of the recuperator; however, in the intercoolers, the hot side is fed by the discharging air from a compression stage, whereas in the recuperator, the cold side is fed with the air coming from the cavern. The intercooler model assumes that the input temperature at its cold side $T_{hx_{in}}$ is lower than the hot side output temperature $T_{c_{out}}$, and that both sides have the same heat capacity rate $C = \dot{m}c_p$. The latter assumption is important because, unlike the recuperator, in which the same air circulates in the cold and hot sides of the heat exchanger, a special refrigerant might be used in the intercoolers to remove the heat; however, the assumption implies that the product of the specific heat capacity at constant pressure of that refrigerant is equal to the product of the specific heat capacity of the air and compressor air flow, i.e., $c_{p_{cold}}\dot{m}_{cold} = c_p\dot{m}_c$ [19]. This also means that the temperature change in the hot side is the same as in the cold side of the intercooler. Hence, the effectiveness of the heat exchanger used at the output of the compression stage j, ϵ_{hx_j}, is defined as follows:

$$\epsilon_{hx_j} = \frac{\dot{m}_c c_p \left(h_{c_{out_j}} - h_{c_{in_{j+1}}}\right)}{\dot{m}_{cold} c_{p_{cold}} \left(h_{c_{out_j}} - h_{hx_{in}}\right)} = \frac{T_{c_{out_j}} - T_{c_{in_{j+1}}}}{T_{c_{out_j}} - T_{hx_{in}}} \tag{3.65}$$

From this equation, the input temperature of the air in the compressor stage $j+1$ can be calculated as a function of the temperature of the previous stage j, as follows:

$$T_{c_{in_{j+1}}} = T_{c_{out_j}} - v_{hx_j} \tag{3.66}$$

where v_{hx_j} is the temperature drop due to the heat removed from the exit air of the stage j in the intercooler, and can be modeled as follows:

$$\frac{dv_{hx_j}}{dt} = \frac{1}{\tau_{hx_j}} \left[\epsilon_{hx_j} \left(T_{c_{out_j}} - T_{hx_{in}}\right) - v_{hx_j}\right] \tag{3.67}$$

where τ_{hx_i} is the time constant of the intercooler j in s. It is also assumed that the temperature $T_{hx_{in}}$ is constant for all heat exchangers.

Aftercooler

The aftercooler model is the same as the intercooler, except that in the former, the temperature of the air at the output of the hot side of the heat exchanger connected after the third-HP compressor, $T_{c_{in_{HP_3}}}$, is the temperature of the air injected in the cavern $T_{s_{in}}$, as shown in Figure 3.1.

Compressor Plus Heat Exchanger Module

By combining (3.43)-(3.45), (3.66) and (3.67), and using the transfer function approximations for (3.57) and (3.58), a complete compression stage of the CAES system can be modeled as a temperature gain $\Gamma_j(\bar{\dot{m}}_c, \bar{\omega}_c)$ plus a heat exchanger, as depicted in Figure 3.11.

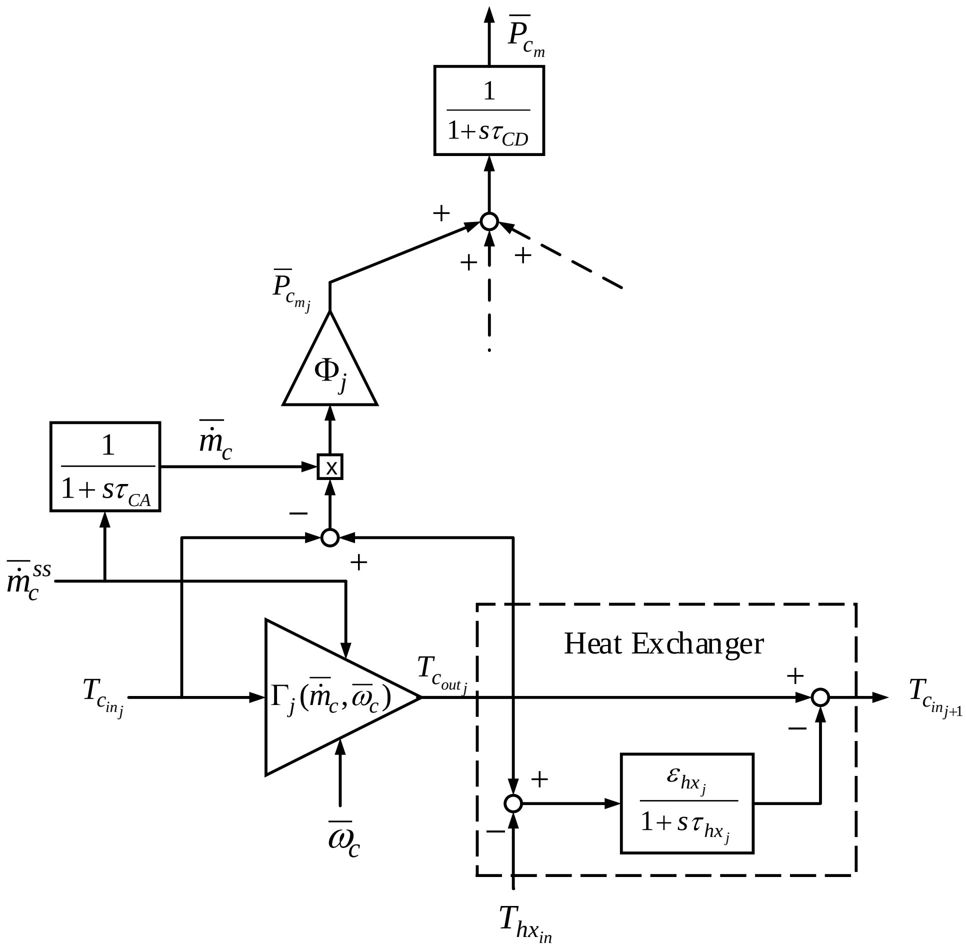

Figure 3.11: Model of one compression stage with a heat exchanger at the output.

Where:

$$\Gamma_j(\bar{\dot{m}}_c, \bar{\omega}_c) = 1 + \frac{\left[\pi_{c_j}(\bar{\dot{m}}_c, \bar{\omega}_c)\right]^{\frac{\gamma-1}{\gamma}} - 1}{\eta_{c_{i_j}}} \tag{3.68}$$

$$\Phi_j = \frac{c_p \bar{\dot{m}}_{c_o}}{10^3 \eta_{c_{mj}} P_{c_{m_o}}} \tag{3.69}$$

3.3.2 Simplified Model

The multi-stage HP compressor can be reduced to a single-stage compressor, assuming ideal operation of the intercoolers, which would maintain the inlet temperature of each stage equal to the inlet condition of the first HP stage (isothermal compression) [85]. Under these assumptions, the CAES system compressor can be modeled using two stages of the compression-heat-exchanger illustrated in Figure 3.11, with $j \in \{\mathrm{LP}, \mathrm{HP}\}$. Hence, the temperature gain $\Gamma_{HP}(\bar{\dot{m}}_c, \bar{\omega}_c)$ and compressor's stage power constant Φ_{HP} can be expressed as:

$$\Gamma_{HP}(\bar{\dot{m}}_c, \bar{\omega}_c) = 1 + \frac{\left[\pi_{c_{HP}}(\bar{\dot{m}}_c, \bar{\omega}_c)\right]^{\frac{\gamma-1}{3\gamma}} - 1}{\eta_{c_{i_{HP}}}} \tag{3.70}$$

$$\Phi_{HP} = \frac{3 c_p \dot{m}_{c_o}}{10^3 \eta_{c_{m_{HP}}} P_{c_{m_o}}} \tag{3.71}$$

accounting for the reduction of the three compressor stages, where $\pi_{c_{HP}}$ is the total pressure ratio of the HP compressor, $\eta_{c_{m_{HP}}}$ and $\eta_{c_{i_{HP}}}$ are the equivalent mechanical and isentropic efficiencies of the single stage HP compressor, respectively. The heat-exchanger for HP stage represents the aftercooler in this model, whereas the LP compressor, electrical motor, and control system remain the same as in the detailed model. The equivalent simplified CAES facility, including the simplified expansion model discussed in Section 3.2.2, is presented in Figure 3.12.

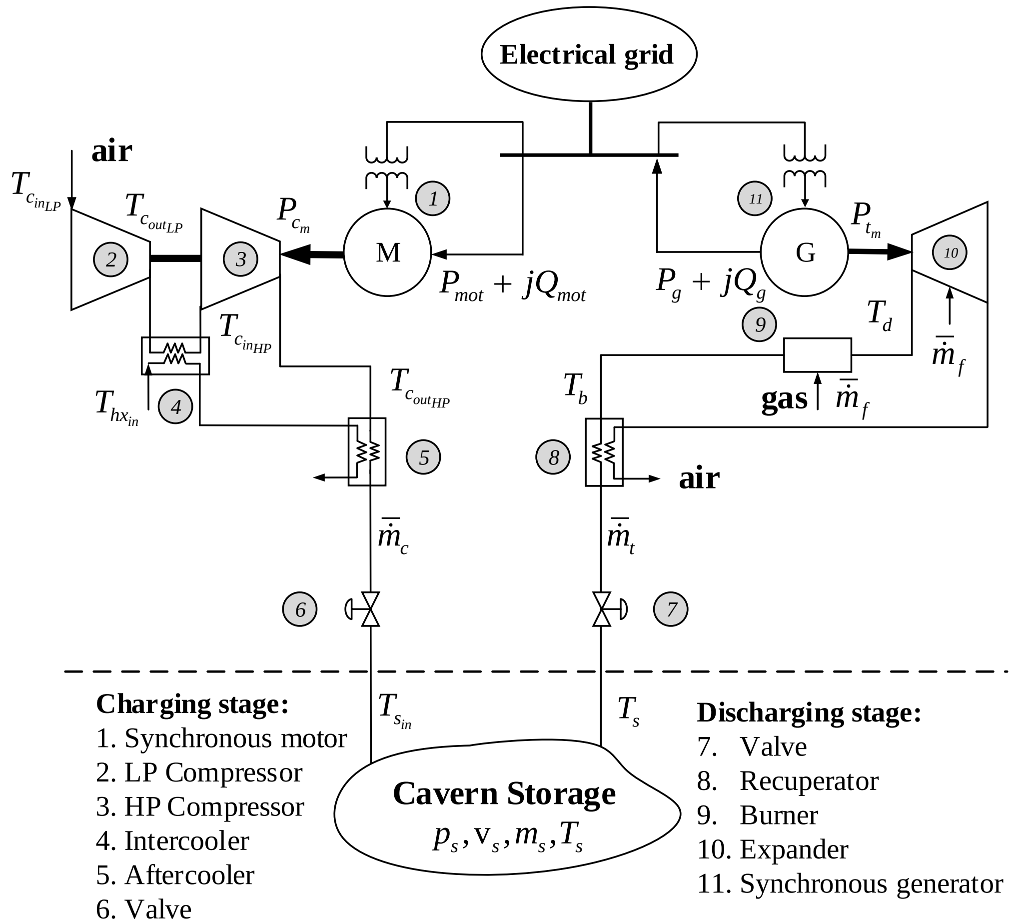

Figure 3.12: Simplified CAES model.

3.3.3 Synchronous Motor

The synchronous machine model described in Section 2.3.1 is used to represent the motor model, with the subindex "c" (compressor) in the mechanical power of (2.5), and $\bar{\omega}_c$ and H_c representing the compressor per-unit rotor speed and inertia constant, respectively. Finally, the subindex "mot" is used to differentiate electrical variables in the motor from generator variables.

3.4 Cavern Model

The cavern is modeled as an open system, i.e., it can exchange energy and matter with its surroundings. If the law of conservation of mass is applied in a control volume established around the cavern, as in Figure 3.13, the rate of change of the mass m_s in the cavern can be calculated as follows:

$$\dot{m}_s = \dot{m}_c - \dot{m}_t \tag{3.72}$$

where $\dot{m}_c$ and $\dot{m}_t$ are the air mass flow rate of the compressor and turbine, respectively.

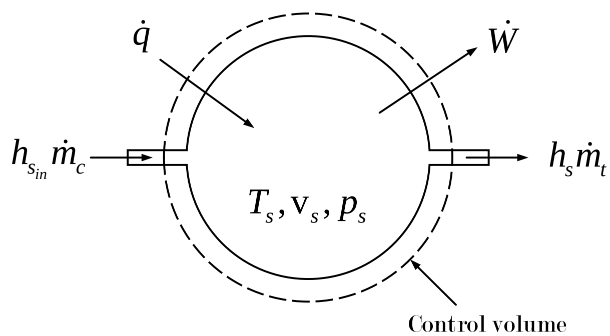

Figure 3.13: Control volume around the cavern.

In an open system, as the cavern in Figure 3.13, the rate of change of the internal energy U of the cavern is given by the following relation [74]:

$$\frac{dU_s}{dt} = \dot{q} - \dot{W} + \dot{m}_c h_{s_{in}} - \dot{m}_t h_s \tag{3.73}$$

where q is the heat added to the system, W is the work done by the system to its surroundings, $\dot{m}_c h_{s_{in}}$ is the rate of energy flow into the cavern from the compressor, and $\dot{m}_t h_s$ is the rate of energy flow out of the cavern. Since the cavern does not perform any work on its surrounding, it follows that:

$$\frac{dU_s}{dt} = \dot{q} + \dot{m}_c h_{s_{in}} - \dot{m}_t h_s \tag{3.74}$$

From the definition of enthalpy $H_s = U_s + p_s \mathrm{v}_s$, the specific enthalpy can be calculated as:

$$H_s/m_s = U_s/m_s + p_s \mathrm{v}_s/m_s \tag{3.75}$$

$$h_s = \sigma_s + p_s \chi_s \tag{3.76}$$

where h_s is the specific enthalpy of the cavern in [J/kg]; σ_s is the specific internal energy in [J/kg]; χ_s is the specific volume in [m^3/kg]; p_s is the cavern pressure [Pa]; and v_s the cavern volume [m^3]. Since $U_s = m_s \sigma_s$, by substituting (3.76) in (3.74) it follows that:

$$\frac{d}{dt}\left(m_s(h_s - p_s\chi_s)\right) = \dot{q} + \dot{m}_c h_{s_{in}} - \dot{m}_t h_s \tag{3.77}$$

$$\frac{d}{dt}\left(m_s h_s\right) - \mathrm{v}_s \frac{dp_s}{dt} - p_s \frac{d\mathrm{v}_s}{dt} = \dot{q} + \dot{m}_c h_{s_{in}} - \dot{m}_t h_s \tag{3.78}$$

Assuming an isochoric cavern, i.e., constant volume, $\dot{\mathrm{v}}_s = 0$, and expanding (3.78) yields:

$$m_s \dot{h}_s = \dot{q} + \dot{m}_c h_{s_{in}} - \dot{m}_t h_s + \mathrm{v}_s \frac{dp_s}{dt} - h_s \dot{m}_s \tag{3.79}$$

Substituting (3.72) in (3.79):

$$m_s \dot{h}_s = \dot{q} + \dot{m}_c h_{s_{in}} - \dot{m}_t h_s + \mathrm{v}_s \frac{dp_s}{dt} - h_s\left(\dot{m}_c - \dot{m}_t\right) \tag{3.80}$$

$$m_s \dot{h}_s = \dot{q} + \dot{m}_c\left(h_{s_{in}} - h_s\right) + \mathrm{v}_s \frac{dp_s}{dt} \tag{3.81}$$

Assuming ideal gas behaviour $dh = c_p dT$, which can be substituted in (3.81) yielding:

$$m_s c_p \frac{dT_s}{dt} = \dot{q} + \dot{m}_c c_p\left(T_{s_{in}} - T_s\right) + \mathrm{v}_s \frac{dp_s}{dt} \tag{3.82}$$

From the ideal gas law:

$$\frac{d}{dt}\left(p_s \mathrm{v}_s\right) = \frac{d}{dt}\left(m_s \mathrm{R} T_s\right) \tag{3.83}$$

$$\mathrm{v}_s \frac{p_s}{dt} + p_s \frac{d\mathrm{v}_s}{dt} = \mathrm{R} T_s \dot{m}_s + \mathrm{R} m_s \frac{dT_s}{dt} \tag{3.84}$$

Substituting (3.72) and (3.82) in (3.84), and since the cavern is isochoric, i.e., $\dot{\mathrm{v}}_s = 0$, it follows that:

$$\mathrm{v}_s \frac{dp_s}{dt} = \mathrm{R}T_s \left(\dot{m}_c - \dot{m}_t\right) + \mathrm{R}m_s \left[\frac{\dot{q} + \dot{m}_c c_p \left(T_{s_{in}} - T_s\right) + \mathrm{v}_s \frac{dp_s}{dt}}{m_s c_p}\right] \tag{3.85}$$

Expanding (3.85), and substituting $\mathrm{R} = c_p - c_v$, where c_p and c_v are the specific heat capacity at constant pressure and constant volume respectively, and $\gamma = c_p/c_v$ is the heat capacity ratio, the dynamics of the pressure in the cavern can be calculated as:

$$\frac{dp_s}{dt} = \frac{\mathrm{R}\gamma}{\mathrm{v}_s} \left(T_{s_{in}}\dot{m}_c - T_s\dot{m}_t\right) + \frac{\dot{q}}{\mathrm{v}_s}\left(\gamma - 1\right) \tag{3.86}$$

where R is the specific gas constant of the air [J/kg.K]; $T_{s_{in}}$ [K] is the temperature of the air that flows into the cavern from the compression stage; $\dot{m}_c$ is the air mass flow rate of the compressor [kg/s], T_s is the cavern temperature [K]; $\dot{m}_t$ is the air mass flow rate of the turbine [kg/s]; and $\dot{q}$ is a function that represents the heat transfer lost through the cavern walls. Therefore, the dynamics of the cavern can be modeled by (3.72), (3.82), and (3.86), which is similar to the cavern model used in [19, 20, 22]; however, if the cavern is assumed adiabatic, i.e., it does not exchange heat with the surroundings, $\dot{q} = 0$, and if the internal temperature T_s is assumed constant (since the rate of change of T_s is very slow), the cavern can be modeled by the following set of equations:

$$\frac{d\bar{m}_s}{dt} = \frac{1}{m_{s_o}} \left(\bar{\dot{m}}_c \dot{m}_{c_o} - \bar{\dot{m}}_t \dot{m}_{t_o}\right) \tag{3.87}$$

$$\frac{d\bar{p}_s}{dt} = \frac{\mathrm{R}\gamma}{10^5\,\mathrm{v}_s\, p_{s_{\max}}} \left(\bar{\dot{m}}_c \dot{m}_{c_o} \bar{T}_{s_{in}} T_{s_{in_o}} - \bar{\dot{m}}_t \dot{m}_{t_o} T_s\right) \tag{3.88}$$

$$m_{s_o} = \frac{10^5 p_{s_{\max}} \mathrm{v}_s}{\mathrm{R}T_s} \tag{3.89}$$

where m_{s_o} is the maximum mass of air in kg that can be stored in the cavern, and $p_{s_{\max}}$ is the maximum pressure the cavern can withstand in bar.

3.5 Controls

3.5.1 State of Charge Logic

The SoC can be calculated by integrating on time the power injected and withdrawn from the storage reservoir. In CAES, this integration should be performed on the enthalpy rate $\dot{H}$ in and out of the cavern [74], as follows:

$$U_s = \int (\dot{m}_c h_{s_{in}} - \dot{m}_t h_s)\, dt \tag{3.90}$$

$$= c_p \int (\dot{m}_c T_{s_{in}} - \dot{m}_t T_s)\, dt \tag{3.91}$$

From (3.88), in (3.91) becomes:

$$U_s = \frac{10^5 c_p \,\mathrm{v}_s\, p_{s_{\max}}}{R\gamma} \bar{p}_s \tag{3.92}$$

The energy in the cavern is maximum ($U_{s_{\max}}$), when the cavern pressure is maximum, $\bar{p}_s = 1$ p.u., and the energy is minimum ($U_{s_{\min}}$), when the cavern pressure is minimum, $\bar{p}_s = p_{s_{\min}}/p_{s_{\max}}$; hence:

$$U_{s_{\max}} = \frac{10^5 c_p \,\mathrm{v}_s\, p_{s_{\max}}}{R\gamma} \tag{3.93}$$

$$U_{s_{\min}} = \frac{10^5 c_p \,\mathrm{v}_s\, p_{s_{\min}}}{R\gamma} \tag{3.94}$$

Equation (3.92) can be expressed in per unit, as follows:

$$\bar{U}_s = \frac{10^5 c_p \,\mathrm{v}_s\, p_{s_{\max}}}{U_{s_{\max}} R\gamma} \bar{p}_s \tag{3.95}$$

Substituting (3.93) in (3.95), the per-unit cavern energy can be simplified as follows:

$$\bar{U}_s = \bar{p}_s \tag{3.96}$$

Assuming that the $SoC \in [0, 1]$ p.u., for the energy range $U_s \in [U_{s_{\min}}, U_{s_{\max}}]$, or pressure range $p_s \in [p_{s_{\min}}, p_{s_{\max}}]$, the SoC can be defined as follows:

$$SoC = \frac{U_s - U_{s_{\min}}}{U_{s_{\max}} - U_{s_{\min}}} \tag{3.97}$$

Thus, in per-unit energy quantities:

$$SoC = \frac{\bar{U}_s - U_{s_{\min}}/U_{s_{\max}}}{1 - U_{s_{\min}}/U_{s_{\max}}} \tag{3.98}$$

or equivalently, using pressure quantities:

$$SoC = \left[1 - \left(\frac{1 - \bar{p}_s}{1 - p_{s_{\min}}/p_{s_{\max}}}\right)\right] \tag{3.99}$$

As in the Huntorf CAES facility [13], the SoC control logic proposed in this section considers the pressure limits $p_{s_{\max}}$ and $p_{s_{\min}}$ for the maximum and minimum cavern pressures, and $p'_{s_{\max}}$ and $p'_{s_{\min}}$ for the maximum and minimum "economic" pressures, as depicted in Figure 3.14, along with their associated values indicated. The pressures $p_{s_{\max}}$ and $p_{s_{\min}}$ are related to the physical limits such as cavern closure, roof collapse, interbed slip or tensil fracturing [86]; on the other hand, $p'_{s_{\min}}$ and $p'_{s_{\max}}$ define the range withing which the relationship between useful work and pumping work is at its optimum [13]. Between $p_{s_{\max}}$ and $p'_{s_{\min}}$, the expander valve should be able to throttle the pressure down to $p_{t_{HPo}}$ when the turbine operates at nominal conditions; defining $\Delta p_{\min} = p'_{s_{\min}} - p_{t_{HPo}}$.

Based on (3.88) and (3.99), a novel SoC logic is proposed in Figure 3.15, which takes into account four pressure limits as in Huntorf [13]. This logic controls the operation of the cavern by limiting the compressor and turbine power as necessary. Thus, when the SoC reaches its maximum limit $SoC_{\max}$ the controller sends the boolean signal $u_c = 0$ to the compressor control to shut it down by bringing the air flow to zero. When the SoC reaches $SoC_{\min}$, the controller sends the signal $u_t = 0$ to the turbine control to close the air valve. Notice that $SoC_{\max}$ and $SoC_{\min}$ can be chosen by the operator; for example, if $SoC_{\min} = SoC(p'_{\min}/p_{\max})$ and $SoC_{\max} = SoC(p'_{\max}/p_{\max})$, the CAES system would only be allowed to operate within its economic range.

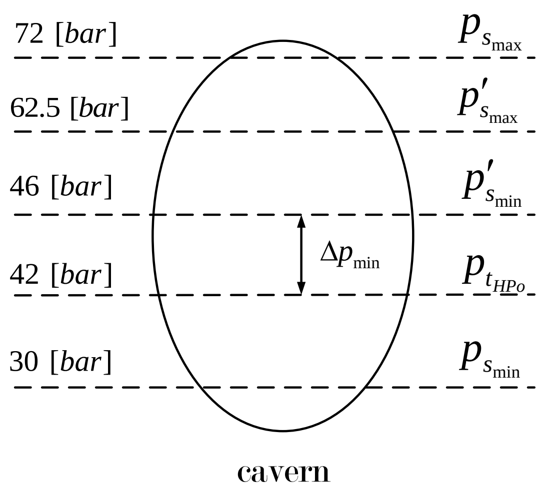

Figure 3.14: Cavern limits as in Huntorf.

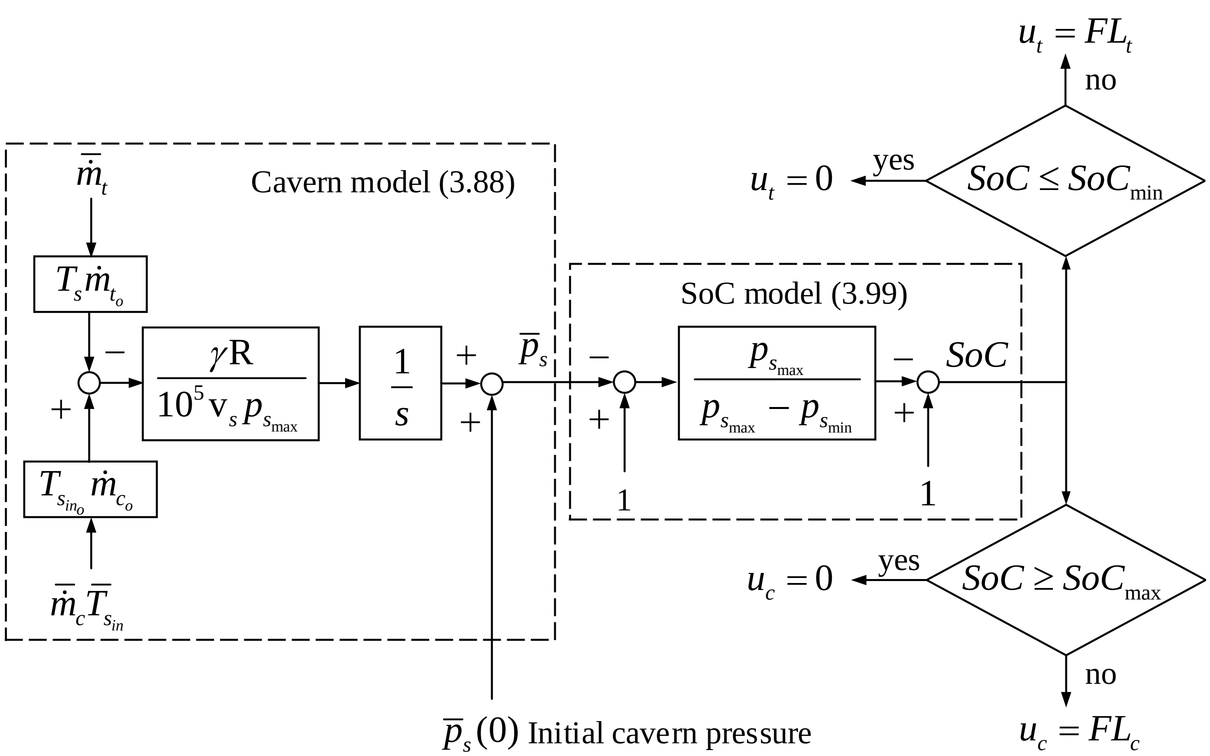

Figure 3.15: Proposed SoC control logic.

3.5.2 Turbine Controls

The control system proposed in this section is based on those discussed in [65, 66, 87] for traditional GTs, and comprises an active power controller and a temperature controller for the LP expander. The former acts on the valve controlling the air flow from the cavern, while the latter acts on the fuel flow.

Active Power Controller

The objective of the active power controller depicted in Figure 3.16 is to adjust the air mass flow rate so that the turbine produces the desired power $\bar{P}_{t_{ref}}$, which is converted into electricity by the synchronous generator. Thus, the speed deviation signal $\Delta\overline{\omega}_t$ is fed as a negative feedback in the active power control loop, modifying the power reference set point to provide PFR according to the proportional gain $1/R$ (regulation characteristic or droop gain), and operate in AGC mode when the parameter $K_{AGC} \neq 0$. The modified power reference is compared with a measured mechanical output power using a power transducer, modeled as a first order transfer function of time constant τ_{TP}, and the error is passed through a PI controller (governor) which can be tuned to provide good tracking error and dynamic response. The output of the governor is the desired valve opening λ'. The control signal u_t is used to shut down the expander when $SoC = SoC_{\min}$ by bypassing the PI output, thus simulating the valve closing; this signal also multiplies the input error to the PI to avoid integral windup when the turbine is shut down. The gains K_{t_p} and K_{t_i} are the proportional and integral gains associated with the governor, and $\lambda(0)$ is the initial condition of the PI controller.

Valve System and Limits

The valve model maps λ values to air flow values $\bar{\dot{m}}_t$; hence, depending on the valve model used (Section 3.2.1), $\bar{\dot{m}}_t$ is calculated differently. In all valve models, a delay is used to represent the actual valve response, based on a first order transfer function of time constant τ_{AV} [87], and rate limits $\{\dot{\lambda}_{\max}, \dot{\lambda}_{\min}\}$. Furthermore, since the air expands almost instantly in a turbine, the thermodynamic modes proposed in Section 3.2 are steady-sate, except for the recuperator. A first-order transfer function of time constant τ_{TD} is proposed in the air flow path, after the valve, to account for delays in the transportation of the air in the turbine. Thus, the simplest valve representation consist of a linear valve with limits, as depicted in Figure 3.17, in which $\bar{\dot{m}}_t = \lambda$. In this case, the valve limits are the air flow

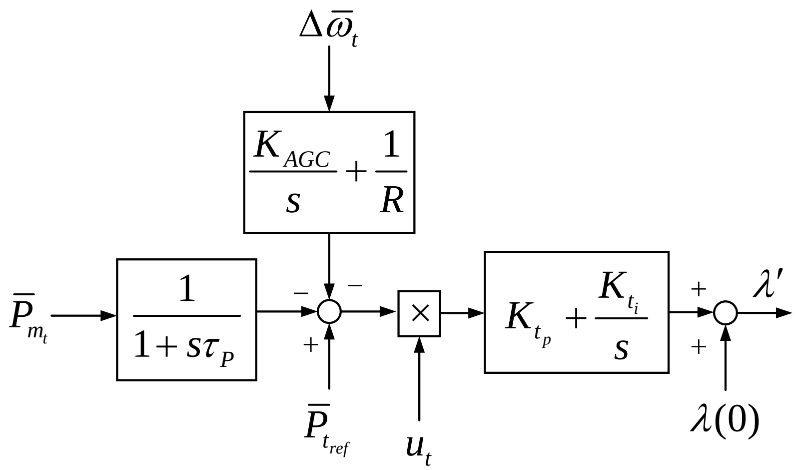

Figure 3.16: Active power controller.

limits $g_{\min}$ and $g_{\max}$, which are associated with the minimum and maximum power that can be extracted from the turbine.

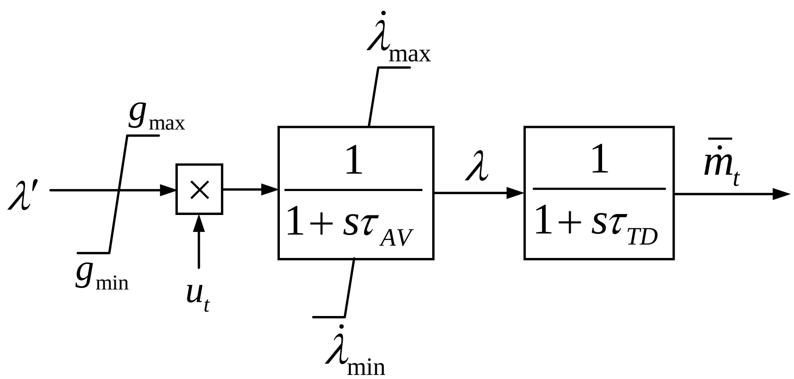

Figure 3.17: Linear valve model with limits.

The model of a choked valve with limits is presented in Figure 3.18, based on (3.30), where λ_{max} and λ_{min} are the maximum and minimum valve openings in per unit. A low value selector is used to account for the limit of the maximum expansion pressure ratio $\pi_t = \pi_{t_{HP}}\pi_{t_{LP}}$ that can be physically obtained from the cavern pressure p_s, expressed in terms of air flow as follows:

$$p_{am}\pi_{t_{HP}}\pi_{t_{LP}} \leqslant p_s \tag{3.100}$$

Substituting (3.22) and (3.23) in (3.100), and assuming $\bar{T}_{d_{HP}} \approx 1$, the maximum air flow

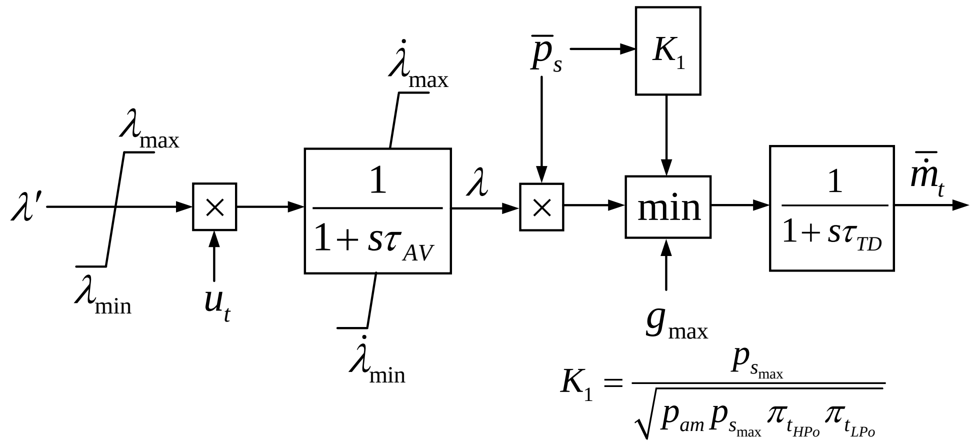

Figure 3.18: Choked valve model with limits.

due to cavern pressure restrictions $\bar{\dot{m}}'_{t_{max}}$ can be calculated as:

$$\bar{\dot{m}}'_{t_{\max}} = \frac{p_s}{\left(p_{am} p_{s_{\max}} \pi_{t_{LPo}} \pi_{t_{HPo}}\right)^{1/2}} \tag{3.101}$$

hence:

$$\bar{\dot{m}}_{t_{\max}} = \min\left\{ g_{\max}, \frac{p_s}{\left(p_{am} p_{s_{\max}} \pi_{t_{LPo}} \pi_{t_{HPo}}\right)^{1/2}} \right\} \tag{3.102}$$

In this control, the g_{min} limit is not used; however, the air flow is indirectly limited by $\lambda_{\min}$.

If an unchoked valve model is used, the expression in (3.33) is used to map the λ values to air flow values:

$$\lambda = \frac{\bar{\dot{m}}_t}{\sqrt{\overline{\Delta p}}} \tag{3.103}$$

where $\overline{\Delta p}$ is the per-unit pressure drop in the valve, defined as $\overline{\Delta p} = \Delta p / \Delta p_{\min}$, where $\Delta p_{\min} = p'_{s_{\min}} - p_{t_{HPo_{in}}}$; hence, (3.103) can be used to find the λ limits as a function of $\bar{\dot{m}}_t$ limits. In Figure 3.19, the plots of $\bar{\dot{m}}_t$ as a function of $\overline{\Delta p}$ for different values of λ are presented, based on (3.103). Notice that the valve must allow any air flow within the limits

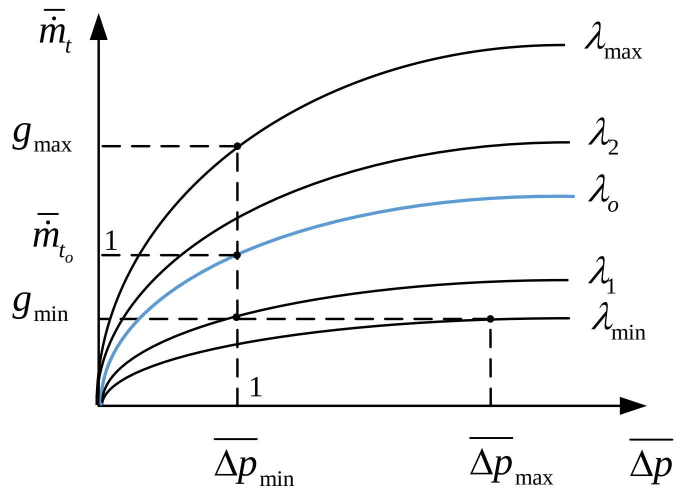

Figure 3.19: Plot of turbine's air mass flow rate $\bar{\dot{m}}_t$ versus the pressure drop $\overline{\Delta p}$ in the valve.

$g_{\max}$ and $g_{\min}$, for the entire range of pressure drops across its terminals from $\overline{\Delta p}_{\min}$ to $\overline{\Delta p}_{\max}$; from (3.103), $\overline{\Delta p}_{\min} = \Delta p_{\min}/\Delta p_{\min} = 1$. On the other hand, since in the unchoked valve model the total expansion pressure ratio ((3.22) and (3.27)) is a linear function of $\bar{\dot{m}}_t$, i.e, $\pi_t = \pi_{t_{HP_o}} \pi_{t_{LP_o}} \bar{\dot{m}}_t$ (assuming $\bar{T}_{d_{LP}} \approx 1$), the inlet pressure at the HP expander $p_{t_{HP_{in}}} = p_{am}\pi_t$ decreases if the air flow rate decreases, while the pressure drop at the valve increases $\Delta p = p_s - p_{t_{HP_{in}}}$. Hence, the maximum pressure drop occurs at minimum air flow, i.e., $\overline{\Delta p}_{\max} = p_{s_{\max}} - g_{\min} p_{am} \pi_{t_{HP_o}} \pi_{t_{LP_o}}$. The former also means that large pressure drops will only occur during small air flows; hence, a point such as $\{g_{\max}, \overline{\Delta p}_{\max}\}$, is not physically feasible. Notice also that the largest valve opening $\lambda_{\max}$ takes place at $\overline{\Delta p}_{\min}$, while the shortest at $\overline{\Delta p}_{\max}$; hence, the λ limits are calculated as function of the air flow limits as follows:

$$\lambda_{\max} = \frac{g_{\max}}{\sqrt{\overline{\Delta p}_{\min}}} \tag{3.104}$$

$$\lambda_{\min} = \frac{g_{\min}}{\sqrt{\overline{\Delta p}_{\max}}} \tag{3.105}$$

Substituting the values of $\overline{\Delta p}_{\max}$ and $\overline{\Delta p}_{\min}$ in (3.104) and (3.105) yields:

$$\lambda_{\min} = \frac{g_{\min}\sqrt{\overline{\Delta p}_{\min}}}{\sqrt{p_{s_{\max}} - g_{\min} p_{am} \pi_{t_{LP_o}} \pi_{t_{HP_o}}}} \tag{3.106}$$

$$\lambda_{\max} = g_{max} \tag{3.107}$$

Finally, an air flow limit is used to maintain a minimum pressure drop in the expansion valve of at least $\overline{\Delta p}_{\min} = 1$, which limits the HP expander input pressure due to cavern pressure dropping below $p'_{s_{\min}}$ (Figure 3.14). Since the cavern pressure is always equal to the HP turbine's inlet pressure plus the pressure drop in the controlling valve, i.e., $p_s = \Delta p + \pi_{t_{HP}} \pi_{t_{LP}} p_{am}$, and a minimum pressure drop $\Delta p_{\min}$ is assumed across the controlling valve, the following condition must be satisfied at any time, based on (3.22) and (3.27):

$$p_s - \Delta p_{\min} \geqslant p_{t_{HP_{in}}} \tag{3.108}$$

$$p_s - \Delta p_{\min} \geqslant p_{am} \pi_{t_{HP_o}} \bar{\dot{m}}_t \pi_{t_{LP_o}} \sqrt{\bar{T}_{d_{LP}}} \tag{3.109}$$

Assuming $\bar{T}_{d_{LP}} \approx 1$, and replacing (3.103) in (3.109) for $\overline{\Delta p}_{\min} = 1$, the maximum valve opening due to pressure drop in the cavern can be calculated as:

$$\lambda_{\max} = \frac{p_s - \Delta p_{\min}}{p_{am} \pi_{t_{LP_o}} \pi_{t_{HP_o}}} \tag{3.110}$$

Hence, from (3.107) and (3.110) the maximum valve opening can be obtained as follows:

$$\lambda_{\max} = \min \left\{ \frac{p_s - \Delta p_{\min}}{p_{am} \pi_{t_{LP_o}} \pi_{t_{HP_o}}}, g_{\max} \right\} \tag{3.111}$$

The limits in (3.106) and (3.111) eliminate the need of adding air flow limits $g_{\max}$ and $g_{\min}$ in the model. From these discussions, the model of the choked valve with limits can be represented as in Figure 3.20.

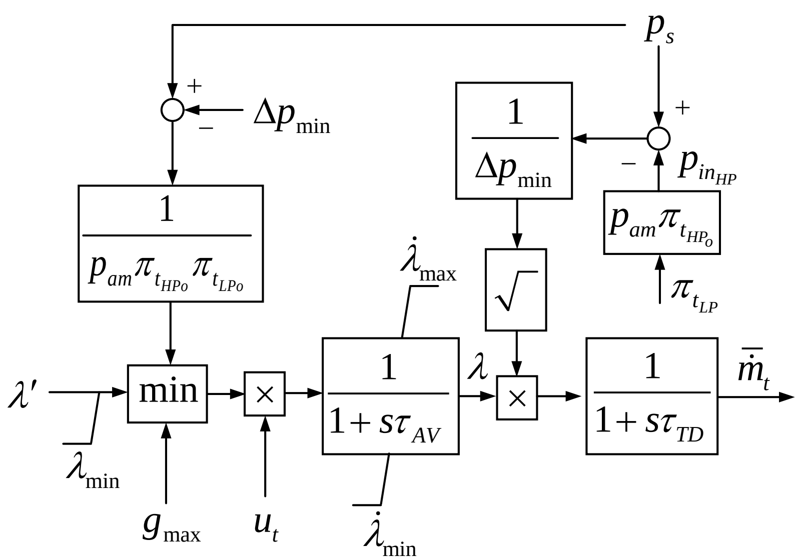

Figure 3.20: Unchoked valve model with limits.

Temperature Controller

The temperature controller regulates the inlet temperature of the expanders by controlling the fuel injected. A simple manipulation of equations (3.12) and (3.13) shows that the turbine power at each stage is a linear function of their corresponding inlet temperatures T_{d_k}; therefore, by keeping these temperatures at their nominal value, less air flow is required for the same output power, thus improving the overall expansion efficiency, especially during partial loading operation.

The proposed temperature control system based on [65], illustrated in Figure 3.21, uses the LP exhaust temperature $T_{x_{LP}}$ to indirectly control the inlet temperature at both expansion stages, $T_{d_{LP}}$ and $T_{d_{HP}}$. The following are the different parts of this control:

- The measurement system for $T_{x_{LP}}$ comprises a thermocouple and a radiation shield, with the latter being used to reduce the radiation errors in the measurement. The time response of the thermocouple is represented by a first order transfer function with time constant τ_4, while that of the radiation shield is modeled with a similar transfer function with time constant τ_3. The gains K_5 and K_4 are chosen such that $K_5 + K_4 = 1$ [65].
- The measured temperature is compared with a reference $\bar{T}_{x_{ref}}$, and the error processed

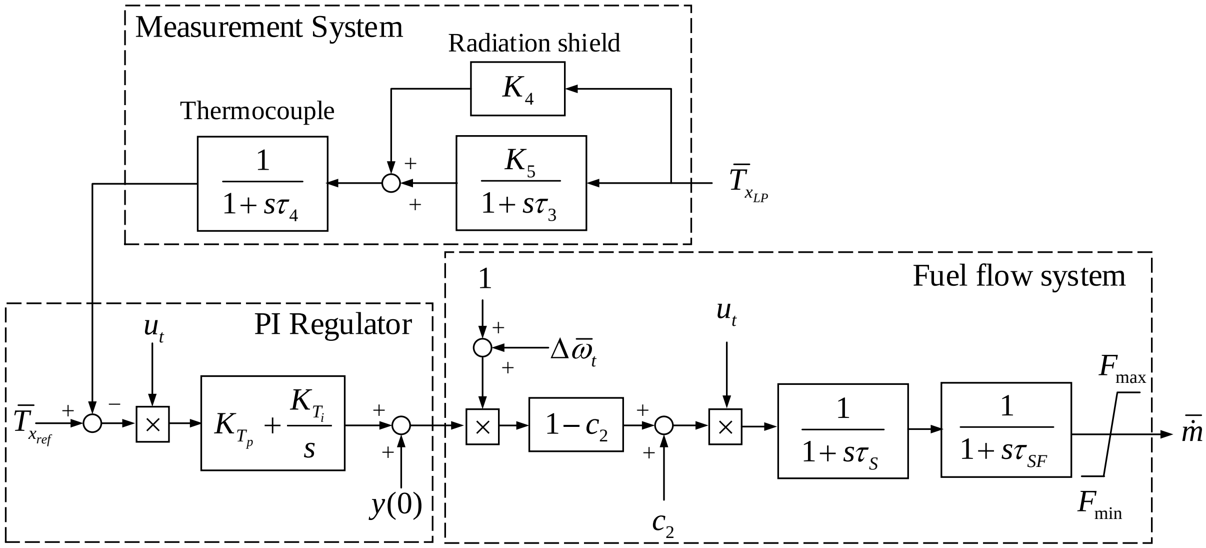

Figure 3.21: Temperature control system.

by a PI compensator with gains K_{T_p} and K_{T_i} that controls the fuel injection; the initial condition of the PI controller is $y(0)$. The output signal of the PI controller is sent to the fuel system, where it is multiplied by the per-unit rotor speed, as the operation of the fuel pumps and associated mechanisms are attached to the rotor shaft as indicated in [87]. This signal is then multiplied by the gain $1 - c_2$ and added to the constant c_2, which represents the fuel consumption at no load in per unit, with $1 - c_2$ compensating for the offset introduced by c_2. The control signal u_t is used to stop the gas supply when the turbine is shut down, and also, when multiplied by the input error to the PI controller, to avoid integration windup.

- There are two delays associated with the fuel system: τ_S for the valve positioning system that controls the amount of fuel injected, and τ_{SF} for the downstream piping and gas distribution manifold; both are modeled as first order transfer functions connected in series when the fuel is a gas [65]. The output of the fuel flow system is $\bar{\dot{m}}_f$, and the flow rates $\bar{\dot{m}}_t$ and $\bar{\dot{m}}_f$, and $\bar{T}_b$ are inputs to the burners and expanders. Hard limits $F_{\max}$ and $F_{\min}$ are used to restrict the fuel flow $\bar{\dot{m}}_f$.

3.5.3 Compressor Controls

The compressor control comprises an active power controller, a discharging pressure limiter and a surge prevention controller.

Active Power Controller

The mechanical power of compressor is controlled by moving the LP compressor's IGV. The proposed active power control shown in Figure 3.22 allows PFR and SFR using the compressor, for which a feedback of the rotor's speed deviation is used to modify the reference power $\bar{P}_{c_{ref}}$, as in the generator case; however, the sign of this feedback is positive in the governor loop, because the compressor has to decrease its power consumption when the frequency drops, and do the opposite when the frequency increases. The error between the measured power $\bar{P}_{c_m}$ and the modified reference power is passed through a PID governor which sends the signal to move the IGVs, whose operation is assumed linear with respect to $\bar{\dot{m}}_c$. Notice that in (3.44), the mechanical power of the compressor is a linear function of $\bar{\dot{m}}_c$; however, $T_{c_{out_j}}$, which is part of the mechanical power calculation, is a nonlinear function of the pressure ratio $\pi_{c_j}(\bar{\dot{m}}_c, \bar{\omega}_c)$ and $\bar{\dot{m}}_c$, as per (3.43). Therefore, depending on the characteristics of the compressor map, when $\bar{\dot{m}}_c$ increases, the output power $\bar{P}_{c_m}$ may decrease; hence, negative PID gains $(K_{c_p}, K_{c_i}, K_{c_d})$ may be necessary for stable operation of the compressor.

The SoC logic control signal u_c is used to completely close the IGV, thus shutting down the compressor, and also to avoid integrating windup as in the turbine case. The gain K_{c_f} is used to define a pole in the differentiator of the PID controller, which acts as a low-pass filter, to avoid amplifying high frequency input signals in the differentiator path, as depicted in Figure 3.22.

Before the desired $\bar{\dot{m}}_c$ control signal is sent to the IGV system represented by a first order transfer function with time constant τ_{IGV}, the limits of the air flow, $\bar{\dot{m}}_{c_{\max}}$ and $\bar{\dot{m}}_{c_{\min}}$, are checked. For these limits, two additional controllers are proposed next to prevent the compressor from surging, and also to limit the discharge pressure to be equal or larger than the cavern pressure. If the compressor map is not modeled as a function of the rotor speed, the effects of the latter on the air flow can be approximated by multiplying the per-unit rotor speed by the output of the IGV control system, as shown in Figure 3.22; otherwise, this multiplication is removed.

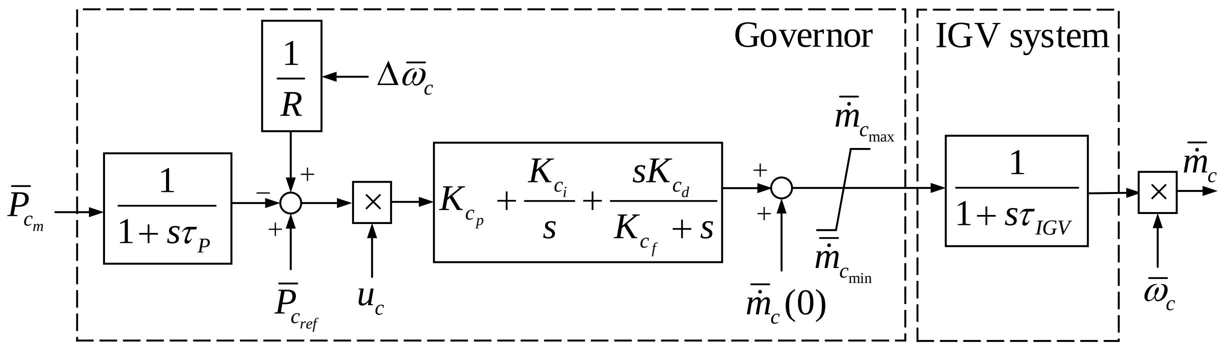

Figure 3.22: Compressor's active power controller.

Surge Prevention Control

Surge is a condition in which a reverse air flow occurs when the compressor operates at reduced air flows. In a compressor map, the pressure ratio increases as the air flow reduces, up to a point known as surge point, in which a further reduction of air flow produces a pressure ratio drop instead. Reaching this point may result in oscillations and instability of the compressor, because the cavern pressure, which is almost constant during this transient event, pushes the air flow towards the compressor, thus further reducing its discharging pressure. Therefore, a special control to prevent the surge condition is necessary. The proposed controls explained next aim to represent the effect of more sophisticated surge control strategies by simply using variable limits in the air flow when surge is detected.

The simplest representation of the surge detection control consists of using hard limits on the air flow: $\bar{\dot{m}}_{c_{\max}} = l_{\max}$ and $\bar{\dot{m}}_{c_{\min}} = l_{\min}$, setting $l_{\min}$ at the approximate air flow point where surge is supposed to occur for nominal speed (usually 60% of the nominal air flow) and $l_{\max}$ to 100% [9].

A more accurate surge detection mechanism consists of using the proposed Surge Logic Control (SLC) block depicted in Figure 3.23 at each compression stage j. This block calculates the partial derivative of the pressure ratio with respect to the corrected air flow, which approaches zero as the compressor is close to the surge point, for a given corrected speed. This requires the compressor map being modeled as an explicit function of the air flow and rotor speed, as proposed in (3.62). When the compressor approaches a surge, which is detected when the partial derivative of the pressure ratio with respect to the air flow is lower than $\Delta\pi_{mrg}$, the Boolean signal $srg \in \{1, 0\}$ takes the value of 1, being 0 otherwise. The margin $\Delta\pi_{mrg}$ determines the sensitivity of the surge detection controller.

In the proposed surge controller, depicted in Figure 3.24, an "OR" operation is per-

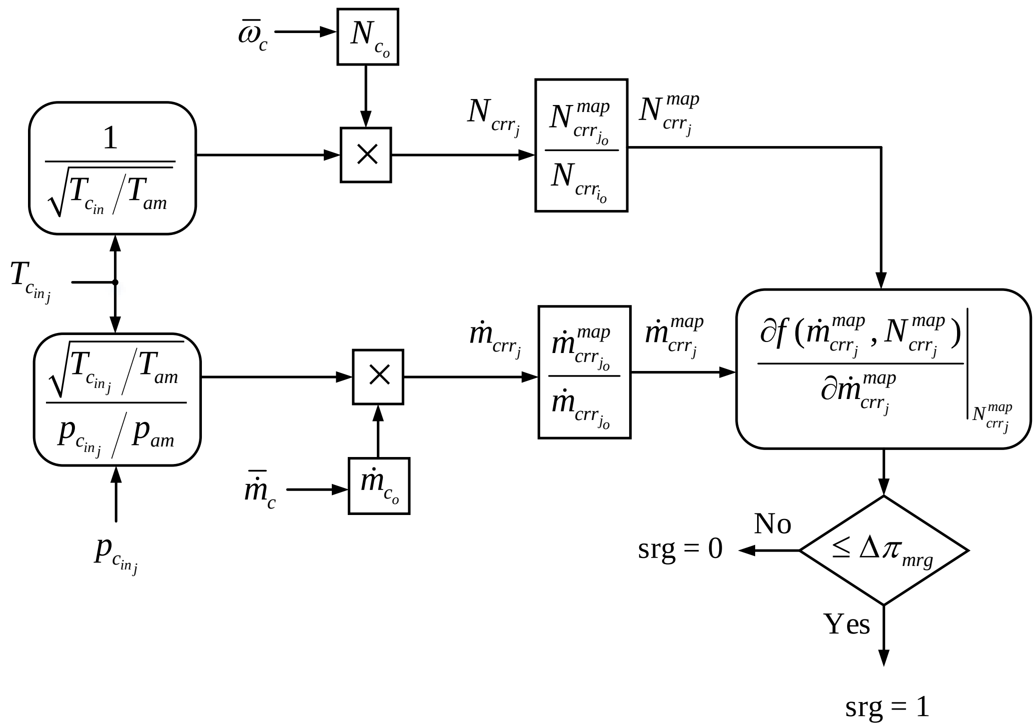

Figure 3.23: Surge Logic Control (SLC) block. The round-corner boxes here, and in other figures later, represent functions of the inputs, as opposed to transfer functions, which are represented with standard rectangular boxes.

formed on all output signals srg_j of the SLC blocks at each compression stage j, to detect if any of these has entered in surge detection zone, and the gains K_{sgp} and K_{sgn} are used to activate and reset the controller, respectively. Whenever one of the compressors enters the surge detection zone, the integrator accumulates positive values from K_{sgp}, thus increasing the $\bar{\dot{m}}_{c_{\min}}$ limit until $\bar{\dot{m}}_c$ is driven to a point where the surge condition is avoided, in which case, the integrator is reset by receiving negative values from K_{sgn} to bring $\bar{\dot{m}}_{c_{\min}}$ to zero. The gain K_{sgp} defines the speed of the anti-surge controller, while K_{sgn} defines the speed of resetting the controller after the surge point has been avoided. Since the surge detection is performed based on compressor map functions, the corrected air flow and speed must be calculated as it was done on the CMB discussed in Section 3.3.1.

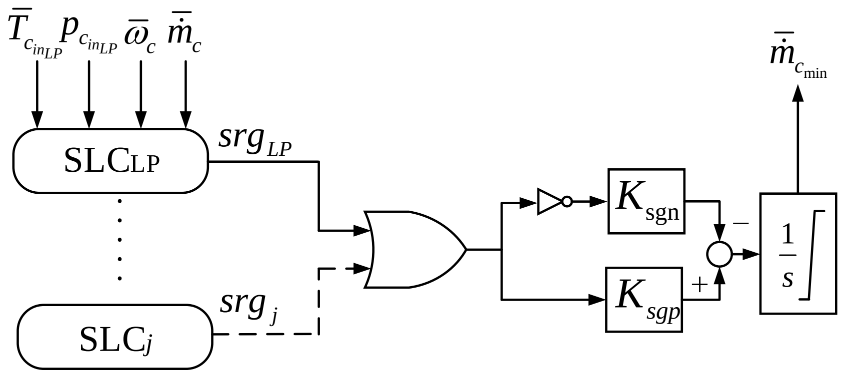

Figure 3.24: Proposed Surge Detection Controller.

Pressure Limiter Controller

The control presented in Figure 3.25 is proposed to prevent the compressor from operating at a discharing pressure lower than the cavern pressure, if commanded by the active power controller to do so. Given the inverse relation between pressure ratio and air flow in a compressor map, the minimum discharing pressure of the last compressor stage can be limited by restricting the maximum air flow to limit the discharging pressure of the last stage of the compressor:

$$p_s + p_{off} \leqslant p_{am} \prod_j \pi_{c_j} \tag{3.112}$$

where p_{off} is an offset used to provide a safety margin with respect to p_s. An integral controller is used to integrate the per-unit pressure difference $\bar{p}_s - (p_{off} + \bar{p}_{c_{out_{HP_3}}})$, whose output is the air flow maximum limit $\bar{\dot{m}}_{c_{\max}}$. If this pressure difference is negative, the integrator reduces the maximum air flow limit, thus also reducing the compressor air flow, until the pressure ratio is larger than the cavern pressure plus the offset. When this condition is met, the controller resets the air flow limit at l_{max}, which is used as a hard limit in the integrator block. The speed of this controller is defined by the gain K_{cv}.

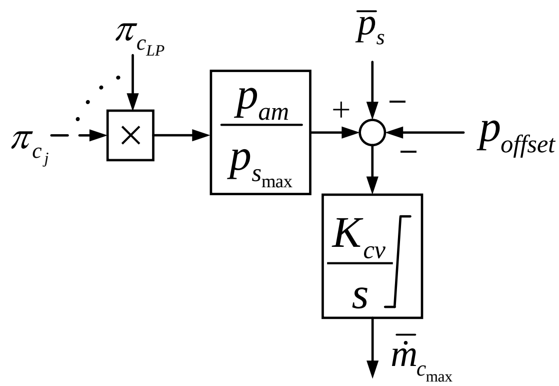

Figure 3.25: Pressure limiter control.

3.5.4 Reactive Power Control

The CAES system is capable of providing reactive power through its two synchronous machines simultaneously to regulate the voltage, which can be used to reduce the machines' loadability, by properly sharing the reactive power between them. For example, in discharging mode, the generator could operate at its rated capacity regardless of the grid conditions, while the reactive power control is provided by the synchronous motor; on the other hand, the generator could be the main source of reactive power when the motor is driving the compressor in charging mode. However, a special control is necessary to avoid instability, as the two independent AVRs act to achieve the same objective, and to also avoid circulating currents between the two machines operating in parallel [88]. Hence, proportional droop controllers are used as shown in Figure 3.26, which modifies the reference voltages in the main AVR loops to achieve the desired reactive power distribution. The model of the excitation system and its components, including the AVR, are discussed in Section 2.3.3.

In Figure 3.26, the reactive power reference values for the motor and generator $\bar{Q}_{mot_{ref}}$ and $\bar{Q}_{g_{ref}}$ are calculated using the factors β_g and β_{mot}, such that $\beta_g + \beta_{mot} = 1$, which distribute the total reactive power produced by the CAES system, so that a fraction of it is assigned to each machine. These reference values are compared with the actual reactive power injections $\bar{Q}_{mot}$ and $\bar{Q}_g$, and the errors passed through the proportional controllers of gain K_{vr}.

The values of β determine the desired reactive power share, based on the following two

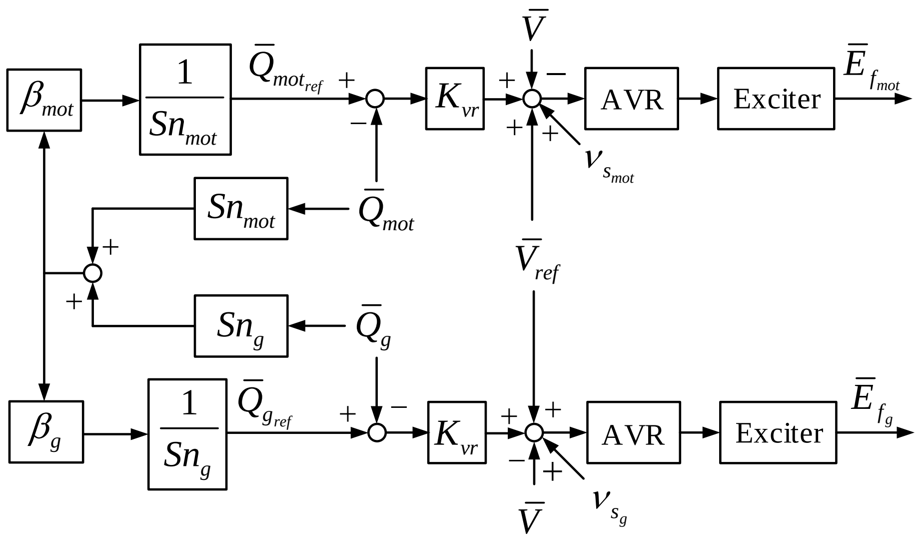

Figure 3.26: Proposed reactive power controls.

alternatives:

$$\beta_{r_1} = \frac{Sn_r \Delta \bar{Q}_{r_{\max}}}{Sn_g \Delta \bar{Q}_{g_{\max}} + Sn_{mot} \Delta \bar{Q}_{mot_{\max}}} \tag{3.113}$$

$$\beta_{r_2} = \frac{\Delta \bar{Q}_{r_{\max}}}{\Delta \bar{Q}_{g_{\max}} + \Delta \bar{Q}_{mot_{\max}}} \tag{3.114}$$

where r is an index representing the generator g or the motor mot; Sn_r is the nominal apparent power of the machine r; and $\Delta \bar{Q}_{r_{\max}}$ is the maximum per-unit reactive power the machine r can produce, given its current active power injections $\bar{P}_r$ and its nominal capacity Sn_r. The proposed parameter β_{r_1} defines the reactive power supplied by the machines r, as a proportion of their remaining capacity $S_{n_r} \Delta Q_{r_{\max}}$ with respect to the total CAES system remaining capacity $S_{n_g} \Delta \bar{Q}_{g_{\max}} + S_{n_{mot}} \Delta \bar{Q}_{mot_{\max}}$, thus the machine with the largest remaining capacity will supply more reactive power. On the other hand, β_{r_2} assigns the reactive power based on the machines' loading, so that the less-loaded machines (largest $\Delta \bar{Q}_{\max}$) supplies more reactive power.

It is assumed that the maximum loadabilities of the machines are determined by the thermal limit of the stator windings only, represented by their rated capacity Sn; hence, $\Delta \bar{Q}_{r_{\max}} = \sqrt{1 - \bar{P}_r^2}$. The choice of β_r depends on the objective sought; thus, β_{r_1} prioritizes the amount of remaining capacity (in MVA) over the machine loading when assigning the reactive power share, while β_{r_2} assigns more reactive power to the machine that is less loaded regardless of its size.

3.6 CAES Model Implementation

Depending on the application, a combination of the models described in the previous sections can be used to simulate a CAES facility. For example, in Load Frequency Control (LFC) studies, the electrical grid does not need to be modeled, since these concentrate on the inertial response of the system, which is mainly governed by the mechanical systems and their controls [61]. Hence, the dynamics of the electric machines and reactive power controllers are not necessary, as opposed to transient stability studies, which involve faster dynamics. In this section, the implementation of models of a CAES facility based on the Huntorf plant in Germany [13] is discussed. For frequency control, Simulink® is used [89], and for transient stability, the Power Flow and Short Circuit Assessment Tool (PSAT®) and the Transient Security Assessment Tool (TSAT®) software packages are used [17, 90].

3.6.1 CAES System Model for Frequency Regulation Studies Using Matlab-Simulink

LFC studies focus on the frequency response of a power system due to imbalances between the demand and generation. The frequency deviation resulting from these imbalances is mostly determined by the inertia of the system and the control actions of governors in the generators, which act on the turbine's sub-mechanical systems, such as hydraulic actuators, valves, etc. The electromechanical dynamics of the generators are usually neglected, as these die out much faster than those in the turbines. In order to compare the different simplifications proposed for some of the CAES system components, three CAES models were implemented in Simulink® for LFC studies, which do not include the synchronous machines and their reactive power controls, as previously justified.

In the detailed model (Model 1), depicted in Figure 3.1, the pressure ratio in the expanders are modeled using (3.16), and the pressure ratio of every compressor stage is modeled with (3.59)-(3.61). The simplified model (Model 2), depicted in Figure 3.12, corresponds to an approximation of Model 1, based on the explanations presented in Sections 3.2.2 and 3.3.2.

Since the simplified model is obtained by reducing the number of compression and expansion stages only, its control system is the same as the one used for the detailed model. The compression stage controller, shown in Figure 3.27, comprises the active power controller exclusively. The control system for the expansion stage comprises the active power controller acting on a linear valve, and the temperature controller, depicted in Figure 3.28. Notice that the per-unit rotor speed deviations $\bar{\omega}_c$ and $\bar{\omega}_t$ are input variables to the control systems, because in LFC studies, the speed deviations in all machines are assumed to be equal to the system frequency deviation.

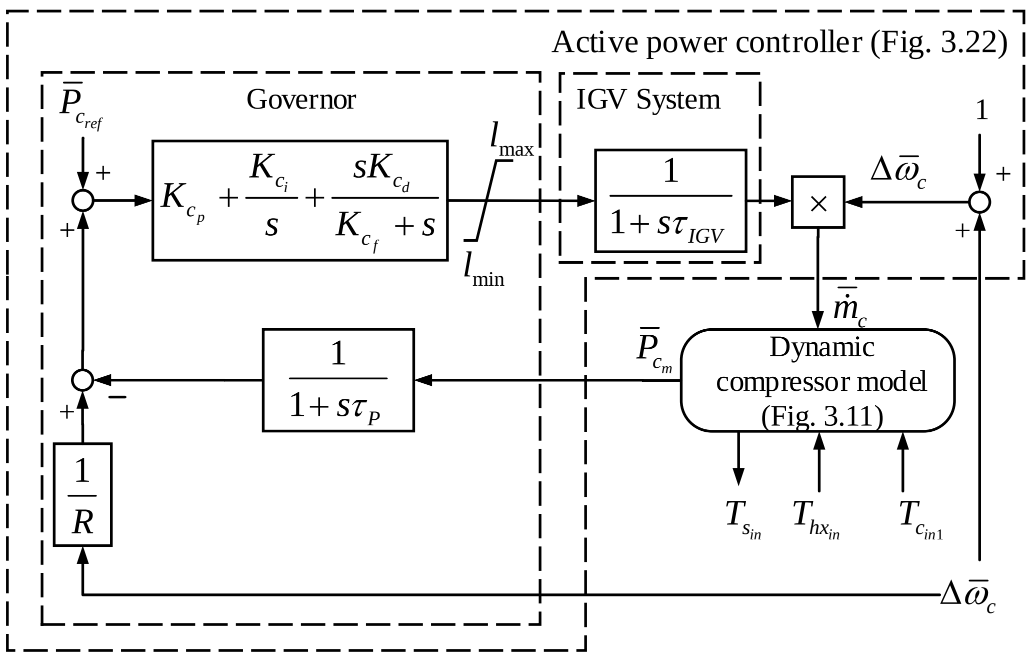

Figure 3.27: Compression stage control for detailed and simplified models (Models 1 and 2).

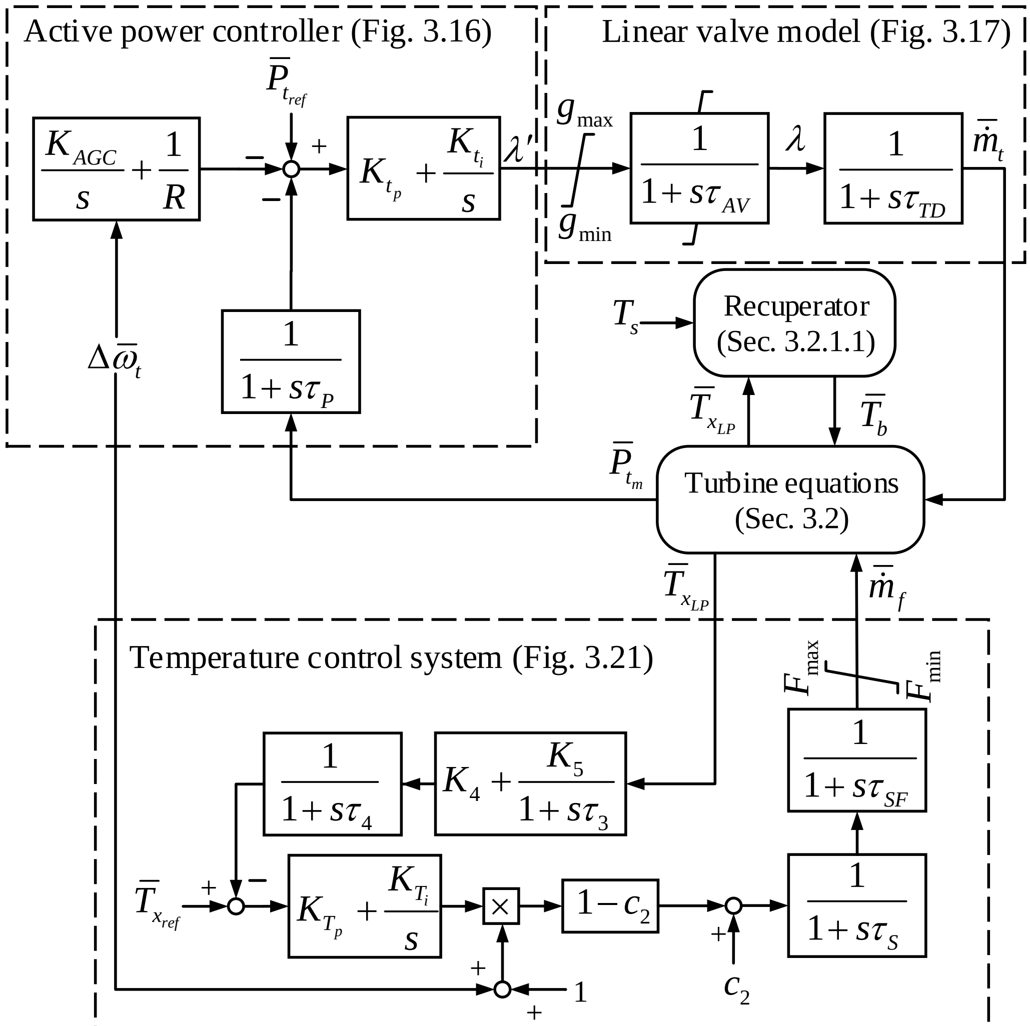

Figure 3.28: Expansion stage control for detailed and simplified models (Models 1 and 2).

The CAES system configuration for Model 3 is presented in Figure 3.29, where the compressor has two stages, LP and HP, where the latter approximates a three stage HP compressor, as is the case of the simplified model. The expander is modeled as a two-stage turbine (HP and LP) which operate chocked, HP and LP burners, a recuperator, and the discharging valve as a chocked flow through a nozzle. The pressure ratio at each compression stage is modeled using the CMB blocks based on the nonlinear map described by (3.62). The compressor control includes the surge detection control and pressure limiter controller, as depicted in Figure 3.30. The expansion control comprises the temperature controller and the power controller acting on a chocked valve (Figure 3.31). The cavern model is described in Section 3.4.

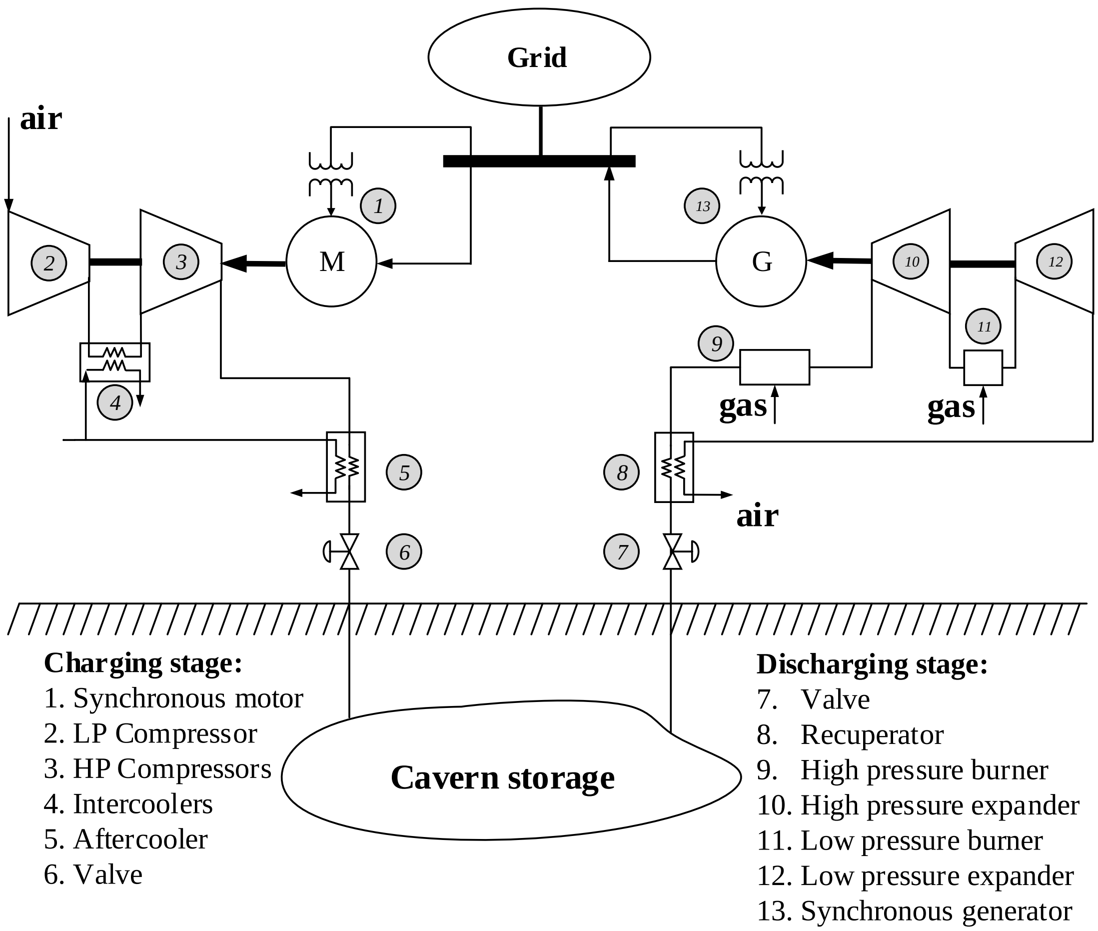

Figure 3.29: CAES system Model 3 configuration.

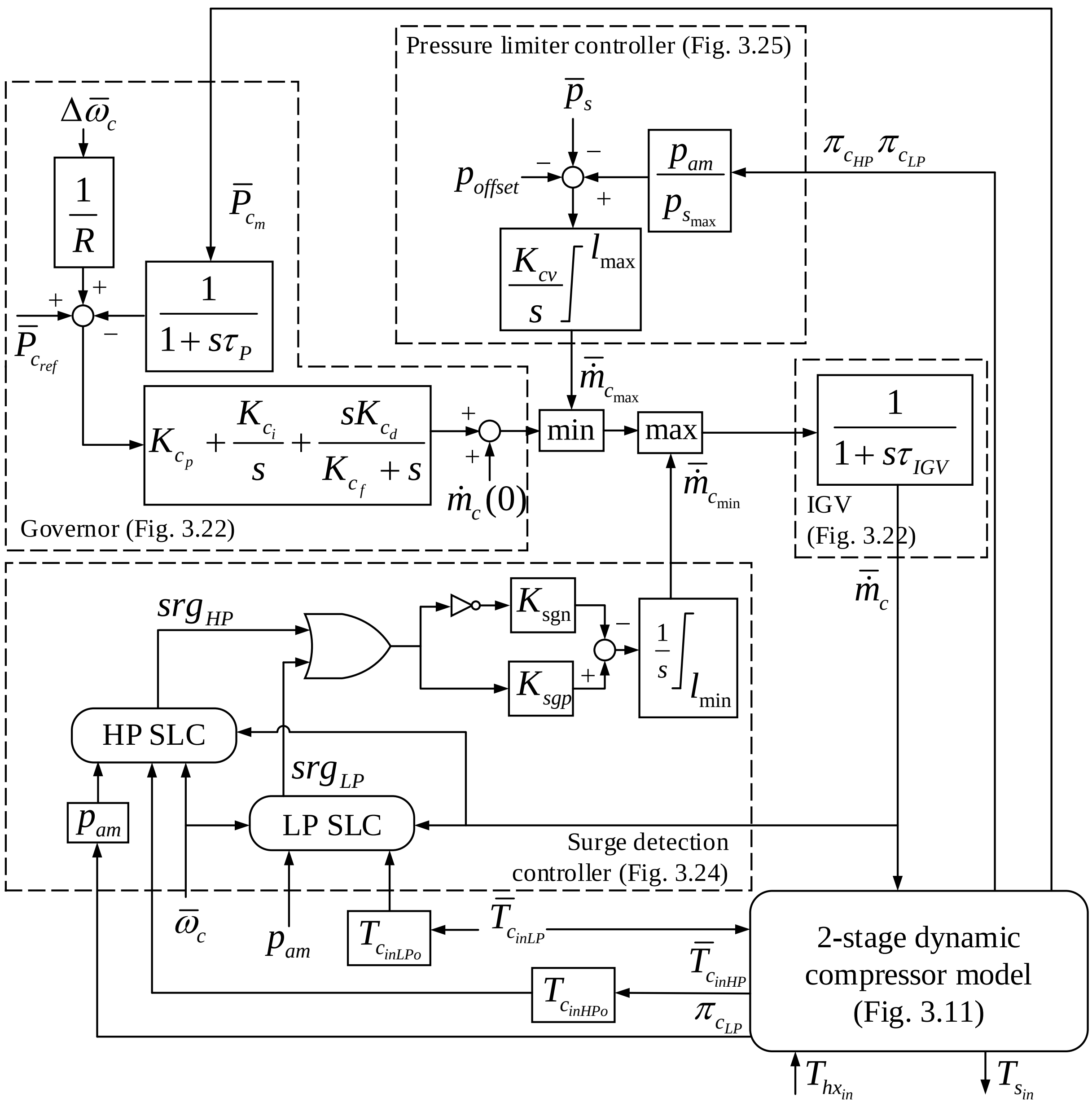

Figure 3.30: Compressor control for CAES Model 3.

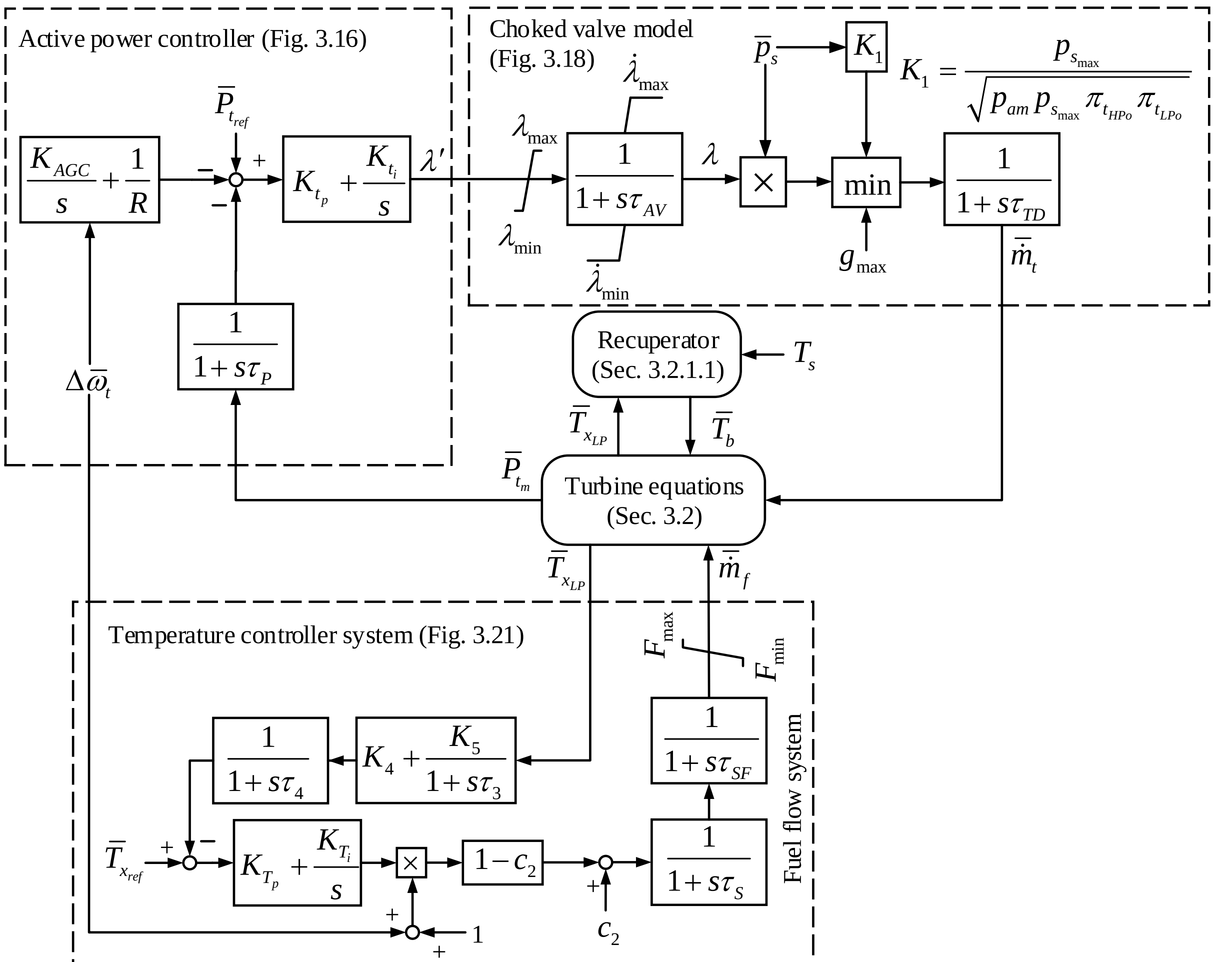

Figure 3.31: Expander control for CAES Model 3.

3.6.2 Transient Stability Model Implementation in DSATools

Time domain simulations in power system software packages require solving a set of DAEs, representing the system's components and their interconnections, using numerical integration methods [73]. However, most commercial packages, such as PSS/E®, DigSilent® or TSAT® provide user-friendly interfaces which ease the modeling of new components through the connection of fundamental blocks, such as gains, summation blocks, transfer functions, etc. Therefore, the proposed CAES transient stability analysis model is developed in block-diagram format so that it can be readily integrated in popular software packages for power system analysis.

The CAES system considered is illustrated in Figure 3.29. The discharging mode comprises HP and LP expanders operating chocked, two burners, and a recuperator, as described in Section 3.2.1. The turbine controls are the active power controllers assuming an unchocked discharing valve, and the temperature controller as described in Section 3.5.2.

For the charging mode, two-stage LP and HP compressors are considered, where the latter approximates a three-stage HP compressor as discussed in Section 3.3.2. The compressor map is modeled through the non-linear function in (3.62), and CMB are used to scale the compressor map to the CAES system expander requirements. The control strategy comprises the active power controller, surge prevention controller based on SLC blocks, and pressure limiter controller, as described in Section 3.5.3. The SoC logic proposed in Section 3.5.1, which imposes additional limits to the compressor and turbine, complements the active power control.

CAES System Model Architecture

The proposed architecture for the CAES system is presented in Figure 3.32. The system is connected to the grid through two synchronous machines which operate synchronized with the grid at all times. The synchronous machines inject the current phasors $\tilde{I}_g$ and $\tilde{I}_{mot}$ into the system, and regulate the input voltage magnitud $\bar{V}$ at the connection point. The compressor and turbine are modeled as turbine/governor blocks, which transfer their respective mechanical powers $\bar{P}'_{c_m}$ (negative) and $\bar{P}'_{t_m}$ (positive), and rotor speeds $\bar{\omega}_c$ and $\bar{\omega}_t$, to the generator and motor blocks, respectively. Notice that, $\bar{P}'_{c_m}$ and $\bar{P}'_{t_m}$ are expressed in per unit of the machine bases Sn_{mot} and Sn_g, respectively. The SoC control logic is modeled within the turbine block. The information exchanged between the various blocks in Figure 3.32 is presented through the vector of control variables $\boldsymbol{\Upsilon}$ and mechanical and electrical variables $\boldsymbol{\Omega}$.

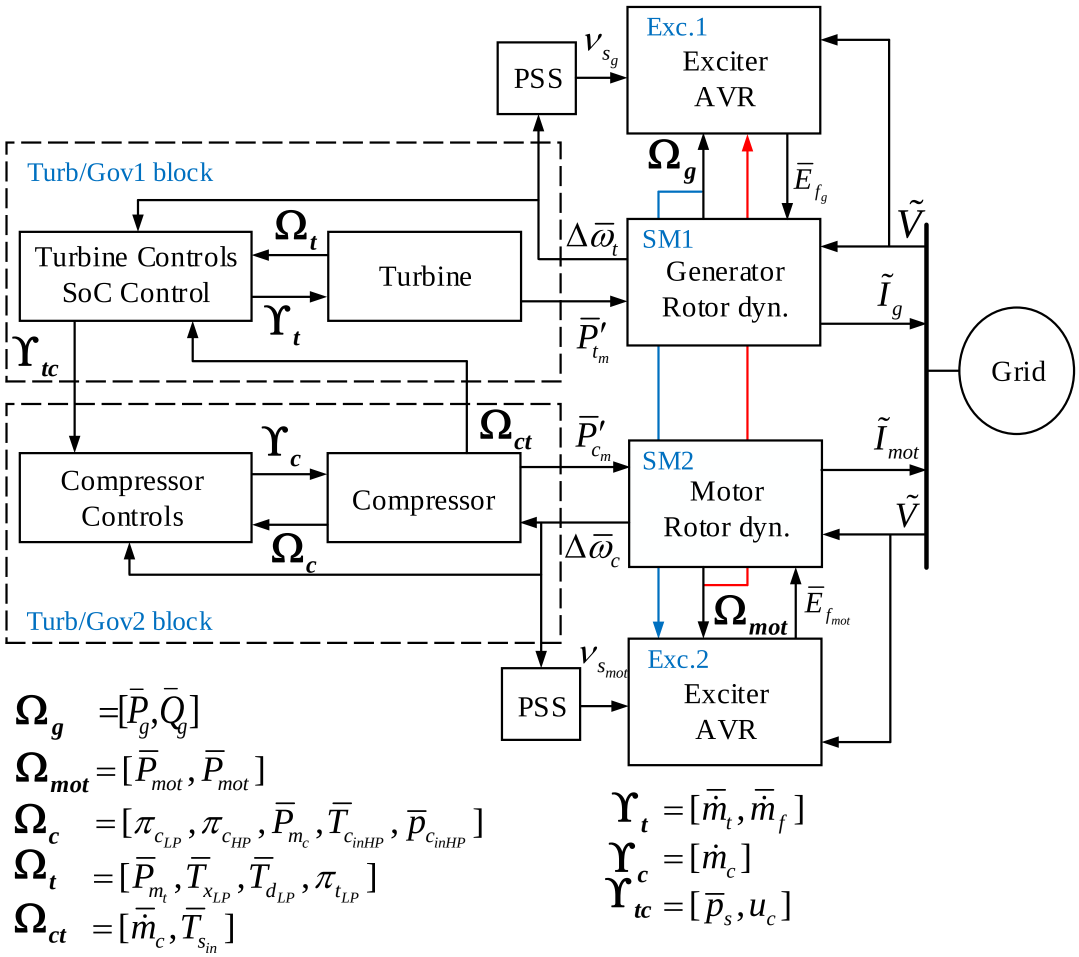

Figure 3.32: Proposed CAES system model architecture.

The reactive power is controlled by the AVRs and the exciters, which define the field voltages $\bar{E}_{f_g}$ and $\bar{E}_{f_{mot}}$ of the machines. Based on the reactive power control proposed in Section 3.5.4, feedback of the active and reactive power of the machines through the vectors $\mathbf{\Omega_g}$ and $\mathbf{\Omega_{mot}}$ to both AVRs is required. PSSs are also modeled, which feed the stabilizing signals ν_{s_g} and $\nu_{s_{mot}}$ into the AVR to damp the low-frequency oscillations in the system.

PSAT® Model of CAES System

In power flow studies, the CAES system can be represented by two generators connected at the same bus, one absorbing active power while charging and the other injecting active power while discharging. As generators are connected to PV buses, the active power of both machines can be specified, whereas the reactive power would be calculated as part of the power flow solution, based on the specified terminal voltage. The reactive power distribution between the two machines may vary depending on the software used; in PSAT®, the reactive power share is in proportion of the active power output, or in proportion of their MVA capacity when one of the machines has zero active power output [90]. The active and reactive power outputs of both CAES machines obtained from the power flow solution are used to initialize the CAES system controllers for steady state condition.

TSAT® Model of CAES System

The CAES system depicted in Figure 3.32 was implemented in TSAT® as a fully parametrizable User Defined Model (UDM) module, which comprises four sub-models: two governors and two exciters, interacting with two synchronous machines modeled using available machine blocks in TSAT®. The excitation system for the CAES machines is the IEEE Type DC1A exciter [62], including the reactive power control described in Section 3.5.4.

The proposed block diagrams of the SoC logic controller, temperature controller, turbine model, active power controller and valve system, implemented in the Turb/Gov1 block (Figure 3.32), are presented in Figures 3.15, 3.21, 3.33, and 3.34, respectively. Note that these are part of the same Turb/Gov1 block, but presented here separately for clarity. Notice that the minimum limit of 0.01 p.u. in the turbine model in Figure 3.33 prevents the model from becoming singular when the air flow is zero during the turbine shut down.

The mechanical model of the compressor is presented in Figure 3.35. Its control system, which includes the active power controller, surge prevention control and pressure limiter controller is presented in Figure 3.36.

The turbine and compressor models were implemented in TSAT® using basic fundamental blocks; however, due to the limitations on the maximum number of 100 blocks per UDM sub-model, the CMB blocks, SLC blocks, recuperator, intercoolers, and thermodynamic relations in the compressor and turbine were modeled using special blocks available in the UDM editor known as Dynamically Linked Control Blocks (DLBs), in which the models are coded in C and then compiled into .dll files read by TSAT® during the dynamic simulations.

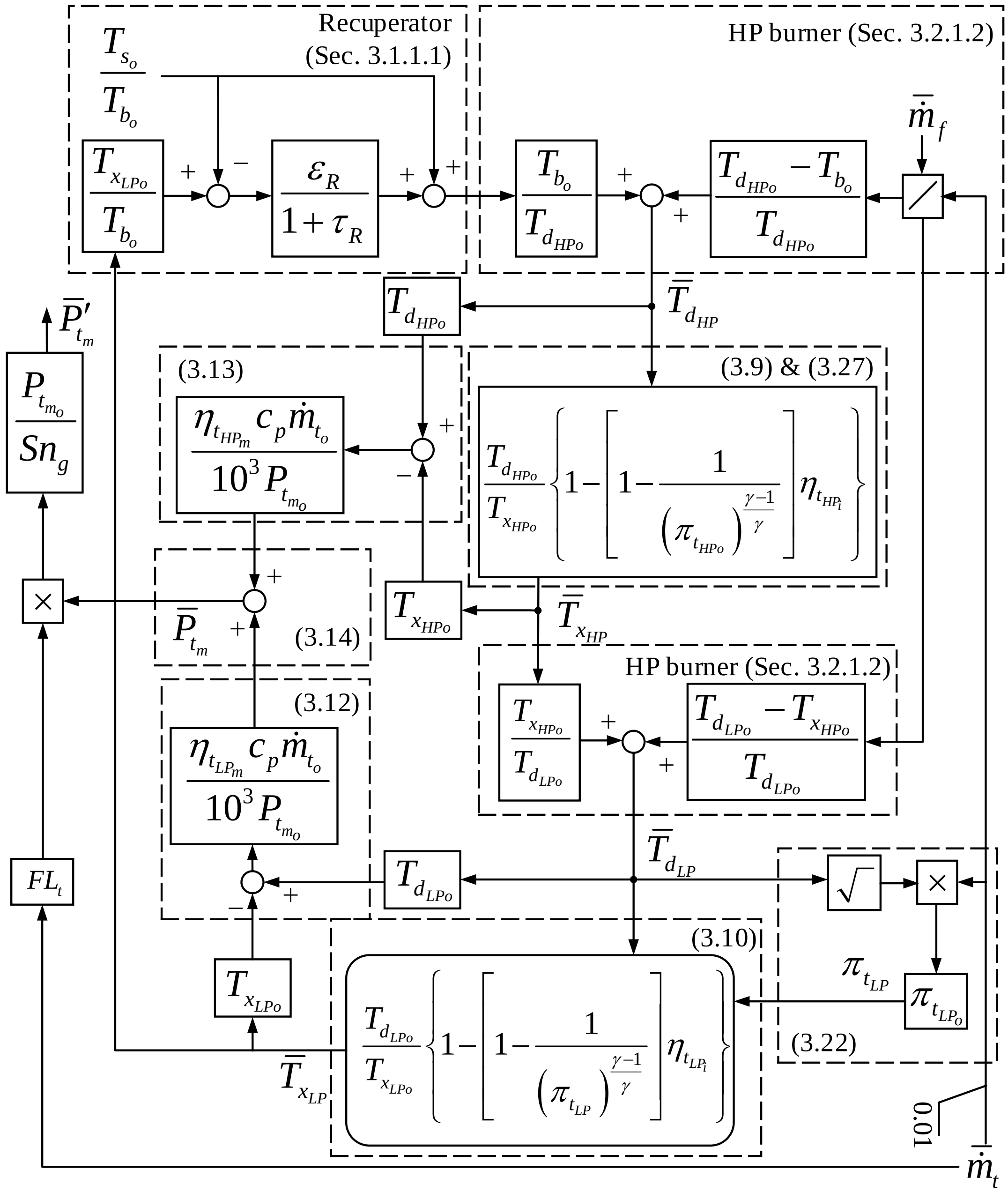

Figure 3.33: Turbine model used in the CAES transient stability analysis model, as per Section 3.2.1.

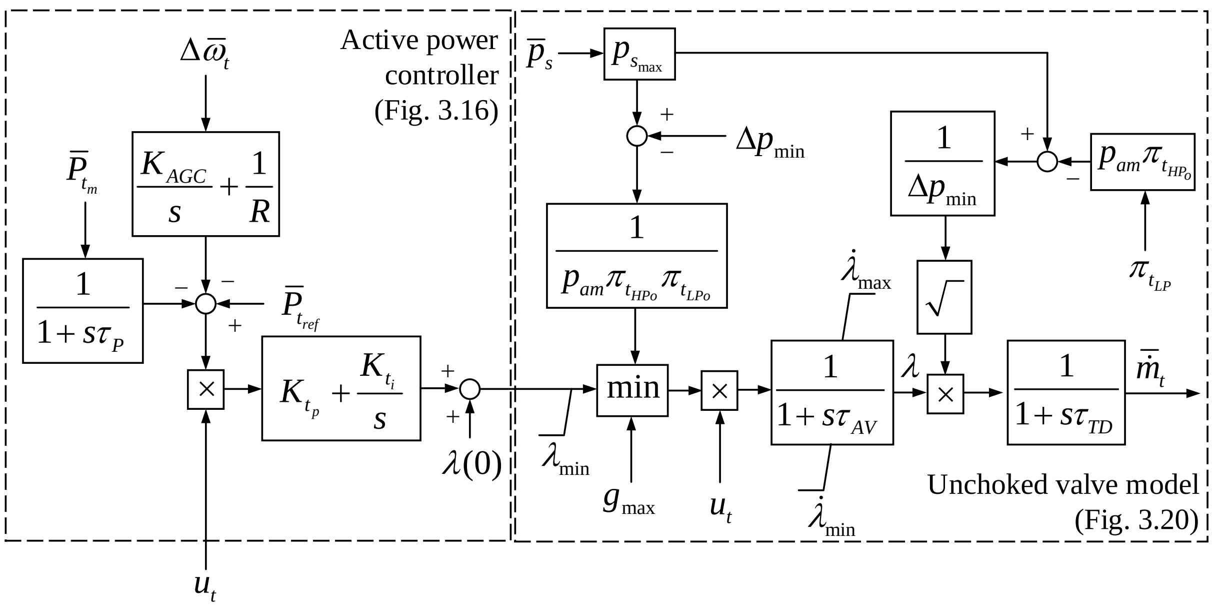

Figure 3.34: Turbine active power controller based on an unchoked valve used in the CAES transient stability model, as per Section 3.5.2.

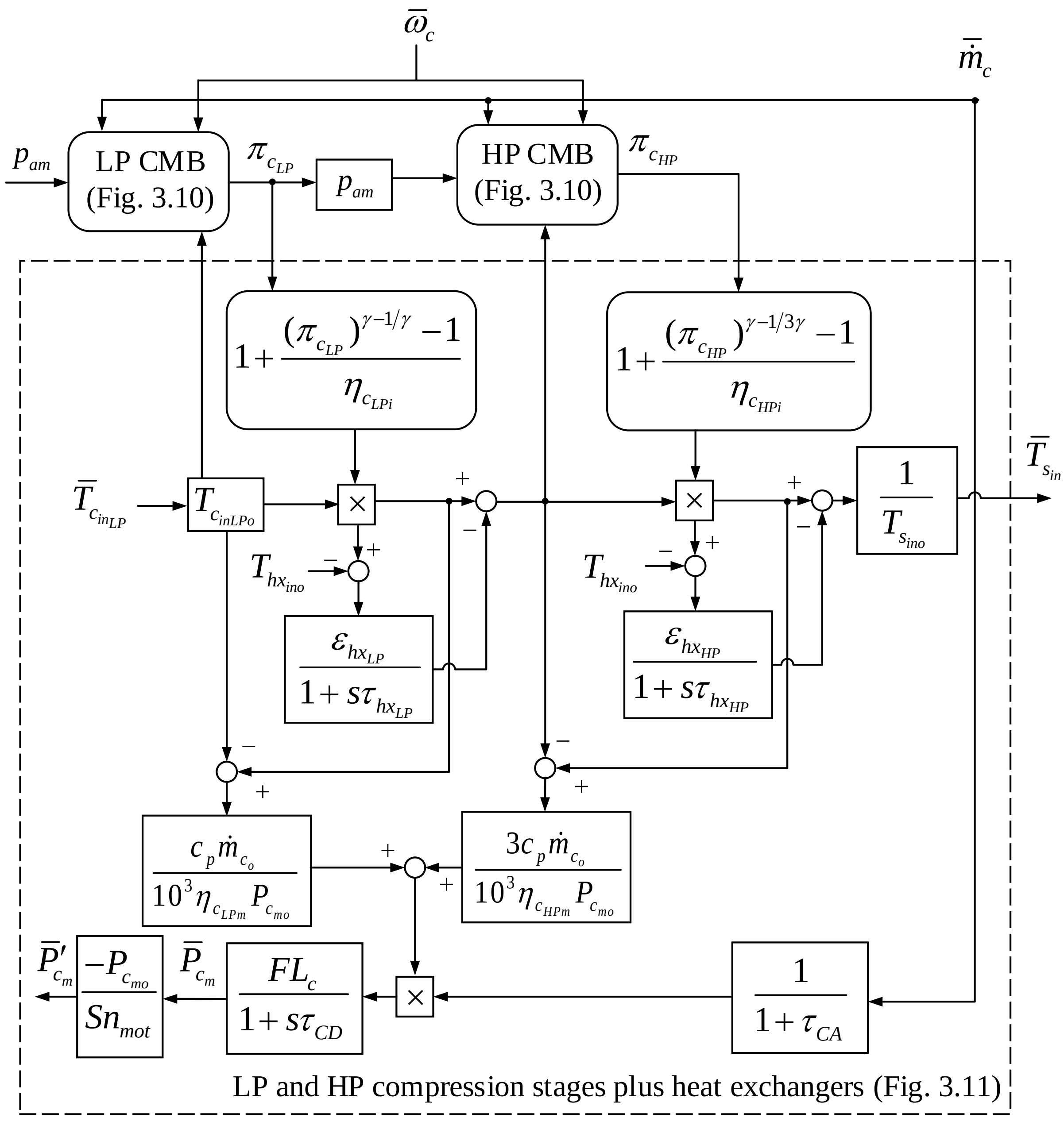

Figure 3.35: Compressor model used in the CAES transient stability analysis model, as per Section 3.3.2.

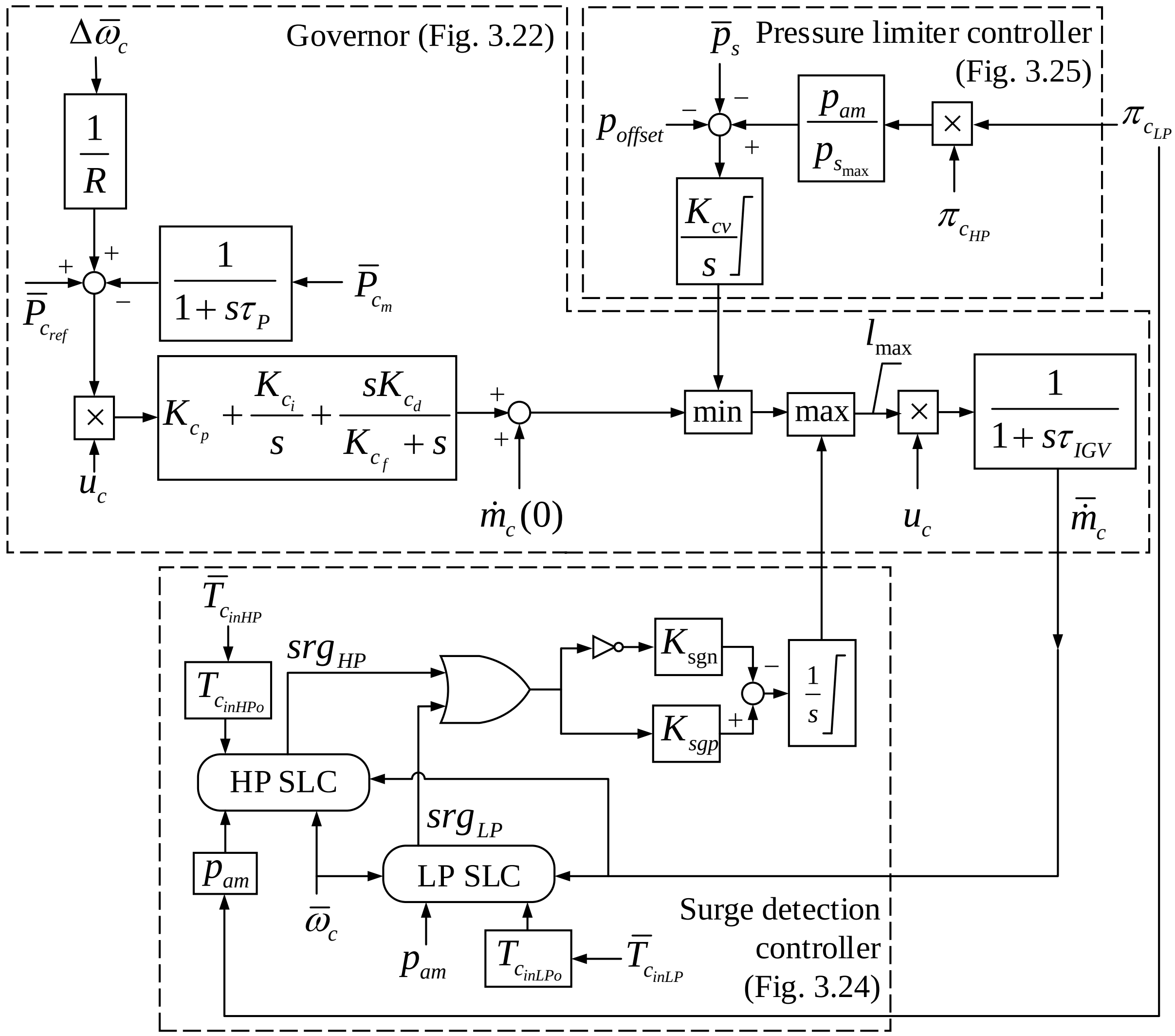

Figure 3.36: Compressor active power controller including surge prevention and pressure limiter used in the CAES transient stability analysis model, as per Section 3.5.3.

Table 3.1: Proposed CAES models summary

	Model 1	Model 2	Model 3	Trans. Stab.
Components				
Turbine model	Detailed	Simplified	Detailed	Detailed
Compressor model	Detailed	Simplified	Simplified	Simplified
Turbine maps	Linear	Linear	Choked	Choked
Compressor maps	Ellipse	Ellipse	NL. func.	NL. func.
Controlling valve (expander)	Linear	Linear	Choked	Unchoked
Cavern model	✓	✓	✓	✓
Controls				
Active power controller (turbine and compressor)	✓	✓	✓	✓
Temperature controller (turbine)	✓	✓	✓	✓
Pressure limiter controller (compressor)			✓	✓
Surge detection controller (compressor)			✓	✓
SoC controller				✓
Reactive power controller				✓
Implemented in	Simulink®	Simulink®	Simulink®	TSAT®

Model Initialization

Initialization of the model involves solving its differential equations for a steady-state condition using power-flow solution as the initial operating point. In some power system analysis software packages, this procedure is performed automatically after the power-flow; however, initial conditions for pure integrator blocks might need to be defined externally.

In the controls proposed, the initialization requires the definition of a vector of initial conditions $\mathbf{x}(0) = [\bar{p}_s(0), y(0), \lambda(0), \bar{\dot{m}}_c(0)]$ for the regulators, as depicted in Figures 3.15, 3.21, 3.34, and 3.36. The initial pressure of the cavern $p_s(0)$ is independent of the power-flow solution, being parameter and input for the model; $\dot{m}_c(0)$ is found by solving the nonlinear system of equations defined by the compressor model in Figure 3.35, considering that $\bar{P}'_{c_m}$ is known; and the turbine's controllers $(\lambda(0), y(0))$ are initialized assuming that $\bar{T}_{X_{LP}} = 1$, and solving the nonlinear system of equations defined by the turbine model in Figure 3.33, considering that $\bar{P}'_{t_m}$ is known.

3.6.3 Models Summary

In Table 3.1, the main characteristics of the proposed CAES models are summarized.

3.7 Summary

In this Chapter, the model and controls of a multi-stage diabatic CAES system, which considers two independent synchronous machines was presented. Physical-based models of the most relevant CAES system components, namely compressor, expander, intercoolers, recuperator, burners, and valves, with different level of details, were discussed. Furthermore, special controllers were proposed for the active and reactive power of the motor-compressor and turbine-generator trains, as well as charging and discharging of the cavern. Finally, the implementation of detailed and simplified CAES models for LFC studies in Simulink®, and a CAES transient stability model in TSAT® were presented.

Chapter 4

Applications of CAES Systems to Power Systems Control and Stability

This chapter focuses on the application, demonstration and evaluation of CAES systems to provide grid services for two test systems, using the mathematical models presented in the previous chapter, which are indirectly validated by comparing them with GTs. Thus, first, the contributions and impact of CAES on the frequency regulation performance is studied using the models with different levels of detail, in a test system model used for frequency control studies with high penetration of renewable energy. Thereafter, the proposed CAES model for transient stability studies is simulated considering the benchmark WSCC 9-bus test system to examine its transient stability, voltage control, oscillation damping, and frequency stability performance.

4.1 CAES System for Load Frequency Control

In this section, step perturbations in the reference setpoints of the CAES compressor and turbine Model 1 (detailed) and Model 2 (simplified) versions, discussed in Section 3.6.1, are simulated, and the results are compared with the models proposed in [26] and [30]. Since the proposed CAES models are highly nonlinear and comprise several dynamic sub-systems and controls, step-changes are first used to study its dynamic performance, with the frequency control loops disabled, and to highlight the differences with respect to existing models. Subsequently, the frequency regulation performance of the proposed detailed and simplified CAES system models are compared with a traditional GT model and the simplified CAES model in [26], for a test grid with high penetration of wind generation. Finally, the impact of considering turbine and compressor maps and associated controls on the frequency regulation capability of CAES is assessed by using Model 3 (Section 3.6.1) in the simulations.

Parameters of the Huntorf CAES plant available from [13], [56], [91], [92] and [93] were used in the simulations; the corresponding dynamic data was taken from [65], [77], [87], [91], and [94], and the turbomachinery inertias were obtained from [62]. The isentropic efficiencies of the expansion stages and HP compression stage were calculated for nominal turbine and compressor conditions. The gains of the PI and PID controllers were obtained by trial and error to produce the best possible dynamic response of the CAES system. All CAES model parameters used in the simulations are provided in Appendix B.

4.1.1 Test System

The model of the power system shown in Figure 4.1 is used to study the impact of CAES on frequency regulation, where the dotted lines signify alternative equipment and control options depending on the case study. The electrical system is approximated by transfer functions, neglecting its fast dynamic responses, as these are much faster than the mechanical systems, which are represented in some detail and significantly impact the system frequency response. The test system comprises realistic models of different generation technologies, and 33% of the load is supplied by wind generation, which is the main source of frequency disturbances. Steam and gas generators were properly sized to be able to supply the demand even when there is no wind power. The following four cases are simulated:

- Case 1: The system has a fixed load of 650 MW, and is comprised of a 200 MW wind farm, two 200 MW steam turbine units contributing to PFR, and a 213.4 MW GT that provides PFR and SFR. The secondary control is obtained by integrating the speed deviation signal to emulate a traditional AGC.
- Case 2: Same as Case 1, but one steam turbine unit is replaced by a 280 MW-discharging/60 MW-charging CAES system, as in the case of Huntorf [13], operating in discharging mode only, and on AGC instead of the GT.
- Case 3: Same as Case 2, but the CAES system operates in simultaneous charging and discharging modes.
- Case 4: Same as Case 3, but the CAES system is simulated using the Model 3 proposed in Section 3.6.1.

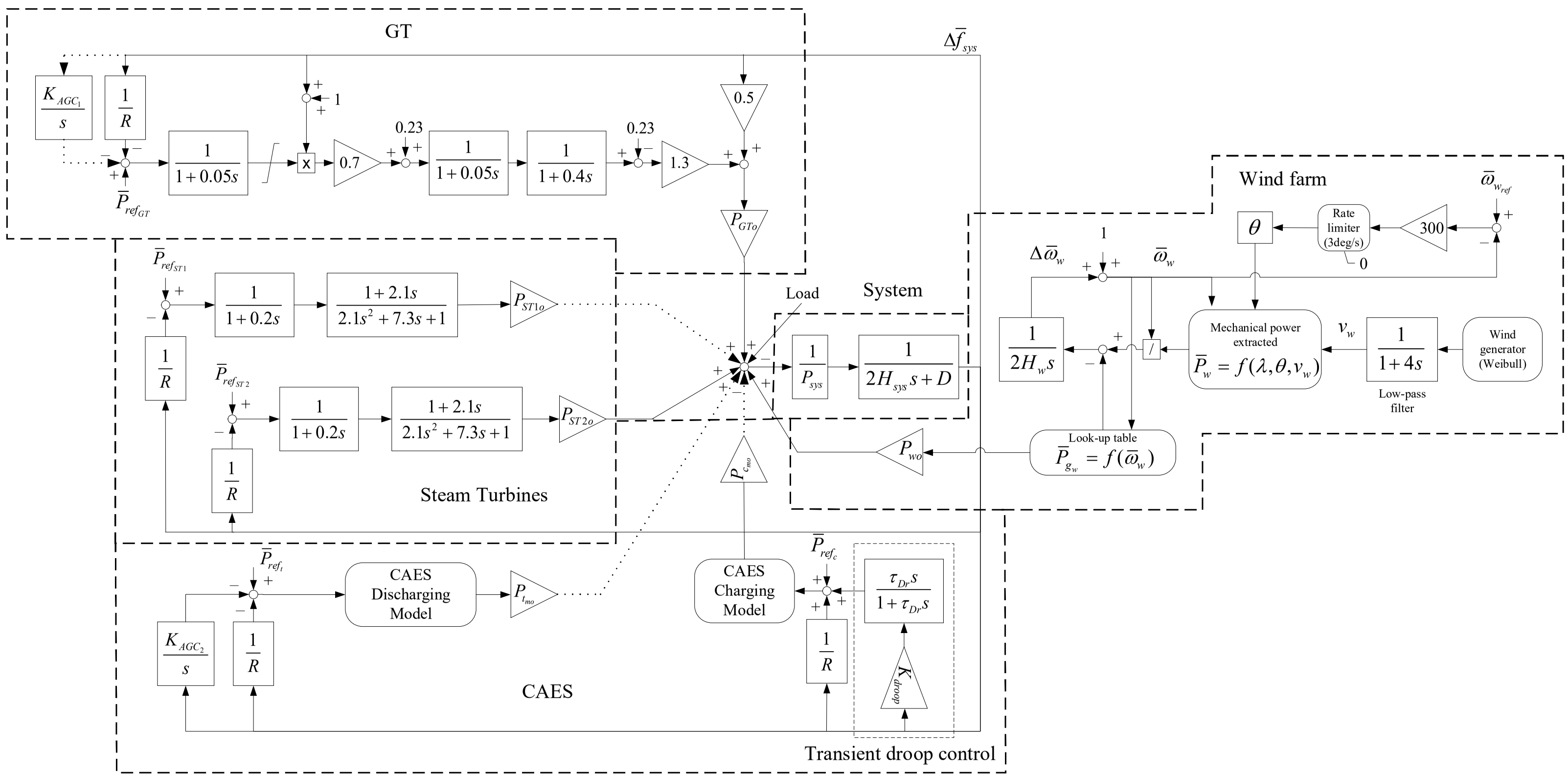

Figure 4.1: Model of the power system with CAES facility for frequency regulation studies.

Table 4.1: Cases summary

	Case 1	Case 2	Case 3	Case 4
Frequency Regulation				
Steam 1	PFR	N/A	N/A	N/A
Steam 2	PFR	PFR	PFR	PFR
GT	SFR	PFR	PFR	PFR
CAES generator	N/A	SFR	SFR	SFR
CAES compressor	N/A	N/A	PFR	PFR
Initial Conditions				
200 MW Steam generation 1 [MW]	175	N/A	N/A	N/A
200 MW Steam generation 2 [MW]	175	175	175	175
200 MW Wind generation [MW]	200	200	200	200
213.4 MW GT generation [MW]	100	100	100	100
280 MW CAES generation [MW]	-	175	221.96	221.96
60 MW CAES compressor load [MW]	-	-	46.96	46.96

A summary of the four cases is presented in Table 4.1, including the frequency control settings and initial conditions of the generators and the CAES system; the rest of system parameters are presented in Appendix B.

The system is in steady-state at 60 Hz nominal frequency before $t = 30\,s$. The gains $K_{AGC_1} = 20$, and $K_{AGC_2} = 60$ for the GT and CAES turbine, respectively, were tuned to achieve the best frequency performance; furthermore, in order to improve the response of the compressor, a transient droop control was added, as shown in Figure 4.1. The wind farm comprises a simple aggregation of 100 2-MW Doubly-Fed Induction Generators (DFIG), based on the models reported in [95] and [96]. The wind profile was created using a Weibull distribution (shape parameter = 2, and scale parameter = 12.1505), which was smoothed out with a low-pass filter as suggested in [73]. The steam turbine model and parameters were taken from [61]. The GT model proposed in [65] (Figure 2.10), is used here, excluding the acceleration control and assuming the use of gasified and not liquified gas as fuel.

4.1.2 Simulations, Results and Discussions

Step Changes to Power Reference

A CAES system comprising a 280 MW turbine and 60 MW compressor, supplying/consuming 196 MW/42 MW, are simulated in Simulink® using the proposed detailed (Model 1) and simplified (Model 2) CAES models discussed in Chapter 3. Step changes of +0.3, -0.3, -0.1, +0.1, +0.5, and -0.5 p.u. are respectively applied at t = 5 s, 20 s, 35 s, 50 s, 65 s, and 80 s in the turbine power reference $\bar{P}_{t_{ref}}$, and at t = 5 s, 30 s, 60 s, 80 s, 120 s, and 140 s in the compressor power reference $\bar{P}_{c_{ref}}$ of the proposed detailed and simplified models. In both cases, the speed deviation feedback with the permanent droop characteristic R is disconnected, to avoid external disturbance interference in the dynamic response of the models. The proposed models are also compared with two existing CAES models described in [26] and [30], with their frequency control loops disabled also. The converters used in [30] as interfaces between the CAES machines and the grid, were not modeled here. The dynamic response of the compression and expansion stages are shown in Figure 4.2 and Figure 4.3, respectively.

Observe in Figure 4.2, that, even though the simplified model considers only the dynamics of one intercooler, it has a similar response as the detailed model, because the dynamics of the air mass flow rate and discharging compressor pressure, are represented using the same transfer functions in both models. Furthermore, since the same time constants were used for all intercoolers, assuming these have similar characteristics, the inlet temperature of the air in each compression stage varies at the same rate, and the contribution of each compression stage to the total power consumed is independent, as shown in Figure 3.11. Notice that, for every step change, there is a fast transient in the mechanical power on both proposed models, which is produced by the rapid change in the air flow and the initial response of the intercoolers. At time t = 130 s, the air flow reaches its maximum limit; however, a dropping air flow is observed because the air flow through the compressor is a function of the rotor speed, as shown in Figure 3.27.

In Figure 4.2(c), notice that since no control action was taken on the compressor's discharge temperature, the temperatures at the different stages present similar transients as $\bar{m}_c$. The input temperature to the cavern $T_{s_{in}}$ in the detailed and simplified models are similar in steady-state, although some differences can be noticed during the transients; however, these differences are not large enough to affect the SoC of the cavern because of its large size.

Dynamic responses obtained with the models from [26] and [30] show significant differences in their transient response in the compression mode as compared to the proposed models. This is because the model in [30] ignores the dynamics associated with the physical components of CAES such as heat exchangers, and explicitly represents only the rotational inertia and the cavern pressure. The compressor model of [30] responds very rapidly in this case, according to the parameters used in the storage controller, which was modeled here to regulate the active power rather than frequency. This model does not include limits in the air flow either; therefore, the air flow is much larger in the interval between 120 s to 140 s (Figure 4.2(a)). The model in [26], on the other hand, uses a rate-of-change limiter that prevents the compressor from changing its operating point too fast; however, only the dynamics of the air-adjusting valve are represented, which makes their response faster than the proposed models, and also more oscillatory.

The expander responses illustrated in Figure 4.3 are more uniform across the models tested than that of the compressor; however, some differences can still be observed. For example, the large air flow excursions, and the air flow and active power transients, occurring after a step change with the proposed detailed and simplified models are not observed in the simulations of models [26] or [30]. Moreover, the model from [26] reaches steady-state faster than the rest, and at larger per-unit values, especially in the turbine active power when the step changes are also large, which demonstrates that it cannot represent an overloading condition properly. The differences in the dynamic responses are due to the combined effect of the controllers (temperature and power), and the simplified valve used in the proposed models, which are not considered in [26] and [30]. Since the CAES model in [30] neglects all dynamics in the turbine, its response is fast and depends exclusively on the parameters of its power controller. Similarly, in [26], the dynamics of the recuperator are not modeled, leaving the governor and pressure valve delays as the only two dynamic components. The differences in the CAES turbine response observed, become relevant when evaluating the performance of a CAES facility providing services such as frequency regulation, as it will be demonstrated later in this section.Note that the main differences between [26] and [30], and the models proposed in this thesis, is the transient response, which, as shown in Figure 4.3(b), can yield differences as large as 0.15 p.u. (42 MW) before reaching steady state a few seconds after the transients die out.

In Figure 4.3(c), the turbine exhaust temperature for the detailed and simplified model are presented. Notice that, in both cases, the exhaust temperature, which is affected by changes in the air flow, is regulated at its nominal value by the temperature controller. The negative overshoots are due to the cooling effect of increasing air flow in the burners. Observe that the nominal temperature is different in both models, the reason being the approximations used in the simplified model, as discussed in Section 3.2.2.

A clear advantage of the simplified model is the reduction in the information required of the parameters. Thus, in the detailed model, the input and output temperatures, ef-

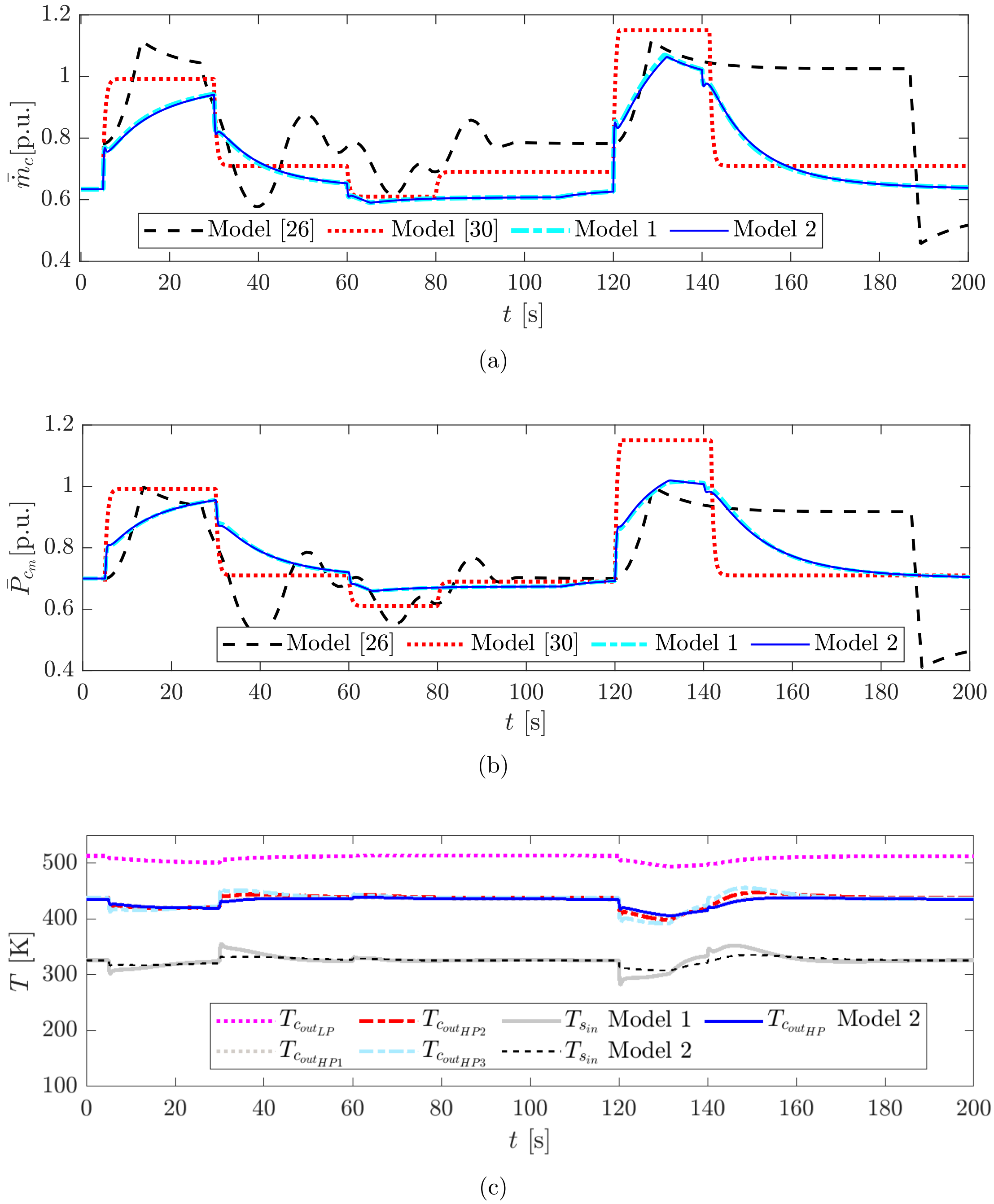

Figure 4.2: Dynamic response of CAES compressor model to step changes in power reference: (a) air flow, (b) active power, and (c) stage temperatures.

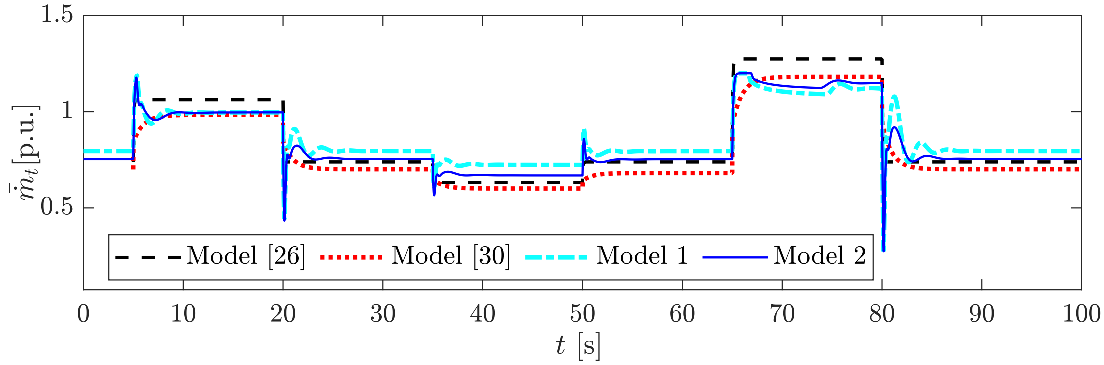

(a)

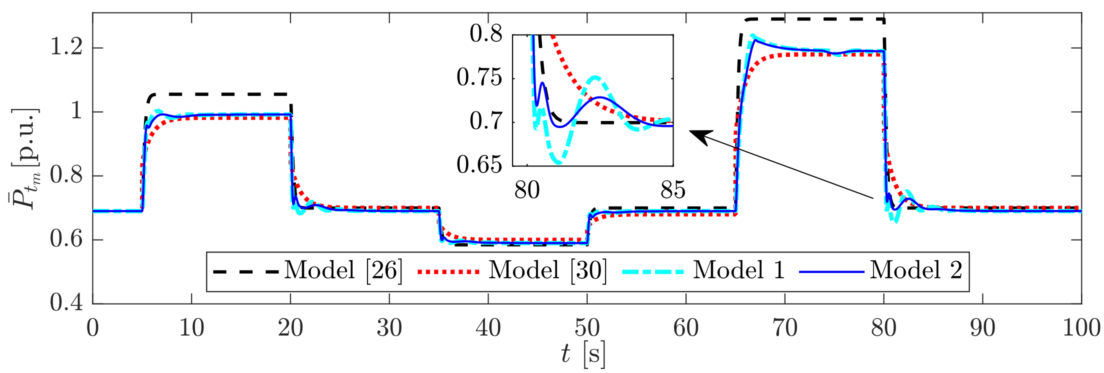

(b)

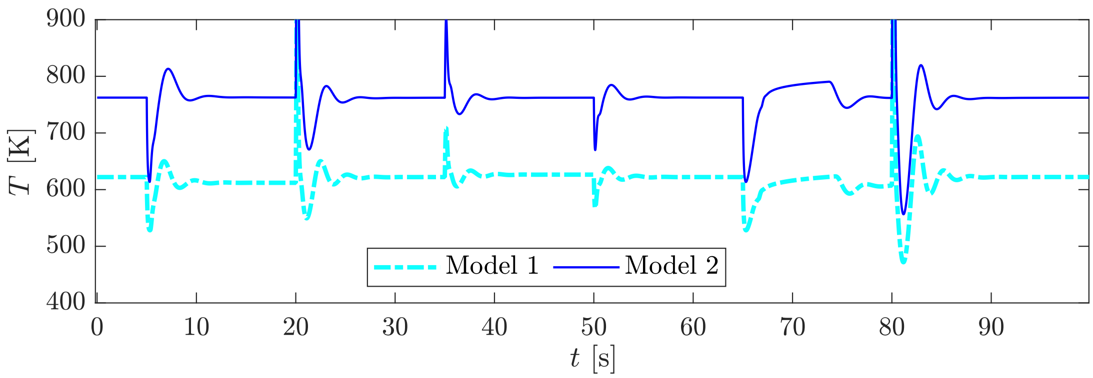

(c)

Figure 4.3: Dynamic response of CAES expander model to step changes in power reference: (a) air flow, (b) active power, and (c) exhaust temperatures.

ficiency, effectiveness and time constants of heat exchangers, pressure ratios, etc., need to be specified for each compression/expansion stage. The required information may be unavailable or may require extensive machine testing and measurements. Estimating these parameters is complicated due to the interrelations between the variables in the different stages. Furthermore, initializing the model is cumbersome. On the other hand, the proposed simplified CAES model involves fewer parameters because of the lumped representation used in this model, such as the nominal pressure ratio of the HP compressor or the inlet temperature of the turbine. Moreover, the complexity of parameter estimation is reduced as several model variables are avoided. However, the simplified turbine model fails to properly represent the turbine exhaust temperature, also showing larger temperature excursions during transients, which could affect the CAES system response under more severe disturbances. Hence, although the simplified turbine model can be suitable for LFC studies, it is not recommended for transient stability studies.

Frequency Regulation

A comparison of the system frequency for Cases 1, 2, and 3 for the proposed detailed and simplified CAES models are presented in Figure 4.4 including the frequency control loops. The normal and abnormal operation limits are as per the Ontario's Independent Electricity System Operator (IESO) [97]. The results show very similar frequency responses for the simplified and detailed CAES models in Cases 2 and 3; the main difference is the magnitude of the frequency excursions, which, as discussed in Section 4.1.2, are better captured by the detailed model. The largest error in frequency deviation between the simplified and detailed models is 0.03 Hz (0.05%). The simplified model has the additional advantage of requiring less than half the time to simulate vis-a-vis the detailed model (17.8s vs. 38.8s for Case 3). Observe that the combined operation of the compressor and turbine in Case 3 produces a better frequency regulation than Cases 1 and 2. Thus, the maximum positive frequency excursion is reduced from 60.39 Hz in Case 1, to 60.17 Hz in Case 2, and 60.16 Hz in Case 3; and the largest negative frequency excursion decreases from 59.68 Hz, to 59.89 Hz, and 59.89 Hz, respectively. Furthermore, for the considered simulation period, in Case 3, the simultaneous charging and discharging is more effective in flattening out the frequency than in the other two cases; this can be attributed to the operation of the compressor using the proposed transient droop control, and the inertia added by the rotating masses of the compressor and synchronous motor. Similarly, the number of frequency excursions beyond limits is reduced from 5 to 0 when comparing Case 1 to Cases 2 or 3.

In Figure 4.5, the cumulative absolute value of frequency deviation is used as a quanti-

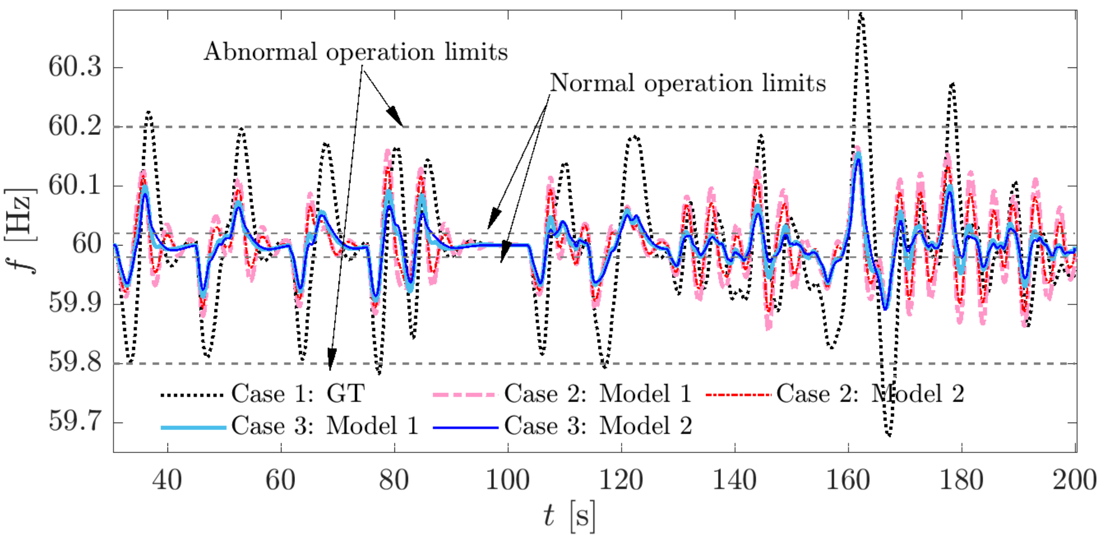

Figure 4.4: Frequency plots for Cases 1, 2, and 3.

tative measurement of the frequency regulation performance of each alternative considered. Note that since larger frequency excursions were obtained with Model 1 with respect to Model 2, for Cases 2 and 3, the cumulative frequency deviations were also larger, especially in Case 2, where the difference between the the two models was bigger. Thus, the cumulative frequency deviation of Model 1 is around 20% larger than that of Model 2, for Case 2, while it is 10% for Case 3. Nevertheless, from this metric, it can be concluded that Case 2 is better than Case 1, and Case 3 is better than the other two. At the end of the simulation time, comparing the results of the detailed models, the value for Case 2 is 58.89% of that in Case 1, and 31.98% for Case 3 with respect to Case 1. A quasi-linear trend is observed in the three plots; thus, the relative proportion of this metric is expected to remain constant in time.

Figure 4.6 shows a comparison of the proposed CAES models and the model in reference [26] for Case 3. It is important to mention that if the gain $K_{AGC_2} = 60$ is used in the CAES charging model from [26], the system is unstable; therefore, the gain was reduced to $K_{AGC_2} = 10$. As highlighted before, observe that because the model in [26] neglects some dynamics, its response is much faster, resulting in smaller frequency deviations.

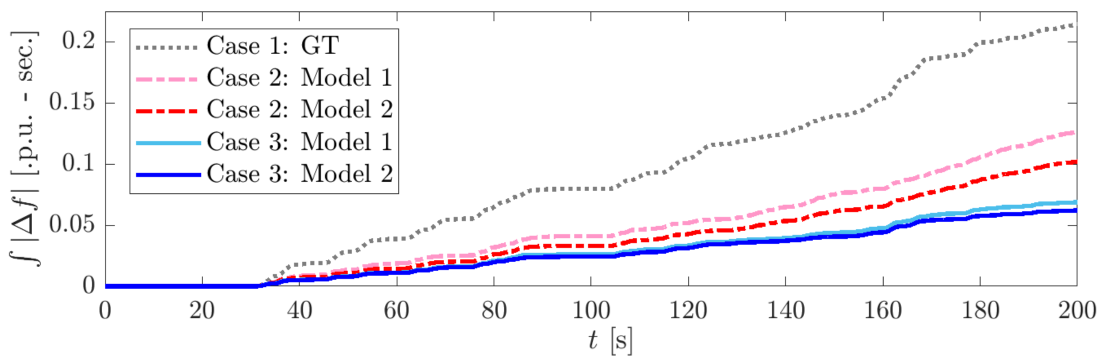

Figure 4.5: Regulation performance for Cases 1, 2, and 3.

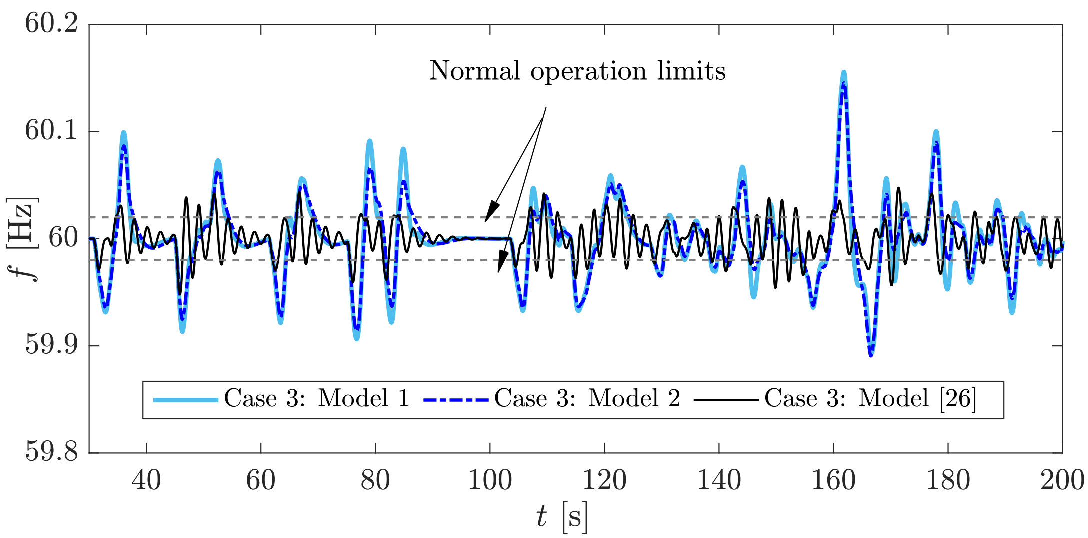

Figure 4.6: System frequency for Case 3.

Impact of the Mechanical System Model

In this Section, the frequency regulation capability of CAES is evaluated considering Case 4, as described in Section 4.1.1, using the proposed Model 3 in Section 3.6.1 (Figures 3.29, 3.30 and 3.31), which includes the compressor and turbine maps, and associated controls. Since in Model 3, the cavern pressure p_s is an important limiting factor in the compressor and turbine operation, a comparison of the frequency regulation performance of the CAES system for two values of p_s is presented in Figure 4.7. In Models 1 and 2, on the other hand, since the surge prevention and pressure limiter controllers are not modeled for the compressor, and only a linear valve is considered in the expansion, the cavern pressure does not constraint the operation of the CAES system.

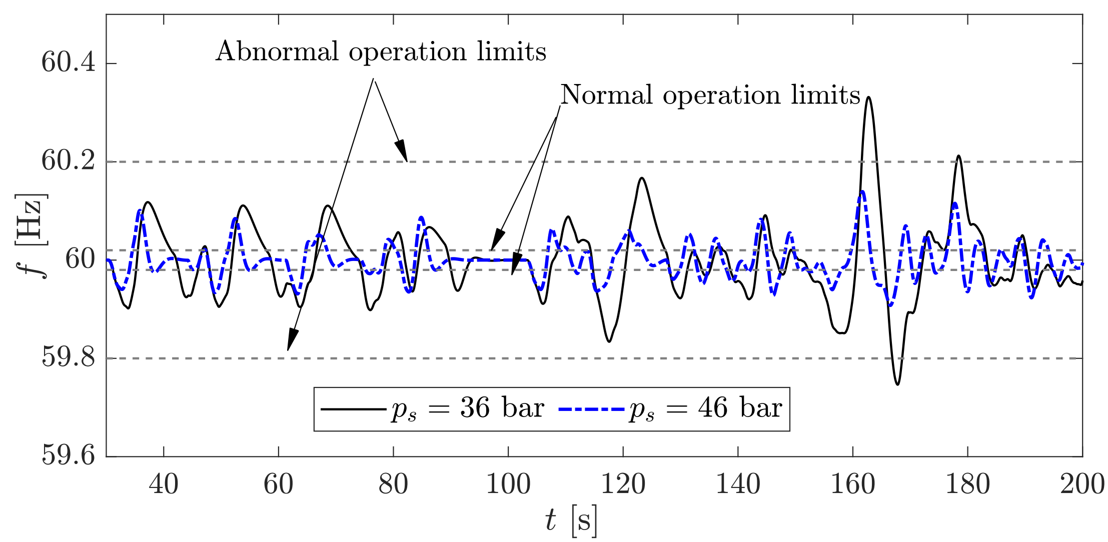

Figure 4.7: System frequency in Case 4 for different cavern pressures.

Notice in Figure 4.7 that, for a low cavern pressure of $p_s = 36$ bar, the frequency regulation of the CAES system is less effective than that at nominal pressure $p_s = 46$ bar, for several reasons. First, for low cavern pressures, the air flow limit $\bar{\dot{m}}_{min}$ in the turbine controller restricts the expander pressure ratio (Figure 4.8), and thus its output power. Second, according to (3.30), low cavern pressures require a larger valve opening λ for a given air flow; therefore, when large power injections are required for regulation, the air flow is limited because λ reaches λ_{max} (defined as 2.4 p.u.), as shown in Figure 4.9. Third, if the compressor's power controller sets the airflow at a value that results in the compressor's discharging pressure being less than the cavern pressure p_s, the pressure limiter controller (Figure 3.30) takes over the compressor control, ignoring the frequency regulation requirements, as presented in Figure 4.10. It can also be observed that, for $p_s = 36$ bar, the surge control acts at three different periods, which worsens the frequency regulation performance, because the sudden air flow increment to avoid surge directly opposes the governor requirements.

Finally, a sensitivity analysis of the cavern pressure p_s is carried out by comparing the cumulative frequency deviation over the simulation period (Figure 4.11). Notice that for p_s lower than the nominal, the frequency regulation performance of the CAES system deteriorates significantly; for example, the cumulative frequency deviation at $p_s = 36$ bar is 0.1690 p.u.-sec., which is 2.35 times larger than that at $p_s = 46$ bar of 0.07 p.u.-sec. The reason for improved frequency performance as the cavern pressure increases, is that the turbine mechanical power is less constrained by its regulating valve, thus contributing more to regulate the frequency. The cumulative frequency deviation stabilizes for $p_s \geq 48$ bar, when the valve no longer limits the turbine. Notice, that the cumulative frequency deviation, for $p_s \geq 48$ bar, in Case 4 is slightly larger than that in Case 3 (Figure 4.5), because in Case 4, larger cavern pressures constrain the operation of the compressor due to the action of the pressure limiter controller.

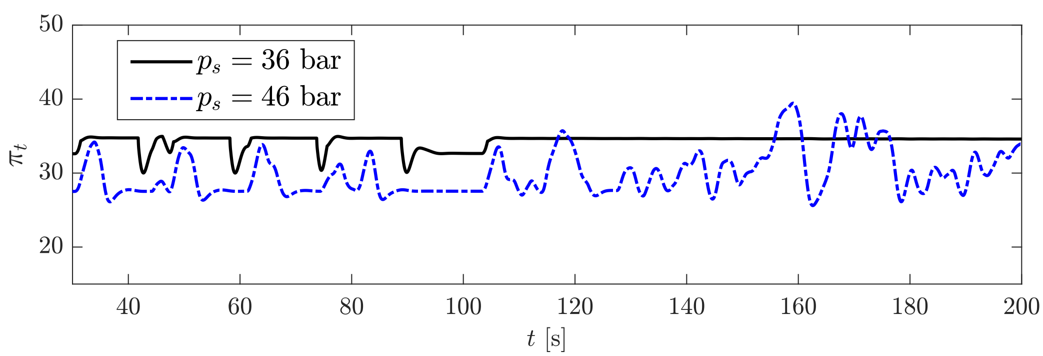

Figure 4.8: Expansion pressure ratio in Case 4.

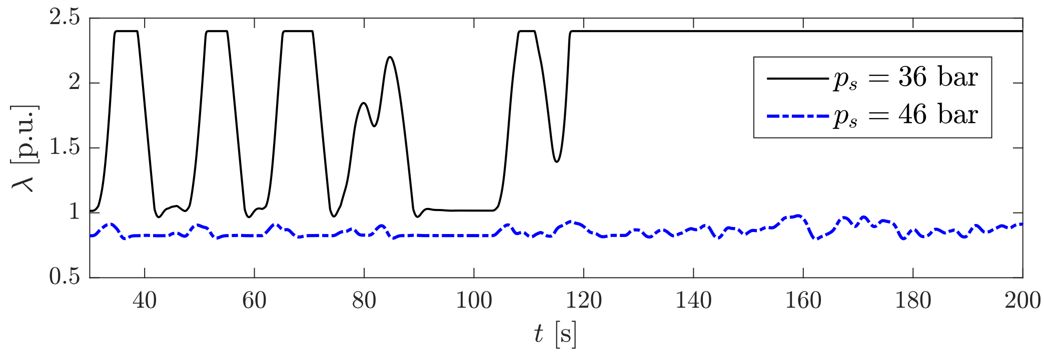

Figure 4.9: Valve opening in Case 4.

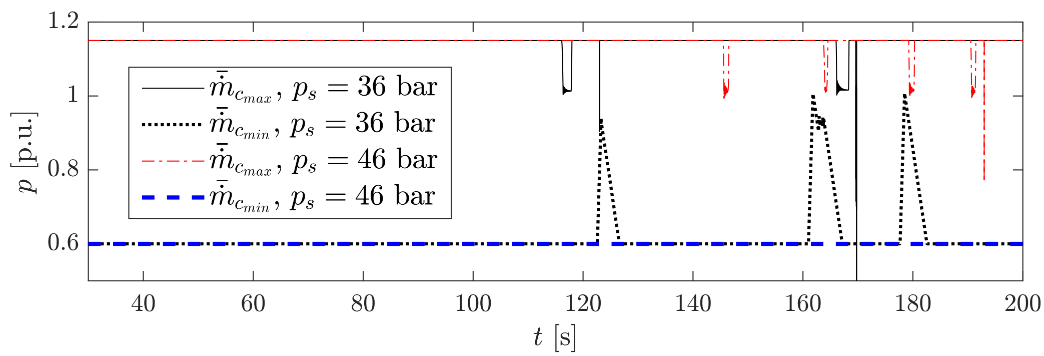

Figure 4.10: Compressor airflow limits due to pressure limiter and surge controller actions, in Case 4.

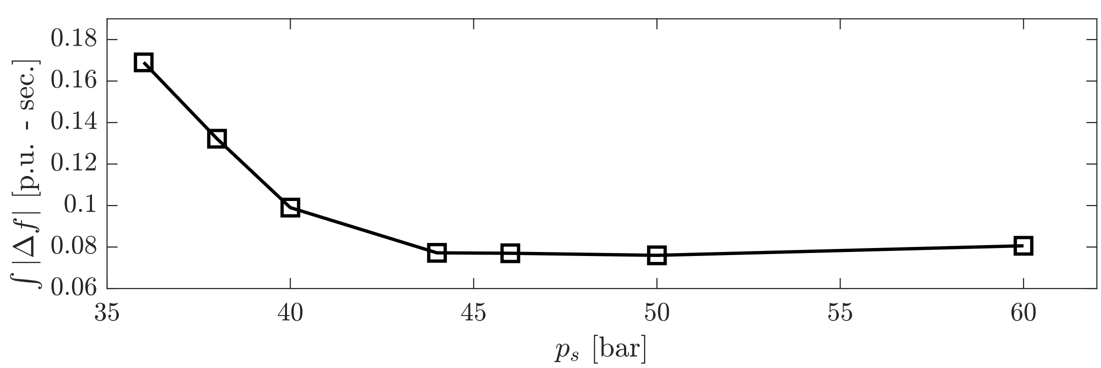

Figure 4.11: Cumulative frequency deviation over 200s of simulation, for different cavern pressures in Case 4.

4.2 Grid System Studies of CAES

4.2.1 Test System

The CAES system model is studied here via dynamic simulations when connected in a modified version of the WSCC 9-bus test system illustrated in Figure 4.12 [62], which has been used in similar studies for other storage technologies [30]. It is assumed that the additional load requires about 350 MVA of additional generation, which is assumed to be supplied by either a set of GT units or a CAES system of equivalent discharging power. The dynamic data of the generators and parameters of the excitation systems were obtained from [62], and for the governors and PSSs from [98]. The speed of the valves of the steam and hydro turbines were set to ± 0.2 and ± 0.1 p.u./s, respectively [99, 100]. The GT model was obtained from [65], and its parameters from [69]. The CAES model parameters are listed in Appendix C, which for the proposed controllers, were tuned to obtain appropriate dynamic response. A voltage droop control with a gain of 5% was used in the AVRs of the GTs for stable parallel operation.

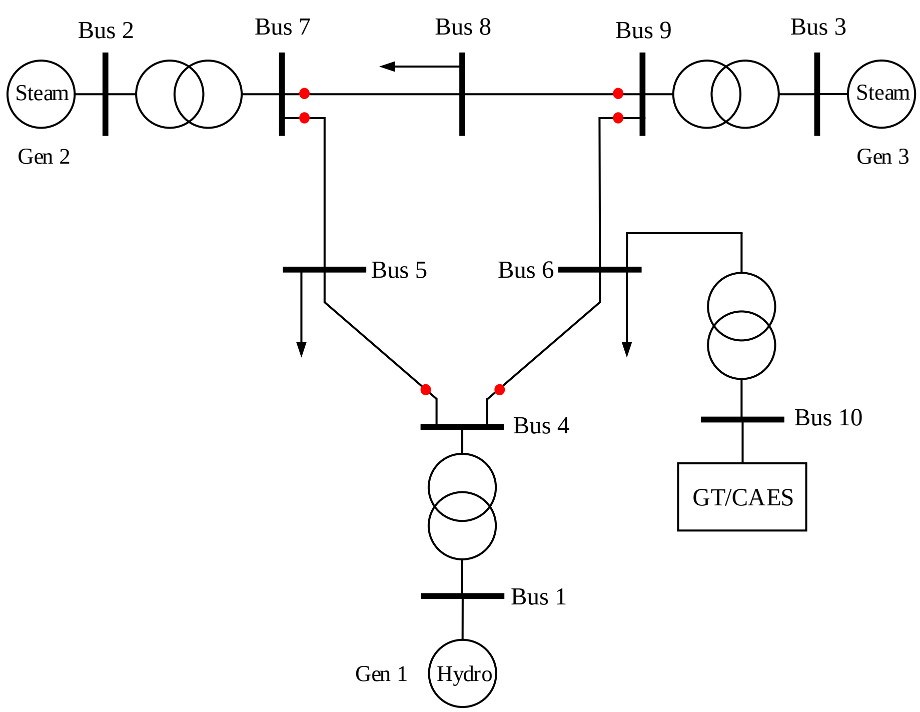

Figure 4.12: Benchmark test system [62].

Seven system configurations were considered to study the dynamic performance of the CAES system model, as follows:

- Case 5: No GTs or CAES are connected, none of the PSS of the generating units are active, and Gen 1 is on AGC.
- Case 6: Same as Case 5, but the PSS of the three generating units are active.
- Case 7: Same as Case 6, with four identical 95 MVA GT units connected at Bus 10, which supply a total of 100 MW, while reducing the generation from Gen 2 and Gen 3.
- Case 8: The GTs at Bus 10 are replaced by a 341 MVA discharging/75 MVA charging CAES system operating in discharging mode, with its PSS active, and the CAES system on AGC instead of Gen 1.
- Case 9: Same as Case 8, but with the CAES system operating in simultaneous charging and discharging mode.
- Case 10: Same as Case 8, but with two different CAES cavern sizes.
- Case 11: The CAES system is charging the cavern, Gen 1 is on AGC, and all PSS are active.

The PSSs' gains were tuned by trial and error to achieve acceptable damping in all the cases.

4.2.2 Transient Stability Analysis

In this section, the benchmark system's transient stability performances for Case 5 to Case 9 are studied by simulating three-phase short circuits on the transmission lines, depicted as dots in Figure 4.12. Thus, in Figures 4.13 to 4.17 and 4.18 to 4.22, the speed deviation and terminal voltages of all the generators and CAES machines, respectively, are presented for a 100 ms three-phase short circuit located at 90% of the line from Bus 6 to Bus 4. The short circuit is cleared by removing the faulted transmission line. Observe that Case 5 is underdamped; by using Prony analysis on Gen 1 speed deviation, a 1.12 Hz frequency component with a damping ratio of 1.58% can be found, which justifies the use of PSS in the rest of the case studies. In Case 6, the oscillations are properly damped, but the generators speeds and terminal voltages take longer time to reach their steady-state than in Cases 7, 8, and 9. When the GTs are connected in Case 7, an improvement in the frequency response is observed and the voltage drop is reduced at all generator buses, which is reasonable since new generation has been added to the system. However, the damping is adversely affected despite the re-calibration of the PSS, resulting in more sustained oscillations. In this case, tuning the PSS is more complex, because of more GT units being equipped with these devices.

In Cases 8 and 9, the oscillations are damped much faster and the system reaches steady-state in less than 4s. The short time constants of the actuators that control the airflow (fast-acting air valve and IGVs), and the effectiveness of the PI regulators to realize the reference power in both compressor and expander are the main reasons for the CAES system being able to stabilize the system faster. The main difference between Cases 8 and 9 is that, in the latter, the compressor also contributes to frequency regulation by adding inertia to the system. Note also that although the compressor does not consume electrical power from the grid in Case 8, it contributes to voltage regulation as it operates synchronized with the grid, with the compressor decoupled from the motor's rotor.

Observe that the dynamic response of the GT in Case 7 is similar to that of the CAES system in Cases 8 and 9, as shown in Figures 4.16 and 4.17, which indirectly validates the active power components of the CAES model. On the other hand, in Figures 4.21 and 4.22, the GT and CAES terminal voltages show similar trends, with the oscillations depending on the PSS tuning.

In order to provide a broader assessment of the impact of the CAES system transient stability performance, the Critical Clearing Times (CCTs) for short circuits located at 90% of the transmission line from a given bus are calculated. In Table 4.2, the CCTs for each contingency and all simulated cases are presented. Observe that for almost all the contingencies, the CCTs improved when the CAES is connected (Cases 8 and 9), except for the SC in the line connecting Buses 4-5, for which Case 7 yielded the largest CCT.

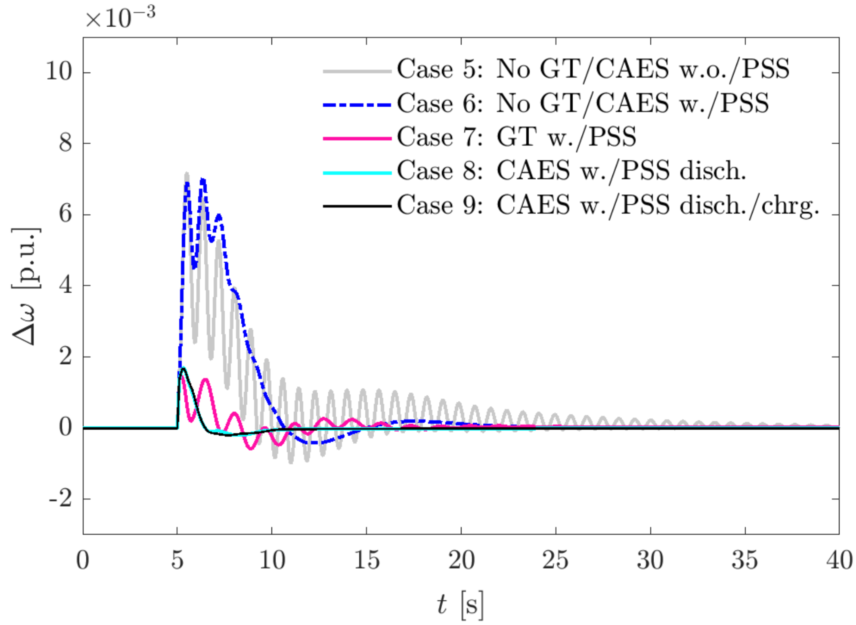

Figure 4.13: Speed deviation of Gen1 for a short circuit on line connecting Buses 6-4.

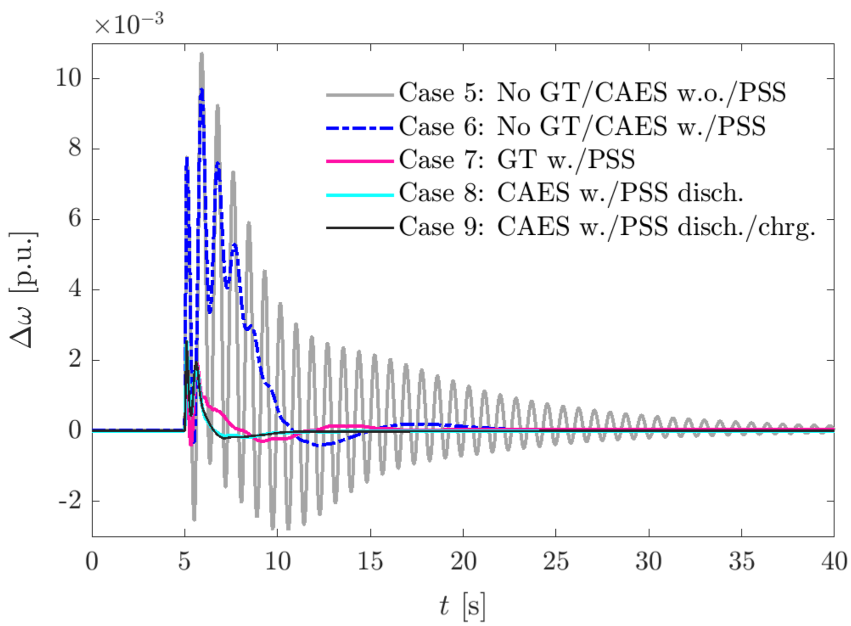

Figure 4.14: Speed deviation of Gen 2 for a short circuit on line connecting Buses 6-4.

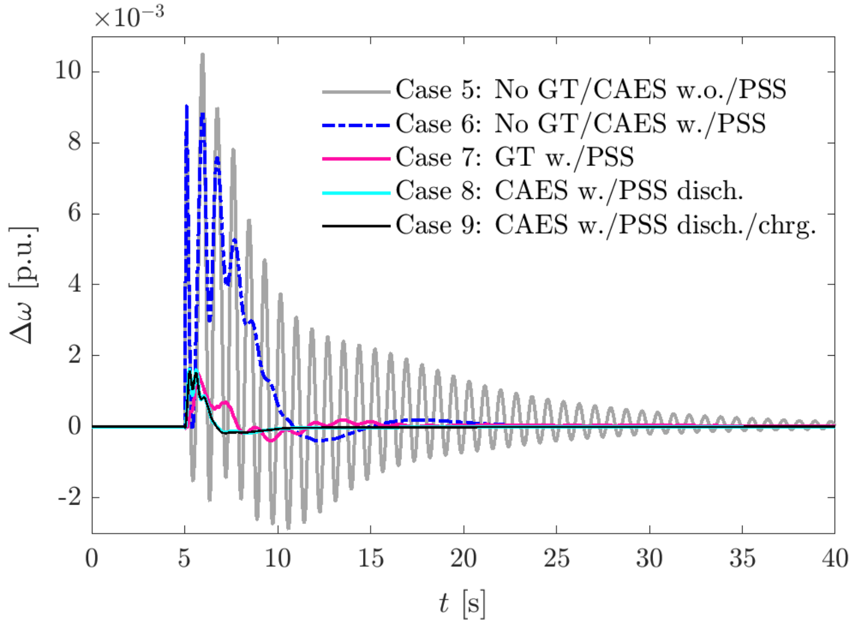

Figure 4.15: Speed deviation of Gen 3 for a short circuit on line connecting Buses 6-4.

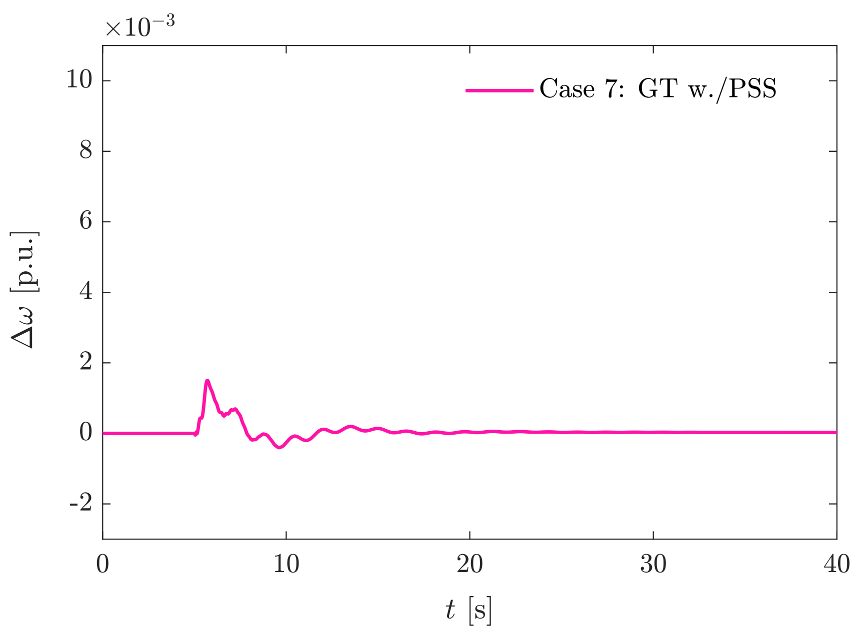

Figure 4.16: Speed deviation of GT for a short circuit on line connecting Buses 6-4.

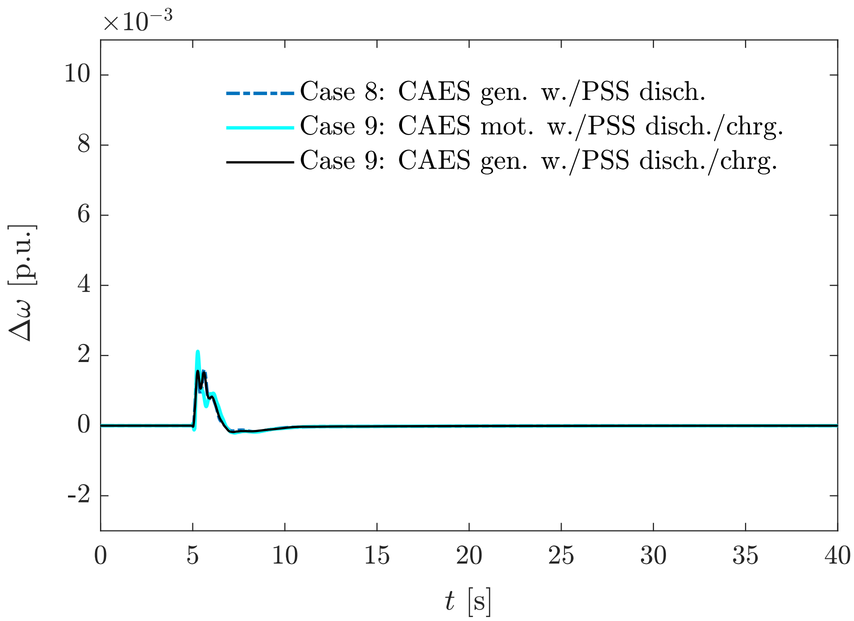

Figure 4.17: Speed deviation of CAES for a short circuit on line connecting Buses 6-4.

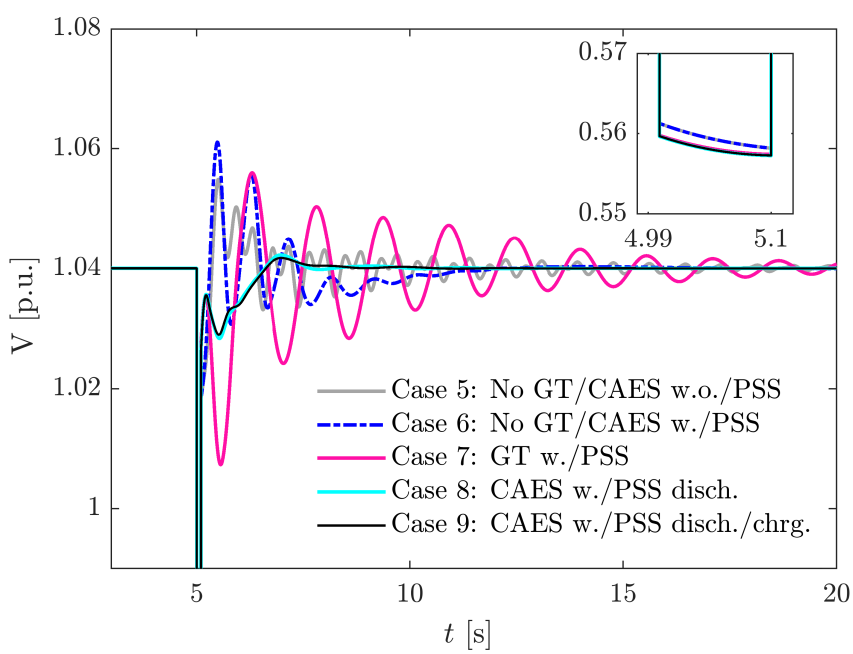

Figure 4.18: Terminal voltage of Gen 1 for a short circuit on line connecting Buses 6-4.

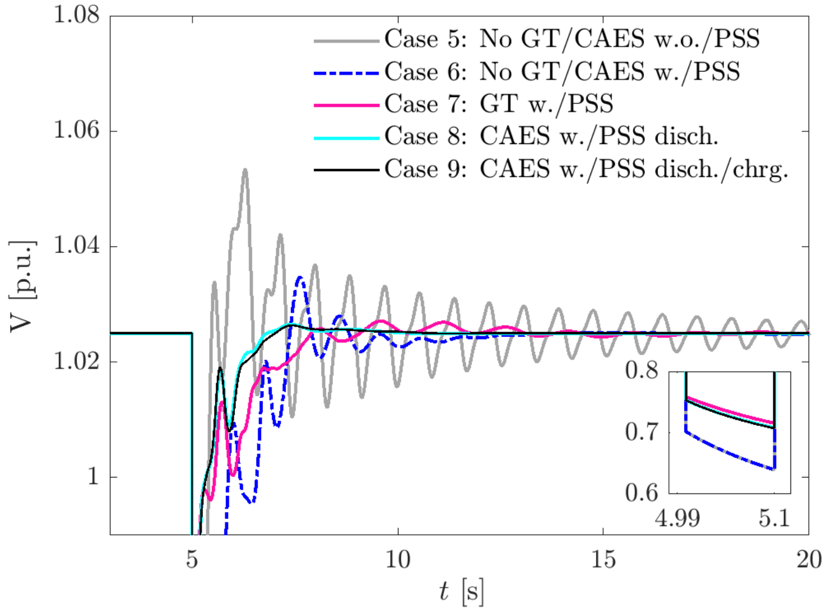

Figure 4.19: Terminal voltage of Gen 2 for a short circuit on line connecting Buses 6-4.

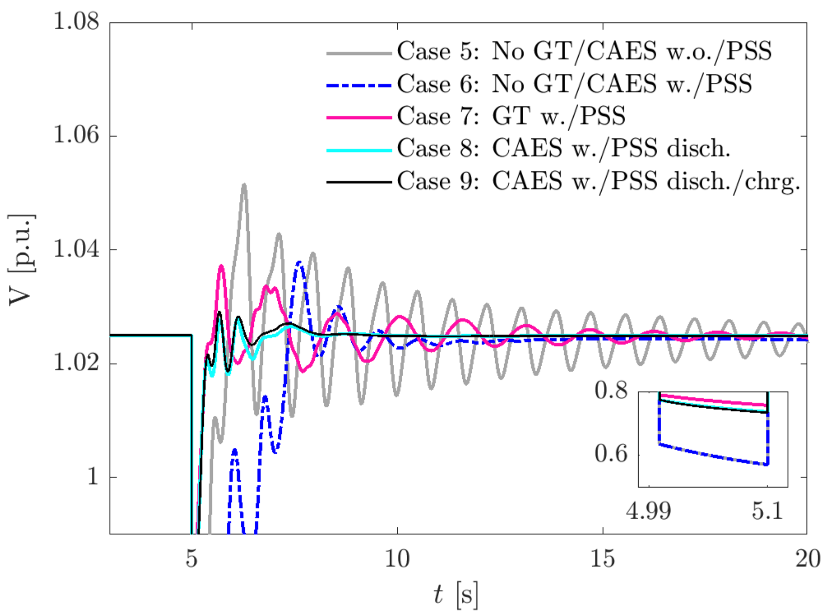

Figure 4.20: Terminal voltage of Gen 3 for a short circuit on line connecting Buses 6-4.

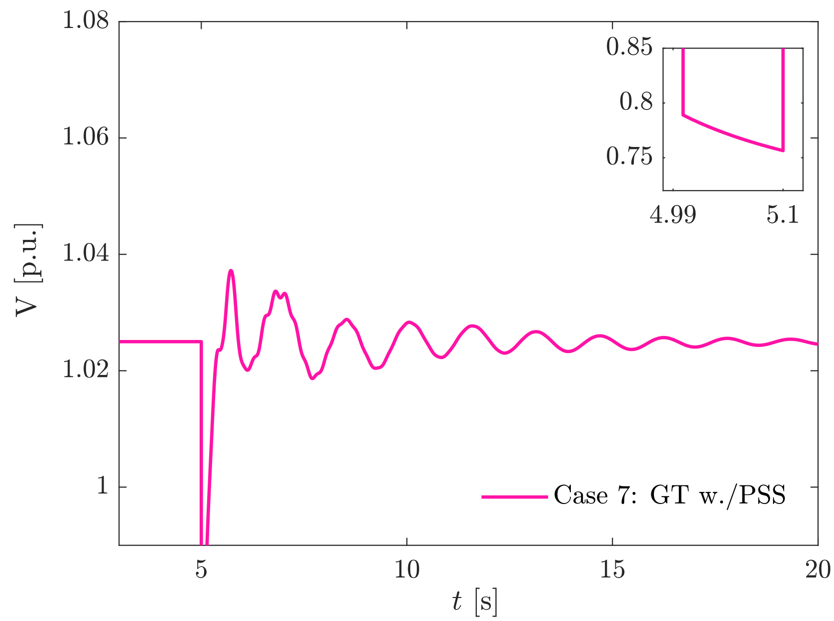

Figure 4.21: Terminal voltage of GT for a short circuit on line connecting Buses 6-4.

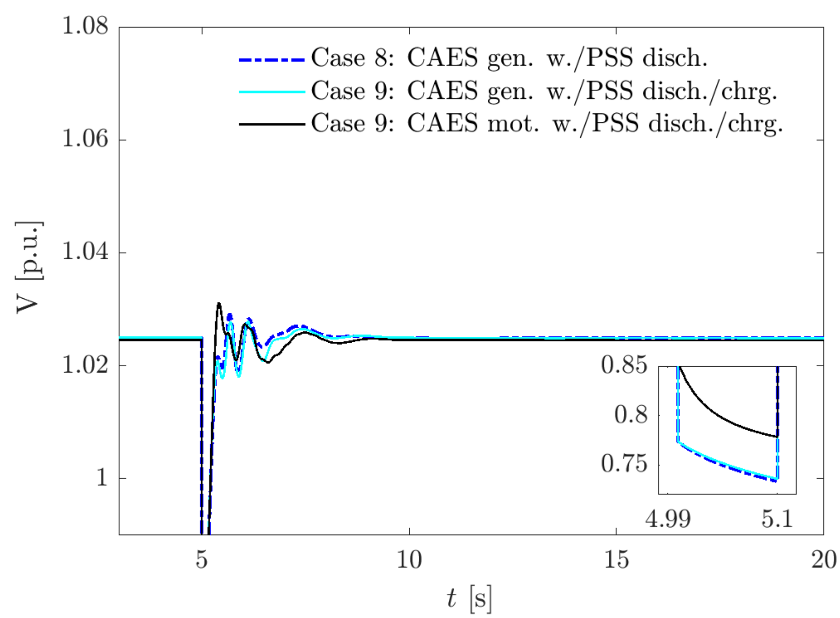

Figure 4.22: Terminal voltage of CAES for a short circuit on line connecting Buses 6-4.

Table 4.2: Critical Clearing Time (CCT) in sec.

Faulted line	Case 5	Case 6	Case 7	Case 8	Case 9
8-9	0.194	0.195	0.513	0.536	0.527
9-6	0	0.164	0.573	0.590	0.573
7-8	0	0.122	0.242	0.247	0.246
6-4	0.255	0.256	1.336	1.567	1.471
4-5	0.247	0.247	2.075	1.782	1.66
5-7	0	0.101	0.287	0.296	0.293

4.2.3 Reactive Power Control

An increase of 30% in the system load in Case 7 is simulated to demonstrate the operation of the proposed reactive power control scheme discussed in Section 3.5.4, which allocates the reactive power dispatch between the two CAES synchronous machines. Before the load increase, the CAES system is supplying 100 MW, and since it is operating on AGC, it takes all the new load reaching a new operating point of 192 MW after the event, while the motor is not consuming active power; in this scenario, $\Delta\bar{Q}_{g_{\max}} = 0.826$ p.u., while $\Delta\bar{Q}_{mot_{\max}} = 1$ p.u.

In Figure 4.23, the reactive power supplied by the CAES motor and generator using the two proposed values of the controller parameter β is presented. When the proposed control is not used (β_o), the CAES generator will consume a large amount of reactive power following the load increase, which will be supplied by the motor, thus unnecessarily overloading the two machines; large and long transients in the CAES reactive power outputs are also observed. On the other hand, when β_1 is used, the generator, as the machine with the largest unused capacity (MVA) supplies most of the reactive power of 13.29 MVAr, while the motor supplies 3.75 MVAr; in this case, the unused capacity (MVA) prevails in determining the reactive power distribution. When β_2 is used, the contribution of the motor increases considerably to 9.75 MVAr versus 7.5 MVAr of the generator, as β_2 improves the loading of the machines. The use of either β_1 or β_2 results in a more stable reactive power supply and eliminates the feeding of reactive power from one machine to the other.

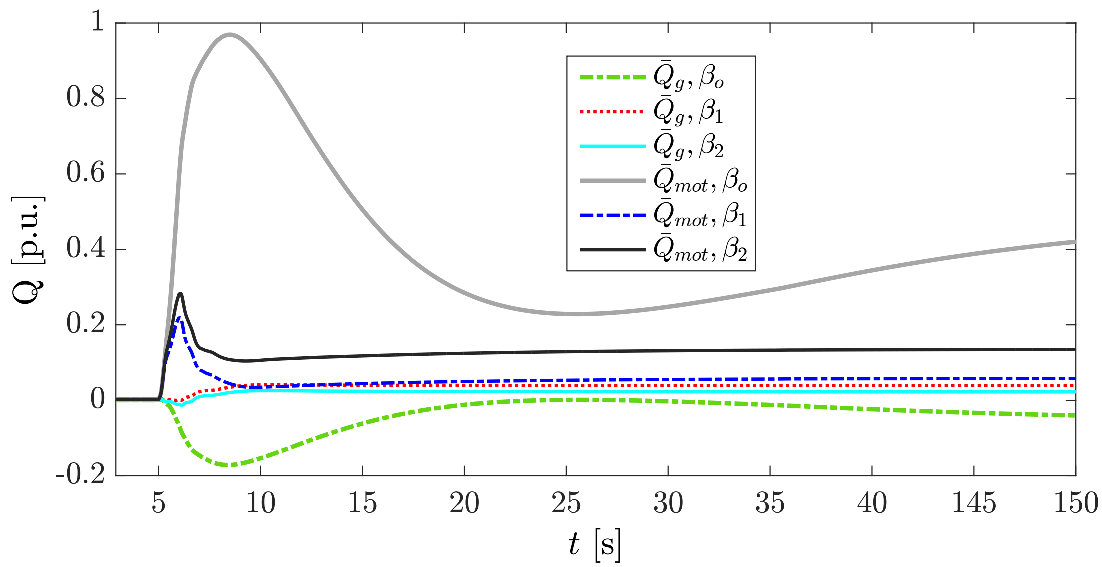

(a)

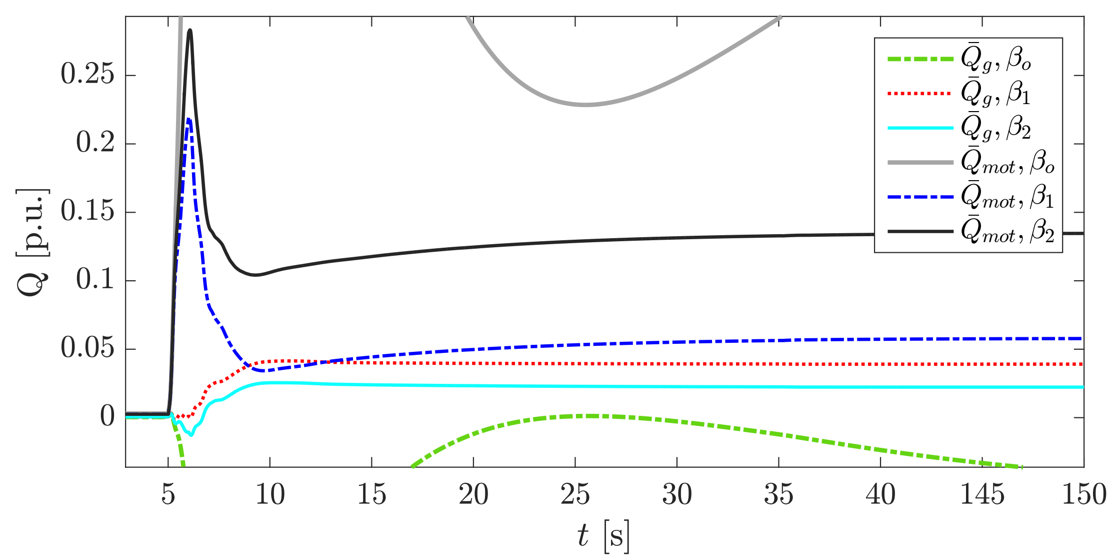

(b)

Figure 4.23: (a) CAES reactive power and (b) expanded view for a 30% system load increase and different reactive compensation control strategies in Case 7.

4.2.4 Impact of Cavern Size on Frequency Stability

The SoC control, proposed as part of the transient stability model, is used here to study the impact of different cavern sizes on the frequency stability of the system when a CAES facility is connected at Bus 10. Thus, two cavern sizes are considered: v_{s_o}=10,000 m^3, and 50%v_{s_o}=5,000 m^3, for the studies presented in Cases 10 and 11. In order to demonstrate the SoC control, a maximum economic pressure of 62.5 bar is used to define the maximum SoC to shut down the compressor, i.e., $SoC_{\max} = 0.77$, with $SoC_{\min} = 0$. The system is perturbed by load changes in the following sequence at all load buses simultaneously: +30% at 1 min, +5% at 2 min, -10% at 3 min, +5% at 4 min, and -15% at 5 min. The results of the simulations are presented in Figures 4.24 to 4.31.

In Case 10, with the CAES system only discharging and its generator on AGC, its discharge power follows the load changes. As the cavern pressure p_s decreases from 55 bar, the SoC falls too, as illustrated in Figure 4.24; the air valve λ opens to maintain the airflow $\dot{m}_t$ at the required value to regulate the frequency, as shown in Figure 4.25. For the reduced cavern volume of 50%v_{s_o}, as soon as the cavern pressure falls below the nominal inlet HP expansion pressure $p_{HP_{in_o}}$ plus the minimum valve pressure $\Delta p_{\min}$ bar, the CAES system loses its regulation capability and $p_{HP_{in}}$, which is limited by the airflow control to ensure the minimum pressure drop in the valve, starts following the cavern pressure, as shown in Figure 4.26. In this scenario, P_g is now determined by the cavern pressure, which along with the frequency, starts to fall, as shown in Figure 4.27 and Figure 4.28. This does not occur when the cavern volume is v_{s_o}, because the pressure drop in the valve $\Delta p = p_s - p_{HP_{in}}$ is always larger than $\Delta p_{\min}$, as noted in Figure 4.26. Note that as soon as the SoC reaches zero at around 6 min in the 50%v_{s_o} case, the CAES turbine is shut down, forcing $P_g = 0$ (Figure 4.27), thus leading to a sustained frequency drop that cannot be recovered (Figure 4.28); for the v_{s_o} case, the frequency is successfully regulated by the CAES system.

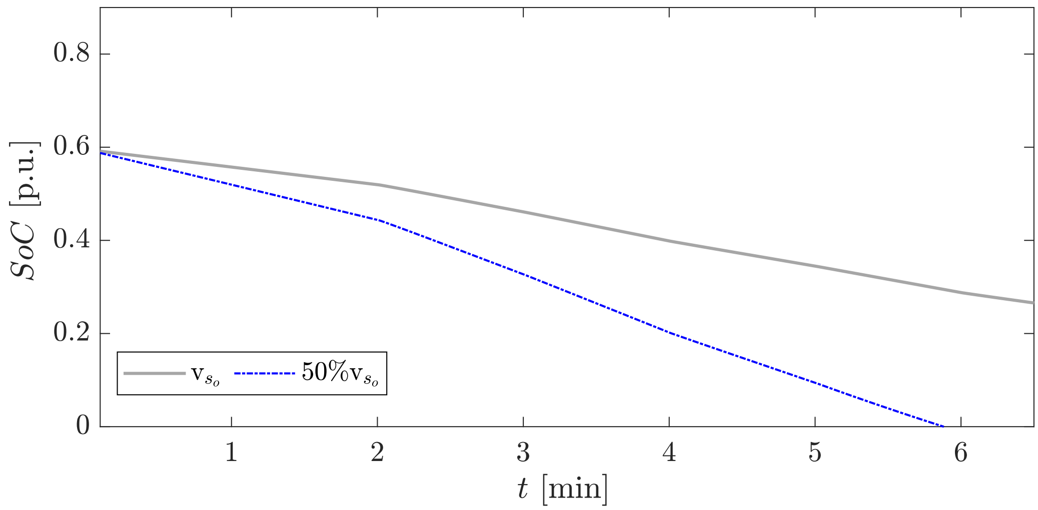

Figure 4.24: CAES SoC for Case 10.

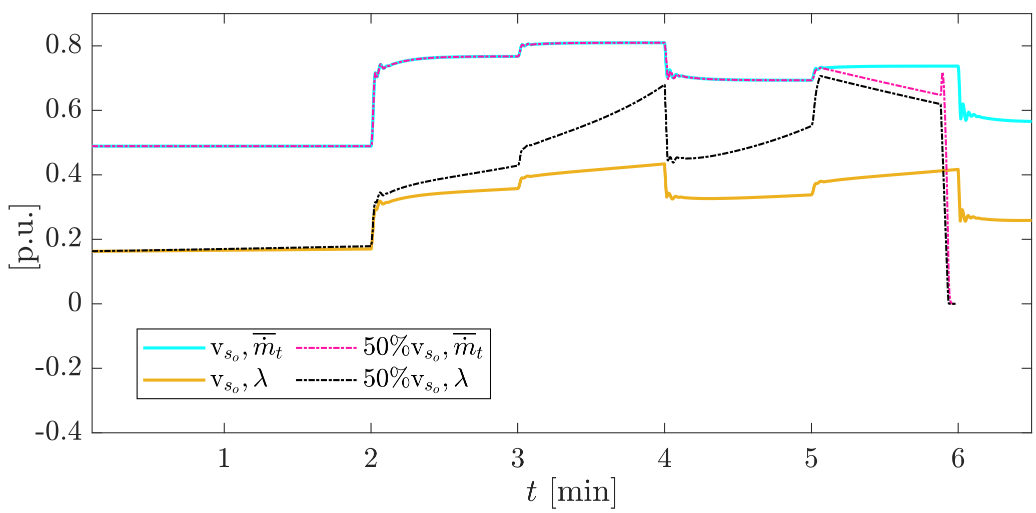

Figure 4.25: CAES turbine's air flow and valve opening for Case 10.

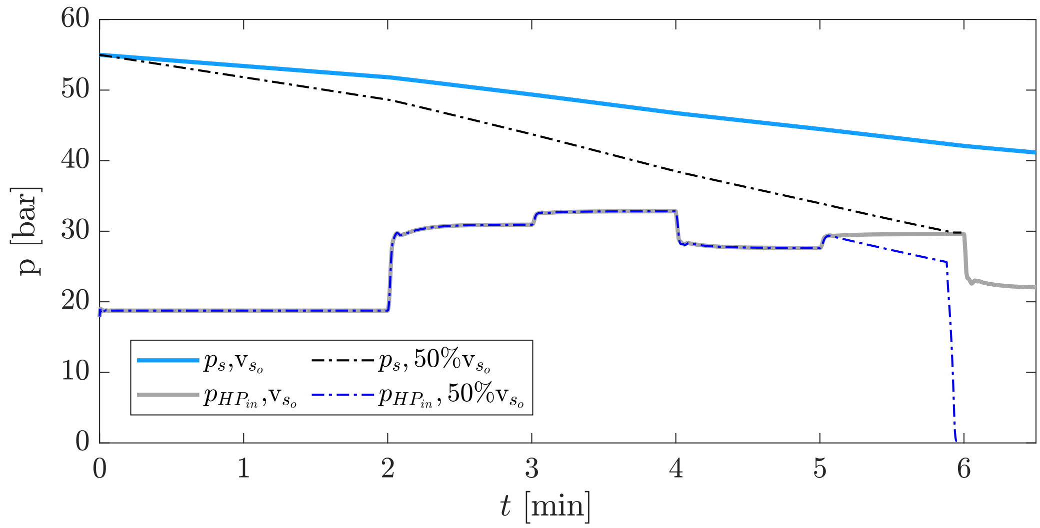

Figure 4.26: Cavern pressure for Case 10.

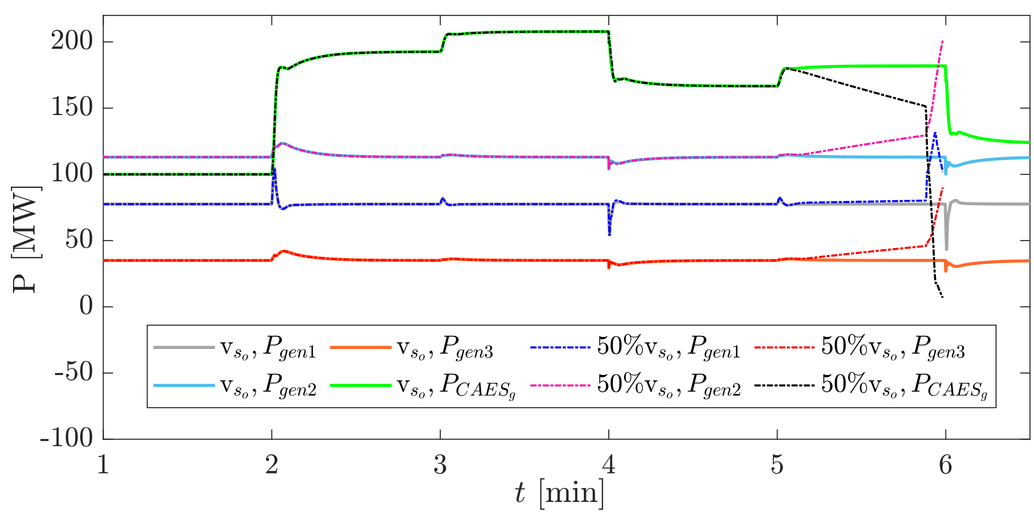

Figure 4.27: System power injections for Case 10.

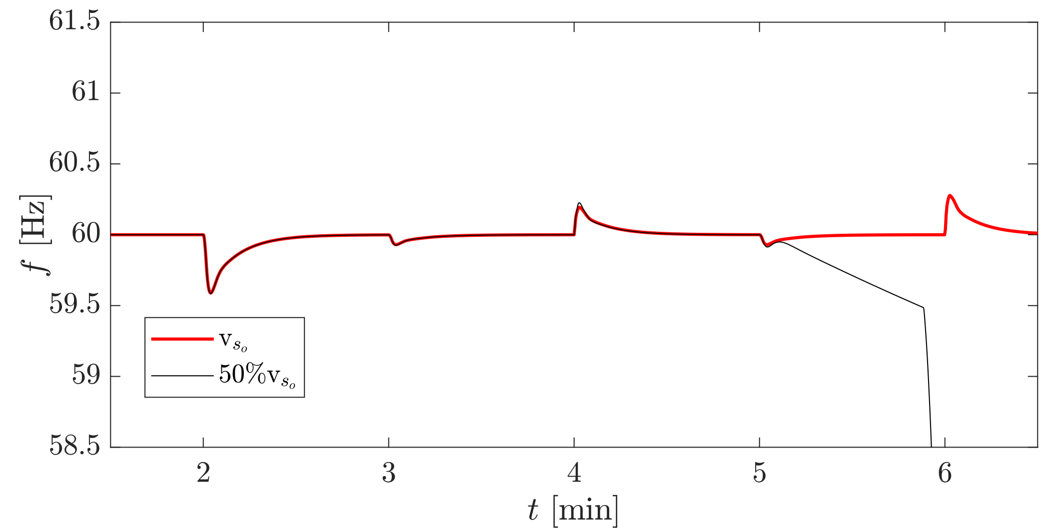

Figure 4.28: System frequency for Case 10.

In Case 11, the compressor only charges at its full power of 60 MW. The SoC and the cavern pressure are presented for this case in Figures 4.29 and 4.30, respectively. Given the relatively large load changes and the rate limits used in the hydro unit's governor, the frequency deviates more than in Case 10, as demonstrated in Figure 4.31. When the cavern volume is $50\%v_{s_o}$, the compressor is shut down at $t = 4.3$ min; however, since the compressor represents a load for the system, the hydro unit is capable of bringing the frequency back to nominal after 45 sec as shown in Figures 4.31 and 4.32. No frequency stability issues were detected in this case; however, this could be due to the small compressor size.

From this analysis, observe that if storage with large power ratings are required for regulation, systems with large energy-to-power ratings such as CAES would be preferable, as these delay the recharging times. This is clearly a disadvantage of other storage technologies such as flywheels, which are able to provide fast regulation, but for a very limited time.

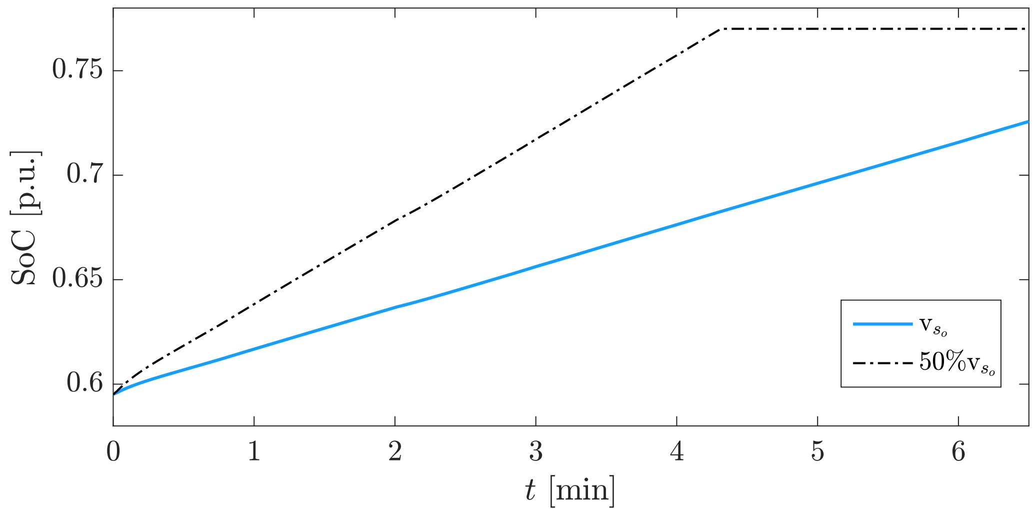

Figure 4.29: CAES SoC for Case 11

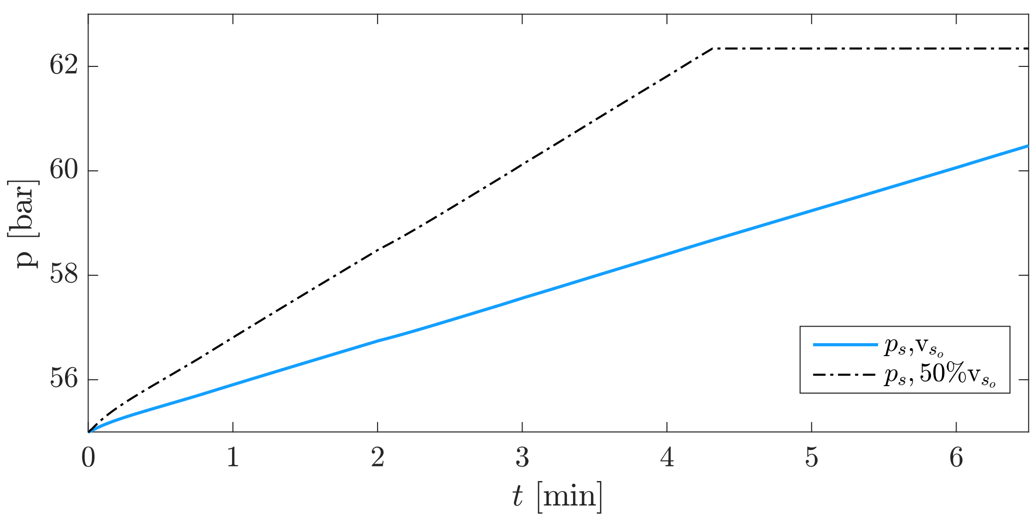

Figure 4.30: Cavern pressure for Case 11.

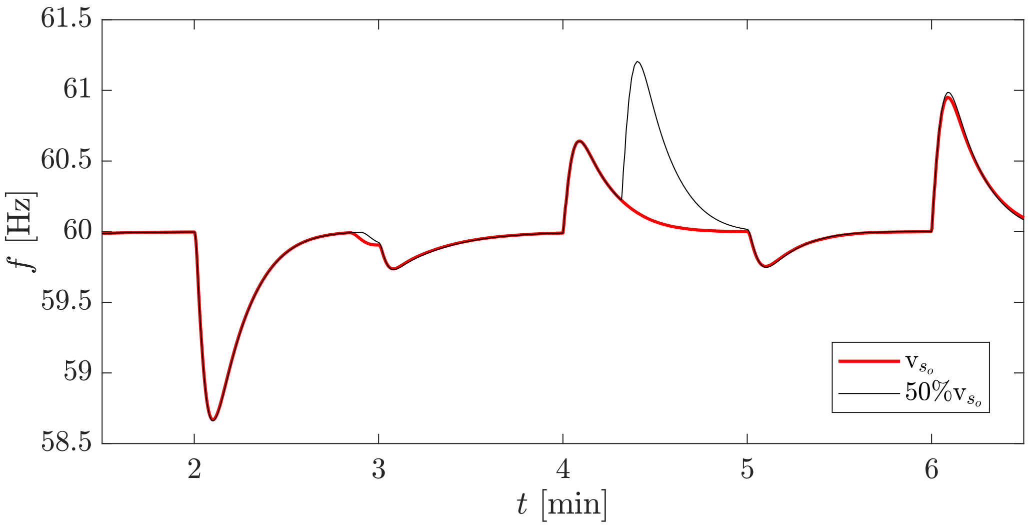

Figure 4.31: System frequency for Case 11.

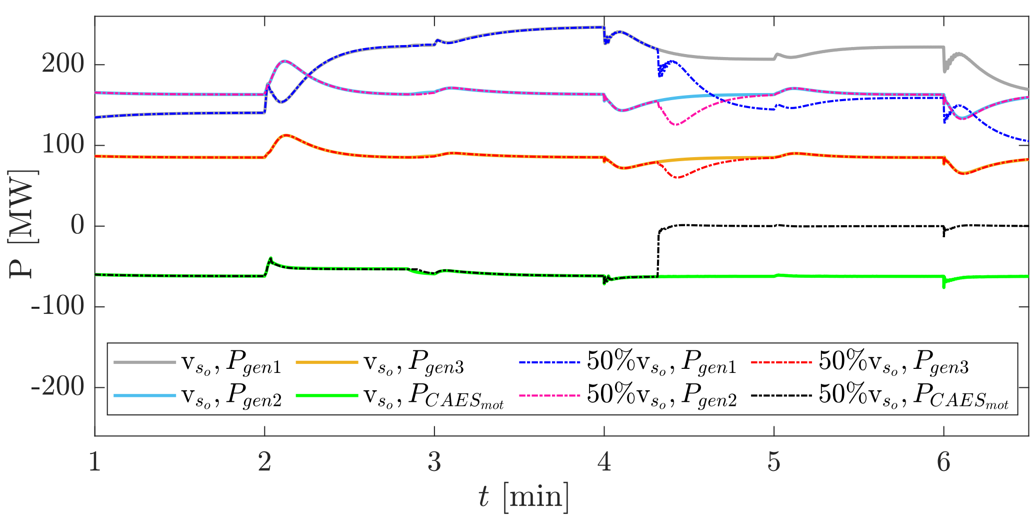

Figure 4.32: System power injections for Case 11.

4.2.5 Summary

In this Chapter, the dynamic responses of the proposed CAES models were first studied through simulations of step changes in their power references, which showed significant differences with respect to two CAES models reported in the literature, especially in the compressor. The proposed models and controls were then used to study a CAES facility connected to a power system, demonstrating that it can help improve the stability of the system, enhance the frequency and voltage regulation, and reduce low frequency oscillations, with respect to an equivalent GT plant.

Chapter 5

Conclusions

5.1 Summary and Conclusions

In this thesis, a comprehensive mathematical model of a diabatic CAES system, considering two independent synchronous machines as interface with the grid, was developed. In the first part of the thesis, detailed and simplified CAES system models and controls, suitable for power system studies, were proposed, based on the configuration of the Huntorf CAES facility in Germany [13] and the CAES system described in [9]. Physical-based models for the main CAES system components, including valves, heat exchangers, burners, expanders, compressors, electrical machines, and the cavern were investigated and independently represented as subsystems, and their interrelations were clearly established through appropriate interfaces. The CAES system detailed model comprised a single-stage LP and 3-stage HP compressors with one intercooler per stage, and an aftercooler, in the charging mode, with HP and LP expanders with burners (reheaters), a recuperator, and an air valve controlling the air flow, in the discharging mode. In the simplified model, the number of stages used to represent the compressor and expander were reduced, i.e., single-stage LP and HP compressors, and a single-stage expander were used. The cavern model was the same for the detailed and simplified models.

The mechanical subsystems were modeled as lumped elements, in order to balance the accuracy and complexity of their representation. Thermodynamic steady-state equations were used to establish the input-output relations of the three main state variables (pressure, temperature and volume) that characterize the gas (air) flowing through these subsystems. The dynamic response of the CAES systems are highly influenced by its controls, as well as the dynamics of the heat exchangers (intercoolers, aftercooler and recuperator), the air inertia in the compressor and expander, and the discharging compressor delay, which complement the thermodynamic models.

In order to address one of the main drawbacks of the existing CAES models proposed in the literature, for power system studies, compressor and turbine maps were modeled in this thesis. NN and nonlinear polynomial functions were used to represent the actual compressor maps, for which special blocks (CMB) were necessary to transform the maps' corrected variables (speed and air mass flow rate) into actual variables. Three approaches were discussed to represent the turbine maps: a fixed pressure ratio at each expansion stage, the pressure ratio as a linear function of the mass flow rate, and the pressure ratio of a compressible flow through a choked nozzle; in the last approach the cavern pressure became a variable in the HP pressure ratio. The valve that controls the air flow in the expansion was modeled as a linear valve, or as a compressible flow through a nozzle. Finally, the cavern was modeled as a constant temperature and constant volume open system, in which only the dynamics of the pressure variable were considered.

The control strategy for the CAES system was also discussed in detail. The cavern pressure was used in the SoC logic control to shut down the compressor or turbine, when the cavern was fully charged or depleted, respectively. Two independent active power controllers were used to control the CAES system power injected into the grid. These controllers regulate the air mas flow rate in the compressor and turbine, acting on the discharging air valve and the compressor's IGVs respectively. Feedback of the rotor speeds were used in these controllers to allow primary and secondary frequency regulation, while charging, discharging, or in simultaneous charging and discharging modes.

In the expansion mode, the output of the active power controller was considered to be the valve opening, which was then used to calculate the mass flow rate depending on the valve model assumed (linear, choked nozzle or unchoked nozzle). A first-order transfer function was used to represent the valve dynamics, while limits were added to account for the maximum expansion pressure determined by the cavern, and minimum mas flow rate. An additional controller was considered, to regulate the air temperature at the inlet of the expanders, aiming to increase the overall CAES efficiency.

A pressure limiter controller was proposed to prevent the compressor from operating at discharging pressures lower than the cavern pressure, thus avoiding reversal air flows from the cavern. Additionally, a surge prevention controller was proposed to represent more complex surge detection mechanisms in the compressor. This controller uses SLC blocks to detect the compressor approaching to surge, by evaluating the derivative of the pressure ratio as a function of the air flow in a given compressor map.

A droop-based reactive power controller was used to allow stable simultaneous voltage regulation through the motor and generator, while both operate synchronized to the grid in charging, discharging or idling mode. This controller allocated the reactive power needs for regulation, based on either the machines' loading (p.u. of their nominal capacity), or their unused capacity in MVAs.

The implementation of three CAES models for frequency regulation studies was discussed, two of which corresponded to the detailed and simplified models of the CAES system, while the third was a combination of the other two. Finally, a block-diagram based transient stability model of the CAES system was proposed, for which generic model architecture of the different CAES system components were developed. This model considered the synchronous machines, excitation systems, reactive power controller, and PSS in addition to the mechanical systems. As an application, the transient stability model was implemented in Powertech's TSAT®.

In the second part of the thesis, the performance of a CAES system providing frequency and voltage regulation, damping low frequency oscillations, and improving the transient stability of an electrical grid, was evaluated through simulations using the proposed models. First, the proposed and existing CAES models were compared, showing significant differences in their dynamic response, especially when the CAES system operated in discharging mode. Then, a CAES facility was simulated to provide frequency regulation for a simplified system model with high penetration of wind generation, demonstrating that the CAES system could significantly reduce the system cumulative frequency deviation, with respect to a similar scenario in which the frequency was regulated by GTs. Furthermore, the effects on the overall frequency regulation performance of incorporating more detailed models of some mechanical subsystems, such as the expansion air valve, compressors, expanders and associated controls, was assessed. Thus, a dependency of CAES system frequency regulation capability on the cavern pressure was observed, concluding that the CAES response to the frequency requirements became constrained as the cavern pressure falls below its nominal value.

Finally, the voltage regulation, oscillation damping capability, and transient and frequency stability impacts of a CAES system were studied on a modified WSCC 9-bus test system using TSAT®. Simulations showed that CAES was more effective than equivalent GTs to regulate the voltage, damp low frequency oscillations, and reduce the CCT of faults. The effect of SoC control on the frequency stability of the system for different cavern sizes were investigated, concluding that if the power rating of the CAES system was large enough, smaller cavern sizes may not allow proper provision of frequency regulation.

The following are the main conclusions from this thesis:

- It was demonstrated that the proposed detailed and simplified CAES models for charging mode, showed very similar responses to step changes in their power reference values, while more noticeable differences were observed in the discharging mode models. However, both the proposed models showed significant differences in their transient response, with respect to two CAES models reported in the literature, due to the assumptions and simplifications these make.

- Even though the deployment of a CAES facility need be justified in the energy arbitrage market, added value could be obtained in other markets, such as the ancillary service market. In particular, it was demonstrated that a CAES system can help improve the frequency and voltage regulation of a system, compared to an equivalent GT plant. Furthermore, simultaneous operation of the turbine and compressor significantly improved the frequency regulation, as evidenced in the reduction of the cumulative system frequency deviation. This is only possible in a CAES system configuration with independent generator and motor, as the one used in this thesis.

- When detailed models of the discharging air valve, compressor and turbine maps, and associated controls were used in the CAES system for frequency regulation, the CAES system operation was constrained by the cavern pressure, limiting not only the pressure ratios of compressors and expanders, but also affecting the valve opening, which reached its limits more often as the cavern depleted. However, CAES still outperformed GTs to improve the system frequency regulation, when the cavern pressure was above its nominal value.

- Although compressor surge control strategies were not addressed in detail in this thesis, the proposed simplified surge logic control allowed modeling the restrictions imposed by other more sophisticated surge controllers, limiting the air flow when approaching the surge condition.

- It was demonstrated that the CAES system improved the transient stability of the system with respect to an equivalent GT connected at the same bus, showing also that the CAES was more effective in regulating the voltage and damping the oscillations.

- It was demonstrated that if the power rating of the CAES system was large enough, small cavern sizes may not allow the provision of frequency regulation as the SoC would limit the charging and discharging capability. This is a disadvantage over traditional generators, whose operation is less constrained due to fuel availability to operate.

5.2 Contributions

The most significant contributions of this thesis can be summarized as follows:

- A new comprehensive dynamic mathematical model of a diabatic CAES system was proposed, which considers two independent synchronous machines as interface with the grid, and comprises electrical subsystems, mechanical subsystems, and controls. Considering two independent machines allowed simultaneous charging and discharging of the cavern.

- A novel active power control strategy was proposed for the CAES system, which included:

  - SoC control logic, based on the cavern pressure and used to shut down the compressor and the turbine when the cavern is fully charged or discharged, respectively.
  - Pressure limiter controllers to force the HP compressor's discharging pressure to be larger, and the inlet pressure at the HP expander to be lower than the cavern pressure.
  - A practical surge detection controller for the compressor.
  - Active power controllers that allow the CAES system to provide primary and secondary frequency regulation when operating in charging and discharging mode.

- New special reactive power controllers for the CAES motor and generator were proposed, which operate synchronized with the grid at all times. These proportional controllers coordinated the reactive power share between the generator and motor, thus preventing one machine from supplying the reactive power needs of the other, while also improving their loading based on the CAES active and reactive power injections and the machines' capability curves.

- A novel model architecture was proposed for the implementation of the CAES model for transient stability studies, which defines the main subsystem blocks, and interfaces between the control systems, electrical systems and mechanical systems, and information flow between subsystems. The modularity of the proposed architecture simplifies the implementation, maintenance, and update of the CAES system components and controls.

- A novel CAES model for transient stability studies was proposed, which considers a multi-stage compressor and turbine, and the cavern. In this model, the nonlinearities resulting from compressor and turbine maps are represented, and special controls are used to prevent the violation of limits imposed by these maps, and the cavern pressure. This model was implemented as a fully parametrizable UDM model in TSAT® which can be readily used by utilities and system operators.

- For the first time, detailed studies have been undertaken to examine the impact of the CAES system on transient and frequency stability, and oscillation damping and voltage regulation performance, considering a benchmark system.

- A new study was presented to understand the potential of CAES systems to provide frequency regulation when operating in charging, discharging and simultaneous charging/discharging modes. A complementary analysis of the effects of modeling compressor and turbine maps, and associated controls, on the CAES system frequency regulation capability, was also presented.

5.3 Future Work

Based on the work presented in this thesis, the following issues may be undertaken in future research:

- Study the small-perturbation stability of the proposed models.

- Even though the proposed CAES system models were indirectly validated by comparing them with GTs, validation using real data from existing CAES facilities, is still a challenge that needs to be addressed.

- Study a CAES facility connected to a realistic system, such as the Ontario's electrical grid, to examine the potential of large ESS systems to improve the electrical grid conditions. This will allow to analyze the benefits of connecting a large CAES facility, at sites where the potential for building salt caverns has been identified in Ontario, or where repurposed caverns exist.

- The models proposed in this thesis assumed constant efficiencies in compressors and turbines. More accurate representations of these efficiencies, which are a function of the mass flow rate and rotor speed, could improve the model accuracy.

References

[1] P. F. Ribeiro, B. K. Johnson, M. L. Crow, A. Arsoy, and Y. Liu, "Energy storage systems for advanced power applications," *Proceedings of the IEEE*, vol. 89, no. 12, pp. 1744–1756, 2001.

[2] R. Carnegie, D. Gotham, D. Nderitu, and P. V. Preckel, "Utility scale energy storage systems, benefits, application, and technologies," State Utility Forecasting Group, June 2013. [Online]. Available: https://www.purdue.edu/discoverypark/sufg/docs/publications/SUFG%20Energy%20Storage%20Report.pdf

[3] J. Deboever and S. Grijalva, "Optimal scheduling of large-scale price-maker energy storage," in *IEEE Power and Energy Conference at Illinois (PECI)*, Urbana, IL, February 2016, pp. 1–6.

[4] B. Cleary, A. Duffy, A. O'Connor, M. Conlon, and V. Fthenakis, "Assessing the economic benefits of compressed air energy storage for mitigating wind curtailment," *IEEE Transactions on Sustainable Energy*, vol. 6, no. 3, pp. 1021–1028, 2015.

[5] V. A. Boicea, "Energy storage technologies: The past and the present," *Proceedings of the IEEE*, vol. 102, no. 11, pp. 1777–1794, 2014.

[6] "EPRI-DOE handbook of energy storage for transmission & distribution applications," Technical report, EPRI and U.S. Department of Energy, Palo Alto, CA, and Washington, DC, 2003.

[7] "Energy storage," Technical report, Ontario Independent System Operator, 2016. [Online]. Available: http://www.ieso.ca/Documents/Energy-Storage/IESO-Energy-Storage-Report_March-2016.pdf

[8] "Goderich A-CAES facility," Hydrostor, 2020. [Online]. Available: https://www.hydrostor.ca/goderich-a-caes-facility/

[9] "SMARTCAES Compressed Air Energy Storage Solutions," Brochure, DRESSER-RAND, 2015. [Online]. Available: https://www.all-energy.co.uk/__novadocuments/458993?v=636573965454930000

[10] J. Konrad, R. Carriveau, M. Davison, F. Simpson, and D. S.-K. Ting, "Geological compressed air energy storage as an enabling technology for renewable energy in ontario, canada," *International Journal of Environmental Studies*, vol. 69, no. 2, pp. 350–359, 2012.

[11] J. Simmons, A. Barnhart, S. Reynolds, and S. Young-Jun, "Study of compressed air energy storage with grid and photovoltaic energy generation," Technical report, The Arizona Research Institute for Solar Energy (AzRISE)-APS, 2010. [Online]. Available: http://u.arizona.edu/~sreynold/caes.pdf

[12] S. Succar and R. H. Williams, "Compressed air energy storage: theory, resources, and applications for wind power," Technical report, Princeton Environmental Institute, 2008. [Online]. Available: https://acee.princeton.edu/wp-content/uploads/2016/10/SuccarWilliams_PEI_CAES_2008April8.pdf

[13] "Huntorf air storage gas turbine power plant," Technical report No. D GK 90 202 E, Brown Boveri (BBC), Germany, 1979.

[14] "Bethel energy center," Apex, 2020. [Online]. Available: http://www.apexcaes.com/

[15] P. Zhao, L. Gao, J. Wang, and Y. Dai, "Energy efficiency analysis and off-design analysis of two different discharge modes for compressed air energy storage system using axial turbines," *Renewable Energy*, vol. 85, pp. 1164–1177, 2016.

[16] P. Pourbeik, "Simple model specification for battery energy storage system," Technical report, EPRI, 2015.

[17] "TSAT user manual," Manual, Powertech Labs Inc., British Columbia, Canada, 2011.

[18] N. Hartmann, O. Vöhringer, C. Kruck, and L. Eltrop, "Simulation and analysis of different adiabatic compressed air energy storage plant configurations," *Applied Energy*, vol. 93, pp. 541–548, 2012.

[19] Y. Mazloum, H. Sayah, and M. Nemer, "Static and dynamic modeling comparison of an adiabatic compressed air energy storage system," *Journal of Energy Resources Technology*, vol. 138, no. 6, p. 062001, 2016.

[20] W. He, X. Luo, D. Evans, J. Busby, S. Garvey, D. Parkes, and J. Wang, "Exergy storage of compressed air in cavern and cavern volume estimation of the large-scale compressed air energy storage system," *Applied Energy*, vol. 208, pp. 745–757, 2017.

[21] R. Kushnir, A. Ullmann, and A. Dayan, "Thermodynamic models for the temperature and pressure variations within adiabatic caverns of compressed air energy storage plants," *Journal of Energy Resources Technology*, vol. 134, no. 2, p. 021901, 2012.

[22] M. Raju and S. K. Khaitan, "Modeling and simulation of compressed air storage in caverns: a case study of the huntorf plant," *Applied Energy*, vol. 89, no. 1, pp. 474–481, 2012.

[23] W. Liu, G. Xu, L. Meng, and Y.-p. Yang, "Thermo-dynamical analysis on electricity-generation subsystem of CAES power plant," in *Asia-Pacific Power and Energy Engineering Conference (APPEEC)*, Shanghai, China, March 2012, pp. 1–4.

[24] T. Xia, L. He, N. An, M. Li, and X. Li, "Electromechanical transient modeling research of energy storage system based on power system security and stability analysis," in *IEEE International Conference on Power System Technology (POWERCON)*, Chengdu, China, October 2014, pp. 221–226.

[25] L. He, T. Xia, F. Tian, and N. An, "Modeling and simulation of compressed air energy storage (CAES) system for electromechanical transient analysis of power system," *Advanced Materials Research*, vol. 860, pp. 2486–2494, 2014.

[26] I. Kandiloros and C. Vournas, "Use of air chamber in gas-turbine units for frequency control and energy storage in a system with high wind penetration," in *IEEE PES Innovative Smart Grid Technology Conference Europe (ISGT-Europe)*, Istanbul, Turkey, October 2014, pp. 1–6.

[27] Y. Takagi, A. Minami, and K. Sakamoto, "A dynamic simulator of adiabatic compressed air energy storage (A-CAES) plant heat medium control simulations," in *11th Asian Control Conference (ASCC)*, Gold Coast, Australia, December 2017, pp. 2188–2193.

[28] M. V. Dahraie, H. Najafi, R. N. Azizkandi, and M. Nezamdoust, "Study on compressed air energy storage coupled with a wind farm," in *IEEE 2nd Iranian Conference on Renewable Energy and Distributed Generation (ICREDG)*, Tehran, Iran, March 2012, pp. 147–152.

[29] V. Vongmanee, “The renewable energy applications for uninterruptible power supply based on compressed air energy storage system,” in *IEEE Symposium on Industrial Electronics Applications*, Seoul, South Korea, July 2009, pp. 827–830.

[30] A. Ortega and F. Milano, “Generalized model of VSC-based energy storage systems for transient stability analysis,” *IEEE Transactions on Power Systems*, vol. 31, no. 5, pp. 3369–3380, 2016.

[31] V. Vongmanee and V. Monyakul, “A modeling of self excited induction generators driven by compressed air energy based on field oriented control principle,” in *IEEE 2nd International Power and Energy Conference*, Johor Bahru, Malaysia, December 2008, pp. 834–838.

[32] N. Hasan, M. Y. Hassan, M. S. Majid, and H. A. Rahman, “Mathematical model of compressed air energy storage in smoothing 2MW wind turbine,” in *IEEE International Power Engineering and Optimization Conference (PEDCO)*, Melaka, Malaysia, June 2012, pp. 339–343.

[33] M. Martinez, M. G. Molina, F. Frack, and P. E. Mercado, “Dynamic modeling, simulation and control of hybrid energy storage system based on compressed air and supercapacitors,” *IEEE Latin America Transactions*, vol. 11, no. 1, pp. 466–472, 2013.

[34] M. Martínez, M. Molina, and P. Mercado, “Dynamic performance of compressed air energy storage (CAES) plant for applications in power systems,” in *IEEE-PES Transmission and Distribution Conference and Exposition: Latin America (T&D-LA)*, Sao Paulo, Brazil, June 2010, pp. 496–503.

[35] Z. Xiaoshu and Z. Hong, “Switched reluctance motor/generator simulation research based on compressed air energy storage system,” in *International Conference on Advanced Mechatronic Systems (ICAMechS)*, Beijing, China, August 2015, pp. 479–484.

[36] Q. Yu and M. Cai, “The process of compressed air energy storage (CAES) analysis,” in *International Conference on Materials for Renewable Energy and Environment (ICMREE)*, Chengdu, China, 2013, pp. 923–925.

[37] F. . Pai, “An improved utility interface for microturbine generation system with stand-alone operation capabilities,” *IEEE Transactions on Industrial Electronics*, vol. 53, no. 5, pp. 1529–1537, Oct 2006.

[38] J. Liu, Y. Miura, and T. Ise, "Comparison of dynamic characteristics between virtual synchronous generator and droop control in inverter-based distributed generators," *IEEE Transactions on Power Electronics*, vol. 31, no. 5, pp. 3600–3611, May 2016.

[39] P. Hasanpor Divshali, S. H. Hosseinian, and M. Abedi, "A novel multi-stage fuel cost minimization in a VSC-based microgrid considering stability, frequency, and voltage constraints," *IEEE Transactions on Power Systems*, vol. 28, no. 2, pp. 931–939, May 2013.

[40] E. Rademaker, "Scaling of compressor and turbine maps on basis of equal flow mach numbers and static flow parameters," Technical report, National Aerospace Laboratory NLR, Amsterdam, The Netherlands, 2012.

[41] C. Krupke, J. Wang, J. Clarke, and X. Luo, "Modeling and experimental study of a wind turbine system in hybrid connection with compressed air energy storage," *IEEE Transactions on Energy Conversion*, vol. 32, no. 1, pp. 137–145, 2017.

[42] Y. Mazloum, H. Sayah, and M. Nemer, "Dynamic modeling and simulation of an isobaric adiabatic compressed air energy storage (IA-CAES) system," *Journal of Energy Storage*, vol. 11, pp. 178–190, 2017.

[43] J. Kim, T. Song, T. Kim, and S. Ro, "Model development and simulation of transient behavior of heavy duty gas turbines," *Journal of Engineering for Gas Turbines and Power*, vol. 123, no. 3, pp. 589–594, 2001.

[44] A. Darwish and R. F. Boehm, "Compressed air energy storage flow and power analysis," in *ASME 5th International Conference on Energy Sustainability*, Washington DC, August 2011, pp. 1407–1415.

[45] J. Gonzalez, "Modelling axial turbomachinery for compressed air energy storage," Master's thesis, University of Waterloo, 2018.

[46] S. A. Kakodkar, "Extensible modeling of compressed air energy storage systems," Master's thesis, University of Waterloo, 2018.

[47] H. T. Le and S. Santoso, "Increasing wind farm transient stability by dynamic reactive compensation: Synchronous-machine-based ESS versus SVC," in *Proceedings of the IEEE-PES General Meeting*, Minneapolis, MN, July 2010, pp. 1–8.

[48] ——, "Operating compressed-air energy storage as dynamic reactive compensator for stabilising wind farms under grid fault conditions," *IET Renewable Power Generation*, vol. 7, no. 6, pp. 717–726, 2013.

[49] J. Wang, J. Wang, and R. McMahon, "Dynamic power system modeling for the integration of energy storage," in *IECON 44th Annual Conference of the IEEE Industrial Electronics Society*, Washington DC, October 2018, pp. 1765–1770.

[50] S. Rampurkar, K. Sandhu, and R. Kumar, "Performance of parallel connected compressed air energy storage for proper utilization of wind energy," in *International Conference on Advances in Mechanical, Industrial, Automation and Management Systems (AMIAMS)*, Allahabad, India, February 2017, pp. 285–290.

[51] S. Vazquez, S. M. Lukic, E. Galvan, L. G. Franquelo, and J. M. Carrasco, "Energy storage systems for transport and grid applications," *IEEE Transactions on Industrial Electronics*, vol. 57, no. 12, pp. 3881–3895, 2010.

[52] R. B. Schainker and M. Nakhamkin, "Compressed-air energy storage (CAES): Overview, performance and cost data for 25MW to 220MW plants," *IEEE Transactions on Power Apparatus and Systems*, no. 4, pp. 790–795, 1985.

[53] T. Das, V. Krishnan, Y. Gu, and J. D. McCalley, "Compressed air energy storage: State space modeling and performance analysis," in *Proceedings of the IEEE-PES General Meeting*, Detroit, MI, July 2011, pp. 1–8.

[54] D. T. Bradshaw, "Pumped hydroelectric storage (PHS) and compressed air energy storage (CAES)," in *IEEE Power Engineering Society Summer Meeting*, Seattle, WA, July 2000, pp. 1551–1573.

[55] K. Allen, "CAES: The underground portion," *IEEE Transactions on Power Apparatus and Systems*, vol. PAS-104, no. 4, pp. 809–812, July 1985.

[56] B. J. Davidson, I. Glendenning, R. D. Harman, A. B. Hart, B. J. Maddock, R. D. Moffitt, V. G. Newman, T. F. Smith, P. J. Worthington, and J. K. Wright, "Large-scale electrical energy storage," *IEE Proceedings A - Physical Science, Measurement and Instrumentation, Management and Education - Reviews*, vol. 127, no. 6, pp. 345–385, 1980.

[57] V. Tola, V. Meloni, F. Spadaccini, and G. Cau, "Performance assessment of adiabatic compressed air energy storage (A-CAES) power plants integrated with packed-bed thermocline storage systems," *Energy Conversion and Management*, vol. 151, pp. 343–356, 2017.

[58] X. Zhang, Y. Xu, X. Zhou, Y. Zhang, W. Li, Z. Zuo, H. Guo, Y. Huang, and H. Chen, "A near-isothermal expander for isothermal compressed air energy storage system," *Applied energy*, vol. 225, pp. 955–964, 2018.

[59] M. Heidari, M. Mortazavi, and A. Rufer, "Design, modeling and experimental validation of a novel finned reciprocating compressor for isothermal compressed air energy storage applications," *Energy*, vol. 140, pp. 1252–1266, 2017.

[60] "Isothermal compressed air energy storage," Brochure, U.S Department of Energy, 2012. [Online]. Available: https://www.energy.gov/sites/prod/files/SustainX.pdf

[61] P. Kundur, N. Balu, and M. Lauby, *Power system stability and control*. NY: McGraw-hill, 1994.

[62] P. M. Anderson and A. A. Fouad, *Power system control and stability*. NJ: John Wiley & Sons, 2008.

[63] A. Gomez-Exposito, A. J. Conejo, and C. Canizares, *Electric energy systems: analysis and operation*. Boca Raton, FL, USA: CRC Press, 2016.

[64] X. Li, C. Yang, Y. Wang, and H. Wang, "A prediction model of compressor with variable-geometry diffuser based on elliptic equation and partial least squares," *Royal Society Open Science*, vol. 5, no. 1, p. 171468, 2018.

[65] W. I. Rowen, "Simplified mathematical representations of heavy-duty gas turbines," *Journal of Engineering for Power*, vol. 105, no. 4, pp. 865–869, 1983.

[66] F. De Mello and D. Ahner, "Dynamic models for combined cycle plants in power system studies," *IEEE Transactions on Power Systems*, vol. 9, no. 3, pp. 1698–1708, August 1994.

[67] L. Pereira, J. Undrill, D. Kosterev, D. Davies, and S. Patterson, "New thermal turbine governor modeling for the WECC," Technical report, WECC Modeling & Validation Work Group, 2002.

[68] Z. Baba *et al.*, "Modeling of gas turbines and steam turbines in combined cycle power plants," Technical report, CIGRE Task Force, 2003.

[69] M. Nagpal, A. Moshref, G. K. Morison, and P. Kundur, "Experience with testing and modeling of gas turbines," in *IEEE-PES Winter Meeting*, Columbus, OH, January 2001, pp. 652–656.

[70] K. Kunitomi, A. Kurita, H. Okamoto, Y. Tada, S. Ihara, P. Pourbeik, W. W. Price, A. B. Leirbukt, and J. J. Sanchez-Gasca, "Modeling frequency dependency of gas turbine output," in *IEEE-PES Winter Meeting*, Columbus, OH, January 2001, pp. 678–683.

[71] E. M. Greitzer, "Surge and rotating stall in axial flow compressorspart i: Theoretical compression system model," *Journal of Engineering for Power*, vol. 98, no. 2, pp. 190–198, 1976.

[72] ——, "Surge and rotating stall in axial flow compressorspart ii: experimental results and comparison with theory," *Journal of Engineering for Power*, vol. 98, no. 2, pp. 199–211, 1976.

[73] F. Milano, *Power system modelling and scripting.* Springer Science & Business Media, 2010.

[74] Y. Cengel and M. Boles, *Thermodynamics: An Engineering Approach.* 8th ed., NY: McGraw-hill, 2002.

[75] T. L. Bergman and F. P. Incropera, *Fundamentals of heat and mass transfer.* 6th ed., NY: John Wiley & Sons, 2007.

[76] S. Camporeale, B. Fortunato, and A. Dumas, "Dynamic modeling and control of regenerative gas turbines," in *ASME International Gas Turbine and Aero-engine Congress and Exhibition*, Stockholm, Sweden, June 1998, pp. V005T15A019–V005T15A019.

[77] H. A. d. S. Mattos, C. Bringhenti, D. F. Cavalca, O. F. R. Silva, G. B. d. Campos, and J. T. Tomita, "Combined cycle performance evaluation and dynamic response simulation," *Journal of Aerospace Technology and Management*, vol. 8, no. 4, pp. 491–497, 2016.

[78] R. Kurz, K. Brun *et al.*, "Gas turbine performance-what makes the map?" in *Proceedings of the 29th Turbomachinery Symposium*, Houston, TX, September 2000.

[79] P. Carlsson, "Flow through a throttle body: A comparative study of heat transfer, wall surface roughness and discharge coefficient," Technical report, Institutionen för ekonomisk och industriell utveckling, 2007.

[80] F. T. Brown, *Engineering system dynamics: a unified graph-centered approach.* CRC Press, 2006.

[81] W. Fuls, "Enhancement to the traditional ellipse law for more accurate modeling of a turbine with a finite number of stages," *Journal of Engineering for Gas Turbines and Power*, vol. 139, no. 11, p. 112603, 2017.

[82] F. K. Moore and E. M. Greitzer, "A theory of post-stall transients in axial compression systems: Part I development of equations," *Journal of Engineering for Gas Turbines and Power*, vol. 108, no. 1, pp. 68–76, 1986.

[83] R. L. Behnken, "Nonlinear control and modeling of rotating stall in an axial flow compressor," Technical report, California Institute of Technology, Pasadena, CA, 1997.

[84] C. H. J. Meuleman, "Measurement and unsteady flow modelling of centrifugal compressor surge," Technical report, Technische Universiteit Eindhoven, 2002.

[85] P. Vadasz and D. Weiner, "The optimal intercooling of compressors by a finite number of intercoolers," *Journal of Energy Resources Technology*, vol. 114, no. 3, pp. 255–260, 1992.

[86] J. Duhan, "Compressed air energy storage in salt caverns: Geomechanical design workflow, CAES siting study from a geomechanics perspective, and deep brine disposal," Master's thesis, University of Waterloo, 2018.

[87] N. Kakimoto and K. Baba, "Performance of gas turbine-based plants during frequency drops," *IEEE Transactions on Power Systems*, vol. 18, no. 3, pp. 1110–1115, 2003.

[88] M. Cimino and P. R. Pagilla, "Reactive power control for multiple synchronous generators connected in parallel," *IEEE Transaction on Power Systems*, vol. 31, no. 6, pp. 4371–4378, 2016.

[89] "Simulink," MathWorks, 2020. [Online]. Available: https://www.mathworks.com/products/simulink.html

[90] "PSAT user manual," Manual, Powertech Labs Inc., British Columbia, Canada, 2011.

[91] E. Macchi and G. Lozza, "A study of thermodynamic performance of CAES plants, including unsteady effects," in *ASME International Gas Turbine Conference and Exhibition*, Anaheim, CA, June 1987, pp. V004T10A008–V004T10A008.

[92] T. Schobeiri and H. Haselbacher, "Transient analysis of gas turbine power plants, using the Huntorf compressed air storage plant as an example," in *ASME International Gas Turbine Conference and Exhibit*, Baden, Switzerland, 1985, pp. V003T10A015–V003T10A015.

[93] W. Liu, L. Liu, L. Zhou, J. Huang, Y. Zhang, G. Xu, and Y. Yang, "Analysis and optimization of a compressed air energy storage combined cycle system," *Entropy*, vol. 16, no. 6, pp. 3103–3120, 2014.

[94] N. Zhao, X. Wen, and S. Li, "Dynamic time-delay characteristics and structural optimization design of marine gas turbine intercooler," *Mathematical Problems in Engineering*, vol. 2014, 2014.

[95] J. Slootweg, S. De Haan, H. Polinder, and W. Kling, "General model for representing variable speed wind turbines in power system dynamics simulations," *IEEE Transactions on Power Systems*, vol. 18, no. 1, pp. 144–151, 2003.

[96] J. Dang, J. Seuss, L. Suneja, and R. G. Harley, "SoC feedback control for wind and ESS hybrid power system frequency regulation," *IEEE Journal of Emerging and Selected Topics in Power Electronics*, vol. 2, no. 1, pp. 79–86, 2014.

[97] "Market manual 7: System operations part 7.1: IESO controlled grid operating procedures," Ontario's Independent Electricity System Operator, 2017. [Online]. Available: www.ieso.ca/rules/-/media/ccdae55168cc4ae8a4b73894ba305ebe.ashx

[98] T. Hiyama, "Rule-based stabilizer for multi-machine power system," *IEEE Transactions on Power Systems*, vol. 5, no. 2, pp. 403–411, May 1990.

[99] F. DeMello, "Dynamic-models for fossil fueled steam units in power-system studies," *IEEE Transactions on Power Systems*, vol. 6, no. 2, pp. 753–761, May 1991.

[100] J. Liang and R. G. Harley, "Pumped storage hydro-plant models for system transient and long-term dynamic studies," in *Proceedings of the IEEE-PES General Meeting*, Minneapolis, MN, July 2010, pp. 1–8.

APPENDICES

Appendix A

Nonlinear Compressor Map

The pressure rise Ψ_c in an axial compressor can be represented as a function of the dimensionless mass flow ϕ_c and rotor speed N in rpm, by the following polynomial function [83, 84]:

$$\Psi_c(\phi_c) = (C_{o3}N^2 + C_{o2}N + C_{o1}) + (C_{13}N^2 + C_{12}N + C_{11})\phi_c^2 + (C_{23}N^2 + C_{22}N + C_{21})\phi_c^3 \tag{A.1}$$

where $\Psi_c(\phi_c)$ and ϕ_c are defined as follows [84]:

$$\Psi_c = \frac{\Delta p_c}{\frac{1}{2}\rho\vartheta_t^2} \tag{A.2}$$

$$\phi_c = \frac{\dot{m}_c}{\rho A \vartheta_t} \tag{A.3}$$

Here, Δp_c is the pressure drop across the compressor; ϑ_t is the compressor's impeller tip speed; A is the equivalent cross sectional area of the compressor; ρ is the air density; and $\dot{m}_c$ is the air mass flow rate through the compressor. The pressure drop Δp_c can be expressed as a function of the pressure ratio π_c and compressor's inlet pressure $p_{c_{in}}$, as follows:

$$\Delta p_c = \pi_c p_{c_{in}} - p_{c_{in}} \tag{A.4}$$

The impeller tip speed can be calculated as a function of the angular speed in rpm, as follows:

$$\vartheta_t = \omega_c \frac{d}{2} = \frac{\pi d N}{60} \tag{A.5}$$

where d is the impeller blade length, in m. Notice that π in (A.5) is not the compressor pressure ratio π_c, but the numerical value 3.1416.

Substituting (A.2)-(A.5) in (A.1):

$$\begin{aligned}\pi_c p_{c_{in}} - p_{c_{in}} = \frac{\rho}{2}\left(\frac{\pi d N}{60}\right)^2 &\left(C_{o3}N^2 + C_{o2}N + C_{o1}\right) \\ &+ \frac{\rho}{2}\left(\frac{\dot{m}_c}{\rho A}\right)^2\left(C_{13}N^2 + C_{12}N + C_{11}\right) \\ &\qquad + \frac{30\rho}{\pi d N}\left(\frac{\dot{m}_c}{\rho A}\right)^3\left(C_{23}N^2 + C_{22}N + C_{21}\right)\end{aligned} \tag{A.6}$$

Expanding (A.6):

$$\begin{aligned}\pi_c p_{c_{in}} - p_{c_{in}} = &\left(\frac{\rho\pi^2 d^2 C_{o1}}{7200}\right)N^2 + \left(\frac{\rho\pi^2 d^2 C_{o3}}{7200}\right)N^4 + \left(\frac{\rho\pi^2 d^2 C_{o2}}{7200}\right)N^3 \\ &+ \left(\frac{C_{11}}{2\rho A^2}\right)\dot{m}_c^2 + \left(\frac{C_{12}}{2\rho A^2}\right)N\dot{m}_c^2 + \left(\frac{C_{13}}{2\rho A^2}\right)N^2\dot{m}_c^2 \\ &+ \left(\frac{30C_{21}}{\pi d\rho^2 A^3}\right)\frac{\dot{m}_c^3}{N} + \left(\frac{30C_{22}}{\pi d\rho^2 A^3}\right)\dot{m}_c^3 + \left(\frac{30C_{23}}{\pi d\rho^2 A^3}\right)\dot{m}_c^3 N\end{aligned} \tag{A.7}$$

By assuming sea level conditions at the compressor inlet ($p_{c_{in}} = p_{am}$ and $T_{c_{in}} = T_{am}$), the mass flow rate $\dot{m}_c$ and rotor speed N can be replaced by their corresponding corrected values in (A.7). Solving (A.7) for π_c:

$$\begin{aligned}\pi_c = 1 &+ \left(\frac{\rho\pi^2 d^2 C_{o1}}{7200 p_{am}}\right)N_{crr}^2 + \left(\frac{\rho\pi^2 d^2 C_{o3}}{7200 p_{am}}\right)N_{crr}^4 + \left(\frac{\rho\pi^2 d^2 C_{o2}}{7200 p_{am}}\right)N_{crr}^3 \\ &+ \left(\frac{C_{11}}{2\rho A^2 p_{am}}\right)\dot{m}_{crr}^2 + \left(\frac{C_{12}}{2\rho A^2 p_{am}}\right)N_{crr}\dot{m}_{crr}^2 + \left(\frac{C_{13}}{2\rho A^2 p_{am}}\right)N_{crr}^2\dot{m}_{crr}^2 \\ &+ \left(\frac{30C_{21}}{\pi d\rho^2 A^3 p_{am}}\right)\frac{\dot{m}_{crr}^3}{N_{crr}} + \left(\frac{30C_{22}}{\pi d\rho^2 A^3 p_{am}}\right)\dot{m}_{crr}^3 + \left(\frac{30C_{23}}{\pi d\rho^2 A^3 p_{am}}\right)N_{crr}\dot{m}_{crr}^3\end{aligned} \tag{A.8}$$

The coefficients of the polynomial in (A.8) are parameters; hence, these can be replaced by constants as follows:

$$\pi_c = 1 + b_0 N_{crr}^2 + b_1 N_{crr}^4 + b_2 N_{crr}^3 + b_3 \dot{m}_{crr}^2 \\ + b_4 N_{crr} \dot{m}_{crr}^2 + b_5 N_{crr}^2 \dot{m}_{crr}^2 + b_6 \frac{\dot{m}_{crr}^3}{N_{crr}} + b_7 \dot{m}_{crr}^3 + b_8 N_{crr} \dot{m}_{crr}^3 \quad \text{(A.9)}$$

Appendix B

CAES Parameters for LFC Studies

Table B.1: System parameters

Parameter	Value	Parameter	Value	Parameter	Value
P_{GTo}[MW]	213.4	P_{ST1o}[MW]	200	P_{ST2o}[MW]	200
P_{wo}[MW]	200	H_{GT}[s]	18.5	H_{ST1}[s]	3.17
H_{ST2}[s]	3.17	H_w[s]	3	K_{AGC_1}[p.u.]	20

Table B.2: CAES cavern parameters

Parameter	Value	Parameter	Value	Parameter	Value
$p_{s_{\max}}$[bar]	72	v_s[m^3]	$300,000$	T_s[K]	323.15
R[J/kg.K]	287.058				

Table B.3: CAES detailed model (Model 1) parameters

Discharging mode					
Parameter	Value	Parameter	Value	Parameter	Value
$T_{d_{HPo}}$[K]	823.15	$T_{d_{LPo}}$[K]	1098.2	$T_{x_{HPo}}$[K]	612.15
$T_{x_{LPo}}$[K]	668.15	$\pi_{t_{HPo}}$	3.818	$\pi_{t_{LPo}}$	10.856
$\eta_{t_{HPm}}$[p.u.]	0.99	$\eta_{t_{LPm}}$[p.u.]	0.99	$\eta_{t_{HPi}}$[p.u.]	0.8065
$\eta_{t_{LPi}}$[p.u.]	0.7926	T_{b_o}[K]	599.15	ϵ_r[p.u.]	0.80
c_p[kJ/kg.K]	1.055	$P_{t_{mo}}$[MW]	280	γ	1.4
$\dot{m}_{t_o}$[kg/s]	417	$\dot{m}_{f_o}$[kg/s]	12	τ_R[s]	25
K_4	0.8	K_5	0.2	τ_3[s]	15
τ_4[s]	2.5	K_{T_p}	7	K_{T_i}	5
τ_S[s]	0.05	τ_{SF}[s]	0.4	F_{max}[p.u.]	1.25
F_{min}[p.u.]	0	c_2[p.u.]	0.05	τ_{AV}[s]	0.1
τ_{TD}[s]	0.3	g_{max}[p.u.]	1.25	g_{min}[p.u.]	0.1
R[p.u.]	0.04	K_{t_p}	3	K_{t_i}	2
τ_P[s]	0.02	H_t[s]	3.9821	D_t[p.u]	2
K_{AGC_2}	60				
Charging mode					
Parameter	Value	Parameter	Value	Parameter	Value
$T_{c_{in1o}}$[K]	283.15	$T_{c_{out1o}}$[K]	497.6	ϵ_{hx_1}	0.8785
$T_{c_{in2o}}$[K]	323.15	$T_{c_{out2o}}$[K]	420.5	ϵ_{hx_2}	0.8
$T_{c_{in3o}}$[K]	323.15	$T_{c_{out3o}}$[K]	421.5	ϵ_{hx_3}	0.8
$T_{c_{in4o}}$[K]	323.15	$T_{c_{out4o}}$[K]	421.2	ϵ_{hx_4}	0.8
$\eta_{c_{i1}}$[p.u.]	0.8200	$\eta_{c_{m1}}$[p.u.]	0.99	$\pi_{c_{1o}}$	5.4290
$\eta_{c_{i2}}$[p.u.]	0.9115	$\eta_{c_{m2}}$[p.u.]	0.99	$\pi_{c_{2o}}$	2.3460
$\eta_{c_{i3}}$[p.u.]	0.9023	$\eta_{c_{m3}}$[p.u.]	0.99	$\pi_{c_{3o}}$	2.3460
$\eta_{c_{i4}}$[p.u.]	0.9097	$\eta_{c_{m4}}$[p.u.]	0.99	$\pi_{c_{4o}}$	2.3460
τ_{hx_1}[s]	12	τ_{hx_2}[s]	12	τ_{hx_3}[s]	12
τ_{hx_4}[s]	12	H_c[s]	12.957	D_c[p.u.]	0
$P_{c_{mo}}$[MW]	58.7	γ	1.4	c_p[kJ/kg.K]	1.055
$T_{hx_{in}}$[K]	298.7	R[p.u.]	0.04	K_{c_d}	0.214
K_{c_p}	0.4147	K_{c_i}	0.1485	K_{c_f}	1.0792
τ_{CD}[s]	0.2	τ_{IGV}[s]	0.2	l_{max}[p.u.]	1.15
l_{min}[p.u.]	0.6	τ_{Dr}[s]	1.5	τ_P[s]	0.02
K_{droop}[p.u.]	2000	$\dot{m}_{c_o}$[kg/s]	108		

Table B.4: CAES simplified model (Model 2) parameters

Discharging mode					
Parameter	Value	Parameter	Value	Parameter	Value
T_{d_o}[K]	823.15	ΔT_o[K]	315.73	T_{x_o}[K]	762.41
η_{t_i}[p.u.]	0.7995	η_{t_m}[p.u.]	0.9801	π_{t_o}	41.451
T_{b_o}[K]	599.15	ϵ_r[p.u.]	0.80	K_{AGC_2}	60
c_p[kJ/kg.K]	1.055	$P_{t_{mo}}$[MW]	280	γ	1.4
$\dot{m}_{t_o}$[kg/s]	417	$\dot{m}_{f_o}$[kg/s]	12	τ_R[s]	25
K_4	0.8	K_5	0.2	τ_3[s]	15
τ_4[s]	2.5	K_{T_p}	7	K_{T_i}	5
τ_S[s]	0.05	τ_{SF}[s]	0.4	F_{max}[p.u.]	1.25
F_{min}[p.u.]	0	c_2[p.u.]	0.05	τ_{AV}[s]	0.1
τ_{TD}[s]	0.3	g_{max}[p.u.]	1.25	g_{min}[p.u.]	0.1
R[p.u.]	0.04	K_{t_p}	3	K_{t_i}	2
τ_P[s]	0.02	H_t[s]	3.9821	D_t[p.u]	2
Charging mode					
Parameter	Value	Parameter	Value	Parameter	Value
$T_{c_{in_{LPo}}}$[K]	283.15	$T_{c_{out_{LPo}}}$[K]	497.6	$\epsilon_{hx_{LP}}$	0.8785
$T_{c_{in_{HPo}}}$[K]	323.15	$T_{c_{out_{HPo}}}$[K]	420.5	$\epsilon_{hx_{HP}}$	0.8
$\eta_{c_{i_{LP}}}$[p.u.]	0.8200	$\eta_{c_{m_{LP}}}$[p.u.]	0.99	$\pi_{c_{LPo}}$	5.4290
$\eta_{c_{i_{HP}}}$[p.u.]	0.9142	$\eta_{c_{m_{HP}}}$[p.u.]	0.9702	$\pi_{c_{HPo}}$	12.9117
$\tau_{hx_{LP}}$[s]	12	$\tau_{hx_{HP}}$[s]	12	H_c[s]	12.957
$P_{c_{mo}}$[MW]	58.7	γ	1.4	c_p[kJ/kg.K]	1.055
$T_{hx_{in}}$[K]	298.7	R[p.u.]	0.04	K_{c_d}	-0.2140
K_{c_p}	-0.4146	K_{c_i}	-0.1485	K_{c_f}	1.0792
τ_{CD}[s]	0.2	τ_{IGV}[s]	0.2	l_{max}[p.u.]	1.15
l_{min}[p.u.]	0.6	τ_{Dr}[s]	1.5	τ_P[s]	0.02
K_{droop}[p.u.]	2000	$\dot{m}_{c_o}$[kg/s]	108	D_c[p.u.]	0

Table B.5: CAES Model 3 parameters

Discharging mode					
Parameter	Value	Parameter	Value	Parameter	Value
$T_{d_{HPo}}$[K]	823.15	$T_{d_{LPo}}$[K]	1098.2	$T_{x_{HPo}}$[K]	612.15
$T_{x_{LPo}}$[K]	668.15	$\pi_{t_{HPo}}$	3.818	$\pi_{t_{LPo}}$	10.856
$\eta_{t_{HPm}}$[p.u.]	0.99	$\eta_{t_{LPm}}$[p.u.]	0.99	$\eta_{t_{HPi}}$[p.u.]	0.8065
$\eta_{t_{LPi}}$[p.u.]	0.7926	T_{b_o}[K]	599.15	ϵ_r[p.u.]	0.80
c_p[kJ/kg.K]	1.055	$P_{t_{mo}}$[MW]	280	γ	1.4
$\dot{m}_{t_o}$[kg/s]	417	$\dot{m}_{f_o}$[kg/s]	12	τ_R[s]	25
K_4	0.8	K_5	0.2	τ_3[s]	15
τ_4[s]	2.5	K_{T_p}	7	K_{T_i}	5
τ_S[s]	0.05	τ_{SF}[s]	0.4	F_{max}[p.u.]	1.25
F_{min}[p.u.]	0	c_2[p.u.]	0.05	τ_{AV}[s]	0.1
τ_{TD}[s]	0.3	g_{max}[p.u.]	1.25	$p_{s_{\max}}$[bar]	72
R[p.u.]	0.04	K_{t_p}	3	K_{t_i}	2
τ_P[s]	0.02	H_t[s]	3.9821	D_t[p.u]	2
K_{AGC_2}	60	$\lambda_{\max}$[p.u.]	2.4	$\lambda_{\min}$[p.u.]	0
$\dot{\lambda}_{\max}$[p.u.]	99	$\dot{\lambda}_{\min}$[p.u.]	-99	p_{am}[bar]	1.01325
Charging mode					
Parameter	Value	Parameter	Value	Parameter	Value
$T_{c_{in_{LPo}}}$[K]	283.15	$T_{c_{out_{LPo}}}$[K]	497.6	$\epsilon_{hx_{LP}}$	0.8785
$T_{c_{in_{HPo}}}$[K]	323.15	$T_{c_{out_{HPo}}}$[K]	420.5	$\epsilon_{hx_{HP}}$	0.8
$\eta_{c_{i_{LP}}}$[p.u.]	0.8200	$\eta_{c_{m_{LP}}}$[p.u.]	0.99	$\pi_{c_{LPo}}$	5.4290
$\eta_{c_{i_{HP}}}$[p.u.]	0.9142	$\eta_{c_{m_{HP}}}$[p.u.]	0.9702	$\pi_{c_{HPo}}$	12.9117
$\tau_{hx_{LP}}$[s]	12	$\tau_{hx_{HP}}$[s]	12	H_c[s]	12.957
$P_{c_{mo}}$[MW]	58.7	γ	1.4	c_p[kJ/kg.K]	1.055
$T_{hx_{in}}$[K]	298.7	R[p.u.]	0.04	K_{c_d}	-0.2140
K_{c_p}	-0.4146	K_{c_i}	-0.1485	K_{c_f}	1.0792
τ_{CD}[s]	0.2	τ_{IGV}[s]	0.2	l_{max}[p.u.]	1.15
l_{min}[p.u.]	0.6	τ_{Dr}[s]	1.5	τ_P[s]	0.02
K_{droop}[p.u.]	2000	$\dot{m}_{c_o}$[kg/s]	108	D_c[p.u.]	0
K_{cv}	0.5	K_{cgn}	0.1	K_{sgp}	0.5
p_{offset}	0.01	p_{am}[bar]	1.01325	$p_{s_{\max}}$[bar]	72

Table B.6: Compressor map parameters for Model 3

Parameter	Value	Parameter	Value	Parameter	Value
T_{am}[K]	283.15	p_{am}[bar]	1.01325	N_{c_o}[p.u.]	1
$N^{map}_{crr_{LPo}}$[p.u.]	0.8925	$\dot{m}^{map}_{crr_{LPo}}$[Kg/s]	2.42	$\pi^{map}_{c_{LPo}}$	2.4917
$N^{map}_{crr_{HPo}}$[p.u.]	0.8000	$\dot{m}^{map}_{crr_{HPo}}$[Kg/s]	2.00	$\pi^{map}_{c_{HPo}}$	2.2950
b_o	-91.14	b_1	-169.60	b_2	247.6
b_3	57.07	b_4	-143.20	b_5	95.06
b_6	-17.96	b_7	43.57	b_8	-28.13

Appendix C

Parameters of CAES Model for Transient Stability Studies

Table C.1: CAES transient stability model parameters

Discharging mode					
Parameter	Value	Parameter	Value	Parameter	Value
$T_{d_{HPo}}$[K]	823.15	$T_{d_{LPo}}$[K]	1098.2	$T_{x_{HPo}}$[K]	612.15
$T_{x_{LPo}}$[K]	668.15	$\pi_{t_{HPo}}$	3.818	$\pi_{t_{LPo}}$	10.856
$\eta_{t_{HPm}}$[p.u.]	0.9900	$\eta_{t_{LPm}}$[p.u.]	0.9900	$\eta_{t_{HPi}}$[p.u.]	0.8065
$\eta_{t_{LPi}}$[p.u.]	0.7926	T_{b_o}[K]	599.15	ϵ_r[p.u.]	0.8000
c_p[kJ/kg.K]	1.055	$P_{t_{mo}}$[MW]	280	Sn_g[MVA]	341
$\dot{m}_{t_o}$[kg/s]	417	$\dot{m}_{f_o}$[kg/s]	12	τ_R[s]	25
K_4	0.8	K_5	0.2	τ_3[s]	15
τ_4[s]	2.5	K_{T_p}	7	K_{T_i}	5
τ_S[s]	0.05	τ_{SF}[s]	0.4	F_{max}[p.u.]	1.25
F_{min}[p.u.]	0	c_2[p.u.]	0.05	τ_{AV}[s]	0.1
τ_{TD}[s]	0.3	g_{max}[p.u.]	1.25	γ	1.4
R[p.u.]	0.027	K_{t_p}	3	K_{t_i}	2
τ_P[s]	0.02	FL_t[s]	1	$\Delta p_{\min}$[bar]	4
K_{AGC}	5	$\lambda_{\max}$[p.u.]	2.4	$\lambda_{\min}$[p.u.]	0
$\dot{\lambda}_{\max}$[p.u.]	99	$\dot{\lambda}_{\min}$[p.u.]	-99	p_{am}[bar]	1.01325
$SoC_{\max}$[p.u.]	0.77	$SoC_{\min}$[p.u]	0	T_s[K]	323.1500
$p_s(0)$[p.u.]	0.73	$p_{s_{\min}}$[bar]	30	$p_{s_{\max}}$[bar]	72
Charging mode					
Parameter	Value	Parameter	Value	Parameter	Value
$T_{c_{in_{LPo}}}$[K]	283.15	$T_{c_{out_{LPo}}}$[K]	497.6	$\epsilon_{hx_{LP}}$	0.8785
$T_{c_{in_{HPo}}}$[K]	323.15	$T_{c_{out_{HPo}}}$[K]	420.5	$\epsilon_{hx_{HP}}$	0.8
$\eta_{c_{i_{LP}}}$[p.u.]	0.9000	$\eta_{c_{m_{LP}}}$[p.u.]	0.99	$\pi_{c_{LPo}}$	5.4290
$\eta_{c_{i_{HP}}}$[p.u.]	0.9142	$\eta_{c_{m_{HP}}}$[p.u.]	0.9702	$\pi_{c_{HPo}}$	12.9117
$\tau_{hx_{LP}}$[s]	12	$\tau_{hx_{HP}}$[s]	12	Sn_{mot}[MVA]	75
$P_{c_{mo}}$[MW]	62	γ	1.4	c_p[kJ/kg.K]	1.055
$T_{hx_{in}}$[K]	298.7	R[p.u.]	0.04	K_{c_d}	-0.2140
K_{c_p}	-0.4146	K_{c_i}	-0.1485	K_{c_f}	1.0792
τ_{CD}[s]	0.2	τ_{IGV}[s]	0.2	l_{max}[p.u.]	1.25
l_{min}[p.u.]	0.7	$\dot{m}_{c_o}$[kg/s]	108	τ_P[s]	0.02
K_{cv}	0.5	K_{cgn}	0.1	K_{sgp}	0.5
p_{offset}	0.01	p_{am}[bar]	1.01325	$p_{s_{\max}}$[bar]	72
FL_c	1				

Table C.2: Compressor map parameters for CAES transient stability model

Parameter	Value	Parameter	Value	Parameter	Value
T_{am}[K]	283.15	p_{am}[bar]	1.01325	N_{c_o}[p.u.]	1
$N^{map}_{crr_{LPo}}$[p.u.]	0.8925	$\dot{m}^{map}_{crr_{LPo}}$[Kg/s]	2.42	$\pi^{map}_{c_{LPo}}$	2.4917
$N^{map}_{crr_{HPo}}$[p.u.]	0.8000	$\dot{m}^{map}_{crr_{HPo}}$[Kg/s]	2.00	$\pi^{map}_{c_{HPo}}$	2.2950
b_o	-91.14	b_1	-169.60	b_2	247.6
b_3	57.07	b_4	-143.20	b_5	95.06
b_6	-17.96	b_7	43.57	b_8	-28.13